

Investigating Glymphatic Function In Alzheimer's Disease Pathology

**A thesis presented in fulfilment of the requirements for the degree of
Doctor of Philosophy to University College London**

Ozama Ismail

Centre for Advanced Biomedical Imaging

Division of Medicine

University College London

Declaration

I, Ozama Ismail, confirm that the work presented in this thesis is my own. Where information has been derived from other sources, I confirm that this has been indicated in the thesis.



Abstract

Alzheimer's disease is fast becoming the greatest healthcare challenge of our time, with no known cure to-date. Brought about by the toxic formation of plaques of amyloid- β and tangles of tau in the brain, much is still unknown about the precise mechanisms that initiate these protein accumulations, thought to occur decades before clinical manifestation of symptoms. One theory is that an imbalance between the production of these proteins and their removal from the brain promotes retention that eventually aggregates into entities that devastate molecular and cellular machinery. Thus, targeting waste clearance mechanisms responsible for removing cerebral metabolites, including amyloid- β and tau, present novel, enthralling research targets. The glymphatic system is one such pathway that has been recently characterised. Considered a surrogate for lymphatics which are largely lacking in the brain, this fluid network relies on the water channel aquaporin-4, expressed highly on glia, thus being named "glymphatics". In this work, first, a surgical protocol was established in the mouse brain to facilitate the delivery of tracer molecules into the cerebrospinal fluid. Direct, single time-point, histological assessment of fluorescent tracer distribution was performed to check consistency with previous characterisation of glymphatics in the mouse brain. Glymphatics were then visualised dynamically across the whole brain using magnetic resonance imaging. Glymphatic patterns were investigated in real-time by imaging fluid dynamics in the brain alongside a potent blocker of aquaporin-4. Next, imaging was used to characterise glymphatic changes and aquaporin-4 profiles in mouse models of Alzheimer's pathology. This revealed a time-dependant relationship between glymphatics and tau accumulation. Finally, the findings were extrapolated onto humans by studying aquaporin-4 modifications in subjects with and without cognitive deficits. Here, the crucial relationship between aquaporin-4 and pathological aggregates of tau and amyloid- β was determined. Furthermore, dystrobrevin, a membrane protein linked to aquaporin-4, was also profiled in the setting of aging and amyloid- β pathology. The work presented herein elucidates the role of glymphatic perturbances in the context of Alzheimer's disease and clarifies the implications of aquaporin-4 mediated clearance in neurodegeneration.

Impact Statement

The work presented in this thesis focuses on a novel research arm in Alzheimer's disease biology. Research in glymphatics is a recent but rapidly developing topic in the neuroscience research domain. The novel knowledge and discoveries presented in this body of work adds significant volume to the current understanding of waste clearance from the brain and its implications in neurodegenerative disease. Hence, it accelerates the understanding of a devastating human disease that is widespread. A clearer understanding of the disease onset is still lacking and thus, these novel data are beneficial in supporting the progress of both clinical and basic science research. Elucidating these new disease mechanisms may also speed up the discovery of disease modifying therapies, which are desperately needed. Alzheimer's disease is the 5th biggest killer globally and is still without a cure. This is largely due to the lack of a full picture of the mechanistic causes underlying disease onset. As such, the innovative research angles and novel data presented here in the context of a still poorly understood malady provides new scientific insights, which are necessary for the development of precise therapeutics in the race for a cure.

Acknowledgements

This PhD has been a turbulent journey and one I would not have survived alone. I am indebted to so many people in my life for getting me this far.

I am beholden to Prof. Mark Lythgoe for taking a chance on me when I first arrived as a bright-eyed research technician and later trusting me with the reigns of CABI's operations, nurturing my professional development whilst tirelessly encouraging me to pursue my scientific interests. Mark also sparked my interest in public engagement, and the many exhilarating activities we undertook together made my time at CABI extraordinary.

I am also grateful for the steadfast care and supervision of Dr Jack Wells. Jack's meticulous approach to science and unparalleled dedication to his students is inspiring. His constant presence, be it for an in-depth intellectual discussion at the lab bench, or a laugh over a silly anecdote by the kitchen sink, made being his student a pleasure. Without Jack's belief in me, I would not have seen this PhD through. I am also deeply thankful for the academic wisdom as well as the delightful friendship of Dr Ian Harrison. Ian has been fiercely supportive of all my work, always making time and never without a smile, whenever I needed lab guidance. I will cherish the days doing those long, difficult experiments, because of his companionship.

CABI holds a special place in my heart because of all the splendid folk that have passed through its doors, enabling me the privilege of many fervent friendships. I treasure the friendships of my fellow "classmates", Yolanda Ohene, Heather Fitzke, Hannah Greenwood, Phoebe Evans, Eleanor Bird, and Payam Nahavandi. I am especially grateful to Dr Daniel Stuckey, Dr Tammy Kalber, Dr Bernard Siow, Dr Claire Walsh and Jen Crouch for their expert advice whenever I needed it. A very special mention goes to the alumni whose brilliance I sorely miss – Holly Holmes, Rupy Ghatrora, Izzy Christie, Niral Patel, Raj Ramasawmy, Ben Duffy, Tom Roberts, Val Taylor, John Connell, Morium Ali, May Zaw-Thin, Jed Wingrove, Yanan Zhu, Niall Colgan and Vin Rajkumar.

My academic development was bolstered by several accomplished collaborators along the way. I am grateful for the guidance of Dr Michael O'Neill, Dr Zeshan Ahmed, Tracey Murray and the many other scientists with whom I worked with at Eli Lilly UK and USA. I am also immensely appreciative of the support of Prof. Elizabeth Fisher and Dr Frances Wiseman at the Institute of Neurology and the many invaluable discussions we shared.

I am indebted to Prof. Jeffrey Iliff at OHSU for taking me under his wing and enhancing my research portfolio. Jeff's patience and careful guidance shaped me into a better scientist and my time under his mentorship will be the yardstick by which all my future research experiences will be measured. I am also grateful for the kindness shown to me by his team – Marie Wang, Jim Goodman, Matt Simon and Marquitta Smith, and the many colleagues at

Anaesthesiology, including members of the histology, microscopy and molecular biology cores at OHSU. I will always remember their unwavering enthusiasm and generosity.

My love for neuroscience was inspired by Dr Helen Barefoot, and I am thankful for her untiring support, starting from my early days as an undergraduate, all the way till today.

I would like to give a special shout out to my fellow cast mates of Why Aren't You A Doctor Yet? – Alex Lathbridge, Hana Ayoob and Suhail Patel. The studio time I shared with them enriched my life with laughter, knowledge and love and made me a better human being. They will forever be my “mandem”.

I am extremely thankful to Dr Steve Cross for bringing me into the stand-up comedy circuit and introducing me to a whole new creative world of science communication, at a time when I was at my lowest and needed it the most. Recruiting me into the Talent Factory was the rejuvenation I needed to keep going, and I am grateful for the life-long friends I made through this scheme. I would especially like to mention Anna Ploszajski, Sarah Jones, Cerys Bradley and Rachel Wheeley whose mirth and endless wit brought me boundless happiness.

I would be lost without those special friends who have stood by me through thick and thin. I express my deepest gratitude to Grace Salisbury, Shannon Shibata-Germanos, Caz Sinclair, Gini Kirkpatrick, Chris Isherwood, Emma Ranade, Ali Thomas, Charuni Mason, Matt Daniels, Steve Chen, José Delgado, Reynaldo Roman, Michelle Millar and Peter Rennes for providing release and escape when things got too tough. I also thank the coaches at Royal Docks for taking a genuine interest in me and cheering me on in both my work and workouts.

I forged many terrific friendships during my brief time in the USA, and the experiences I shared with them will go down as some of my life's most treasured moments. I particularly want to thank Steven Carter, Sara Charney, Jimmie Erwin and Brittani Price whose warmth, humour and generosity I will forever cherish. I am especially grateful to Grace Bierman for being an incredible counsellor and confidante. I am also thankful to the lovely folk at Intrepid PDX for their unfailing zest and compassion, and for making my time in the USA so joyous.

My utmost gratefulness goes to my family, first, to my loving parents, Hameed Ismail and Zareena Ismail, for dedicating their lives work to solely bettering the lives of their children and putting me where I am today. Also, to my brother Dilshad Ismail whose continued support has brought me constant warmth. Words fail me when it comes to thanking my biggest cheerleaders – my sister Nadiya Ismail and my brother-in-law Ashish Puliyeel, who have also occasionally been a akin to a second set of parents. Their unrelenting support, infinite love and constant encouragement were, at times, the only things that kept me going.

And finally, to the newest member of the family, Ezra Rumi Ismail Puliyeel, for bringing me so much joy when I penned this thesis, making the final stages of my PhD an absolute delight.

Selected Publications

The following is a selection of my authored publications from my time in the AD Research team at the UCL Centre for Advanced Biomedical Imaging.

Manuscripts in preparation

Epothilone D as a microtubule stabilizing agent in a mouse model of tauopathy: a multiparametric quantitative MRI study. Ozama Ismail, Ian F. Harrison, Holly E. Holmes, Jack A. Wells, Da Ma, Niall Colgan, James M. O'Callaghan, Nicholas M. Powell, Tracey K. Murray, Alice Fisher, Zeshan Ahmed, Marc Modat, M. Jorge Cardoso, Simon Walker-Samuel, Elizabeth M. C. Fisher, Sebastian Ourselin, Ross A. Johnson, Emily C. Collins, Michael J. O'Neill, Mark F. Lythgoe.

Impaired glymphatic function and clearance of tau in an Alzheimer's disease model. Ian F. Harrison, **Ozama Ismail**, Asif Machhada, Niall Colgan, Yolanda Ohene, Payam Nahavandi, Zeshan Ahmed, Alice Fisher, Soraya Meftah, Tracey K. Murray, Ole P. Ottersen, Erlend A. Nagelhus, Michael J. O'Neill, Jack A. Wells, Mark F. Lythgoe.

Non-invasive MRI of blood-cerebrospinal fluid barrier function. Phoebe G. Evans, Magdalena Sokolska, Adrianna Alves, Ian F. Harrison, Yolanda Ohene, Payam Nahavandi, **Ozama Ismail**, Elena Miranda, Mark F. Lythgoe, David L. Thomas, Jack A. Wells.

Published manuscripts

Non-invasive MRI of brain clearance pathways using multiple echo time arterial spin labelling: An Aquaporin-4 study. Yolanda Ohene, Ian F. Harrison, Payam Nahavandi, **Ozama Ismail**, Eleanor V. Bird, Ole P. Otterson, Erlend A. Nagelhus, David L. Thomas, Mark F. Lythgoe, Jack A. Wells. *Neuroimage*. 2018 Dec 15; doi: 10.1016/j.neuroimage.2018.12.026.

Non-invasive imaging of CSF-mediated brain clearance pathways via assessment of perivascular fluid movement with diffusion tensor MRI. Ian F. Harrison, Bernard Siow, Aisha B. Akilo, Phoebe G. Evans, **Ozama Ismail**, Yolanda Ohene, Payam Nahavandi, David L. Thomas, Mark F. Lythgoe, Jack A. Wells. *eLIFE*. 2018 Jul 31; e34028 DOI: 10.7554/eLife.34028 .

In vivo imaging of tau pathology using magnetic resonance imaging textural analysis. Niall Colgan, Balaji Ganeshan, Ian F. Harrison, **Ozama Ismail**, Holly E. Holmes, Jack A. Wells, Nicholas M. Powell, James M. O'Callaghan, Michael J. O'Neill, Tracey K. Murray, Zeshan Ahmed, Emily C. Collins, Ross Johnson, Ashley Groves, Mark F. Lythgoe. *Frontiers in Neuroscience*. 2017 Nov 6;11:599. doi: 10.3389/fnins.2017.00599.

Tissue magnetic susceptibility mapping as a marker of tau pathology in Alzheimer's disease. James M. O'Callaghan, Holly E. Holmes, Nicholas M. Powell, Jack A. Wells, **Ozama Ismail**, Ian F. Harrison, Bernard Siow, Ross Johnson, Zeshan Ahmed, Alice Fisher, S Meftah, Michael J. O'Neill, Tracey K. Murray, Emily C. Collins, Karin Shmueli, Mark F. Lythgoe. *Neuroimage*. 2017 Oct 1;159:334-345. doi: 10.1016/j.neuroimage.2017.08.003. Epub 2017 Aug 4.

Comparison of in vivo and ex vivo MRI for the detection of structural abnormalities in a mouse model of tauopathy. Holly E. Holmes, Nicholas M. Powell, Da Ma, **Ozama Ismail**, Ian F. Harrison, Jack A. Wells, Niall Colgan, James M. O'Callaghan, Ross A. Johnson, Tracey K. Murray, Zeshan Ahmed, Morten Heggenes, Alice Fisher, M. Jorge Cardoso, Marc Modat, Michael J. O'Neill, Emily C. Collins, Elizabeth M. C. Fisher, Sebastien Ourselin, Mark F. Lythgoe. *Frontiers in Neuroinformatics*. 2017 Mar 31;11:20. doi: 10.3389/fninf.2017.00020.

Imaging the accumulation and suppression of tau pathology using multi-parametric MRI. Holly E. Holmes, Niall Colgan, **Ozama Ismail**, Da Ma, Nicholas M. Powell, James M. O'Callaghan, Ian F. Harrison, Ross A. Johnson, Tracey K. Murray, Zeshan Ahmed, M. Heggenes, Alice Fisher, Jorge M. Cardoso, Marc Modat, Simon Walker-Samuel, Elizabeth M. C. Fisher, Sebastien Ourselin, Michael J. O'Neill, Jack A. Wells, Emily C. Collins, Mark F. Lythgoe. 2015. *Neurobiology of Aging*. 39:184-194: DOI: 10.1016/j.neurobiolaging.2015.12.001.

Application of neurite orientation dispersion and density imaging (NODDI) to a tau pathology model of Alzheimer's disease. Niall Colgan, Bernard Siow, James M. O'Callaghan, Ian F. Harrison, Jack A. Wells, Holly E. Holmes, **Ozama Ismail**, Simon Richardson, Daniel C. Alexander, Emily C. Collins, Elizabeth M.C. Fisher, Ross Johnson, Adam J. Schwarz, Zeshan Ahmed, Michael J. O'Neill, Tracey K. Murray, H. Zhang, Mark F. Lythgoe. 2015. *Neuroimage*, 125:739-744. DOI: 10.1016/j.neuroimage.2015.10.043.

In vivo imaging of tau pathology using multi-parametric quantitative MRI. Jack A. Wells, James M. O'Callaghan, Holly E. Holmes, Nicholas M. Powell, Ross A. Johnson, Bernard Siow, Francisco Torrealdea, **Ozama Ismail**, Simon Walker-Samuel, Xavier Golay, Marilena Rega, Simon Richardson, Marc Modat, Jorge M. Cardoso, Sebastian Ourselin, Adam J. Schwarz, Zeshan Ahmed, Tracey K. Murray, Michael J. O'Neill, Emily C. Collins, Niall Colgan, Mark F. Lythgoe. 2015. *Neuroimage*. 1 (111): DOI: 10.1016/j.neuroimage.2015.02.023.

Increased cerebral vascular reactivity in the tau expressing rTg4510 mouse: evidence against the role of tau pathology to impair vascular health in Alzheimer's disease. Jack A. Wells, Holly E. Holmes, James M O'Callaghan, Niall Colgan, **Ozama Ismail**, Elizabeth M.C. Fisher, Bernard Siow, Tracey K. Murray, Adam J. Schwarz, Michael J. O'Neill, Emily C. Collins and Mark F. Lythgoe. 2014. *Journal of Cerebral Blood Flow & Metabolism*, 35(3):359-62. DOI: 10.1038/jcbfm.2014.224.

Selected Conference Proceedings

Characterising the Astrocytic Profile of Dystrobrevin in the Brain during Alzheimer's Disease. Ozama Ismail, Marie X. Wang, Jeffrey J. Iliff. 2019. *Alzheimer's Association International Conference*.

Dynamic Contrast-Enhanced MRI to Assess Glymphatic Function in the NL-F Mouse Model of Alzheimer's Disease. Ozama Ismail, Ian F. Harrison, Jack A. Wells, Payam Nahavandi, Yolanda Ohene, Phoebe Evans, Zeshan Ahmed, Katherine Sung, Tracey K. Murray, Michael J. O'Neill, Frances Wiseman, Elizabeth Fisher, Mark F. Lythgoe. 2019. *Alzheimer's Association International Conference*.

Glymphatic Function During Early Stage Amyloid Pathology: Dynamic Contrast-Enhanced MRI In The J20 Mouse Model Of Alzheimer's Disease. Ozama Ismail, Ian F. Harrison, Jack A. Wells, Payam Nahavandi, Yolanda Ohene, Zeshan Ahmed, Alice Fisher, Tracey K. Murray, Michael J. O'Neill, Frances Wiseman, Elizabeth M. C. Fisher, Mark F. Lythgoe. 2018. *Alzheimer's Association International Conference*.

Pharmacological Blockade of Aquaporin-4 Inhibits Glymphatic Flow and Clearance of Tau from the Mouse Brain. Ian F. Harrison, Ozama Ismail, Yolanda Ohene, Payam Nahavandi, Jack A. Wells, Mark F. Lythgoe. 2018. *Alzheimer's Association International Conference*.

Non-Invasive Imaging of Brain Clearance Pathways using Multiple Echo Time ASL: An Aquaporin-4 Study. Yolanda Ohene, Ian F. Harrison, Payam Nahavandi, Ozama Ismail, Ole P. Ottersen, Erlend A. Nagelhus, David L. Thomas, Mark F. Lythgoe, Jack A. Wells. 2018. *Alzheimer's Association International Conference*.

Investigating Glymphatic Function during Early Tau Pathology using Dynamic Contrast-Enhanced MRI. Ozama Ismail, Ian F. Harrison, Jack A. Wells, Yolanda Ohene, Payam Nahavandi, Alexander V. Gourine, Zeshan Ahmed, Alice Fisher, Tracey K. Murray, Ross A. Johnson, Emily C. Collins, Michael J. O'Neill, Mark F. Lythgoe. 2017. *Alzheimer's Association International Conference*

Imaging the Efficacy of Microtubule Stabilizing Agent Epothilone D in The rTg4510 Mouse Model of Tauopathy. Ozama Ismail, Ian F. Harrison, Holly E. Holmes, Jack A. Wells, Da Ma, Nick M. Powell, Niall Colgan, James M. O'Callaghan, Sebastian Ourselin, Tracey K. Murray, Alice Fisher, Zeshan Ahmed, Ross A. Johnson, Emily C. Collins, Michael J. O'Neill, Mark F. Lythgoe. 2015. *Alzheimer's Association International Conference & British Chapter of the International Society for Magnetic Resonance Imaging Annual Conference*.

A Multi-Scale MRI Approach to Investigate Novel Drug Treatment Strategies in Mouse Models Of Alzheimer's Disease. Ozama Ismail, Holly E. Holmes, Niall Colgan, Da Ma, Jack A. Wells, Nicholas Powell, James M. O'Callaghan, Ian F. Harrison, Simon Walker-Samuel, Marc Modat, M. Jorge Cardoso Sebastian Ourselin, Elizabeth M. C. Fisher, Tracey K. Murray, Zeshan Ahmed, Michael J. O'Neill, Ross A. Johnson, Emily C. Collins, Mark F. Lythgoe. 2015. *Alzheimer's Association International Conference & British Chapter of the International Society for Magnetic Resonance Imaging Annual Conference.*

Glymphatic Clearance Impaired in a Mouse Model of Tauopathy: Captured Using Contrast-Enhanced MRI. Ian F. Harrison, Asif Machhada, Niall Colgan, Ozama Ismail, James M. O'Callaghan, Holly E. Holmes, Jack A. Wells, Alexander V. Gourine, Tracey K. Murray, Zeshan Ahmed, Ross A. Johnson, Emily C. Collins, Michael J. O'Neill, Mark F. Lythgoe. 2015. *Alzheimer's Association International Conference & British Chapter of the International Society for Magnetic Resonance Imaging Annual Conference.*

An Imaging Strategy to Characterise Tau Pathology *in vivo* in a Model of Alzheimer's disease using Multi-Parametric MRI. Ozama Ismail, Holly E. Holmes, Jack A. Wells, James M. O'Callaghan, Da Ma, Nicholas Powell, Sebastian Ourselin, Tracey K. Murray, Zeshan Ahmed, Michael J. O'Neill, Ross A. Johnson, Emily C. Collins, Niall Colgan, Mark F. Lythgoe. 2014. *Alzheimer's Association International Conference & British Chapter of the International Society for Magnetic Resonance Imaging Annual Conference.*

Awards

Alzheimer's Association – **Travel Fellowship**

(July 2018)

University College London – **Bogue Research Fellowship**

(March 2018)

University College London – **Graduate Research Scholarship**

(March 2017)

Alzheimer's Association – **Lead Volunteer Award**

(July 2017)

Alzheimer's Association – **Student Volunteer Award**

(July 2016)

British Chapter of ISMRM Annual Meeting – **Poster Pitch Award Runner-Up**

(September 2015)

Alzheimer's Association International Conference – **Student Poster Award**

(July 2015)

Alzheimer's Imaging Consortium – **Best Poster Award**

(July 2014)

British Chapter of ISMRM Annual Postgraduate Meeting – **People's Award for Best Oral Presentation**

(April 2014)

Table of contents

Declaration.....	3
Abstract.....	5
Impact Statement.....	7
Acknowledgements.....	9
Selected Publications.....	11
Selected Conference Proceedings.....	13
Awards.....	15
Table of contents.....	17
Index of figures.....	21
Abbreviations.....	25
1. Alzheimer’s Disease.....	29
1.1 A brief history of Alzheimer’s disease.....	29
1.2 Present day prevalence of dementia.....	32
1.3 Pathogenesis of AD.....	33
1.3.1 The spread of pathology in the AD brain.....	33
1.3.2 Amyloid.....	36
1.3.3 Tau.....	40
1.3.4 Neuroinflammation.....	43
1.3.5 Cholinergic hypothesis.....	44
1.4 Risk factors for AD.....	45
1.4.1 Genetics.....	46
1.4.2 Modifiable risk factors.....	48
1.5 Mouse models.....	51
1.6 Current approaches to therapeutics.....	54
1.7 Biomarkers for diagnosis.....	58
1.7.1 CSF biomarkers.....	60
1.7.2 PET.....	60

1.7.3	MRI	63
1.7.4	The next generation of biomarkers	66
2.	The Glymphatic System	69
2.1	Cerebrospinal fluid	69
2.2	The blood brain barrier	71
2.3	Glymphatic exchange	73
2.4	Aquaporin 4	77
2.5	A β and tau in the extracellular space	78
2.6	A β and tau as glymphatic substrates	80
2.7	Aims of this project.....	82
3.	A Surgical Mouse Model to Assess Glymphatic Inflow	83
3.1	Summary	83
3.2	Introduction.....	84
3.3	Methods.....	85
3.3.1	Intracisternal infusion of tracers into the mouse subarachnoid space.....	85
3.3.2	Evans blue dye to assess superficial tracer distribution	86
3.3.3	Fluorescent dyes to assess parenchymal tracer distribution	87
3.3.4	Analysis of fluorescent dye penetration	88
3.4	Results	89
3.4.1	Macroscopic assessment with Evans blue dye.....	89
3.4.2	Microscopic assessment with fluorescent tracers	91
3.5	Discussion	94
4.	Magnetic Resonance Imaging and Pharmacological Inhibition of Glymphatic Function in the Mouse Brain	99
4.1	Summary	99
4.2	Introduction.....	100
4.3	Methods.....	101
4.3.1	Mice and aquaporin-4 blocking agent.....	101
4.3.2	Surgical preparation for contrast enhanced MRI.....	102
4.3.3	Magnetic resonance image acquisition	103

4.3.4	Image processing and analysis	104
4.3.5	Intracerebral infusion of tau homogenate and CSF collection.....	106
4.3.6	Tau enzyme linked immunosorbant assays.....	107
4.3.7	Statistical analysis.....	108
4.4	Results.....	109
4.4.1	Spatial and temporal profile of glymphatic inflow in the mouse brain	109
4.4.2	Effect of pharmacological inhibition of aquaporin-4 on glymphatic function....	111
4.5	Discussion	115
5.	Glymphatic Function in a Tauopathy Model of Alzheimer’s Disease	119
5.1	Summary	119
5.2	Introduction.....	120
5.3	Methods	121
5.3.1	Mice	121
5.3.2	Surgical preparation, magnetic resonance imaging and image analysis	121
5.3.3	Tau, GFAP and AQP4 Immunohistochemistry.....	121
5.3.4	AQP4 Immunofluorescence	123
5.3.5	Quantification of AQP4 Expression Across Blood Vessel Cross Sections	123
5.3.6	Quantification of AQP4 Polarisation	124
5.3.7	Statistical analysis.....	124
5.4	Results.....	125
5.4.1	Glymphatic inflow, tau and AQP4 in rTg4510 transgenic mice with age	125
5.4.2	Regional differences between the rostral and caudal cortices of the rTg4510 mouse model	130
5.5	Discussion	132
6.	Glymphatic Function in Amyloidosis Models of Alzheimer’s Disease	137
6.1	Summary	137
6.2	Introduction.....	138
6.3	Methods	139
6.3.1	Mice	139
6.3.2	Surgical preparation, magnetic resonance imaging and image analysis	140

6.3.3	Amyloid Immunohistochemistry	140
6.3.4	Statistical Analysis	141
6.4	Results	141
6.4.1	Glymphatic inflow in J20 transgenic mice	141
6.4.2	Glymphatic inflow in NL-F transgenic mice.....	144
6.5	Discussion	146
7.	Relationships Between Alzheimer’s Disease Pathology and Aquaporin 4 in Humans	
	151	
7.1	Summary	151
7.2	Introduction.....	152
7.3	Methods.....	154
7.3.1	Human subjects and tissues	154
7.3.2	Immunostaining of human brain sections.....	155
7.3.3	Western blotting of human brain sections.....	156
7.3.4	Manual counting of plaques and tangles.....	156
7.3.5	Threshold analysis of aquaporin-4	158
7.3.6	Mice and tissue collection.....	159
7.3.7	Western Blotting of mouse brain samples	160
7.3.8	Immunostaining of mouse brain samples	161
7.3.1	Statistical analyses	162
7.4	Results	163
7.4.1	Measurements of plaque and NFT burden.....	163
7.4.2	Quantification of aquaporin-4.....	165
7.4.3	Testing relationship to the rs3763043 SNP	171
7.4.4	Probing DTNA changes during aging and A β pathology in the mouse brain...	172
7.5	Discussion	175
8.	Concluding Remarks	183
	References	187

Index of figures

Figure 1. Drawings by Alzheimer of Auguste Deter's brain preparations, showing different tangle staging of the disease.

Figure 2. Drawings by Fischer showing detailed staging of plaque pathology as well as tangle pathology.

Figure 3. Cartoon of a coronal human brain section illustrating the macroscopic changes that are visible in the most severe forms of AD.

Figure 4. Diagrammatic depiction of the spread of plaques and tangles during AD. Darker shading represents density of spread.

Figure 5. The hypothesised cascade of events leading from A β production to dementia.

Figure 6. Schematic representation of tau oligomerisation and the role of each form in the different stages of tau pathology.

Figure 7. Hypothesised schema depicting the cascade of neuroinflammatory events leading to AD onset.

Figure 8. Cartoon depicting an example of a transgenic mouse model.

Figure 9. Summary of drugs in Phase III trials targeting mechanistic pathways of AD.

Figure 10. Hypothetical model of AD biomarker detection.

Figure 11. Representation of disease progression against diagnosis by MRI.

Figure 12. Diagram depicting CSF flow within the cranium.

Figure 13. Cross sectional schematic showing a diving feeding pial artery and its cellular associations as it variegates into the capillary bed.

Figure 14. Structural elements of the BBB and the neurovascular unit.

Figure 15. Diagrammatic depiction of CSF-ISF exchange via glymphatic flow.

Figure 16. Surgical method to introduce tracers into the SAS.

Figure 17. Flow diagram showing an example of the analysis approach taken to calculate percentage penetration of fluorescent tracers.

Figure 18. Photographs of brains collected following intracisternal infusion of EBD at 2 μ l/min.

Figure 19. Photographs of brains collected following intracisternal infusion of EBD at 0.6 μ l/min.

Figure 20. Coronal brain sections from mice infused with small molecular weight Alexa Fluor 594 Hydrazide.

Figure 21. Coronal brain sections from mice infused with medium molecular weight Texas Red.

Figure 22. Coronal brain sections from mice infused with large molecular weight fluorescein isothiocyanate.

Figure 23. Percentage penetration of large, medium and small molecular weight dyes infused into the cisterna magna at 0.6 μ l/min.

Figure 24. *Surgical setup and MRI bed preparation for intracisternal contrast infusion and DCE-MRI acquisition.*

Figure 25. *Schematic with brain regions visualised and timeline illustrating experiments used to determine the pattern of glymphatic inflow in the mouse brain.*

Figure 26. *Schematic describing the processing steps following acquisition of T1 weighted MR images.*

Figure 27. *Schematic and timeline illustrating experiments used to determine the effects of pharmacological inhibition of AQP4 on clearance of tau from the mouse brain.*

Figure 28. *Glymphatic Inflow in the Mouse Brain Cortex.*

Figure 29. *Schematic illustrating direction of contrast agent flow into the brain following cisterna magna infusion.*

Figure 30. *Representative pseudocolored DCE-MRI scans of vehicle (20% Captisol) and TGN-020 treated animals with Gd-DTPA infusion.*

Figure 31. *MRI T1 signal intensity vs. time data acquired from the cortex, striatum and hippocampus demonstrating significant inhibition of glymphatic inflow in three aspects of the TGN-020 treated animal brain..*

Figure 32. *Total tau and pTau concentration of CSF samples extracted from mice injected with tau homogenate demonstrating reduced clearance of tau from the TGN-020 treated animal brain.*

Figure 33. *MRI T1 signal intensity vs. time data acquired from the 2.5 month, 5 month and 7.5 month animals.*

Figure 34. *Slopes of the sigmoidal curves of the time course data in each of the brain regions from Figure 32, as a surrogate measure of rates of glymphatic inflow.*

Figure 35. *MRI and histological analyses grouped by genotype and age.*

Figure 36. *MRI T1 signal intensity vs. time data acquired from the rostral and caudal cortices of rTg4510 animals.*

Figure 37. *MRI T1 Signal Intensity (% change from baseline) vs. time plots from J20 (PDGF-APP^{Sw,Ind}) and wild type animals.*

Figure 38. *Representative immunohistochemistry images of 6 month old J20 and wildtype sections.*

Figure 39. *Percentage immunoreactivity of amyloid quantified in a subset of brains in the mice from the J20 cohort.*

Figure 40. *MRI T1 Signal Intensity vs. time plots from homozygous transgenic NL-F and wildtype animals.*

Figure 41. *Representative immunohistochemistry images of 8 month old NL-F and wildtype sections.*

Figure 42. *Percentage immunoreactivity of amyloid quantified in a subset of brains in the mice from the NL-F cohort.*

Figure 43. *Schematic representation of the dystroglycan anchoring complex and associated end foot elements, including aquaporin-4 and dystrobrevin.*

Figure 44. *Widefield representative composite (red, green, blue) micrographs of human sections stained for AQP4, nuclear stain DAPI and tau or A β .*

Figure 45. Workflow used for analysing AQP4 stain on micrographs and the formulae used to compute the AQP4 measures investigated in these analyses.

Figure 46. Widefield example micrographs of hemisections of mouse brains used for DTNA analyses.

Figure 47. Manually counted plaque and NFT densities in frontal cortex grey matter, white matter and hippocampal CA1, CA2 and CA3 regions.

Figure 48. Manually counted pathology correlated to clinical scores.

Figure 49. Test analyses of AQP4 polarisation ratio on a subset of ROIs.

Figure 50. Composite micrographs of frontal cortex sections showing AQP4 and DAPI nuclear stains.

Figure 51. AQP4 expression by Western blot.

Figure 52. AQP4 polarisation and area coverage measures calculated using threshold analyses in frontal cortex grey matter, white matter and hippocampal CA1, CA2 and CA3 regions.

Figure 53. AQP4 polarisation and area coverage measures in the frontal cortex grey matter correlated to manual plaque counts, manual NFT counts and AQP4 expression by Western blot.

Figure 54. AQP4 measures and pathology by SNP status.

Figure 55. Representative micrographs of young and aged mouse brain sections stained for AQP4, nuclear stain DAPI and DTNA.

Figure 56. Representative micrographs of wildtype and Tg2576 mouse brain sections stained for AQP4, nuclear stain DAPI and DTNA.

Figure 57. Whole brain DTNA expression by Western blot and DTNA polarisation by immunofluorescence quantified in young vs aged mice and wildtype vs Tg2576 mice.

Abbreviations

ACh	acetylcholine
AChE	acetylcholinesterase
AD	Alzheimer's disease
ADNI	Alzheimer's Disease Neuroimaging Initiative
AF594-H	Alexa Fluor 594 hydrazide
ANOVA	analysis of variance
AP	probable Alzheimer's disease
APOE	apolipoprotein E
APP	amyloid precursor protein
AQP4	aquaporin-4
Aβ	amyloid beta
BACE	beta-site amyloid precursor protein cleaving enzyme
BBB	blood brain barrier
CA	Cornu Ammonis areas of the hippocampus
Ca²⁺	calcium ion
CAA	cerebral amyloid angiopathy
CAMKIIα	calcium/calmodulin-dependent protein kinase type II alpha
CBF	cerebral blood flow
CERAD	Consortium to Establish a Registry for Alzheimer's Disease
ChAT	choline acetyltransferase
CI	cognitively impaired
CNS	central nervous system
CSF	cerebrospinal fluid
CTE	chronic traumatic encephalopathy
CTF	C-terminal fragment
DAC	dystroglycan anchoring complex
DCE-MRI	dynamic contrast enhanced magnetic resonance imaging
DIAN	Dominantly Inherited Alzheimer Network
DMN	default mode network
DTI	diffusion tensor imaging
DTNA	dystrobrevin
EBD	Evans blue dye
ECS	extracellular space

ELISA	enzyme linked immunosorbant assays
EMCI	early mild cognitive impairment
FCG	frontal cortex grey matter
FCW	frontal cortex white matter
FDG	fluorodeoxyglucose
FITC-d2000	fluorescein isothiocyanate–dextran-2000
FTDP-17	frontotemporal dementia with Parkinsonism linked to chromosome 17
GFAP	glial fibrillary acidic protein
GWAS	genome-wide association studies
HC	healthy control
IACUC	Institutional Animal Care and Use Committee
ICP	intracranial pressure
ISF	interstitial fluid
J20	J20(PDGF-APP ^{Sw} ,Ind) mouse model
LMCI	late mild cognitive impairment
LOAD	late onset Alzheimer’s disease
M1	aquaporin-4 M1 isoform
M23	aquaporin-4 M23 isoform
MAP	microtubule-associated protein
MAPT	microtubule-associated protein tau
MCA	middle cerebral arteries
MCI	mild cognitive impairment
MMSE	mini mental state examination
MRI	magnetic resonance imaging
Na⁺	sodium ion
ND	not demented
NfL	neurofilament light chain
NFT	neurofibrillary tangles
NIH	National Institute of Health
NL-F	APP NL-F Knock-in mouse model
NMDA	N-methyl-D-aspartate
NP	neuritic plaques
NSE	neuron specific enolase
NT	neuropil threads
OHSU	Oregon Health and Science University
PBB	phenyl/pyridinyl-butadienyl-benzothiazoles/benzothiazolium
PBS	phosphate buffered saline

PBS-T	phosphate buffered saline with 0.05% Tween-20
PDGF	platelet derived growth factor
PET	positron emission tomography
PHF	paired helical filaments
PiB	Pittsburgh Compound B
PS	presenilin
PS1 / PSEN1	presenilin 1
PS2 / PSEN2	presenilin 2
P-tau	phosphorylated tau
ROI	regions of interest
rTg4510	rTg(tauP301L)4510 mouse model
SAS	subarachnoid space
SNPs	single nucleotide polymorphisms
SNTA	alpha1-syntrophin
TBI	traumatic brain injury
TBS	tris-buffered saline
TBS-T	tris-buffered saline with 0.1% Tween-20
Tg	transgenic
Tg2576	Tg2576 APP mouse model
TR-d3	Texas Red–dextran-3
TREM2	triggering receptor expressed on myeloid cells 2
T-tau	total tau
UCL	University College London
VLP-1	visinin-like protein 1
WT	wildtype

1. Alzheimer's Disease

This chapter aims to provide an introductory snapshot of the Alzheimer's disease landscape, starting from its early beginnings, to the current state of understanding and progress made within its research avenues.

1.1 A brief history of Alzheimer's disease

The first published case of Alzheimer's disease in 1907 remains a seminal piece of work in a disease which, over a century later, still remains to be cured. In the original publication by German psychiatrist and neuropathologist Alois Alzheimer, entitled "*Über eine eigenartige Erkrankung der Hirnrinde (About a Peculiar Disease of the Cerebral Cortex)*", he described behavioural changes in patient Auguste Deter, who at age 51 had begun to experience such severe cognitive and behavioural decline, that it was deemed rare, curious and clinically unusual. Upon her death four and a half years later, neuropathological assessment would reveal that the changes to her central nervous system were clinically distinct from any other previously reported disease. Using the then state-of-the-art silver protocol of Bielschowsky staining, Alzheimer defined the presence of tangled bundles of neurofibrils, the deposition of "peculiar matter" (Figure 1) and the disappearance of numerous ganglion cells in the upper layers of the cortex [1,2].

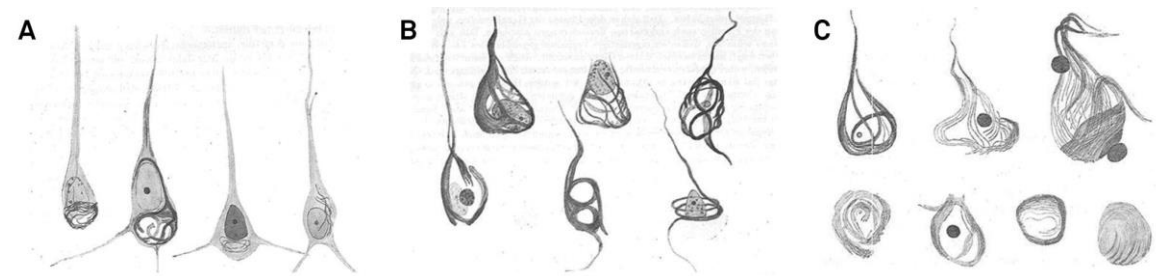


Figure 1. Drawings by Alzheimer of Auguste Deter's brain preparations, showing different tangle staging of the disease. Reproduced from Engelhardt et al., 2015 [3].

Given the young age of this patient, the case was subsequently designated as presenile dementia. With reports of 4 additional cases presenting similar clinical and neuropathological features, Alzheimer's colleague Emil Kraepelin, a prominent psychiatrist, named the disease after Alzheimer, citing the young age, distinct behavioural anomalies and severe dementia presented in these cases as the reason to distinguish this condition from senile dementia [4].

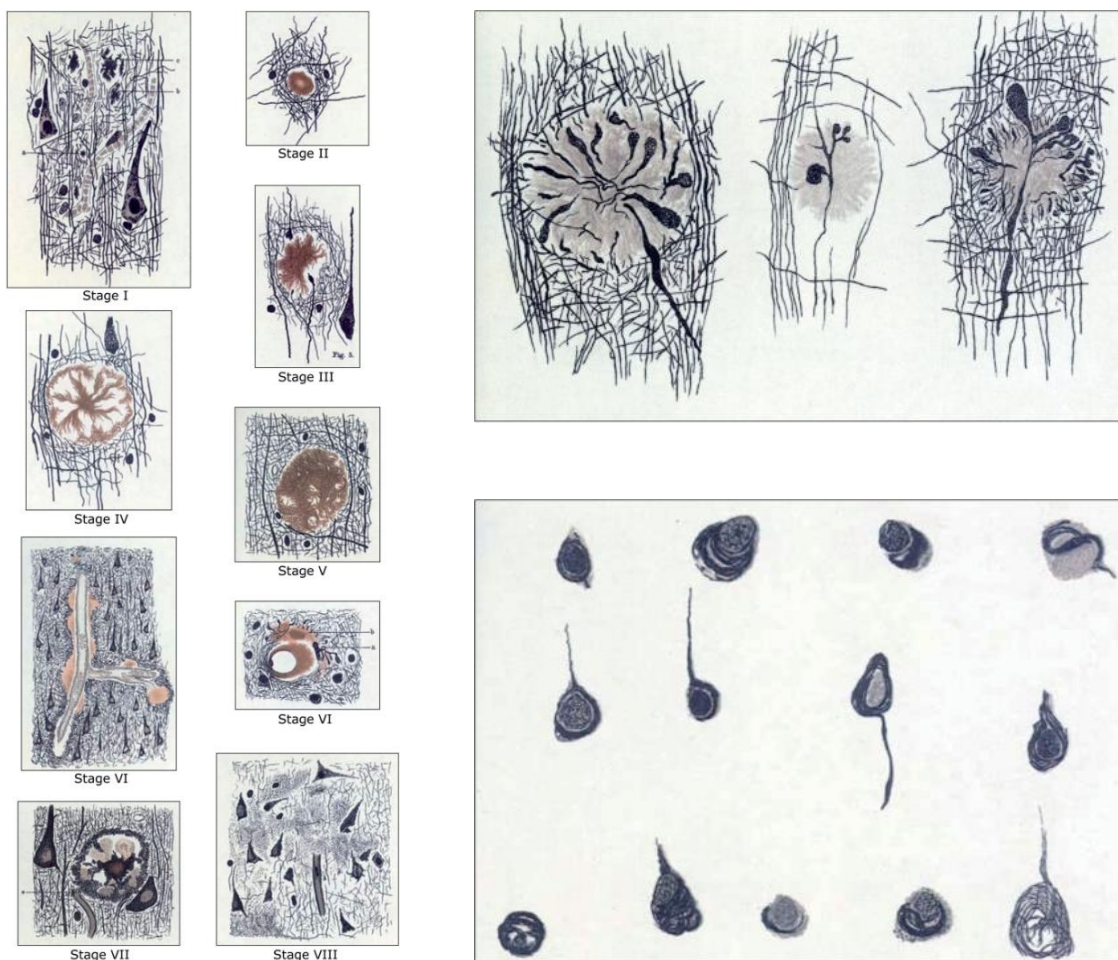


Figure 2. Drawings by Fischer showing detailed staging of plaque pathology as well as tangle pathology. Reproduced from Goedert, 2009 [4].

Interestingly, in the same year, a Czech psychiatrist and neuropathologist Oskar Fischer also described the presence of neuritic plaques in 12 of 16 cases of presenile dementia. He subsequently published a larger study of 56 cases, describing the presence of neurofibrillary tangles alongside plaques, in a selection of cases that showed a clinical presentation of what

he described as presbyophrenic dementia. Whilst the drawings of the pathologies both scientists describe appear remarkably similar, Fischer went on to describe these plaques in much greater detail (Figure 2). Some early texts, including one written by Alzheimer, would even refer to plaques as “Fischer's plaques”, with presbyophrenic dementia and Alzheimer’s disease being used interchangeably [4].

However, the two scientists did not believe they were describing the same condition, with there being much academic debate between the rivals. Alzheimer’s career thrived, until ill health brought about his untimely death in 1915, but his legacy carried on [4,5]. With the rise of the National Socialist regime, in the late 1930s Fischer’s career declined, ending tragically with his arrest in 1941 and death a year later whilst in captivity. Despite his significant research contributions, by 1955 much of Fischer’s work on presbyophrenic dementia was considered obsolete (until the rediscovery of his work in the 2000s) and presenile dementia with plaques and tangles became widely known as Alzheimer’s disease (AD) [4,6].

Primarily only covering the presenile form of dementia when observed under the age of 65, the definition of AD was widely discussed and argued by academic scholars throughout the 20th century. In the 50s, presenile and senile dementias were classified under the umbrella term “chronic organic brain disease”, which covered all neurodegenerative conditions leading to a diagnosis, owing to the lack of understanding of the diseases underlying dementia [5]. Increasing evidence of the presence of plaque and tangle pathology in what was then separately known as “senile dementia of the Alzheimer’s type” (when observed over the age of 65) emerged from the 60s through to the 70s. By the late 70s, substantial evidence of both conditions pointing to a single disease had gathered [7], and given that the two conditions were neuropathologically indistinguishable, both presenile and senile forms were categorised singly into what is now known as AD [8].

This categorisation marked a turning point for AD research. Senile dementia was no longer considered a normal by-product of aging. The need for improved understanding and research into AD began to grow urgent, particularly after World War II. As life expectancy increased

through the 20th century, the incidence of AD also began to rise, bringing with it an ever increasing socioeconomic burden. Understanding the aetiology of AD quickly became a research priority. By the 80s, discernible scientific and public interest in AD encouraged increased funding to be pushed towards this cause [5].

Today, dementia is a global epidemic. Although it has come a long way since 1907, the field of dementia noticeably took time to gain momentum. We now know the pathological characteristics as originally described in the case of Auguste Deter, as the hallmark triad of AD neuropathology – neurofibrillary tangles, amyloid plaques and neuronal loss. Recent rediscovery and reanalysis of material from this historic patient case has confirmed that the nature and severity of pathology observed still stands as a typical diagnosis of AD by current standards [9]. Whilst the revisiting of this original work may serve as a symbolic demonstration of the scientific progress made within the field, the need for this re-examination of the first known case also highlights the lack of understanding of a complex disease, which began as a rare curiosity but became a global crisis.

1.2 Present day prevalence of dementia

Dementia is a syndrome brought about by one or more diseases, characterised by a range of symptoms including memory loss, language problems, psychological difficulties and psychiatric disturbances, all of which severely affect day to day living and quality of life for sufferers and their caregivers. AD is the most common cause, accounting for approximately 75% of dementia cases. Several other forms of dementia causing diseases are now known, including vascular dementia, dementia with Lewy bodies, frontotemporal dementia, as well as mixed dementia where one or more forms exist together. Huntington's disease, corticobasal degeneration, Creutzfeldt-Jakob disease and normal pressure hydrocephalus are also known causes but are less common by comparison [10].

The World Health Organisation lists AD and other dementias as the 5th biggest cause of death [11]. Globally, the incidence of dementia continues to climb. Dropping global fertility

rates combined with increased life expectancy is contributing rapidly to overall population ageing, resulting in a surge in age-related chronic conditions such as dementia. In 2015, there were an estimated 900 million people living over the age of 60, with 46.8 million people living with dementia [12]. 58% of these cases come from low and middle income countries. It is forecast that the total number of global cases will double every 20 years, reaching a staggering 131.5 million by 2050. The World Alzheimer Report estimates that this translates to one new case of dementia every 3.2 seconds worldwide [12].

This predicts an overwhelming global socioeconomic burden. The estimated global cost of dementia in 2015 was 818 billion US dollars, accounting for medical expenses, social care, residential, nursing and unpaid care costs [12]. Given the rate at which new diagnoses are predicted and the cost this will amount to, dementia is fast becoming one of the greatest social and healthcare challenges of our time.

1.3 Pathogenesis of AD

Despite decades of investigation, the root cause of the physiological events leading up to AD are still not clear. Research advances over the many decades have given rise to several key hypotheses which now provide the framework for AD research today. This section will explore these hypotheses, beginning with the macroscopic clinical picture of AD, and then briefly delve into the biology underpinning the current understanding of its pathogenesis.

1.3.1 The spread of pathology in the AD brain

AD is characterised by the build-up of extracellular amyloid plaques and intracellular tangles of tau, subsequently leading to neurodegeneration. During the later and most severe stages of the disease, shrinkage of the brain (Figure 3) results in the devastating symptoms observed in those suffering from the disease. Whilst these behavioural changes usually manifest much later in life, it is now widely believed that the formation of the hallmark lesions of AD occur decades before clinical symptoms are observed [13].

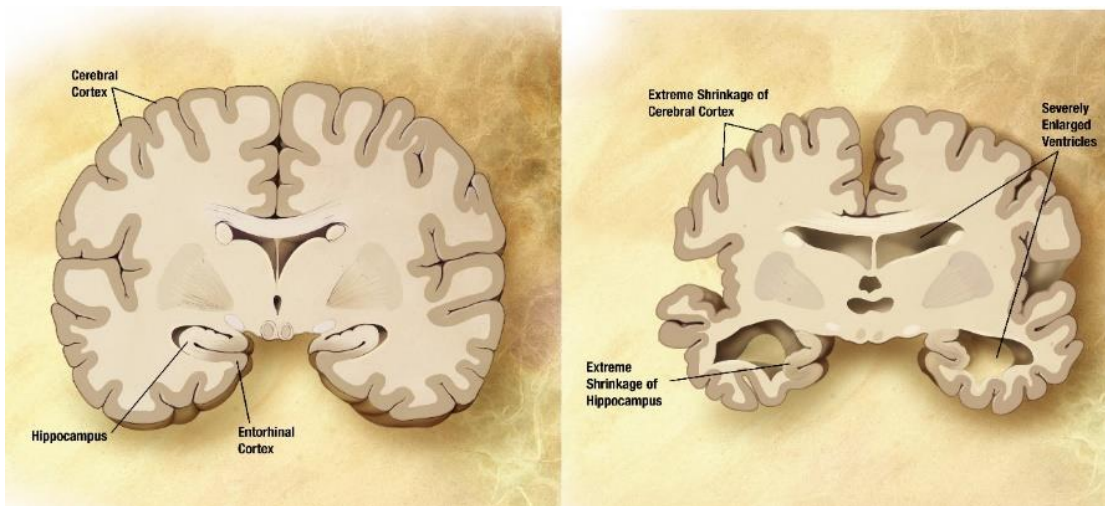


Figure 3. Cartoon of a coronal human brain section illustrating the macroscopic changes that are visible in the most severe forms of AD. Image reproduced from the Wikimedia Commons free media repository.

Plaques and tangles have a characteristic pattern of spread through the brain during AD pathogenesis. Plaque burden can be highly variable between individuals, but is broadly categorised into three neuropathological stages, clinically designated A, B and C (Figure 4). In the first stage, the earliest amyloid deposits are seen in the isocortex, mostly limited to the frontal, temporal and occipital lobes, with no deposits observed in the hippocampal formation. By the second stage, a higher density of amyloid deposits are observed in all isocortical regions, with some hippocampal involvement. In the third and most severe stage, a very high density is observed throughout the isocortex, with some also present in the striatal, thalamic and hypothalamic regions [14]. This neuropathological staging has been adapted into a standardised practical clinicopathological scoring system, based on analysis of post-mortem brain samples, instigated by the Consortium to Establish a Registry for Alzheimer's Disease (CERAD). CERAD assessment utilises selected anatomical brain regions in its scoring protocol – middle frontal, superior and middle temporal gyri, inferior parietal lobule, hippocampus, entorhinal cortex and substantia nigra. A minimum of five requisite sections are stained and neuropathologically scored for plaque density based on standardised representative diagrams. The scores are then cross-correlated against age and integrated with clinical dementia status to compute a final post-mortem score [15].

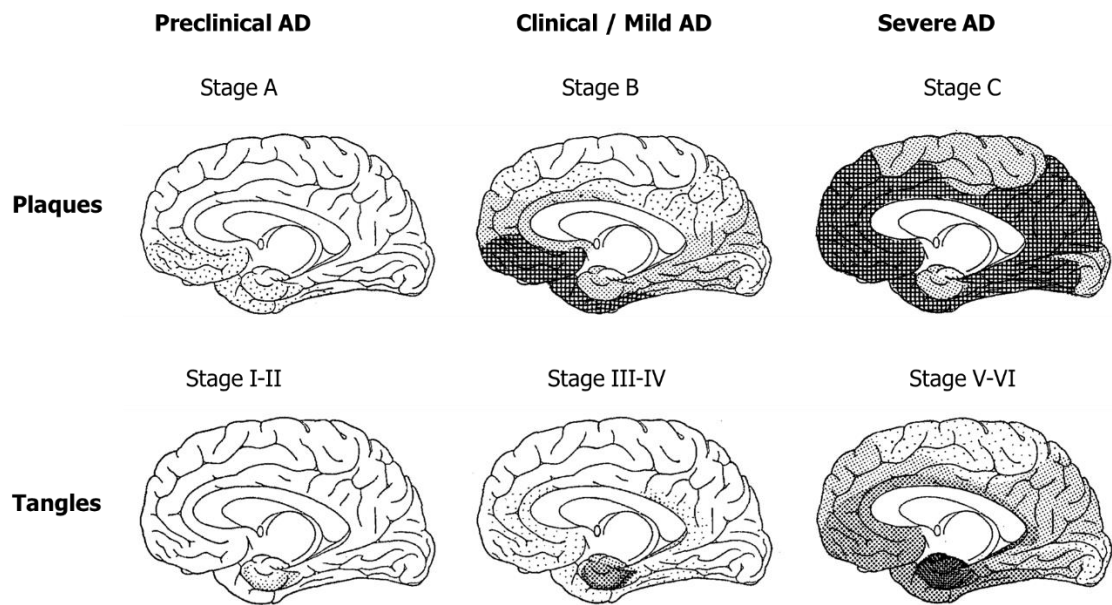


Figure 4. Diagrammatic depiction of the spread of plaques and tangles during AD. Darker shading represents density of spread. Modified from Braak and Braak, 1991 [14].

Tangles have a more distinct pattern of spread, and can be visualised in six stages. Stages I – II represent the prodromal phase, where tangles appear in a single layer of the transentorhinal cortex with mild hippocampal involvement in the CA1 region. During stages III – IV, the severity of the transentorhinal and entorhinal regions increases, with the appearance of ghost tangles – the remnants of a neuron containing NFTs. Increased tangle populations in the CA1 hippocampal subfield is observed, with an equivalence to the clinically diagnosed stage of AD. Stages V – VI sees the infestation of the isocortex and all hippocampal regions to a devastating degree, corresponding to fully developed AD [14]. This staging has gained prominence in neurology since it was first defined by Braak and Braak, and is now canon in AD neuropathological assessment. Braak staging uses three standardised anatomical blocks, which capture the anteromedial portion of the temporal lobe, parahippocampal and occipito-temporal gyri, medial and superior temporal gyri, and the base of the occipital lobe. The selected sections are histologically stained, and a score of I – VI is allocated based on the topographical spread of tangle pathology. Scoring requires expert knowledge of neuroanatomy and familiarity of tangle progression [16], and post-mortem Braak staging is

now a routine clinicopathological praxis alongside CERAD scoring, to reach a conclusive AD diagnosis.

Whilst these semi-quantitative scores form the crux of AD diagnosis, it still leaves a confirmed verdict only possible post-mortem. Clinical diagnosis relies on an array of neuropsychological evaluations to measure cognitive changes, alongside neuroimaging tests which currently only reliably detect brain changes that occur in the mid to late stages of the disease [17] (discussed in more detail in section 1.7), and the majority of these evaluations are triggered only when a patient enters a clinic experiencing cognitive disturbances. AD urgently requires robust biomarkers sensitive to the diverse array of lesions and biological changes that arise decades before the onset of cognitive decline. To that end, understanding the biology underlying the earliest in-life changes in the AD brain is paramount.

1.3.2 Amyloid

Since the isolation of amyloid as the main constituent of brain plaques [18], and through much of the early years of AD research, amyloid protein biology has taken centre stage in understanding AD aetiology. This was strengthened by the proposal of the amyloid hypothesis, put forward by Hardy and Allsop in 1991, which described a cascade of events leading from the accumulation of plaques to neuronal death (Figure 5) [19].

The hypothesis postulates that amyloid is the key component of AD pathogenesis. Within the scope of this hypothesis, genetic mutations or other environmental factors may give rise to altered amyloid processing. This is then thought to result in the accumulation of amyloid into plaques - the presumed initiator of AD pathogenesis, followed by the downstream phosphorylation of tau and the formation of tangles, consequently causing neuronal damage and ultimately manifesting as dementia [19]. A closer look at the biochemical, structural and genetic elements of plaques provide evidence for the instigation of this hypothesis.

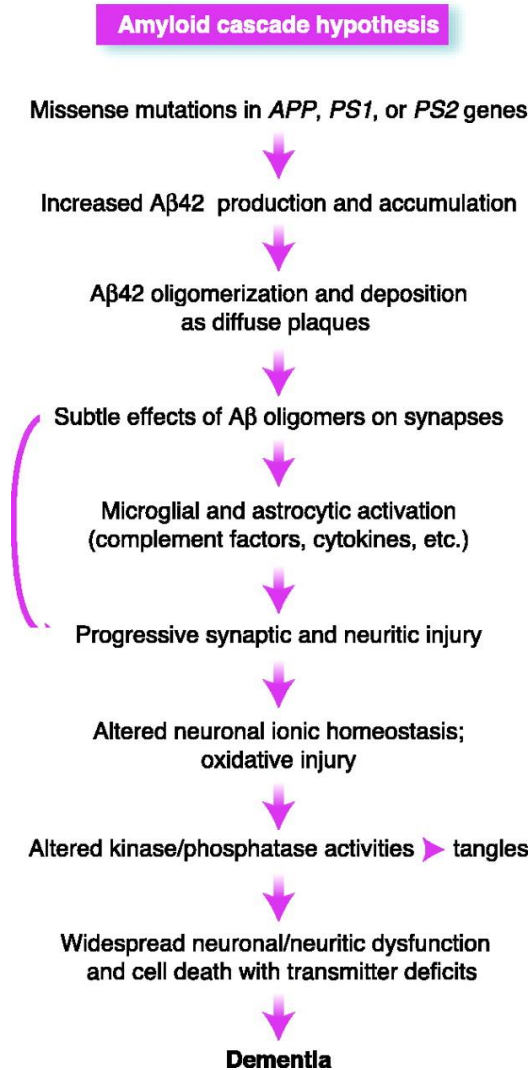


Figure 5. The hypothesised cascade of events leading from Aβ production to dementia. Reproduced from Hardy and Selkoe, 2002 [20].

The classic plaque is formed of a dense aggregate of extracellular amyloid beta (Aβ) peptide, with closely packed abnormal axons and dendrites, or neurites. This deposit is usually surrounded by a halo of reactive astrocytes and activated microglia, thus forming a complex lesion of multiple cell types, with Aβ at its core [21]. Whilst this paints a classic picture of the well-known amyloid plaque, plaques are structurally diverse, and a more abundant variant of these deposits are diffuse plaques. These granular Aβ lesions are less distinct in structure, lack reactive glia and have far fewer abnormal neurites. Thought to be an early form of the plaque, these deposits represent a complex continuum of Aβ aggregation during AD pathogenesis [21]. An additional variant of plaque pathology is amyloid

angiopathy, where deposition of A β occurs in the walls of meningeal and parenchymal arterioles, venules and capillaries [22].

The A β peptide, found consistently in all these plaque variants, arises from the proteolytic cleavage of amyloid precursor protein (APP), a membrane glycoprotein associated with a range of biological functions including the regulation and maintenance of synapses [23] and axonal transport [24]. Proteolytic cleavage of this protein can occur via the non-amyloidogenic or amyloidogenic pathways. In the non-amyloidogenic pathway, APP is cleaved via the enzyme α -secretase, giving rise to a membrane tethered α -C-terminal fragment (CTF), and releasing soluble APP α . In the amyloidogenic pathway, APP is first cleaved at the N-terminus via the enzyme β -secretase, also known as beta-site APP cleaving enzyme (BACE), found abundantly in neurons, resulting in a β -CTF, which is then sequentially cleaved by γ -secretase [25]. γ -secretase is a complex membrane protein formed of four other protein subunits – presenilin (PS), nicastrin, presenilin enhancer 2, and anterior pharynx-defective 1, with PS forming the catalytic subunit of this composite enzyme [26]. The final cleavage step by γ -secretase causes extracellular release of A β .

This monomeric A β can assemble into a myriad of oligomeric forms as well as fibrils. Fibrils, which form the main makeup of A β plaques, are large in molecular weight and insoluble. Oligomers are heterogenous, assuming medium to low molecular weight forms, and are soluble [25]. Whilst the plaque-associated fibrillar form was always thought to be linked with neurotoxicity in AD, the oligomeric soluble form is emerging as a close contender, given its ability to readily spread throughout the brain and bind to extracellular receptors [27]. The formation of these different conformations is facilitated by the very nature of amyloidogenic processing by γ -secretase. Cleavage can occur at several sites, giving rise to multiple amino acid lengths ranging from 37 – 46 residues [25], including the 40 and 42 length isoforms A β 40 and A β 42, which are abundantly found during AD pathogenesis. A β 42 more readily aggregates into fibrils whilst A β 40 forms a more soluble variant [28].

Whilst the biochemistry of A β paints a complex picture of its dynamics, it is key to understanding the basis of the amyloid hypothesis, as modifications to amyloid metabolism via changes to the APP gene reliably establishes AD pathology. The earliest evidence to support this theory came from studying patients with Down syndrome, a condition which triplicates chromosome 21, where the APP gene is also located in humans. Virtually all patients with Down syndrome go on to develop AD pathology, with the deposition of amyloid plaques preceding neurofibrillary tangle formation [29]. A notable phenotype in these cases is that the predominant species of A β found in dense and diffuse plaques is the A β 42 isoform, whilst the A β 40 species is more readily detectable in angiopathy, when observed in these patient groups [30]. The next evidence backing the amyloid hypothesis came from discovery of familial mutations in the APP gene that gave rise to cerebral amyloid angiopathy (CAA) [31] and AD [32,33] in Dutch and Swedish populations. Subsequent study of mutations in the PS genes revealed that mutations in presenilin 1 (PS1 / PSEN1) and presenilin 2 (PS2 / PSEN2) result in an increase in the A β 42 to A β 40 ratio [34,35]. Moreover, when A β species from familial AD cases were assayed, the A β 42 isoform, known for its fibrillar properties and susceptibility to aggregate, was consistently found to be elevated [36,37]. This cemented the notion that amyloid biology is fundamental to disentangling the complex neuropathology of AD.

Nevertheless, not everyone with an AD diagnosis carries mutations in these genes, with these cohorts only accounting for a small subset of all cases. In addition, amyloid load does not correlate well with cognitive impairment in human patients [38]. Furthermore, it is also now known that some individuals can maintain a high cognitive reserve during neuropathology. This is the brain's ability to cope when it undergoes damaging changes and compensate efficiently to preserve cognitive abilities during pathology [39]. These individuals can live a lifetime without an AD diagnosis, despite developing considerable plaque pathology. As such, the amyloid hypothesis has come under scrutiny, with research focus being directed towards a wider view of the pathophysiological cascade of AD.

1.3.3 Tau

Though debate over the validity of the amyloid hypothesis prevails, it still forms a central dogma of AD aetiology. Within the amyloid cascade, the formation of neurofibrillary tangles (NFT) of phosphorylated tau is said to form an intermediary link between plaque formation and dementia onset (Figure 5) [20]. Notably, NFT spread reliably precedes the pattern of neurodegeneration in AD, and this regional pattern of atrophy is closely correlated to the impairment of brain function [14]. Thus, tau is perhaps the molecular candidate closest to revealing the precise mechanisms driving neurodegeneration. As such, in recent years, tau has emerged as a strong candidate towards illuminating the precise pathophysiological cascade of AD.

Prior to the isolation of tau, NFTs were known as intracellular filamentous aggregates composed of a little known polypeptide, structurally termed paired helical filaments (PHF). Isolation of PHF from AD brains enabled the biochemical identification of the polypeptide within PHF to be microtubule-associated [40], and subsequently, it was identified to be abnormally phosphorylated tau protein [41]. In the AD brain, deposition of tau can occur as a spectrum, ranging from small PHF and straight filaments in neuronal processes or neurites, known as neuropil threads (NT), to larger NFT deposits within the cell body of a neuron, which go on to become “ghost tangles” upon death of the neuron. Tau in dystrophic neurites can also be associated with amyloid plaques, morphologically recognised as neuritic plaques (NP) [42].

The discovery of mutations in the tau gene leading to frontotemporal dementia with Parkinsonism linked to chromosome 17 (FTDP-17) hinted strongly at tau’s causative role in the development of neurodegenerative disease. Individuals with FTDP-17, brought about by tau mutations, show frontotemporal atrophy, neuronal loss and tau deposits in neuronal and glial cells. In some cases, these tau deposits are identical to the PHF and filamentous forms of tau seen in AD [43]. This put tau in the spotlight as the molecule that may hold the key to uncovering mechanisms behind neuronal death in AD.

Tau is now fairly well characterised as an intracellular microtubule-associated protein (MAP), expressed highly in the axons of central nervous system (CNS), and to a lesser degree, in the peripheral nervous system [44]. Microtubules are polymeric proteins that form the cellular cytoskeleton. Tau is required for microtubule assembly and stabilisation [45], cellular polarity and transport [46]. The microtubule-associated protein tau (*MAPT*) gene, located on chromosome 17, expresses six isoforms of tau in the CNS. These isoforms are broadly recognised based on the number of microtubule binding repeat domains they possess on the carboxy-terminal – 3R tau, containing 3 repeats and 4R tau, containing 4. The ratio of these two tau isoforms in the brain is roughly one to one, but alterations in this ratio are recurrently observed in tau-driven pathologies [47].

Hyperphosphorylation of tau is another significant feature that is consistently observed in tau aggregates in the AD brain. Phosphorylation is a requisite regulatory mechanism in protein function and in its regular form, tau is a highly soluble protein, containing up to 85 phosphorylation sites [47]. Tau phosphorylation is regulated by a variety of kinase and phosphatase activity, and it is thought that imbalances in activity between these enzymes can result in hyperphosphorylation. In turn, proteolytic cleavage of tau and its misfolding into abnormal conformations are also influenced by phosphorylation status. Species of tau that are hyperphosphorylated, have undergone cleavage or have altered conformations are all found in the brains of several tauopathies [47]. Thus, the regulation of tau going awry is a pivotal component in the neurodegenerative process.

The isoform and phosphorylation status of tau is crucial to its various biological roles, including the regulation of its microtubule binding affinity [48]. It is widely theorised that hyperphosphorylation of tau causes it to dissociate from microtubules, and that this unbound tau is prone to aggregate [44]. Once dissociated, monomeric hyperphosphorylated tau structures gain affinity for each other and begins to oligomerise. Oligomers can assume two intermediate forms – a soluble oligomer, and a granular insoluble form [49]. The granular oligomer can polymerise even further to form the characteristic fibrils that then aggregates into NFTs [50] (Figure 6).

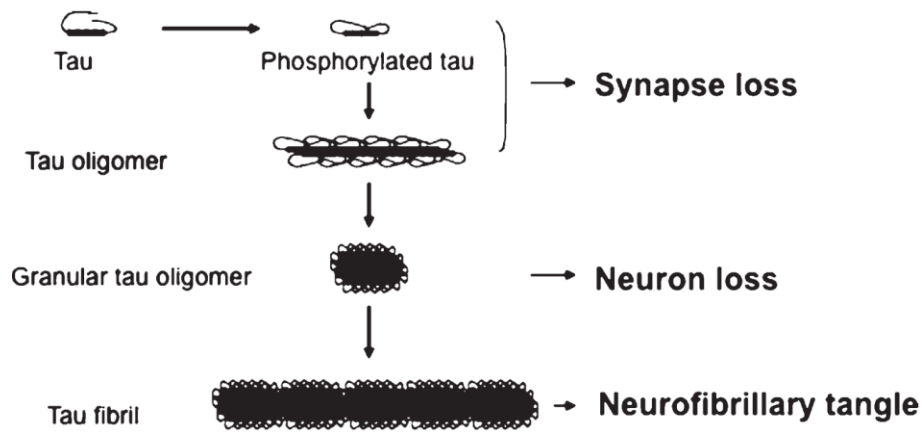


Figure 6. Schematic representation of tau oligomerisation and the role of each form in the different stages of tau pathology. Reproduced from Takashima, 2013 [49].

However, it is not NFTs themselves that are considered cytotoxic. The generation and characterisation of transgenic mouse models of tauopathy have fostered the understanding of tau pathogenesis and driven the tau hypothesis forward by leaps and bounds. One such mouse model, known as Wtau-Tg which expresses wildtype human tau, revealed that hyperphosphorylated tau alone can cause synaptic loss, resulting in learning and memory defects, without the aggregation into insoluble species or neuronal loss [51]. Furthermore, mouse models of FTDP-17 that do show neuronal loss reveal the presence of oligomeric insoluble tau aggregates. Taken together, these serve as testimony that the intermediate oligomeric forms are responsible for neurotoxicity, with tangles being the final tell-tale residual marker of neuronal death [49].

Whilst several mutations are now known to be associated with FTDP-17, a missense mutation known as P301L is the most common. This mutation has been studied in depth by integration into a transgenic mouse line, known as JNPL3. This mouse line exhibits progressive motor and behavioural dysfunction, with a gene-dose dependence on NFT accumulation. Additionally, the insolubility of tau species and hyperphosphorylation status matches the degree of NFT formation in these mice [52]. Thus, this tau mutation produces a phenotype that is strikingly similar to that observed in AD, strengthening the speculative role tau may have in its pathogenesis over A β .

Interestingly, when A β 42 was injected into the brains of P301L transgenic mice, it exacerbated the NFT pathology, normally observed with just the transgene alone [53]. This therefore suggests that A β still has a steadfast role in accelerating AD pathogenesis via tau-driven neurodegeneration. Furthermore, much like in the case of the familial mutations linked to A β pathology, mutations in tau are not requisite for the development of all tauopathies. So, whilst tau holds an undeniable role in the neurodegenerative and dementing process, it cannot be interrogated in isolation to disentangle AD pathogenesis.

1.3.4 Neuroinflammation

Neuroinflammatory changes are a significant observation in AD and the activation of glial cells are a known occurrence in its pathogenesis. Microglia, the primary immune cells of the CNS, police the brain by scanning for pathogens, cellular debris or insults. They play a key role in regulating synaptic remodelling and maintaining neuronal plasticity. Pathological insults such as protein aggregation or neuronal death in AD can cause microglia to become reactive [54]. Studies of post-mortem plaque pathology and *in vitro* experimental evidence shows that pathogenic A β can be engulfed by microglia to facilitate clearance. The binding of A β to scavenger receptors activates microglia, initiating phagocytosis but also causes the release of proinflammatory cytokines [55]. However, the signalling feedback mechanisms triggered as a consequence of cytokine release can be damaging to neuronal cells. In addition, these neuroinflammatory processes can also contribute to tau phosphorylation [56], further contributing to pathology.

Astrocytes, the cell type most abundant in the CNS, are also known to respond during AD pathogenesis. Reactive astrogliosis, that is an increase in the number of astrocytes at the area of pathology, is a feature of AD reported in both humans and mouse models [57]. Both *in vivo* and *in vitro* evidence suggests that astrocytes are recruited in AD for the clearance of A β – in mouse models of amyloid pathology, astrocytes closest to plaques express neprilysin, an enzyme that degrades amyloid [58]. In culture, astrocytes demonstrate the ability to mobilise towards A β and degrade it, with this observation also replicated on brain sections *in situ* [59]. This suggests a protective role for astrocytes during pathology. However, astrocyte

activation, much like microglial activation, can also trigger cytokine expression, which can trigger oxidative stress and cascade into neuronal damage, thereby contributing to neurodegeneration [60].

Thus, the neuroprotective and neurotoxic mechanisms of neuroinflammation are blurred. Nonetheless, activated microglia, astroglia and elevated cytokines are a consistent feature of AD pathology (Figure 7), and thus form another branch in studying the neurodegenerative process in AD and present additional targets in the search for therapeutics.

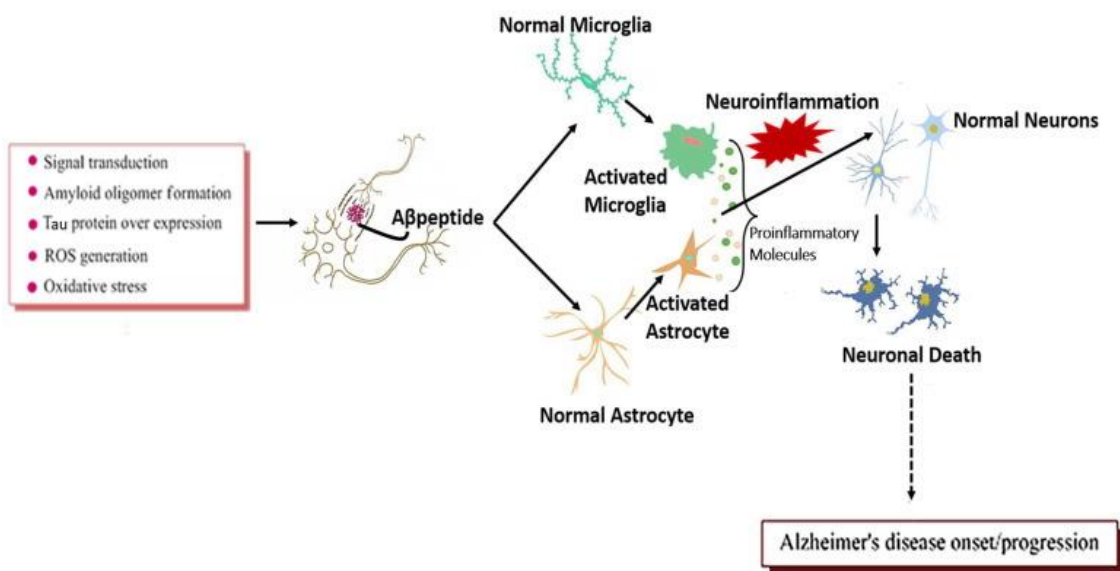


Figure 7. Hypothesised schema depicting the cascade of neuroinflammatory events leading to AD onset. Reproduced from Ahmed et al., 2019 [60].

1.3.5 Cholinergic hypothesis

The loss of cholinergic neurons of the basal forebrain is another feature of AD. This observation led to the proposal of the cholinergic hypothesis of AD, which postulated that the loss of cholinergic neurotransmission held responsibility for cognitive decline observed in AD [61]. The cholinergic system is implicated in learning and memory, sleep and wakefulness, stress responses and attention – functions in the brain that are all affected during AD. Cholinergic neurons are widespread in the brain, and utilise acetylcholine (ACh), a

major neurotransmitter in the CNS. ACh is synthesised by choline acetyltransferase (ChAT), and when released into the synapse can activate muscarinic receptors or nicotinic receptors, triggering the action of the enzyme acetylcholinesterase (AChE) to hydrolyse it and remove it from the synapse [62].

In post-mortem brains of individuals with AD and cognitive impairment, ChAT activity declines with increasing NP density. Cholinergic loss also correlates with NFT burden in the AD cortex [63]. Rodent studies have recapitulated similar findings, demonstrating that lesions in cholinergic neurons increased A β deposition and tau hyperphosphorylation [64]. Further experimental studies have shown that A β accumulation can deplete cholinergic synapses [65]. Thus there is ample evidence for cholinergic involvement during AD pathogenesis. Whilst the precise mechanisms behind this hypothesis continues to be a topic of research interest, the robust loss of cholinergic neurons are a sufficient feature to warrant its perusal in comprehending AD aetiology. Furthermore, drugs to target the cholinergic system are currently the most prevalent strategy used clinically to improve the cognitive symptoms of AD.

1.4 Risk factors for AD

Advancing age is the biggest known risk factor for AD onset. From the age of 65, the risk increases markedly – currently 3% of individuals between the age of 65 and 74 suffer from the disease. This jumps to 17% in individuals aged 75 – 84, and even further to 32% in those aged 85 and up [66].

Alongside age, a family history of AD can also be useful to clinicians when trying to identify dementia risk. This however is not purely based on a shared genetic makeup predisposing individuals to the disease. Common environmental influences and lifestyle factors play into inherited disease risk, and thus, studying ancestral history is beneficial in understanding familial risk [67]. AD is a chronic disease, and decades of study have teased out a range of

modifiable risk factors, in addition to genetic predispositions, that contribute to disease onset. These risk factors are discussed in brief in this section.

1.4.1 Genetics

Whilst genetics play an indisputable role in familial AD cases, it is useful to parse if genetic risk patterns are polygenic – where generationally shared environmental factors act together with genetic variations to increase sporadic disease risk, or if they follow Mendelian genetics – where a mutation in a single gene that is passed on, causes the familial form of the disease. Notably, it is only a small number of familial cases that account for AD, with just over 500 families in the global population of AD sufferers reported to have known disease-causing mutations [67].

The most extensively studied mutations for familial AD are those in genes that influence A β metabolism – *APP*, *PSEN1* and *PSEN2*. Mutations in any of these three genes, or duplication of *APP*, results in autosomal dominant AD in 50% of affected cohorts, usually manifesting as an early-onset form of the disease. Symptoms become apparent as early as 30 – 50 years of age in carriers of *PSEN1* mutations. *APP* mutation carriers typically have an age of onset between 45 and 60, and *PSEN2* mutation carriers display a wider range of onset age. Whilst mutations in these three genes can have varied mechanisms of aberrant A β processing, a commonality observed in these cases is that they increase A β ₄₂ production, thereby altering the A β ₄₂: A β ₄₀ ratio [68].

A significant genetic risk factor for sporadic AD is the apolipoprotein E (*APOE*) gene. APOE is a glycoprotein which facilitates lipid metabolism by receptor-mediated endocytosis of lipoproteins, and in the brain, it is mostly expressed in astrocytes and some microglia [69]. Single nucleotide polymorphisms (SNPs) – a single-base mutation that naturally gives rise to variants of genes in the human genome – can influence the level of risk a gene can impose. The *APOE* gene has three common SNPs that give rise to variants of the gene, or alleles – designated ϵ 2, ϵ 3 and ϵ 4, which encode the isoforms APOE2, APOE3 and APOE4. Possession of one ϵ 4 allele increases the risk of AD up to 3 fold, whereas possession of two

can increase the risk up to 12 fold. Conversely, the $\epsilon 2$ allele is known to be associated with reduced AD risk [69]. The precise pathogenic mechanisms underlying APOE in AD are not fully understood, but clinical and experimental evidence would suggest that the $\epsilon 4$ allele increases the propensity of A β to accumulate by running interference with APP trafficking, encouraging A β oligomerisation or impairing A β clearance [70]. Some research also indicates that APOE4 is neurotoxic and may encourage NFT formation by influencing levels of tau phosphorylation. Genetically, *APOE* $\epsilon 4$ poses the strongest susceptibility to late-onset AD, with over 50% of sporadic late-onset cases being influenced by *APOE* allele status [70]. This suggests that other genetic components and environmental influences still account for a large proportion of sporadic AD cases. However, given the strong predisposition to disease onset, *APOE* and its mode of action in AD pathogenesis is of significant interest in disease understanding and drug discovery.

Interestingly, APOE is also a substrate for a receptor called “triggering receptor expressed on myeloid cells 2” (TREM2), expressed on microglia [71]. *TREM2* has more recently been identified via genome-wide association studies (GWAS), as a candidate gene whose variants have a strong association with increased risk for late-onset AD [72]. Heterozygous possession of *TREM2* variants can confer risk to AD to a similar degree to those carrying one copy of *APOE* $\epsilon 4$ [73]. Whilst the biology underlying these variants and their contribution to AD pathology is still under rife investigation, it is now well established that *TREM2* variants can contribute to a 2 – 4 times increase in AD predisposition [74].

Mutations for tau have not been implicated in AD risk per se, but *MAPT* mutations have been widely studied in related dementias such as frontotemporal dementia, particularly FTDP-17. Variants in *MAPT* have also been identified in families who clinically present with an AD phenotype, mixed dementia or have other known AD risk alleles, but there is insufficient data from population studies to conclusively identify genetic tau variants as a risk for pure AD [75,76]. Nonetheless, extensive investigation of these mutations has bolstered the field of tau biology, and in doing so, continues to provide crucial clues towards advancing the understanding of AD pathogenesis.

With the advent of GWAS and whole-exome sequencing technology, the potential to uncover more gene variants contributing to AD risk has been enabled. These new advances could help further our understanding of both polygenic and Mendelian genetic risk patterns for AD, and the identification of new gene variants could also divulge novel mechanistic links to the pathogenic pathways of AD.

1.4.2 Modifiable risk factors

Sporadic AD cannot be fully explained by genetic factors, and as such, a range of other modifiable risk factors have been identified through population studies. As yet, no single factor has been identified as one that could reverse or halt AD. But recognising these contributors to disease risk is helping the AD research community make evidence based recommendations to lifestyle changes in an effort to reduce AD risk in populations. Meta-analyses across populations have enabled the identification of a range of modifiable risk factors.

The strongest modifiable risk factor for AD and other dementias is cardiovascular health. Circumstances that are detrimental to cardiovascular health all contribute to increased dementia risk, which include smoking, diabetes, hypertension and obesity [66]. This risk can be modulated by lifestyle changes that are protective to heart health, which consequently also protect brain health. Physical activity is one such factor that is now known to be modestly protective against AD and cognitive decline. The exact nature, duration and regimen of activity that is most effective in reducing AD risk remains to be clarified, but it is thought that the mechanistic link between increased physical activity and reduced AD risk lies contemporaneously with reducing the risk of metabolic conditions such as cardiovascular disease and diabetes [77]. In a comparable manner, nutrition too has been reasonably recognised as a protective factor in AD prevention. The mechanisms of protection are predominantly attributed to improved heart health and reduced risk of diabetes arising from diets rich in fruit, vegetables, whole grains, fish, chicken and nuts, and low in saturated fats and sugar [66,78]. Moderate alcohol intake has also shown some protective effect against AD. The direct role this plays in reducing risk is unclear, but it must be noted that this is

outweighed by the damaging health effects that are brought about by excessive alcohol intake, which include neurotoxicity and a higher predisposition to dementias [79].

A strong association between the level of education and dementia risk has also been established. Individuals with fewer years of formal education are at higher AD risk than those with more years of education [80]. A further association between education level and socioeconomic status is also linked to AD risk. People from lower socioeconomic backgrounds are less likely to have good access to healthcare, tend to suffer poorer diets and are less likely to take up physical activity, factors which then predispose them to cardiovascular disease and diabetes risk, which therefore increases their AD risk. Level of education being protective is also believed to be in part due to a higher level of cognitive reserve in those who remain in education for longer, as well as in those who take up professions that are mentally engaging [66]. Thus, this presents an ostensive protective factor. But it must also be noted that though AD sufferers with higher cognitive reserve and more education have a delayed clinical age of onset, they can experience faster decline in cognitive ability post diagnosis [39].

On a related theme, cognitive training activity has similarly been explored for protective effect against AD. Whilst evidence from observational studies would suggest that engaging in cognitive activity lowers AD risk, the results are not clear cut. Whether interventional cognitive training is an effective strategy for AD remains inconclusive. Nonetheless, it is recognised that engaging in physical and social activities that are mentally stimulating can be beneficial in maintaining a better quality of life for older adults [81].

As we are a social species, it is perhaps unsurprising that remaining socially engaged throughout life is vital for maintaining brain health. Social engagement is linked to a reduced risk of AD later in life, possibly by building and maintaining cognitive reserve [66]. The purported mechanisms through which this is protective is unknown, however, there is evidence demonstrating that social isolation and loneliness is associated with poorer cognition [82] and increased AD risk later in life [83], and that amyloid burden increases in cognitively normal older adults experiencing loneliness [84]. Hearing loss in older adults is

also known to accelerate cognitive decline, in part by increasing vulnerability to social isolation and exhausting cognitive reserve [85]. This thus highlights social isolation as a multifaceted risk factor for AD.

Head injury is another factor that can increase the risk of dementia. Clinically known as traumatic brain injury (TBI), it was first identified as a risk in the early 90s after studying boxers who began to show neurodegenerative symptoms [86]. More recent evidence shows that mild TBI and repetitive concussions sustained from contact sports or warfare can precipitate a neurodegenerative condition known as chronic traumatic encephalopathy (CTE), which is clinically indistinguishable from AD. CTE is classified as a tauopathy, featuring NFTs and NPs, but can only be diagnosed neuropathologically on post-mortem examination [87].

Sleep disturbances are common in patients with mild to moderate AD, with around 25 – 40% experiencing this symptom. Experimental evidence alludes to $A\beta$ imbalances brought about by disrupted sleep physiology as the mechanistic link here. [88]. Furthermore, sleep fragmentation has been implicated in faster cognitive decline and increased risk for AD. This implicates sleep disorder as a feature underlying the degenerative process, presenting it as a risk factor for AD [89]. Thus, sleep research offers an additional interventional avenue for AD research.

The factors presented above are not an exhaustive list of risk factors for AD onset. Additional factors including depression, statin use, nutritional supplements and several others [90] have been investigated within this context, but aren't discussed here. Nonetheless, with increasing population studies across international cohorts, the list continues to grow. Overall, the overarching evidence would suggest that a healthy approach to aging is the key to reducing dementia risk later in life.

1.5 Mouse models

AD research has taken giant strides with the advent of transgenic mouse models of the disease, which have enabled researchers to dissect out the various pathophysiological pathways and study them in isolation as well as in tandem. Transgenic technology has been developed and honed over decades and generating transgenic models of disease in mice offers several advantages over other model organisms. Mice share almost 99% of the genome with humans, and have comparable anatomy, physiology and development [91]. The mouse genome has also been well characterised by international large-scale sequencing efforts, and this, combined with the power of transgenic manipulation of the genome, makes the laboratory mouse a powerful research tool [91]. Furthermore, mice are relatively inexpensive to maintain and have quick lifespans enabling cost-effective acceleration of research output. Over a hundred different lines of mouse models are currently in use amongst the AD research community [92]. This not only represents the complexities of studying human disease in a separate host species, but also demonstrates the value of this approach in understanding disease aetiology and drug discovery. An ideal transgenic model organism requires the disease to have a genetic origin, as well as have fairly well characterised pathology, physiology and behaviour in humans that can be recapitulated for in depth experimental exploration [93]. As such, AD mouse models largely rely on the known mutations in AD-causing genes as well as the known features of plaque and tangle pathology to recapitulate clinical AD-like phenotypes in mice.

The *APP*, *PSEN1* and *MAPT* gene mutations identified in human AD cohorts feature heavily in AD transgenic models, with *PSEN2*, *APOE* and *TREM2* mutants also providing valuable alternative models for the mechanistic exploration of the AD pathophysiological cascade. Mutant forms of these genes have been used in isolation to generate single gene transgenic models, as well as in combination for multi-transgene models based on the research question the model aims to address [92]. In the work presented in this thesis, a selection of these models have been utilised. These are described in brief below and discussed further in the relevant upcoming chapters.

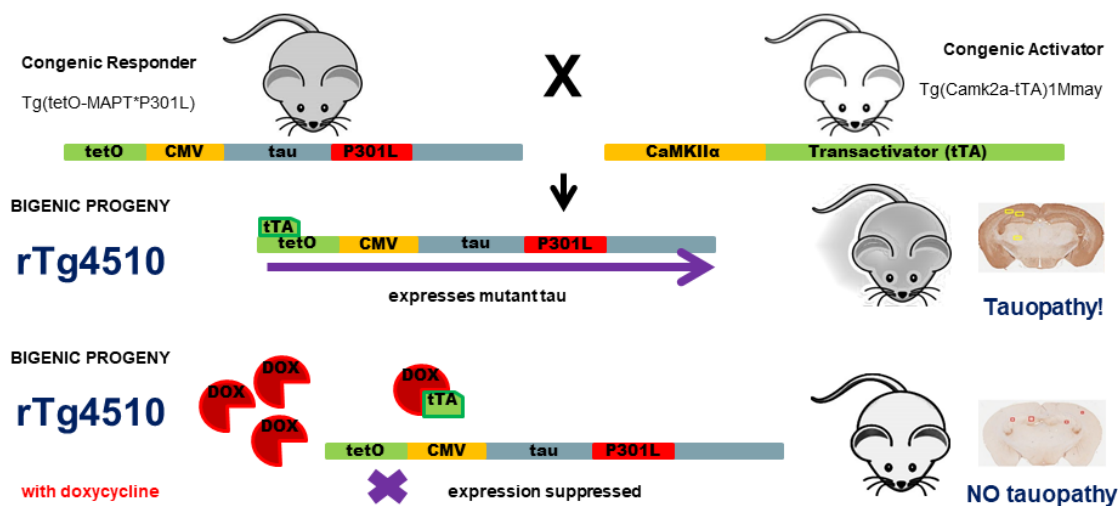


Figure 8. Cartoon depicting an example of a transgenic mouse model. Here, the transgenic constructs that generate and modulate tau pathology in the rTg4510 mouse model are shown. This model is generated by crossing a transgenic mouse containing the P301L human tau mutation, with a second transgenic containing a transactivator under the CaMKII α promoter which drives forebrain expression of mutant tau in the bigenic progeny. Expression of this construct can be halted by tetracycline analogue, Doxycycline.

The rTg(tauP301L)4510 (rTg4510) mouse model is a model of tauopathy that has prominently been used in the laboratory study of tau physiology. The model is generated out of a transgenic line which carries the human *MAPT* gene harbouring the P301L mutation, crossed with a second transgenic line that carries a forebrain specific expression promoter, calcium/calmodulin-dependent protein kinase type II alpha (CAMKII α). The bigenic progeny of these two mouse lines therefore results in robust overexpression of human mutant tau throughout the forebrain. The genetic design of this line also enables the systemic modulation of transgene expression by manipulating the tetracycline-controlled transactivator built into the transgenic construct; forebrain expression of mutant tau can be halted using the tetracycline analogue doxycycline [94] (Figure 8). The model rapidly develops insoluble hyperphosphorylated tau species, accumulates NFTs, and exhibits neuronal loss, gliosis and atrophy in an age-dependant pattern, with impairments in cognition and behaviour which are phenotypically relatable to AD [95].

Incorporating the earliest familial *APP* mutations into transgenic lines has advanced the study of A β pathology, and one such line is the J20(PDGF-APP^{Sw,Ind}) (J20) [96]. This

transgenic line incorporates the Swedish *APP* mutation as well as an additional *APP* mutation identified in Romanian kindreds, first isolated by a research group in Indiana. The transgene is driven by a neuron-specific promoter called platelet derived growth factor (PDGF), and the model expresses elevated levels of A β and robust plaque pathology, with gliosis, some neuronal loss in the hippocampus but no gross atrophy. Learning and memory deficits are also observed in J20 mice [97], thus enabling the study of the cognitive and pathological changes of AD solely driven by plaques, without being confounded by aggressive tangle-driven neurodegeneration.

Whilst these and other murine models continue to propel the understanding of AD aetiology, overexpression models have faced criticism due to their propensity to drive phenotypes in an artificial way, thus making data interpretation challenging. These criticisms are fuelling the evolution of new models to address these challenges. One such line is the APP NL-F Knock-in (NL-F). This mutant line combines the Swedish mutation along with an *APP* mutation from a patient of Iberian ancestry, but is only expressed at endogenous levels [98]. The phenotypes seen in this model are only driven by the combined effects of the two mutations and avoid being confounded by overexpression. The resulting mouse model develops cortical plaque pathology at an early age, but does not show cognitive deficits till later in its lifespan, thus recapitulating a more realistic disease progression. Generation of such innovative lines is unlocking new potential in the use of transgenic technology to uncover the complex nature of AD pathogenesis.

But newer mouse lines have not devalued the use of long-existing transgenics, which still prove useful today. One of the earliest overexpression models, known as Tg2576, which incorporates only the Swedish mutation [99], is still widely in use in AD basic science research today. This line displays a similar phenotype to the J20, but progresses plaque pathology at a slower rate. Such utilisation of various transgenic lines targeting different aspects of pathology with differential progression, highlights the pressing need to target the cascade of AD pathophysiology with fine detail in order to fully comprehend a disease which is still not fully understood.

Scores of other mouse models that replicate tauopathy, amyloidopathy and the other molecular and cellular characteristics of AD pathology continue to be the subjects of extensive research investigation [100]. It must be noted however, that no mouse model exists that fully recapitulates all neuropathological features, behavioural changes and progression of AD in one, and has thus proven to be an added challenge in the search for candidate therapies that can interfere with the pathophysiological cascade.

1.6 Current approaches to therapeutics

The pursuit of a disease modifying therapy for AD has been vigorous and met with many challenges and failures. This is owing to the fact that we still do not fully understand the complete picture of AD pathogenesis, nor have we conclusively identified the root cause of the disease. Drugs that are currently in use in the clinic only help alleviate the symptoms of mild to moderate AD, but none exist that fully cease the neurodegenerative process.

204 candidate therapeutics for AD have entered investigative trials to date, of which 78 are already discontinued. Five of these are currently approved for use by the Federal Drug Administration (FDA), all of which target neurotransmission – Donepezil, Galantamine, Rivastigmine and Tacrine which target the cholinergic system by inhibiting AChE, and Memantine an antagonist of N-methyl-D-aspartate (NMDA) glutamate receptors [101]. During AD development, AChE activity increases, thereby hydrolysing an excess of ACh, causing a decrease in the availability of this neurotransmitter at the synapse, and this impairment at synapses manifests as cognitive deficits observed in patients [102]. AChE inhibitors act by targeting this process, thus facilitating symptomatic relief by increasing ACh availability.

NMDA receptors on the other hand work by reducing neurotransmitter activity. Whilst this may seem counter intuitive, NMDA receptor overactivity is thought to contribute to the neurodegenerative process by becoming neurotoxic – a phenomenon known as excitotoxicity [103]. Normally, NMDA receptors are implicated in synaptic plasticity. They act by binding

glutamate, a potent neurotransmitter, which then results in postsynaptic depolarisation via ionic sodium (Na^+) and calcium (Ca^{2+}) influx [104]. During AD, it is thought that overactivity of NMDA glutamate receptors causes an excess of Ca^{2+} influx, to a level which triggers cellular injury or death [103]. Thus, NMDA glutamate receptor antagonists mode of action is to reduce excitotoxic neurodegeneration. This is a challenging strategy, as therapeutics that block synaptic neurotransmission have to act such that they do not then cause further neurological adverse effects in trying to prevent excitotoxicity. Memantine is the only clinically used drug that uses this strategy, and it is designed such that it only blocks the NMDA receptor once the receptor has been activated for a long time by an excess of glutamate [103].

Whist these strategies are a step in the right direction, the holy grail of AD drug discovery would be one that ameliorates $\text{A}\beta$ and tau accumulation. Numerous disease modifying therapies targeting these hallmark proteins have entered drug discovery pipelines but to little or no avail. In 2018, 26 candidates reached Phase III trials, of which 14 aimed to target amyloid and one was aimed at tau [105]. This not only provides a snapshot of the challenging landscape of AD drug discovery, but also alludes to the ebb and flow of therapeutic approaches to AD.

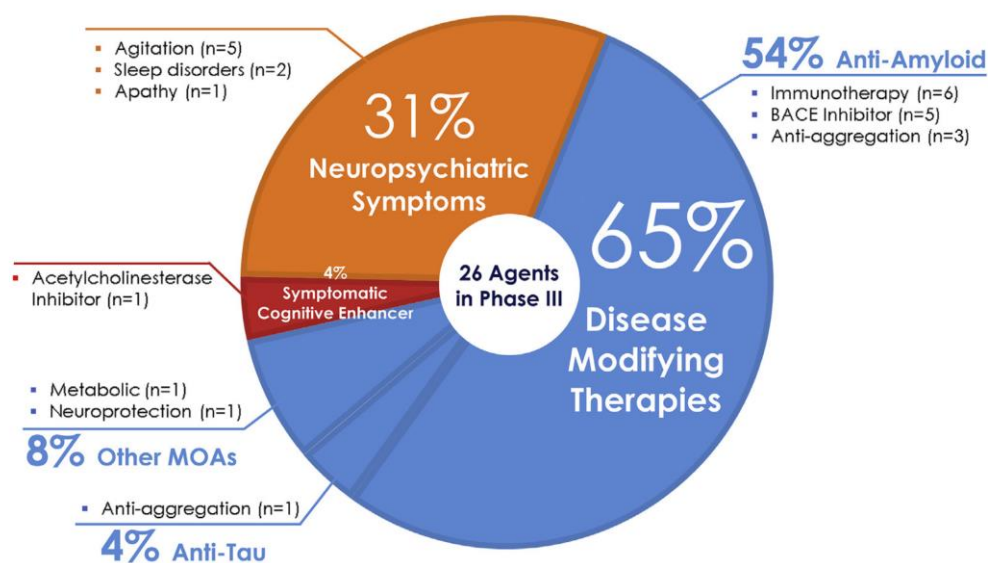


Figure 9. Summary of drugs in Phase III trials targeting mechanistic pathways of AD. Reproduced from Cummings et al., 2018 [105].

In the search for a disease modifying therapy, amyloid research still dominates the AD drug discovery arena (Figure 9) [105]. A β targeted therapies aim to intervene at the early stages of the amyloid cascade by interfering with production, preventing aggregation or reducing deposition [106]. As such, targeting APP cleavage has been of significant focus, either by inhibiting β - or γ -secretase activity or upregulating the non-amyloidogenic pathway via α -secretase activity. Targeting α -secretase may seem a viable strategy, however, more APP is processed via this non-amyloidogenic pathway, and several other substrates for this enzyme exist. Thus this pathway would need to be upregulated significantly to elicit a therapeutic effect, and the consequence to its other substrates are unknown. Whilst inhibiting γ -secretase activity seems more feasible, and has been approached, it is now known that several other substrates for γ -secretase are vital components for development, thus posing toxicity issues and preventing its therapeutic use [107]. This leaves β -secretase as the front runner in this strategy, and several BACE inhibitors have entered therapeutic trials. However, this is not without its challenges – numerous previous BACE trials were halted from not passing safety standards, or due to lack of therapeutic effect in mild to moderate AD. The focus of using BACE inhibitors is thus now shifting towards its use in asymptomatic individuals at risk of developing AD [108].

Immunotherapy approaches have also shown promise in targeting A β , with much of the early evidence coming from active immunotherapy approaches in mouse models, where a synthetic version of the peptide is used to induce an immune response against endogenous A β . Immunotherapy against A β by anti-amyloid antibodies is thought to work via three different approaches – by microglial activation and phagocytosis, by preventing aggregation or by sequestering A β and draining it into circulation [107]. Initial trials in humans were halted due to adverse effects brought about by active immunisation in 6% of subjects, with autopsy of two of these cases revealing an autoimmune T-cell response, thought to arise from the C-terminus region of the peptide. However, a further three autopsies from these trials also showed no cortical plaques thus providing some confidence in this therapeutic approach [106]. The next generation of immunotherapy candidates are being designed to take a passive

immunisation approach using monoclonal antibodies against A β , or by modifying the peptide conformation to overcome autoimmune responses associated with the active approach [109]. Whether these approaches will be fruitful are yet to be revealed, with several vaccines still in trials.

Tau is emerging as a more lucrative target for AD drug development in recent years, particularly with the failure of large numbers of amyloid-focussed therapies. This is perhaps unsurprising given the indisputable role it plays in the neurodegenerative process, as tau burden in AD and other dementias correlates well with clinical measures [38]. Early approaches to tau targeted therapy focused on manipulating kinase and phosphatase activity to circumvent hyperphosphorylation, preventing aggregation of tau [106] or restabilising microtubules. Success with these strategies waxed and waned, and eventually proved unfruitful, so more recently, immunotherapy against tau has gained popularity. Tau antibodies may act extracellularly by sequestering aggregates and activating microglial phagocytosis, thus preventing further spread, or may also bind intracellularly and promote removal via lysosomal degradation. Animal studies have shown promising results with both active and passive immunisation strategies, and several tau vaccines are entering trials on this basis [110]. However, it is too early to tell if these approaches will yield the desired outcome, particularly as translating therapeutic improvements from animals to humans is challenging.

Developing a drug to halt AD is an arduous task. The ideal candidate needs to be a small molecule capable of crossing the blood-brain barrier, not produce deleterious effects, be able to reverse or halt the neurodegenerative process and alleviate cognitive and neuropsychiatric symptoms. It is likely that a combination approach tackling multiple aspects of the disease may be efficacious and this can only be elucidated once ongoing trials are complete. There is also a shift in focus towards targeting the prodromal phase of AD, which may be a more prudent strategy. But this requires reliable markers for screening and thus highlights the urgent need for robust biomarkers that are sensitive to the earliest cellular and molecular changes in the AD brain.

1.7 Biomarkers for diagnosis

In the original clinical criteria, biomarkers did not play a part in AD diagnosis. Without the use of biomarkers, diagnosis was tiered – the highest tier, “definite AD”, was only designated upon post-mortem neuropathological confirmation. During life, the diagnoses allocated were “probable AD”, described by amnesic disorders with gradual functional and cognitive impairment, or “possible AD”, the lowest of the three tiers, identified as an atypical amnesic patterns with mixed aetiology. These clinical diagnoses took into account the patient’s medical history, along with measures of cognition, social function, depression and anxiety, assessed using the Mini Mental State Examination (MMSE), the Blessed Dementia Scale, the Hamilton Depression Scale and the Present State Examination. In addition, further sensory and motor tests, as well as psychiatric evaluations were performed to eliminate all other causes, thus reaching a diagnosis of AD by process of elimination [111].

With the identification of AD as a continuum of disorders, the term “mild cognitive impairment” (MCI) was later introduced. This categorisation identified those individuals who fell in the symptomatic spectrum between normal aging and probable AD, thus signifying AD at its prodromal phases. Individuals with MCI show some neuropathological features of dementia diseases, such as NFTs and atrophy, and is thus thought to be predictive of AD onset [112]. Updates to the diagnostic criteria aimed to improve the accuracy of AD and MCI diagnoses, and thus introduced the use of biomarkers alongside the battery of neuropsychological measures. Its use is now recommended in those who approach the criteria for probable AD [17].

An ideal biomarker is defined as a reproducible measure that can accurately quantify physiological changes brought about by disease. Ideally, the perfect AD biomarker would enable the detection of the disease prior to the significant loss of neurons, thus enabling beneficial interventions to halt the disease. Biomarker use in AD diagnosis currently takes a two-pronged approach – one looks at the markers of amyloid, measuring levels of A β 42 in cerebrospinal fluid (CSF) and amyloid positron emission tomography (PET) imaging. The second looks more broadly at markers of neurodegeneration, by measuring CSF tau,

including levels of total tau (T-tau) and phosphorylated tau (P-tau), ¹⁸fluorodeoxyglucose (¹⁸F-FDG) PET and structural magnetic resonance imaging (MRI) [17]. Patient data from those recruited into large scale longitudinal human cohort studies, such as the Alzheimer’s Disease Neuroimaging Initiative (ADNI) and the Dominantly Inherited Alzheimer Network (DIAN), have enabled researchers to track and detect the patterns of these biomarkers in sufferers and those predisposed to AD [113,114]. Such studies have revealed that biomarker changes accelerate during the initial stages of the pathology and decelerate in the later stages of the disease, thus assuming a sigmoidal trajectory [114]. The use of multi-factorial analyses of data from these cohorts have continually facilitated the understanding of the temporal specificity of discrete biomarkers with disease progression [115]. As such, a model of the pathological cascade against biomarker detectability has been proposed, demonstrating the order of sensitivity against disease progression (Figure 10).

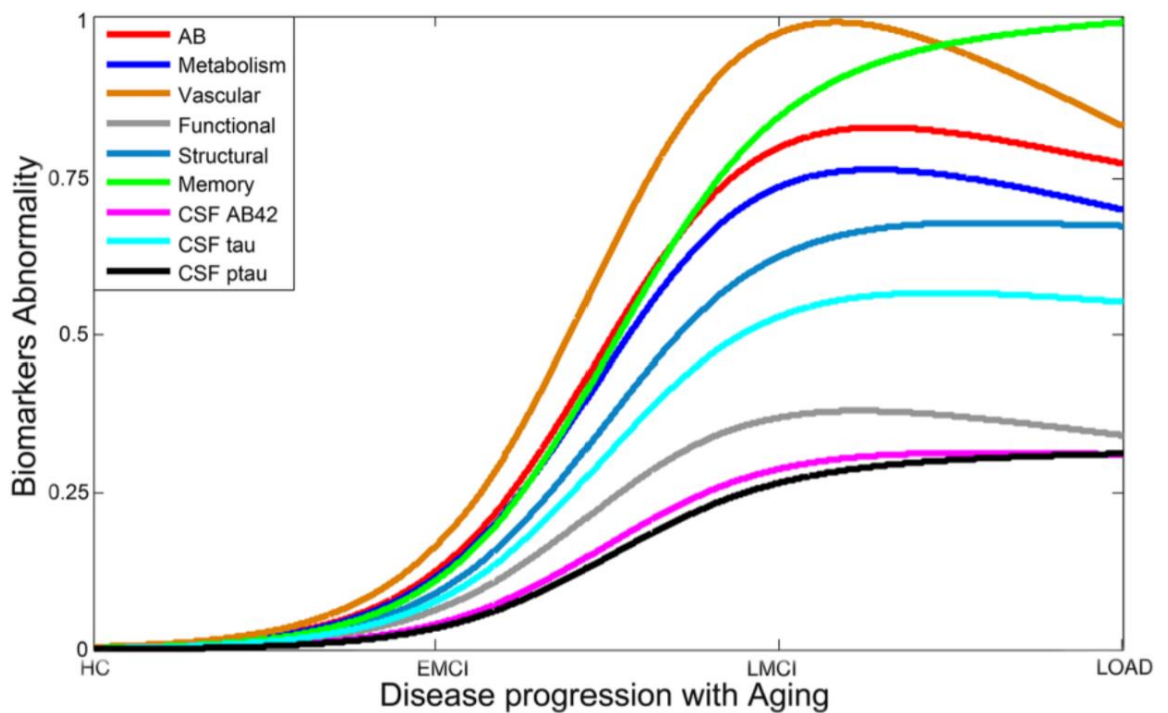


Figure 10. An updated model of AD biomarker detection. Using data from ADNI, each biomarker is modelled to a sigmoidal trajectory as it changes from the healthy state to AD. This model reveals that vascular dysfunction is the earliest change, followed by A β deposition and metabolic dysfunction. CSF biomarkers come later in the temporal cascade of pathophysiological events and increase in sensitivity with disease progression (HC = healthy controls; EMCI = early MCI; LMCI = late MCI; LOAD = late onset AD). Reproduced from Iturria-Medina et al., 2016 [115].

1.7.1 CSF biomarkers

CSF for diagnosis is extracted via lumbar puncture, using a needle placed into the subarachnoid space between the 3rd and 4th lumbar vertebrae. The technique is safe and relatively quick, but can induce a mild post-lumbar puncture headache in some cases [116]. Meta-analyses of vast datasets from human cohort studies have provided validation for numerous fluid biomarkers, including the core CSF measures, A β 42, T-tau and P-tau, which have up to 90% accuracy for detecting AD and MCI [117].

CSF A β 42 decreases with AD progression. As this decrease correlates well with increased parenchymal amyloid counts, it is discernibly hypothesised that A β 42 accumulation into plaque pathology is responsible for the decline of this species in CSF. Low CSF A β 42 is also concordant with amyloid PET positivity in AD patients. Although A β 40 is relatively unaffected, the ratio of A β 42:A β 40 has particularly proven itself a strong biomarker for AD and is usually used in conjunction with A β 42 [118]. CSF T-tau and P-tau on the other hand, increases with AD. CSF T-tau is taken as a measure of neuronal damage, as this metric is also elevated in other conditions such as stroke and TBI, where it also correlates to the degree of tissue damage. P-tau, a measure of phosphorylation status, correlates reliably with NFT pathology and hippocampal atrophy [116].

More recently, a class of phosphorylated neuronal proteins known as neurofilaments are emerging as promising markers for axonal damage. Neurofilaments are cytoskeletal proteins made of three subunits. Elevated levels of the neurofilament light chain (NfL) subunit are reliably detectable in AD compared to controls. This may provide a new and robust CSF biomarker for AD [117], but at present is only used as a research tool.

1.7.2 PET

The development of *in vivo* imaging technologies sensitive to the pathological features of AD provide a rare yet crucial opportunity to visualise the pathogenic features of AD during the lifetime of a patient, which previously was only possible at autopsy. Nuclear imaging

techniques such as PET do so by highlighting regions of pathology by means of systemically administered radioactively labelled compounds, sensitive to the target features of pathology.

Pittsburgh Compound B ($[^{11}\text{C}]\text{PiB}$) is one of the earliest PET ligands developed for $\text{A}\beta$ visualisation, and is still in use today [119]. $[^{11}\text{C}]\text{PiB}$ has high affinity to fibrillar forms of amyloid and thus recognises vascular and parenchymal plaque pathology. Increased uptake of $[^{11}\text{C}]\text{PiB}$ is seen in the in cortical regions as well as the cingulate gyrus, precuneus and striatum, thus following a characteristic pattern of disease spread which also correlates well with plaque distribution at autopsy. $[^{11}\text{C}]\text{PiB}$ can also predict the conversion of MCI to AD with high specificity, thus providing an early indicator of disease onset [120].

But the carbon-11 radionucleotide gives $[^{11}\text{C}]\text{PiB}$ a relatively short half-life (20 minutes) [121], and so it is impractical for routine use, as it requires cyclotron technology to be in close proximity to scanning sites. This has paved the way for the development of durable ligands with longer half-lives. $[^{18}\text{F}]\text{Florbetapir}$ is one such ligand which is conjugated to fluorine-18. With a longer activity (100 minute half-life) [121], it enables sufficient time for transport and handling, thus facilitating widespread use [122]. $[^{18}\text{F}]\text{Florbetapir}$ has slightly less sensitivity compared to $[^{11}\text{C}]\text{PiB}$, but reliably replicates the detection specificity observed with $[^{11}\text{C}]\text{PiB}$, and its binding to fibrillar $\text{A}\beta$ has been confirmed by autopsy [123]. Development of fluorinated compounds are gaining popularity in neuroimaging, and an array of other compounds continue to enter this research domain, namely, $[^{18}\text{F}]\text{florbetaben}$, $[^{18}\text{F}]\text{flutemetamol}$, $[^{18}\text{F}]\text{AZD4694}$ and $[^{18}\text{F}]\text{FIBT}$ all of which show promise as agents with high specificity to AD [120].

$^{18}\text{F}\text{-FDG}$ PET has also long been used in AD research and quantifies glucose metabolism in the brain, which is reduced during AD due to synaptic decline. Thus it provides an indirect measure of synaptic activity. Hypometabolism measures using $^{18}\text{F}\text{-FDG}$ have up to 70% specificity in detecting AD from healthy controls, and through the differential stages of the disease. During the early stages, it is observed in the posterior cingulate cortex and precuneus, later in the posterior temporo-parietal cortex and finally in the frontal cortex during the most advanced stage. $^{18}\text{F}\text{-FDG}$ can also reliably predict the progression of MCI

individuals to AD, as those subjects that progress to AD show lower uptake in the temporal and parietal cortices [120].

The development of tau PET ligands however, has been faced with a plethora of challenges. Primarily, the predominant intracellular location of tau requires a ligand to be able to overcome the blood brain barrier (BBB) and then also cross the cell membrane. Tau also assumes multiple isoforms, which undergo various post translational modifications and these pose challenges to the structural design of a viable molecule. Furthermore, tau is lower in concentration compared to A β , can assume similar structural conformations to A β sheets and is also found in white matter regions, thus posing multiple complications with binding specificity [124].

The first generation of tau PET tracers that overcame these hurdles were fluorinated quinoline derivatives, collectively known as THKs, and although they showed good affinity to tau, the use of these agents were continually hampered by white matter binding and off target binding [125]. Subsequent development of carbon-11 conjugated phenyl/pyridinyl-butadienyl-benzothiazoles/benzothiazolium (PBB) tracers have achieved greater success. [^{11}C]PBB3 has high affinity for dystrophic neurites and NFTs, is retained in the medial temporal region, precuneus and frontal cortex and correlates well with cognitive decline [126]. Fluorinated versions of this compound are currently in development. Another fluorinated tracer that has made strides in tau neuroimaging is a molecule called AV-1451. The spatial distribution of [^{18}F]AV-1451 localises well to tau deposition in a way that can be linked to Braak staging, thus enabling the progressive tracking of disease severity [125].

However, development of these novel ligands is not without its challenges. It is recognised that each of these ligands have differential affinity to the various sub species of tau associated with different proteinopathies – for instance, THKs recognise NFTs which contain both 3R and 4R tau, but are less competent at recognising tauopathies which only have one of these species, unlike PPBs which detect all tau compositions [127]. Furthermore, off target binding is not fully resolved even in these ligands. These issues call into question the veracity of tau PET as a biomarker, and validation of tau PET ligands in further longitudinal studies is

crucial for its advancement into the clinic [128]. Thus, the utility of tau PET remains as a developmental research tool for now.

1.7.3 MRI

MRI has long served as a reliable and useful diagnostic tool to assess macroscopic brain changes that occur during mid and severe stages of AD. The regional and progressive pattern of atrophy measurable by MRI reliably mirrors the cognitive and behavioural changes reported in clinic [129]. The earliest changes are seen in the entorhinal cortex, hippocampus and posterior cingulate cortex, correlating to memory impairments, whereas the later stages see atrophy take hold of the temporal, parietal and frontal cortices, reflecting the observed deficits in language, and behaviour [130].

Hippocampal and medial temporal lobe atrophy measures taken using structural MRI are consistently calculable with roughly 80% specificity for both AD and MCI, with hippocampal volume also correlating well with NFT Braak staging. Additionally, rates of change of cortical regions as well as ventricular enlargement, measurable by MRI, correlate well with the cognitive changes clinically observed. It is important to note that the various structural markers obtainable by MRI are differentially useful for the various stages of disease progression. Although measures have sensitivity to the prodromal stages of the AD continuum, markers of $A\beta$ pathology still provide greater sensitivity to the early stages. These markers plateau later during the diseased state, and regional differences in atrophy then provide better information on disease progression (Figure 11) [131]. Although these macroscopic changes observed by MRI provide a valuable clinical biomarker, the use of this modality to probe the microstructural and functional changes that precede the macroscopic changes can profoundly increase its potential to provide a more sensitive biomarker for early detection. To this end, MRI is profusely pursued in AD biomarker research.

Hippocampal volume reductions have been a predominantly useful measure in assessing those with MCI and genetic predispositions to AD. But the predictive power of hippocampal volume changes can be markedly strengthened by using hippocampal subfield measurements. In particular, the CA1 region of the hippocampus has consistently been found

to be reduced in volume in MCI subjects compared to healthy controls, and is able to predict the conversion from MCI to AD. Probing subregions of the brain most vulnerable to AD therefore increases the effectiveness of MRI as an early biomarker, as this could detect subtle brain changes up to a decade before clinical onset [132].

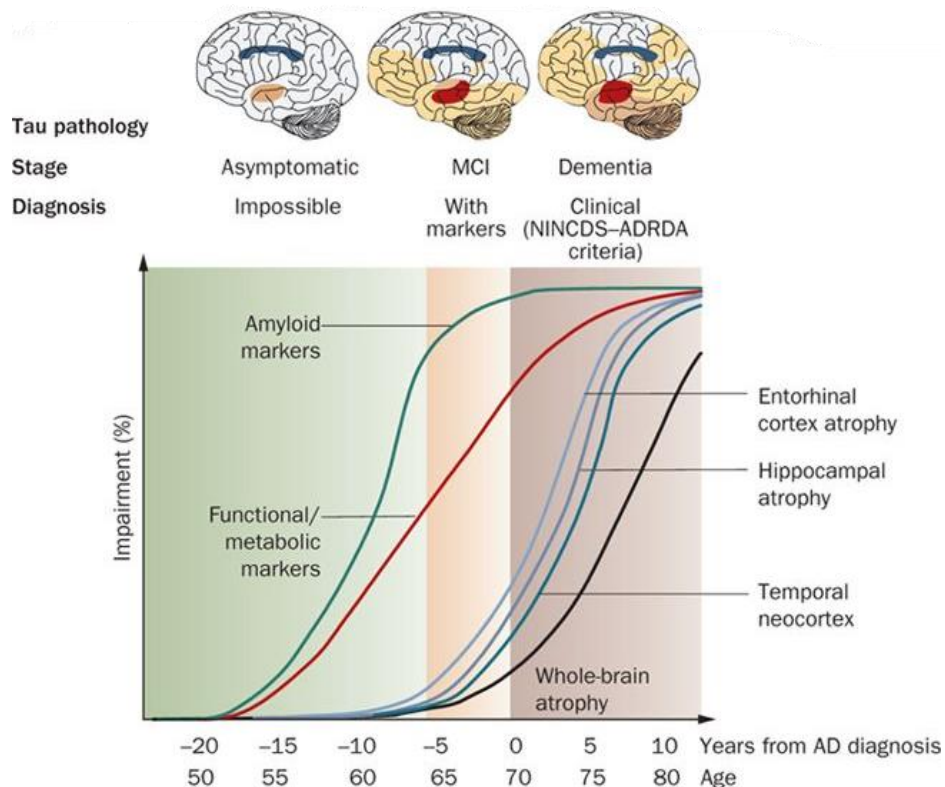


Figure 11. Representation of disease progression against diagnosis by MRI. The preclinical stages are better diagnosed with non-MRI markers, whilst the clinical stages have sensitivity to disease stage. Reproduced from Frisoni et al., 2010 [131].

MRI has also gained repute in detecting microstructural changes that occur in the brain during neurodegenerative disease. White matter lesions are a commonly observed feature of AD, believed to be brought about by axonal loss and demyelination [133]. Diffusion tensor imaging (DTI), which measures the Brownian motion of water, is particularly useful in following these white matter changes brought about by pathology. In myelin fibres, this pattern of movement is restricted to the structural tracts of the tissue. The consequential change and directionality of diffusion can be quantified using DTI [134]. Disarray of white

matter tracts driven by AD pathology can therefore be assessed. At present, MCI can be differentiated from AD using DTI, but the sensitivity does not exceed that attained from volumetric measures [135], and so while it can add profound diagnostic value to other biomarkers, it may not be a steadfast marker specific to AD in isolation.

Being the most energy intensive organ in the body, the brain requires good blood flow to maintain brain health. Significant evidence implicates vascular pathology and cerebral hypoperfusion as a causative element in the pathogenesis of AD [136]. Thus, it is pertinent to explore cerebral perfusion as a marker. MRI measures of cerebral blood flow (CBF) have been widely explored in AD patients and they consistently show a reduction in CBF by approximately 40%, with regional correlations to NFT pathology. The outlook of this marker in MCI present a mixed picture. Both hyperperfusion and hypoperfusion are reported in MCI subjects. It is hypothesised that hyperperfusion alludes to a compensatory mechanism that precedes the hypoperfusion that indicates the disease onset [137]. Until there is resolute understanding of these observations, it is difficult to perceive CBF as a clinically translatable biomarker for early onset. However, its use in AD research is prolific in exploring the pathogenic changes via non-invasive imaging.

Brain connectivity is another aspect that is gaining research interest in AD, given the implication of synaptic dysfunction in the disease, and this can be measured using functional MRI (fMRI). fMRI enables the quantification of blood oxygenation as a measure of brain activity, and this measure can be used as a surrogate for functional connectivity of neural networks. In particular, the default mode network (DMN) has been extensively studied within this context [132]. The DMN describes a functionally connected network of brain regions which include the medial prefrontal cortex, posterior cingulate cortex, inferior parietal lobule, lateral temporal cortex and hippocampus [138]. The DMN is understood to be highly metabolically active at rest and is downregulated during task-based activities that require attention, a feature measurable using fMRI. This downregulation is impaired in individuals with MCI, and impaired even further during AD. Furthermore, depletion of DMN activity is distinguishable in mild AD compared to healthily aging individuals [139].

Functional measures using MRI show promise in biomarker utility and may be particularly apt for early detection, as functional changes precede the detrimental morphological changes of the AD brain.

Several laboratories, including ours, continue to develop and refine quantitative MRI techniques sensitive to the early changes of AD, including methodologies sensitive to the pathogenic accumulation of proteins. It is also advantageous over PET measures of brain function, as it overcomes the requirement for radioactive tracers, and MRI is a modality that is more widely accessible, thus lends itself readily for clinical translation. Nonetheless, much like the case of novel PET ligands, any given quantitative MRI biomarker remains a research tool until it is sufficiently validated via human cohort studies.

1.7.4 The next generation of biomarkers

Although neuroimaging is undeniably valuable in assessing the various stages of AD, a significant challenge with its utility as a routine biomarker remains to be its cost, accessibility and throughput. This has spurred efforts to rapidly identify fluid biomarkers, which are more readily accessible. As such, blood based biomarkers are rapidly developing [140]. Blood presents a tangible source of markers, as blood withdrawal is quick, inexpensive, and inflicts minimal discomfort to patients over CSF extraction.

Plasma markers of A β and tau have gained notable research interest, but thus far only plasma T-tau has reached the strengths of sensitivity their CSF counterparts can achieve. Other indirect markers of neuronal markers such as NfL, as well as visinin-like protein 1 (VLP-1), a neuronal cytoplasmic protein, and neuron specific enolase (NSE), a neuronal enzyme, are gaining attention due to their significant CSF presence in AD [117]. Plasma NfL as a marker of axonal damage in particular has come through as a strong biomarker, correlating well with CSF levels [118]. These new candidates provide promising new accessible markers for early detection.

AD is also widely understood to be caused by an imbalance between production and clearance of pathogenic proteins [141]. If imaging accumulation indicates a point in the AD continuum that is too little too late, then useful biomarkers sensitive to the physiological processes that precede accumulation or impede clearance need to be developed. Tests sensitive to the pathways implicated in clearance may therefore provide fruitful avenues for novel biomarker development and viable therapeutic intervention, and also advance our understanding of disease cause, which still remains elusive.

2. The Glymphatic System

This chapter will introduce and define the glymphatic system, a focal theme of the work presented in this thesis, and explore its implication in Alzheimer's disease pathology.

The glymphatic system describes a fluid network of exchange between cerebrospinal fluid (CSF) which surrounds the brain, and interstitial fluid (ISF) found in the extracellular space. It is considered a surrogate for conventional brain lymphatics, which are largely lacking in the brain. It gets its name from its close association with glia, as it is highly reliant on astrocytes for its function. This system facilitates the flushing of solutes and metabolic waste from the extracellular space by influx of CSF into the brain parenchyma, and thus CSF dynamics form an important facet of its function.

2.1 Cerebrospinal fluid

The brain, being such a vital organ, is protected by several physiological layers, the meninges. Beneath the skull, the dura mater forms the first tough meningeal membrane, followed closely by leptomeninges – the arachnoid mater and pia mater. The space between the leptomeninges forms the subarachnoid space (SAS), which holds a layer of CSF surrounding the entire brain. CSF is dynamic – it pulsates and flows around the brain and spinal cord, and through the ventricular network (Figure 12). Multiple forces contribute to these dynamics – CSF appears to follow a pulsatile pattern mirroring the cardiac cycle [142], as well as respiratory stimuli [143]. In addition, rapid bulk flow occurs through the ventricular system [144]. CSF production at the choroid plexus drives it through the lateral ventricles and into the third ventricle, down the aqueduct and into the fourth ventricle, which exits into the SAS via the cisterna magna. Reabsorption of CSF occurs at the arachnoid villi which protrude through the arachnoid membrane into the superior sagittal sinus at the top of the skull, where it drains into venous blood. Additionally, CSF can also drain along cranial

nerves to reach the extracranial lymphatics [145]. Careful physiological equalisation of production and reabsorption maintains intracranial pressure, which is vital for brain health.

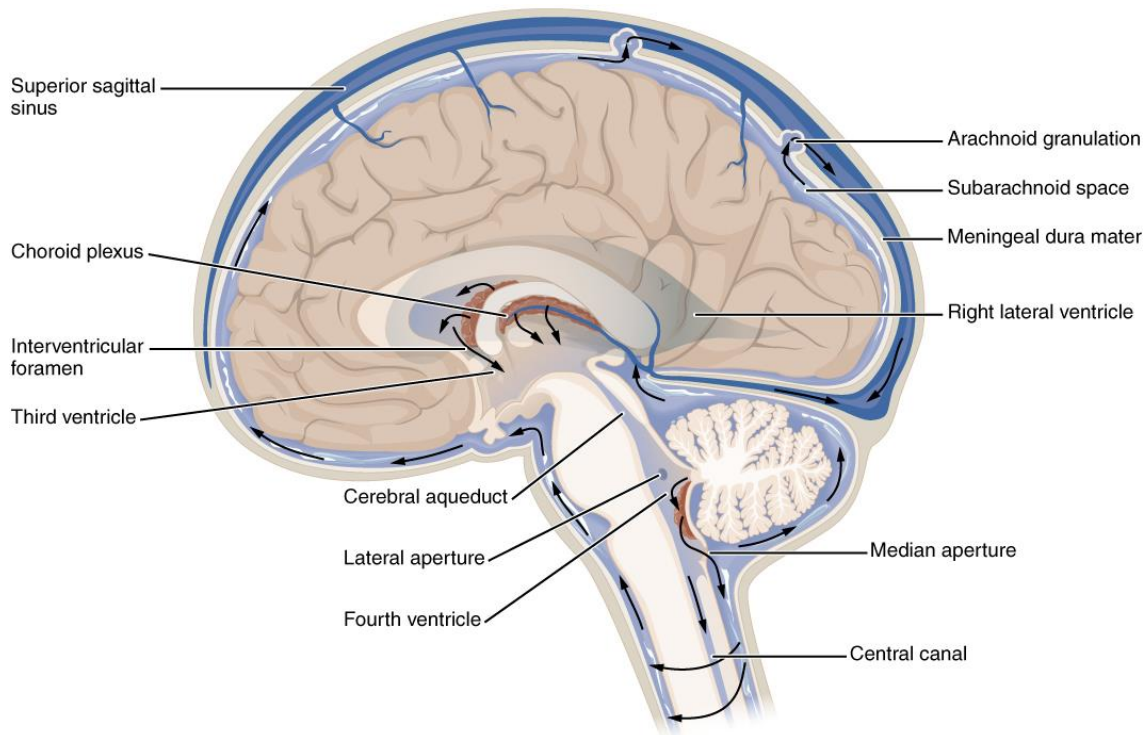


Figure 12. Diagram depicting CSF flow within the cranium. CSF is produced at the choroid plexus within the lateral ventricles, flows through the third ventricle, into the aqueduct down to the fourth ventricle. From here, it flows into the cisterna magna via the median aperture and spreads into the spinal chord and recirculates around the skull, draining into the superior sagittal sinus via the arachnoid granulations. Image reproduced from the Wikimedia Commons free media repository.

The extension of the CSF space into the parenchyma occurs along the main penetrating vessels. The main vessels feeding the brain originate at the circle of Willis at the base of the brain, which separate into three pairs of major arteries – the anterior, the middle and the posterior cerebral arteries. These pial vessels which sit within the SAS, between the leptomeninges, are surrounded by CSF and branch further into arteries and arterioles. The arterioles that begin to dive into the brain parenchyma create a continuation of the SAS between the pial and parenchymal vessels, called the Virchow-Robin space, taking with it a continuation of the pia and the glia limitans – a layer formed of astrocytic end feet that sit directly underneath the pia (Figure 13). As these arterioles branch deeper into the brain, they

change structurally. The layers of the pia and glia limitans discontinue and eventually, the vessels form the capillary bed. This then feeds into the venous drainage system, but an important feature of the capillary microcirculation network is that it forms the neurovascular unit and blood brain barrier (BBB) [146].

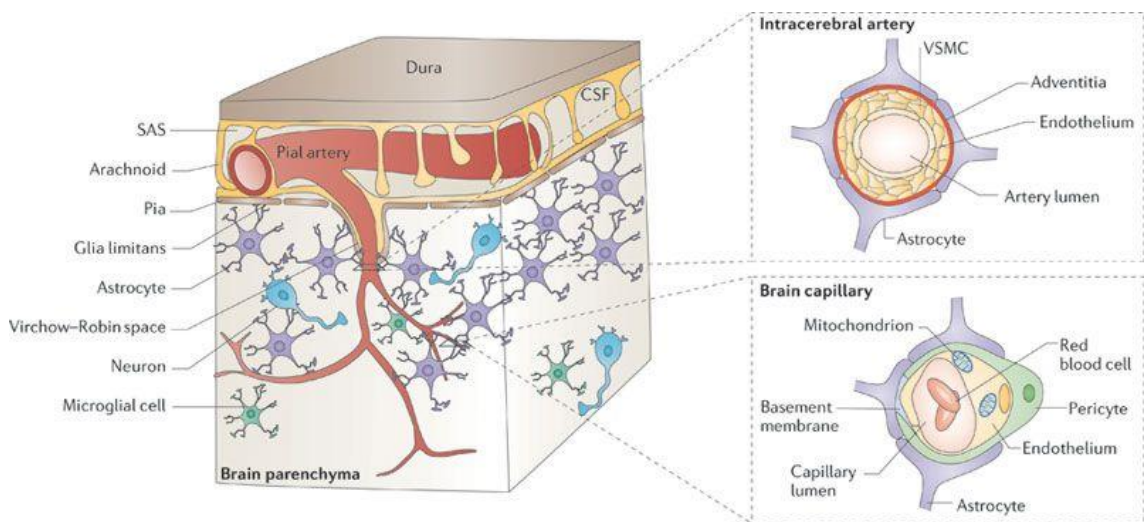


Figure 13. Cross sectional schematic showing a diving feeding pial or leptomeningeal artery and its cellular associations as it variegates into the capillary bed. Pial arteries dive into the brain along with the pia and glia limitans forming the Virchow-Robin space. As vasculature branches and penetrates deeper into the brain, it changes structurally. Arteries are distinguishable from their multiple layers of vascular smooth muscle cells (VSMC). Capillaries are formed of a single layer of endothelium and associated with pericytes. Astrocytic processes surround the entire network of brain vasculature. Reproduced from Zlokovic, 2011 [147].

2.2 The blood brain barrier

The BBB is formed of the endothelial lining of microvasculature throughout the brain. Specialised contractile cells called pericytes sit on endothelial cells of the microvasculature, and together are encased in the basal lamina, formed of a variety of extracellular matrix proteins [146]. The endothelial layer is largely impermeable to macromolecules, with tight junctions between cells acting as a seal preventing plasma proteins from leeching from the blood into the brain, which can otherwise have damaging consequences. In order to transport nutritional molecules from circulation to parenchyma, this seal is specifically equipped with

a variety of transport systems. [148]. The barrier is permeable to other small lipophilic molecules, oxygen and carbon dioxide [147].

A uniquely important feature of the entire vascular network of the brain is that it is closely associated with astrocytes via astrocytic end foot processes that almost wholly ensheath the entirety of brain vasculature. The overlap between these end feet form clefts of roughly 20nms, and these inter-end feet gaps allow microglial processes to interact with the basal lamina [149]. Gap junctions present between individual astrocytic processes also facilitate intercellular exchange between astrocytes, and this unique feature enables a network of communication via the formation of a non-overlapping syncytium [150]. The inter-end feet gaps may provide an entry route for proteins and other macromolecules within this size range to move between the parenchyma and the CSF, but restricts entry into circulation. Thus the BBB serves a crucial protective function in maintaining brain health.

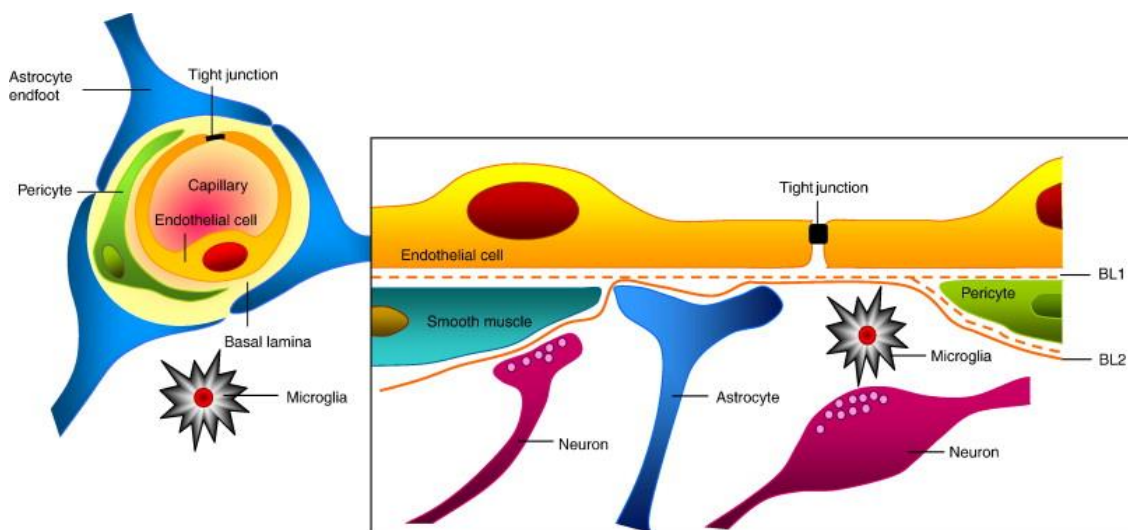


Figure 14. Structural elements of the BBB and the neurovascular unit. At the capillary bed, astrocytic end feet processes surround the pericyte and capillary endothelial cell. Tight junctions between endothelial cells prevent passive entry and exit of molecules between blood and brain tissue. Microglia can interact with the endothelium via gaps between end feet. Reproduced from Abbott et al., 2010 [148].

The close association of the microcirculation with neurons as well as astrocytes, microglia and pericytes also forms an important physiological entity known as the neurovascular unit (Figure 14). The neurovascular unit works carefully to control the chemical makeup of the

interstitium around it, to ensure healthy physiological function. The interplay and cross communication between this myriad of neuronal and non-neuronal cell populations in the brain serves to regulate BBB permeability and cerebral blood flow, thus monitoring critical aspects of normal brain function [147].

2.3 Glymphatic exchange

The continuous fluid network formed from CSF penetrating the brain, first along the Virchow-Robin spaces, and then following the perivascular spaces along the basal lamina to reach the interstitium bathing the cells of the brain, gives way for fluid exchange. The forces of CSF movement, which include cardiac pulsation, respiration and CSF production provide driving forces for CSF to move along this low-resistance pathway to reach the brain parenchyma. Here, CSF moves into the brain parenchyma and exchanges with ISF by convective bulk flow [151]. This enables rapid exchange of CSF with ISF, which then, driven by vectorial convective flux, is drained along the perivascular spaces around draining veins (Figure 15), then getting flushed into the recently discovered meningeal lymphatic vessels [152] and ultimately into the cervical lymph nodes [153].

The mechanisms by which this process occurs have long been debated and probed. Early work by Cserr *et al.* measured the exit rates of radioactive tracers of varying sizes injected into the rat brain, expecting smaller molecules to clear faster if diffusion was the only fluid driving force in the interstitium. They found that tracers cleared at similar rates, thus pointing to bulk flow [154]. Shortly afterwards, work by Rennels *et al.* in cats and dogs showed that infusing tracers into the SAS caused them to travel along perivascular routes and enter the parenchyma, with this effect being diminished by partially ligating the brachiocephalic artery. They deduced that cerebral arterial pulsations were requisite to the entry of solutes into the brain along this pathway [155].

More recently, the workings of this system have reproducibly and comprehensively been demonstrated in the mouse brain. Using fluorescent dyes infused into the SAS and confocal

microscopy, Iliff *et al.* showed that the entry of fluorescently tagged CSF occurs along the penetrating arteries, and also attributed this to the pulsatility of the smooth muscle in the arterial walls [151]. In a subsequent experiment, they verified the crucial role of arterial pulsation, by showing that glymphatic flux was impaired when the carotid artery was ligated to reduce arterial pulsatility in the brain by 50%, and conversely, increasing pulsatility by 60% using an adrenergic agonist sped up this mechanism [156]. The initial experiments also elegantly demonstrated the unique reliance of periarterial and perivenous routes for entry and exit respectively. Using a combination of genetic reporter mice that fluorescently distinguish arteries from veins, and fluorescent tracers injected into the SAS and the parenchyma, they showed that while CSF entry occurred along periarterial routes, exit routes for all these fluid solutes were along the margins of central draining veins. In this work, they also showed the requirement of aquaporin-4 (AQP4) for convective exchange into the parenchyma.

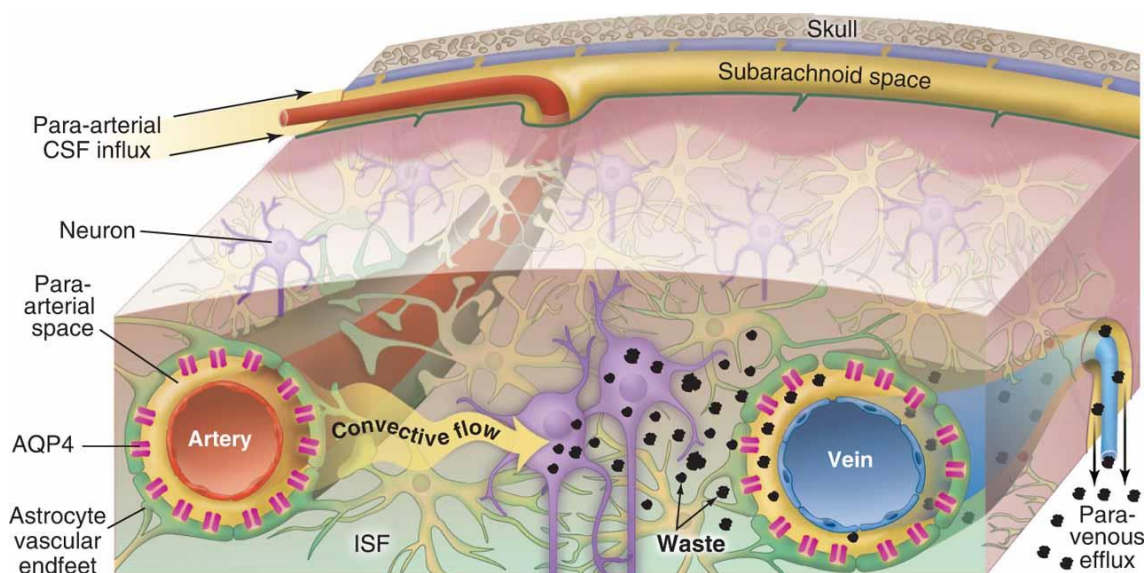


Figure 15. Diagrammatic depiction of CSF-ISF exchange via glymphatic flow. Arterial pulsations drive CSF along periarterial spaces, where AQP4 can facilitate exchange with ISF. Bulk flow drives waste metabolites along with CSF towards perivenous drains [157].

Using AQP4 deficient mice, they found that bulk CSF flow into the Virchow-Robin spaces was unaffected, but CSF tracer exchange into the parenchyma was impaired in the absence

of AQP4. Additionally, they found that tracers injected into the AQP4 null brain interstitium were not efficiently removed, reporting up to a 70% impairment. This crucially demonstrated that the glial water channel AQP4, which is densely expressed at the abluminal surface of the astrocytic end feet which wall the perivascular space, had a significant responsibility in facilitating this fluid exchange network. Because this system behaves as a substitute for brain lymphatics, and relies on glia, the term “glymphatics” was coined [151].

Although evidence demonstrating the workings of this pathway continues to build [158], the precise origin of the driving forces of convective exchange remain dubious. Global CSF flow, diffusion and arterial pulsation have all been put forward, but not fully proven as drivers. The aforementioned early work by Cserr *et al.*, demonstrated that diffusion alone would be insufficient to facilitate the exit rates of tracers [154]. Further studies combining mathematical modelling to infusion studies continued to support the notion that diffusion alone was insufficient to drive influx, and additional forces driving bulk flow within the ISF were at play [159]. Iliff *et al.* put forward the concept of a hydrostatic arteriovenous gradient, created by the combination of arterial pulsation, rapid fluid exchange into tissue via AQP4 and low pressure sinks in perivenous routes [151]. Recent mathematical experiments modelling perivascular CSF inflow and exchange with ISF have suggested that arterial pulsation may not be the sole driving force of inflow. Asgari *et al.* propose the concept of rapid dispersion, described as a combined effect of diffusion in the brain and macroscopic ventricular CSF motion arising from cardiac and respiratory brain deformation. Based on their model, they suggest that rapid dispersion of solutes as a consequence of arterial pulsation facilitates fast transport along perivascular routes, and net bulk flow would require additional driving forces [160]. Physiological evidence for this hypothesis as well as the driving forces for bulk flow is yet to be pinpointed. It is fathomable that the multitude of flow vectors at play within the cranium and the various fluid compartments contribute variably to net flow. A recent study by Ray *et al.* simulated both interstitial bulk and diffusive flow and compared it to a wealth of experimental data that supported both these mechanisms. This study concluded that both these mechanisms are relevant to fluid transport in the

interstitium, with their findings pointing to bulk flow is an important facilitator in moving larger molecules, which diffuse less readily and slowly in the tortuous extracellular space than smaller molecules [161].

The crucial contribution of AQP4 in this system has also been modelled to test the movement of fluid from the periarterial to perivenous side. Asgari *et al.* modelled the astrocytic syncytium between these two locations, by including AQP4 on the plasma membranes, an abundance of AQP4 on the perivascular surfaces, 20nm inter-end feet gaps and gap junctions within their model (Figure 15). They demonstrated the movement of fluid through both a tortuous extracellular route (around astrocytes and cells of the brain neuropil) as well as a simpler intracellular route (through astrocytes, via AQP4 and gap junctions), occurring in parallel. They note that these parallel routes work in harmony, as depleting AQP4 at the end foot domain hinders the net flow, including reduction of movement through gap junctions and the inter-end feet gaps, where metabolites would be expected to move through, possibly driven by a pressure gradient, although the presence of such a gradient has not been physiologically proven [162]. These observations however mirror *in vivo* data and reinforce the idea that effective CSF-ISF exchange relies on a high density of AQP4 on the perivascular domains.

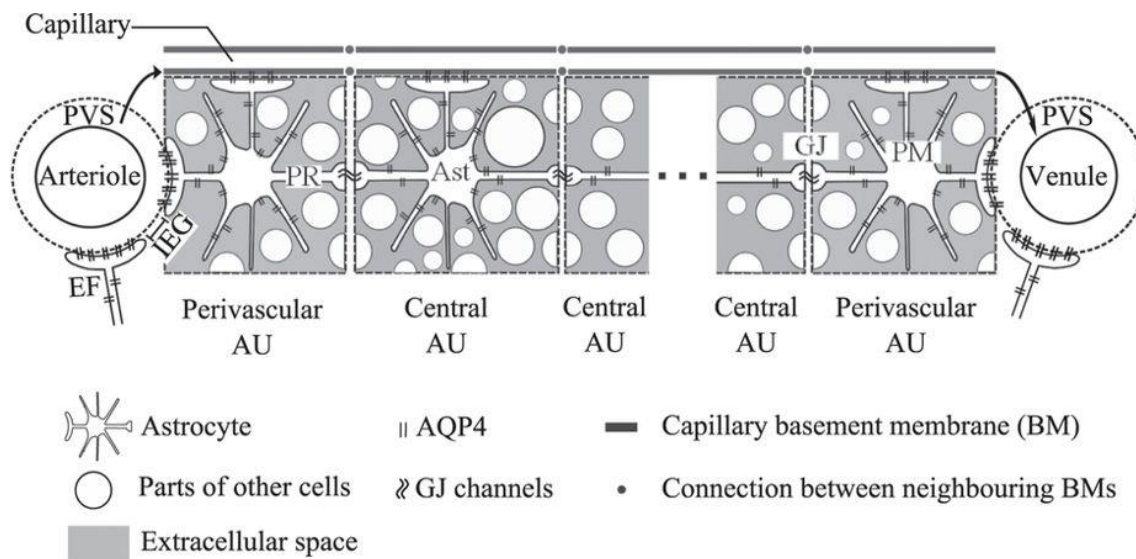


Figure 15. Schema of the mathematical model to simulate periarterial inflow, AQP4 mediated fluid flow and perivenous drainage. A continuous non-overlapping network of astrocytes with AQP4 is modelled here to test the movement of fluid from periarterial to perivenous compartments. Reproduced from Asgari *et al.*, 2015 [162].

2.4 Aquaporin 4

AQP4 is one of several aquaporins which form a family of cellular water channels. Earliest investigations of aquaporins were focused on organs such as the kidneys where a high level of water exchange is crucial in function [163], and subsequently also studied in the eye, lungs and brain of rodents [164]. Aquaporins are crucial in the brain, where careful control of water homeostasis is critical in regulating normal function. AQP1 is found on the epithelial cells of the choroid plexus, whereas AQP4, 5 and 9 are present on the ependymal cells that line ventricles, and on astrocytes [165]. AQP4 is the most abundant form in the brain, highly expressed on astrocytes, and expressed in two isoforms – M1 and M23. The M23 isoform assembles in highly complex structured orthogonal arrays, with a preference towards the end foot process, whereas the M1 isoform individually spreads and moves through the plasma membrane, with a regional preference towards extending membranes [166]. High densities of AQP4 are found at the end feet processes of astrocytes that surround the vasculature network, and also form the glia limitans [164]. This astrocytic feature gives AQP4 a key role in water homeostasis in the brain.

AQP4 has been implicated in a range of brain conditions including neuroinflammation, stroke, oedema and traumatic brain injury (TBI) and experimental evidence in mice have provided a wealth of evidence towards this. For example, in experimental models of water intoxication and stroke, AQP4 null mice show lowered susceptibility to brain oedema and neurological impairment than their wildtype counterparts, providing evidence for its role in water homeostasis during disease [167]. In studying post TBI seizures, AQP4 null mice experienced more severe seizures, increased microgliosis and decreased astrogliosis compared to wildtypes, which contributed to weaker scar formation, thus giving AQP4 a protective role [168]. In a model of TBI, AQP4 has been found to undergo an overall increase in expression along with astrogliosis, but a reduction in polarisation [169].

If AQP4 changes occur in the brain in response to an insult, and polarisation is an important feature in the fluid-mediated transit of brain metabolites, then probing pathologies of the brain within the context of the glymphatic system is of interest. In AD, this system provides

a viable route for tau and A β spread through and clearance from the brain. In order for this to be feasible, these proteins need to reach the interstitial fluid in the extracellular space.

2.5 A β and tau in the extracellular space

The imbalance between protein production and clearance has implicated impaired clearance as a potential mechanism contributing to aggregation during proteinopathies [170]. The initiators of A β and tau pathology remain elusive, but investigation into the spread of these pathogenic proteins provide insights into the possible mechanisms underlying AD onset. A β is an extracellular lesion which appears early during the disease, whereas tau pathogenesis begins intracellularly and later in the AD cascade, and they both have distinct patterns of spread. Thus, the mechanisms by which this occurs can be regarded individually and mouse models have been valuable assets in exploring these mechanisms.

APP processing at the plasma membrane releases A β into the extracellular space which oligomerises and accumulates into plaques [25]. It is however increasingly evident that intracellular A β oligomers are neurotoxic over the fibrillar extracellular plaque forms [27]. *In vitro*, A β can be internalised at distal axons and travel to cell bodies in a retrograde manner, and then transneuronally spread to neighbouring neurons. *In vivo*, A β is seen to spread via neuroanatomically connected regions in the mouse brain [171]. It is hypothesised that oligomeric A β is secreted extracellularly via exosomes, and then internalised endosomally, where it then collects in lysosomal vesicles. Support for this theory is evident in cell culture, where endosomal-lysosomal trafficking of oligomeric intracellular A β 42 has been demonstrated [172]. When internalised, A β is devastating to cellular machinery, as it can interfere with synaptic function, disrupt enzymatic activity and disturb calcium homeostasis [173]. In mice, oligomeric extracellular A β can also act as seeds around existing plaques, thereby promoting formation of new plaques [174].

Hyperphosphorylation of tau inside the neuron causes it to dissociate from microtubules and aggregate in an incremental manner until it forms an NFT. Although tau is an intracellularly

aggregating protein, the appearance of P-tau in CSF during AD indicates that the release of pathogenic tau species into the extracellular space is a key event in initiating its spread. It is hypothesised that pathogenic conformations of tau in the extracellular space can act as a seed and propagate misfolding and spread through synaptically connected neurons in a prion-like manner [175]. This has been demonstrated in mice [176]. When insoluble tau species extracted from mutant tau mice are injected into the brains of transgenic mice expressing wildtype human tau, it induces the formation of pathogenic tau fibrils, which spreads through anatomically connected regions and progresses with age [177]. The transmission of tau from cell to cell has been probed *in vitro*, and when cells with fluorescently tagged tau is cocultured with naive cells, it is seen to leave one cell and enter neighbouring cells when cocultured. Unlike A β , it is the filamentous form of tau that exacerbates propagation, whereas the oligomeric forms do not succeed in propagating pathology [178].

It is clear that spread of the pathogenic forms of A β and tau require its presence in the extracellular space. It is also apparent that transmission of these abhorrent proteins is encouraged, pointing to an inefficiency in clearance mechanisms at play within the brain during pathogenesis. Thus, probing dysregulation of clearance may offer vital clues towards the onset of AD. In addition, understanding the failure of clearance may offer new targets for therapeutic intervention.

Protein waste can be degraded via a myriad of mechanisms, including and not limited to enzymatic degradation (both intracellular and extracellular), bulk ISF flow and BBB transport, and whilst several clearance systems have been widely studied, the relative contributions of each system remain unknown. It has long been understood that BBB was the prime site of clearance of metabolites, including A β clearance [179]. However, research in glymphatics has demonstrated that it has the potential to clear A β with up to 65% efficiency [151]. It is important to note that whilst glymphatic system has been proposed as a surrogate solution for the lack of brain lymphatics, meningeal lymphatic vessels have also recently been identified in the dural sinuses of the mouse brain, bringing important new insights into waste removal routes in the brain [152]. Evidence for a further perivascular

clearance pathway along basement membranes of capillaries and arterial walls in the reverse direction to glymphatic flow also exists, with important implications in the development of cerebral amyloid angiopathy CAA [180]. The glymphatic system offers a new mechanistic window into the efficient removal of pathogenic substances from the extracellular space and therefore warrants investigation in the AD setting, given that much is still undiscovered in its pathogenesis.

2.6 A β and tau as glymphatic substrates

The entry and exit of parenchymal metabolites via the glymphatic system has been demonstrated using a variety of techniques. In the preliminary experiments by Iliff *et al.*, in addition to characterising the pattern of periarterial to perivenous transit, they also showed that A β is a substrate for removal via this mechanism. Using fluorescently labelled A β , they showed its presence along capillaries and draining veins, and when radioactively labelled A β 40 was injected into the parenchyma, they showed gradual removal of this substrate over time. When injected into the SAS, an increase in tagged A β was detected in the brain over time. Importantly, both these observations were significantly marred when repeated in AQP4 null mice [151]. Glymphatic A β clearance has also been investigated with sleep cycles, as both APP mice, as well as human subjects show increases in ISF A β levels that correlate with wakefulness. In addition, APP mice that are sleep deprived show increased cortical plaque burden [181]. Based on this finding, and the observation that sleep disturbances are prevalent in AD subjects, Xie *et al.* measured glymphatics in awake and sleeping mice by infusing fluorescent tracers onto the SAS. They found that wakefulness impaired the amount of tracer influx, and attributed this to extracellular space changes, as they found that the interstitial volume increased by up to 60% during anaesthesia-induced sleep. They then tested the clearance of radioactively labelled A β and found a twofold increase in clearance in sleeping mice [182]. In another study which looked at the relationship between aging and A β removal, clearance of radiolabelled A β was seen to be impaired with advancing age of the mouse, at a rate comparable to co-infused tracers which would exclusively be cleared via

bulk flow. These observations were attributed to reductions in arterial pulsatility also observed within these aging mice [183]. Taken together, these studies collectively pose A β as a substrate for glymphatic clearance.

The evidence for tau as a glymphatic substrate comes from studies investigating TBI. When mice that underwent TBI were assessed for changes in their glymphatic components, several observations were made. First, the inflow of fluorescent tracers and clearance of radiotracers were reduced in the post-TBI brain. In addition, AQP4 polarisation was reduced following TBI. P-tau levels were elevated following TBI, but importantly, when this experiment was repeated in AQP4 null mice, a significant elevation in P-tau and neurodegeneration was observed [184]. These findings imply that perturbances of AQP4 can contribute to elevated tau pathology via glymphatic impairment.

These experimental findings lay important groundwork for investigating novel clearance mechanisms of A β and tau to further our understanding of AD progression. The work presented in the context of aging is of particular relevance, given that age is the biggest risk factor for AD [66]. In addition to the experimental observations cited here in models of AD and TBI, glymphatic fluctuations are also observed in mouse studies investigating stroke [185], alcohol use [186], exercise [187]. This is fascinating, given that these are all known factors that pose risk for or modulate AD. This growing body of work in this emerging field is paving the way for new avenues in neurodegenerative research. Thus, it is prudent that these findings are expanded upon in order to develop new ideas for AD treatment.

2.7 Aims of this project

The glymphatic system is a newly discovered clearance pathway which has been implicated in clearing waste from the brain, and the workings of this system during AD pathology, which are not fully explored, have been interrogated in the work in this thesis. Within this research programme, I set out to quantify glymphatic inflow in mouse models of AD, taking a whole-brain 3-dimensional imaging approach. My thesis aimed to:

1. Set up a robust surgical methodology which would provide a suitable experimental system to image glymphatics in mouse models.
2. Build on the understanding of the role of AQP4, by modulating it pharmacologically to determine if artificial impairment of glymphatics are reliably measurable *in vivo* using MRI.
3. Identify if glymphatic changes precede pathology, by carrying out whole brain MRI at select time points on mouse models of tau and A β , to better understand if fundamental variations in clearance bring about AD-related molecular changes.
4. Extend my findings to human AD, to bridge the gap between basic science and clinical data, by studying AQP4 profiles in post mortem brains and their relationship to pathological burden.

Quantifying glymphatic function during pathology and modulating AQP4 as a therapeutic intervention are emerging concepts in AD research and the novel data presented in this thesis contributes to that growing body of work.

3. A Surgical Mouse Model to Assess Glymphatic Inflow

In this chapter, a surgical method to measure glymphatic inflow in the mouse brain is established as a proof of concept. This in vivo setup serves as the basis for experiments in wildtype and transgenic mice in subsequent chapters.

3.1 Summary

The recently described glymphatic system may provide a novel route for the effective clearance of proteins such as amyloid- β and tau from the brain, and its role in Alzheimer's disease pathology is intriguing. To study glymphatics *in vivo* by probing the dynamics of the physiologically sensitive fluid spaces in the brain, a model system needs to be robust and reproducible. Here, a surgical methodology that would enable dynamic imaging of the mouse brain with continuous infusion of contrast is established based on previous study of glymphatic function in rodent models. The technique is assessed using a series of dyes of varying sizes and infusion rates to confirm concordance with previous experimental evidence. This work provides confidence in the subsequent imaging studies, in the use of this method to capture real-time dynamics of cerebrospinal fluid ingress into the brain.

3.2 Introduction

In the brain, an imbalance between production and clearance of the pathogenic proteins of Alzheimer's Disease (AD), amyloid- β ($A\beta$) and tau, is hypothesised to be a contributing factor to disease onset. The lack of robust treatment for AD has fuelled renewed interest in exploring novel ways in how the brain clears itself of pathogenic proteins, and has paved way for new research advances in the neurodegenerative disease. The glymphatic system has only been recently characterised as a clearance mechanism for $A\beta$, and is still in fairly early stages in research exploration, but is gaining momentum and recognition as an important removal route for brain metabolites [188–191]. As described in the previous chapter, using experimental mouse models, Iliff *et al.* elegantly demonstrated a periarterial influx route of cerebrospinal fluid (CSF) from the subarachnoid space (SAS) into the brain. They also showed the need for the water channel aquaporin-4 (AQP4), found highly abundant at the astrocytic end feet that ensheath brain vasculature, for exchange of CSF solutes with parenchymal interstitial fluid (ISF). In addition, they provided evidence for the exit of parenchymal solutes along perivenous routes [151]. They used an intracisternal tracer infusion approach and showed that tracers from the SAS entered the brain along cortical arteries. In this work, they also demonstrated a size-based selectivity in the penetration depth of solutes into the brain, using both radioactive and fluorescent solutes infused into the SAS. The smallest molecules penetrated the deepest regions of the brain, whereas larger tracer molecules were restricted to the more superficial perivascular regions, an observation which was attributed to the 20nm gaps between the astrocytic end feet [149], sieving out molecules larger than this size and preventing their movement from the perivascular space into the brain tissue. Crucially, it was also noted that maintaining the hydraulic integrity of the intracranial space was requisite for the maintenance of glymphatic flow – that is, the introduction of a small unsealed hole into the dura was found to markedly reduce measured rates of perivascular contrast movement from the SAS to the brain tissue [151,192]. This demonstrates that careful experimental control is required when manipulating and testing parameters within this finely balanced system.

In this work the methodology employed in the previous work is reproduced, to demonstrate that the surgical methodological protocol is reproducible and yields results concordant with previous studies. First, measures of glymphatic inflow were macroscopically assessed by using dyes that could be visualised by the naked eye, to confirm movement of solutes along penetrating vessels on the surface of the mouse brain. Next, this was advanced to microscopic visualisation using fluorescent tracers in order to detect parenchymal penetration, and to test the size based patterns of glymphatic inflow previously described in Iliff *et al.* This provided reassurance that the surgical methodological protocol yielded measures that were robust and concordant with previous work, prior to extrapolating this work onto magnetic resonance imaging (MRI) experiments, which comes with its own distinct set of technical and practical challenges.

3.3 Methods

3.3.1 Intracisternal infusion of tracers into the mouse subarachnoid space

8.5 month old wildtype female C57BL/6 mice were used, imported from Charles River (Wilmington, Massachusetts, USA). N numbers used for each experimental set are provided in the subsections below. All animal work was performed in accordance with the United Kingdom's Animals (Scientific Procedures) Act of 1986 and was previously approved by University College London's (UCL) internal Animal Welfare and Ethical Review Body. Mice had unrestricted access to food and water, and were housed under automatically controlled temperature, humidity, ventilation and 12h light/dark cycle settings.

Mice were anaesthetised with 2% isoflurane delivered in O₂ at a delivery rate of 1l/min, and positioned in a stereotaxic frame (Kopf) with the head flexed to 50°. Mice were maintained at 37°C (±2°C) using a feedback controlled heated mat connected to a rectal core temperature monitor (Harvard Apparatus). A midline incision was made at a midpoint between the skull base and the occipital margin to the first cervical vertebra (Figure 16). The underlying muscles were parted to expose the atlanto-occipital membrane and dura mater overlaying

the cisterna magna, and a durotomy was performed using a 23-gauge needle. An intrathecal catheter (35-40 mm port length, 80-90 mm intravascular tippet length, Sandown Scientific, Middlesex, UK) extended with polyethylene tubing (0.4 mm x 0.8 mm, Portex) and attached to a 100 μ L glass Hamilton syringe driven by a microinfusion pump (sp210iw syringe pump, World Precision Instruments, Sarasota, Florida, USA) was filled with the desired contrast agent. The catheter was advanced <1mm into the cisternal space, sealed and anchored in place using superglue. This setup is shown below in Figure 16.

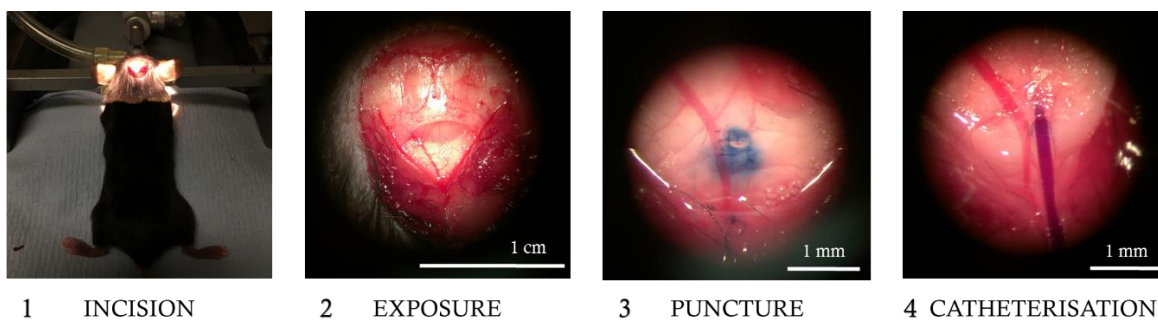


Figure 16. Surgical method to introduce tracers into the SAS. **1.** The anaesthetised mouse is secured on a stereotaxic frame. An incision of the skin is made to expose muscle from occipital bone to atlas. **2.** The of splenius capitis, semispinalis muscles and atlanto-occipital membrane are removed, revealing the cisterna magna. **3.** The dura mater is punctured with a needle (diameter \sim 0.25mm). The needle tip is stained with ink to visualise the puncture, seen here as a blue residue around the puncture. **4.** The intrathecal catheter advanced <1mm into cisterna magna and secured with superglue. In this image, the catheter contains Alexa Fluor 594 hydrazide dye.

3.3.2 Evans blue dye to assess superficial tracer distribution

A flowrate of 2 μ L/min (n = 4) as used in the original work by Iliff *et al.* [130] was tested, as well as a slower, more physiologically compatible flow rate [193] of and 0.6 μ L/ min (n = 5), with the intention of using this in subsequent MRI experiments. 4% Evans blue dye (EBD) (molecular weight 961 Da) (Sigma catalogue# E2129) prepared in filtered 0.9% NaCl was infused into the cisterna magna for a total of 10 μ L delivered volume for each flow rate. 30 minutes after the start of the infusion, mice were euthanized by overdose with sodium pentobarbital (10ml/kg, i.p.). Brains were removed and photographed dorsally, ventrally and

laterally to capture dye distribution around the outer brain surface (my hypothesis being that dyes would be preferentially distributed along the para-arterial space of surface vessels).

3.3.3 Fluorescent dyes to assess parenchymal tracer distribution

In the fluorescent tracer experiments, only the 0.6 μ l/ min infusion rate (n = 4 per dye) was used. 0.5% solutions of Alexa Fluor 594 hydrazide (AF594-H) (molecular weight 759 Da; emission/excitation wavelengths: 588/613 nm) (ThermoFisher catalogue# A10438), Texas Red-dextran-3 (TR-d3) (molecular weight 3 kDa; emission/excitation wavelengths: 595/615 nm) (ThermoFisher catalogue# D3329) and fluorescein isothiocyanate-dextran-2000 (FITC-d2000) (molecular weight 2000 kDa; emission/excitation wavelengths: 490/520 nm) (Sigma, catalogue# 52471) in filtered cortex buffer (pH 7.4) were infused into the cisterna magna for a total of 10 μ l for each flow rate. Cortex buffer was chosen as the vehicle for delivery here to maintain a salt solution that was more physiologically compatible with the brain. To collect sections without fluorescence as a reference control, one mouse was infused with cortex buffer without fluorescent tracers. Recipe for cortex buffer used is as follows:

<i>Reagent</i>	<i>Amount to add</i>	<i>Final concentration</i>
<i>NaCl</i>	7.31 g	125 mM
<i>KCl</i>	0.373 g	5 mM
<i>Glucose</i>	1.802 g	10 mM
<i>HEPES</i>	2.38 g	10 mM
<i>1 M CaCl₂</i>	2 mL	2 mM
<i>MgSO₄·7H₂O</i>	0.493g	2 mM
<i>H₂O</i>	to 1 L	--

Tracers were infused for a total of 10 μ l. 55 minutes after the start of the infusion, mice were euthanized by overdose with sodium pentobarbital (10ml/kg, i.p.). Mice were perfused with 15 ml 0.9% saline followed by 50ml 10% buffered formalin (VWR catalogue# 9713.1000). Brains were rapidly removed and snap frozen in isopentane pre-chilled on dry ice to prevent further diffusive movement of tracers. 50 μ m coronal sections of the brain were collected onto RNase-free SuperFrost® Plus slides, using a cryostat. Slides were imaged on an Invitrogen EVOS FL Auto fluorescence microscope and images were analysed on ImageJ. Each slide

with fluorescent sections was scanned alongside a slide with sections from the control mouse infused with cortex buffer only.

3.3.4 Analysis of fluorescent dye penetration

The most medial section from each brain with minimal slicing artefacts was selected. The image was binarized on ImageJ and the mean intensity of the image obtained. An ROI was drawn around the selected slice and a threshold of 3 standard deviations from the mean signal of each brain was then applied to the image. The % area coverage of this threshold was taken as a measure of penetration into the tissue for each section. This image analysis pipeline is shown in Figure 17. Statistical comparisons between groups were performed via one-way analysis of variance (ANOVA) followed by Tukey's multiple comparisons tests. Data is represented as mean \pm SEM for the n number of animals in each group. Statistical testing was performed using GraphPad Prism (v7 for Windows, San Diego, CA, USA).

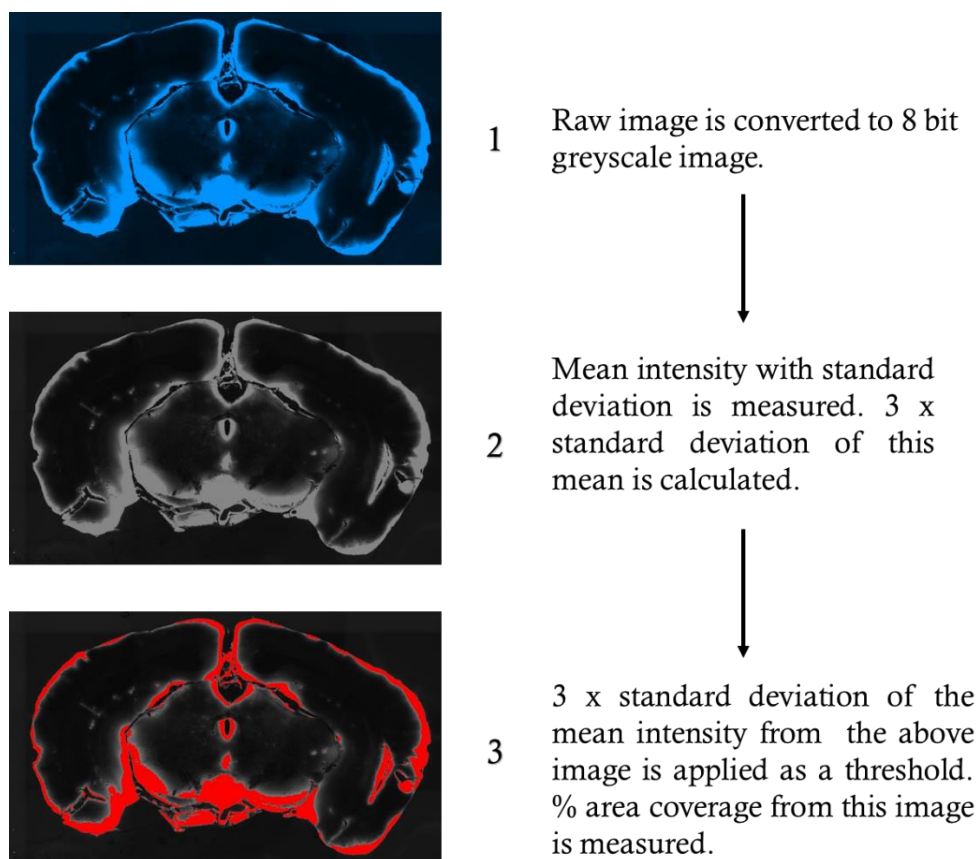


Figure 17. Flow diagram showing an example of the analysis approach taken to calculate percentage penetration of fluorescent tracers.

3.4 Results

Prior to the data reported here, I performed this surgical procedure in a total of 32 mice, which collectively enabled me to better control for important sources of experimental variation such as anaesthetic delivery, stereotaxic positioning and contrast agent buffering (data not shown). Once my surgical skill was honed, I commenced data collection on the experiments described in sections 3.3.2 and 3.3.4.

3.4.1 Macroscopic assessment with Evans blue dye

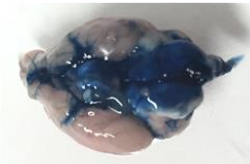
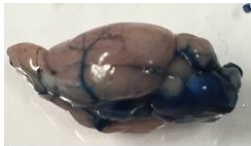
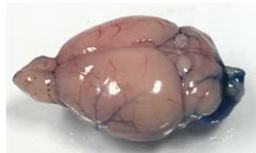
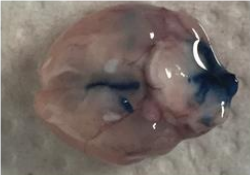


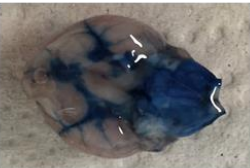
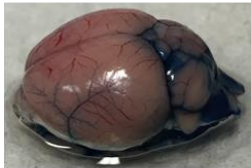



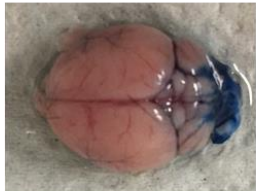
	Ventral	Lateral	Dorsal
M2_1			
M2_2			
M2_3			
M2_4			

Figure 18. Photographs of brains collected following intracisternal infusion of EBD at $2\mu\text{l}/\text{min}$. Each row represent a single mouse brain, photographed ventrally, laterally and dorsally. EBD distribution is visible in blue.

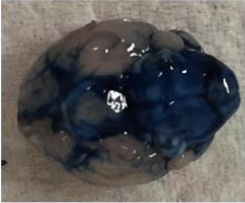

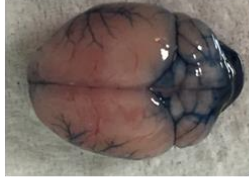

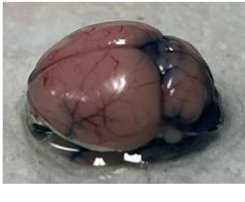
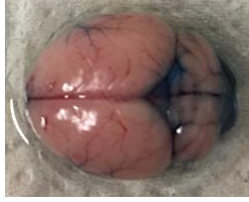





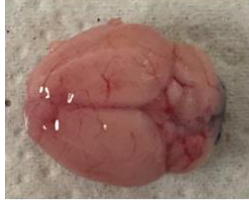



	Ventral	Lateral	Dorsal
M0.6_1			
M0.6_2			
M0.6_3			
M0.6_4			
M0.6_5			

Figure 19. Photographs of brains collected following intracisternal infusion of EBD at 0.6 $\mu\text{l}/\text{min}$. Each row represent a single mouse brain, photographed ventrally, laterally and dorsally. EBD distribution is visible in blue.

In the 2 $\mu\text{l}/\text{min}$ group (Figure 18), a high amount of tracer retention was observed around the brain stem close to the cisterna magna infusion site. EBD infused into the cisterna magna was visible at the base of the brain around the circle of Willis. Tracer was also visible along the middle cerebral arteries (MCA) and along the branches of the leptomeningeal arteries, towards the surface of the cortex. One mouse in the 2 $\mu\text{l}/\text{min}$ group died shortly after the infusion commenced. Upon necropsy, EBD was not visible on the surfaces of the brain in

this mouse (Figure 18, M2_2) and further dissection revealed that EBD had filled all the ventricles.

In the 0.6 μ l/min group (Figure 19), tracer distribution was highly similar to the observations in the 2 μ l/min group. Tracer retention along the branches of the MCA were noticeably more prominent. In one mouse from this group, tracer appeared to pool in the cisterna magna and drained out upon necropsy. No dye was observed on the brain surface (Figure 19, M0.6_4) or within the ventricles. EBD was not observed in the ventricles of any other mice.

3.4.2 Microscopic assessment with fluorescent tracers

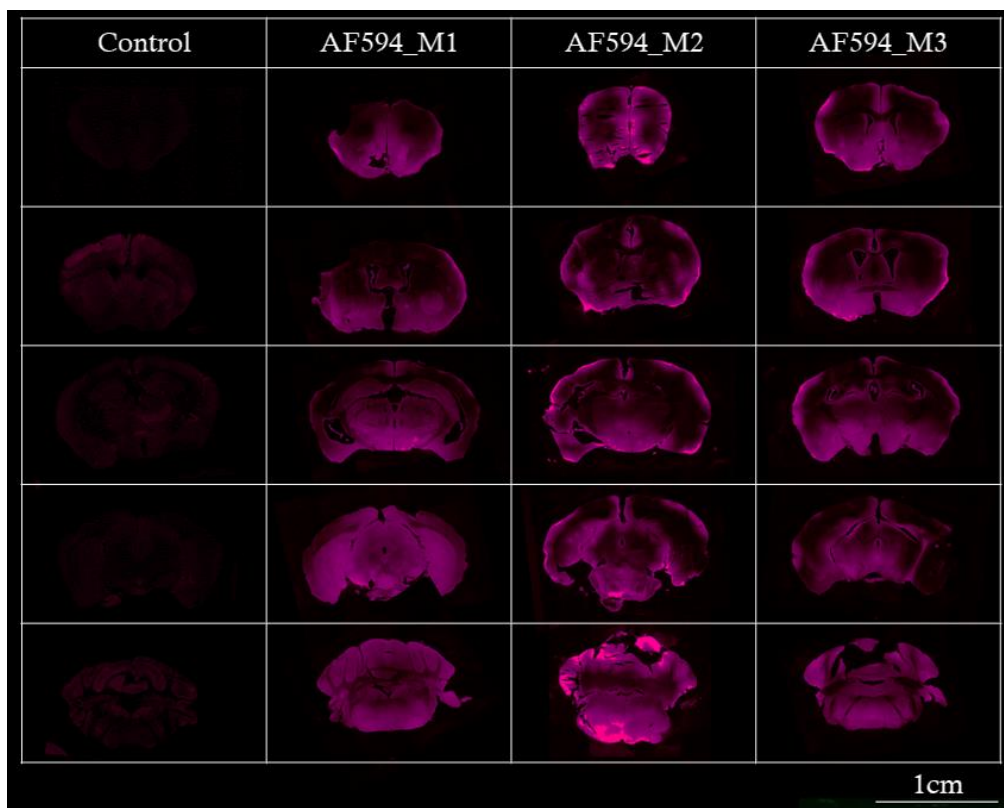


Figure 20. Coronal brain sections from mice infused with small molecular weight Alexa Fluor 594 Hydrazide (0.76 kDa), sliced from rostral (top) to caudal (bottom) regions. Each column contains images from an individual mouse. Control sections were obtained from one mouse infused with cortex buffer only (AF594 Emission /Excitation wavelengths: 588/613 nm).

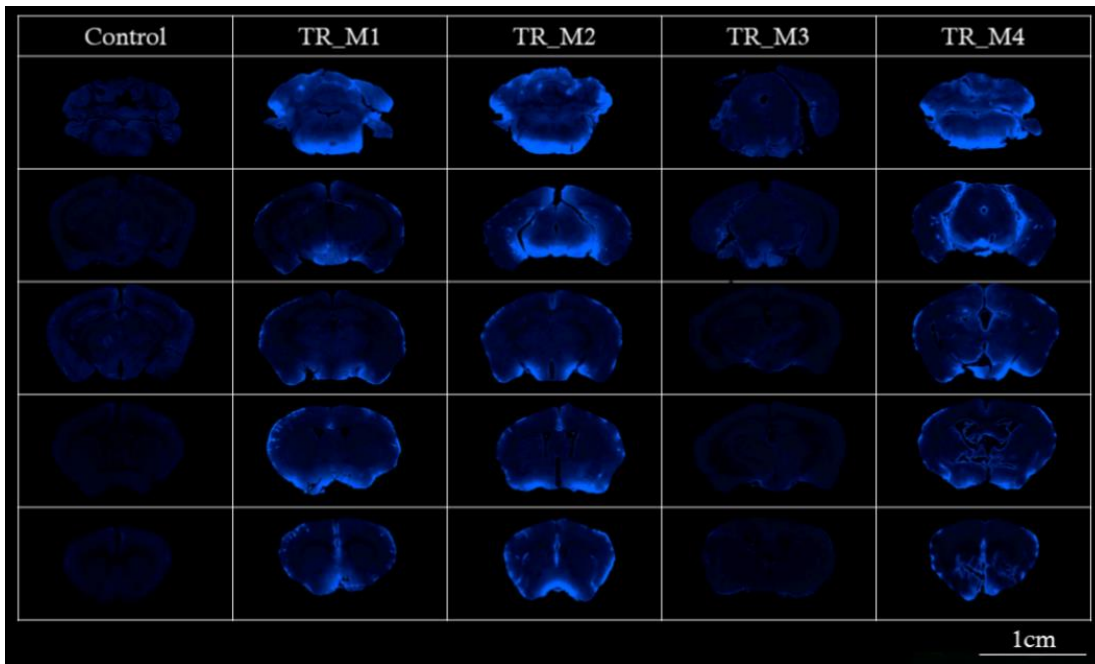


Figure 21. Coronal brain sections from mice infused with medium molecular weight Texas Red (3 kDa) sliced from caudal (top) to rostral (bottom) regions.. Each column contains images from an individual mouse. Control sections were obtained from one mouse infused with cortex buffer only (TR Emission /Excitation wavelengths: 595/615 nm).

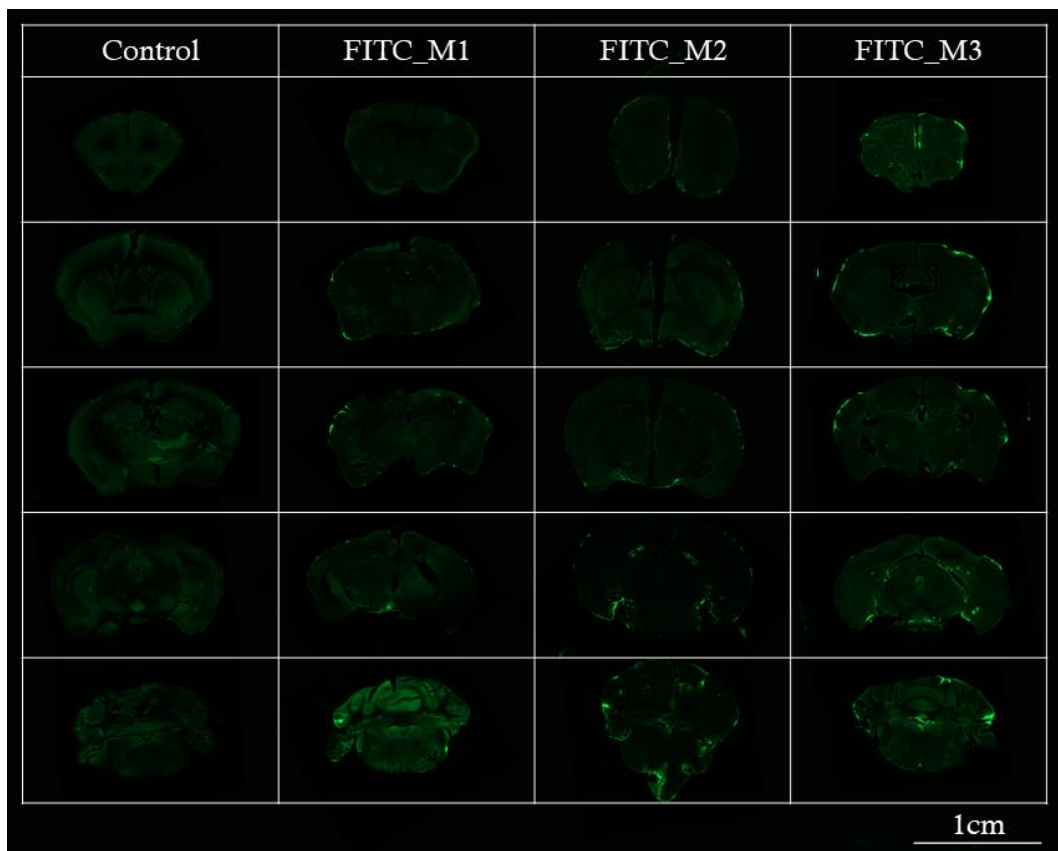


Figure 22. Coronal brain sections from mice infused with large molecular weight fluorescein isothiocyanate (2000kDa), sliced from rostral (top) to caudal (bottom) regions. Each column contains images from an individual mouse. Control sections were obtained from one mouse infused with cortex buffer only (FITC Emission /Excitation wavelengths: 490/520 nm).

The large molecular weight FITC-d2000 penetrated the brain the least ($1.7\% \pm 1.4$ SEM). On the micrographs (Figure 22), tracer was mostly visible on the peripheries of the brain tissue. This was followed by medium molecular weight TR-d3 (Figure 21) which penetrated up to $16\% (\pm 5.8$ SEM), travelling deeper than FITC-d2000. AF594-H, the smallest dye, travelled the deepest (Figure 20), achieving up to $60\% (\pm 2.6$ SEM) penetration. This tracer penetrated significantly deeper than TR-d3 ($p= 0.0005$) and FITC-d2000 ($p = 0.0001$, Figure 23 A) and visibly illuminated the brain sections on the micrographs (Figure 20). This data was also plotted against tracer size, producing a single phase decay, as modelled in Figure 23 B. This enabled the rough estimation of penetration that could be expected with other potential tracers. The experiments started with 4 mice in each tracer cohort. However, one mouse from the FITC-d2000 group was removed from analysis as the infusion line was visibly blocked and prevented tracer from entering the cisterna magna. A mouse from the AF594-H group was also removed from analysis due to a leak at the infusion site during the experiment and thus had to be terminated. In the TR-d3 group, one mouse (TR_M3; Figure 21) appeared to have reduced penetration compared to the others in this cohort. However, no visible experimental observations or errors warranted its removal and thus was included in the analysis.

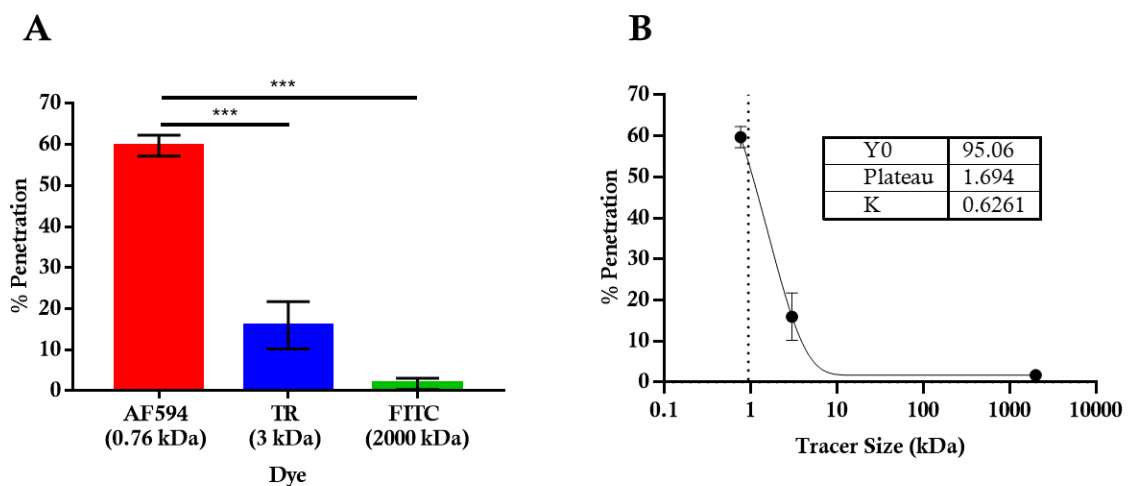


Figure 23. (A) Percentage penetration of large (FITC-d2000; $n=3$), medium (TR-d3; $n=4$) and small (AF594-H; $n=3$) molecular weight dyes infused into the cisterna magna at $0.6\mu\text{l}/\text{min}$. (B) The data from A, modelled against one phase decay curve. Vertical dotted line denotes the size of a proposed MRI contrast agent, Gd-DTPA. Error bars represent standard error of the mean (SEM). Statistical significance denoted by asterisks: $***=p<0.001$.

3.5 Discussion

This work aimed to develop a methodological protocol for reproducible assessment of glymphatic inflow in the mouse brain and to use this protocol to replicate previous experimental observations: namely the characteristic spatial distribution of tracers and the tracer-size dependence of these distributions [151]. Using EBD, the characteristic movement of tracers in the SAS along the main feeding leptomeningeal vessels was macroscopically observed. When fluorescent tracers were used, they were visible in the brain parenchyma, and followed a size-based pattern, with the smallest tracers achieving the deepest penetration depths.

A key aim of these experiments was to establish a method that would enable the extension of these studies into MRI, to enable dynamic assessment of whole brain glymphatic function in AD. Anticipating that capturing dynamic real-time MRI scans would require a protocol with a larger volume infused over a longer period based on similar imaging experiments carried out in rat brains [194], the need to calibrate the infusion rate was recognised. Given that intracranial hydraulic integrity is a key component of maintaining CSF flow patterns, an infusion rate of $0.6\mu\text{l}/\text{min}$ was implemented, theorising this to be physiologically compatible whilst still enabling detectable contrast, and the rationale is explained henceforth.

First, tracer movement was macroscopically tested using the infusion rate from the original work by Iliff *et al.* of $2\mu\text{l}/\text{min}$ as well as the proposed rate of $0.6\mu\text{l}/\text{min}$. Both experimental cohorts showed tracers moving along the leptomeningeal vessels and branches moving towards the cortical surface, however, this was more prominent in the $0.6\mu\text{l}/\text{min}$ group. The $0.6\mu\text{l}/\text{min}$ flow rate is likely to disrupt endogenous brain fluid movement to a lesser extent than the $2\mu\text{l}/\text{min}$ flow rate and interestingly, it was observed that this resulted in more prominent perivascular distribution of tracers, seen by qualitative, visual assessment of EBD distribution (Figure 19). This observation indicates that high infusion rates may underestimate rates of glymphatic inflow relative to lower infusion rates.

One explanation for this may be that faster rates could disrupt fluid dynamics in the SAS, possibly by interfering with intracranial pressure (ICP) and thus diminishing the pattern of pulsatile flow along feeding vessels. In the original work using an infusion rate of 2 μ l/min, the senior authors only noted a transient disturbance in ICP, and in a protocol subsequently published, they recommended a rate of 1 μ l/min for cisterna magna infusions [195]. Prior work from a different group, using a cisterna magna bolus of tracer infused at 3 μ l/min, had shown no detectable changes in ICP 10 minutes following the infusion [196]. More recently, a study using cisterna magna tracer infusions continuously tested ICP whilst gradually increasing the infusion rate. They found that a rate of 0.34 μ l/min increased ICP from a baseline reading of 4.1 ± 0.4 mmHg to 4.2 mmHg, and at 1 μ l/min ICP reached 5.3 mmHg, but gradually decreased after the end of the infusion [197]. Thus it would seem that a variety of flow rates and infusion volumes do not produce marked increases in ICP using the experimental design implemented here. In this study, one mouse that died from the 2 μ l/min group showed tracer filled ventricles, but none along the vessels. It may have succumbed to adverse effects from this infusion, possibly due to a combination of the faster rate as well as erroneous placement of the catheter, forcing the tracer in the wrong direction, which may have then detrimentally disrupted cerebral physiology.

Glymphatic inflow has previously been visualised in the rat brain by contrast-enhanced MRI and that study used an infusion rate of 1.6 μ l/min [194]. In a separate study, this group also used this same infusion rate in fluorescence experiments in mice alongside rats, where a comparable pattern of tracer distribution was observed in both species. ICP recordings taken in these rat brains showed no perturbances [198]. Another study in the rat brain has shown that intracisternal infusion only increases ICP at $\geq 3\mu$ l/min [199]. But, the adult mouse brain is approximately 4 - 5 times smaller than the adult rat brain [200] and has 4 times less total CSF volume [201]. Based on these metrics, an infusion rate of 0.4 μ l/min would seem pragmatic. This rate would also be similar to the rate of CSF production in the mouse brain which is estimated at 0.37 ± 0.04 μ l/min [193], and thus be physiologically compatible. However, a challenge posed by the MRI experiments was that an infusion rate too slow, or

a total volume of tracer delivered too small could impede meaningful signal detection. I therefore concluded that a compromised rate needed to be reached – whilst the ideal infusion rate for the mouse brain would be 0.4 μ l/min, the aforementioned studies provided the understanding that this could be pushed beyond 1 μ l/min without changing ICP, and thus conceded here at 0.6 μ l/min moving forward. I reasoned this rate would not markedly change ICP but allow reasonable infusion of contrast agent volume and detection of signal in MRI. It must be noted that one mouse from the 0.6 μ l/min cohort in the EBD experiments also did not show tracer along the vessels, however, it did not suffer any adverse effects and the mouse survived the end of the experiment. As the tracer appeared to pool around the infusion site, with some draining out during necropsy, it is unlikely that a block in the SAS was responsible for this, as such a physiological change would be devastating to its physiology. Dissection of this brain confirmed a complete lack of tracer in any brain region. Thus, it is likely that a technical error caused a blockade in the infusion line of this mouse. The remaining 4 mice in that group prominently displayed the characteristic distribution of tracer along the cortical vessels. Overall, an affirming observation in these experiments was how the macroscopic spatial tracer distribution on the ventral aspect of the brain and along cortical vessels were on par with the observations reported in the previous rat brain MRI experiments [194] and mouse brain fluorescence studies [151].

The next set of experiments used fluorescent tracers infused at 0.6 μ l/min and demonstrated that CSF tracers can enter the parenchyma. In the TR-d3 infused brains, some sections revealed tracer entry along penetrating cortical vessels. This is as expected, as the pulsatile pattern of fluid movement is thought to move solutes towards the Virchow-Robin spaces to facilitate parenchymal ingress [160]. A size based preference in solute size is apparent as previously described – smaller molecules penetrate deeper in the brain and large molecules are more restricted in movement [151]. Glymphatic inflow partially relies on this pulsatile movement for CSF to enter the brain along penetrating arteries [156], and fluid exchange into the parenchyma is facilitated by aquaporin-4 (AQP4) channels, found highly polarised at the end feet of astrocytes that surround vessels [149]. Water enters the brain through AQP4

and can move through both extracellular and intracellular routes, whereas other solutes are restricted by cellular boundaries and may enter the brain only through the gaps between end feet, thought to be driven by a pressure gradient, and flow through the extracellular space (ECS) [162]. The restriction of larger molecules is attributed to the size of these gaps, which are roughly 20 nm wide [149]. Additionally, the width of the ECS in the brain is estimated to be around 38 – 64 nm [202]. FITC-d2000 has an estimated diameter >32nm, TR-d3 is estimated to be between 2.7 – 3.2nm and AF594-H is around 1.1nm [203]. The large size of FITC-d2000 would thus prevent it from moving further than the Virchow-Robin spaces, as observed in these and previous data. Smaller molecules such as TR-d3 and AF594-H may reach the parenchyma via the end foot clefts. But in the tortuous parenchymal ECS, the smallest molecules diffuse more freely, whereas larger molecules rely more heavily on bulk flow, as demonstrated by a combination of modelling and experimental data [161]. Thus the smallest of molecules such as AF594-H would be expected to reach the parenchyma fastest and move through the ECS more rapidly, thus achieving greater penetration depths than TR-d3 and FITC-d2000. Based on these observations, one can expect a small contrast agent such as Gd-DTPA to penetrate the brain parenchyma with up to 55% efficiency (Figure 23 B).

These preliminary experiments emphasised the fine technicalities of working within a small physiological space, and thus highlighted the need for careful technical and physiological control for reliable utility of this methodological protocol. These data provide evidence as to the reproducibility of the measurement of glymphatic inflow in wildtype mice, and that contrast agents infused using this method follow the characteristic size-dependant pattern of glymphatic flow previously characterised. The data also yielded confidence that with use of a small MRI contrast agent, good penetration efficiency may be attained in the mouse brain. In order to move into MRI experiments, a suitable infusion rate that would provide efficacious image contrast was also established. Using these parameters, the next study aimed to image glymphatic flow in the mouse brain, by combining the surgical procedures developed and described in this chapter, with MRI.

4. Magnetic Resonance Imaging and Pharmacological Inhibition of Glymphatic Function in the Mouse Brain

The work characterising glymphatic inflow in the previous chapter is advanced to in vivo whole brain imaging. The work presented herein also demonstrates that the influence of pharmacological modulation of aquaporin-4 function on glymphatic inflow can be imaged in vivo using magnetic resonance imaging.

4.1 Summary

Aquaporin-4 facilitated exchange of cerebrospinal with interstitial fluid via the glymphatic system, may provide a pathway by which amyloid- β and tau are cleared from the brain, and as such, represents an exciting new target for Alzheimer's disease. Here, glymphatic inflow is dynamically imaged in real time using whole brain contrast enhanced magnetic resonance imaging, to investigate the spatial-temporal dynamics of contrast agent egress into the mouse brain. Measurements of glymphatic outflow are also performed by intracerebrally injecting tau and measuring clearance. The influence of aquaporin-4 on these measures of CSF-ISF exchange was then investigated by using a potent aquaporin-4 inhibitor. These findings present aquaporin-4 as a novel drugable target for the treatment of Alzheimer's disease.

I would like to thank Ian Harrison for performing the intracerebral injections and CSF assays included in this chapter. I would also like to thank Niall Colgan for setting up the MRI sequence and Payam Nahavandi for assistance with image post-processing. Parts of these data are currently being prepared for a manuscript.

4.2 Introduction

Exchange of cerebrospinal fluid (CSF) with interstitial fluid (ISF) via glymphatic flow is thought to be facilitated by the expression of aquaporin-4 (AQP4) channels on astrocytic end feet; animals lacking AQP4 exhibit a ~70% reduction in CSF influx and a ~55% reduction in parenchymal solute clearance [151,158]. Evidence demonstrating the role of AQP4 in exchange of fluid and solutes through the brain has spurred investigations into its implication in neurodegenerative conditions such as Alzheimer's disease (AD).

Deletion of AQP4 in APP/PS1 amyloid mice has been shown to potentiate the development of amyloid- β (A β) pathology and memory deficits in this disease model [204]. It has also been shown that the appropriate spatial expression pattern of AQP4 polarisation to astrocytic end feet is required for efficient glymphatic function [183,184], and that this polarisation in the brain declines with age [183,205]. Moreover, in mouse models of traumatic brain injury (TBI), AQP4 polarisation is demonstrably reduced, glymphatic function is impaired and AQP4 null mice that experience TBI are shown to experience an elevation in CSF phosphorylated tau (P-tau) levels [184]. These studies suggest that suppressed glymphatic function is capable of inducing or advancing AD pathology. Furthermore, it was shown recently that AQP4 polarisation itself is associated with AD status [205], suggesting that impaired glymphatic function may play a role in rendering the aging brain vulnerable to aberrant protein deposition. Therefore, the ability to visualise glymphatic changes and AQP4 driven perturbances to fluid movement can provide important insights into the changes preceding protein accumulation in the AD brain.

In this study, the glymphatic system is characterised across the mouse brain in real-time using dynamic contrast enhanced MRI (DCE-MRI). Having previously established a surgical protocol for reproducible assessment of glymphatic inflow in the brain using fluorescent dyes and histological assessment, in this chapter I attempted to translate this technique from the bench to high field MRI measurement. This aimed to enable dynamic whole brain mapping of glymphatic function but came with considerable methodological challenges due to strong magnetic fields and confined space inside the bore of the magnet. Furthermore, I aimed to

test the sensitivity of the technique to detect a relatively marked change in glymphatic function prior to application to mouse models of AD. Thus, I chose to pharmacologically target the function of AQP4, a critical component of the glymphatic pathway, using the novel inhibitor TGN-020.

By using DCE-MRI, a spatial and temporal description of the glymphatic system in the mouse brain is provided, and the spatially heterogeneous nature of glymphatic inflow is highlighted. The critical role of AQP4 to facilitate glymphatic inflow is assessed by pharmacologically inhibiting its function and visualising dynamic changes on MRI. The impact of AQP4 inhibition on outflow is also queried by testing the clearance of parenchymal tau using intracerebral injections and CSF sampling.

4.3 Methods

4.3.1 Mice and aquaporin-4 blocking agent

Wildtype female C57BL/6 mice at 8.5 months of age were used for MRI, imported from Charles River (Wilmington, Massachusetts, USA) into the United Kingdom for study at University College London's (UCL) Centre for Advanced Biomedical Imaging. N numbers used for each experimental set are provided in each results subsection. rTg4510 transgenic mice were used to extract tau for intracerebral injections. Generation of homozygous rTg4510 transgenic mice has been described previously [95]. The rTg4510 mice were licensed from the Mayo Clinic (Jacksonville, Florida, USA) and bred for Eli Lilly by Taconic (Germantown, Maryland, USA). For accompanying TGN-020 experiments, where stated, AQP4 knockout mice, generation of which has been described previously (59), (henceforth referred to as Aqp4^{-/-} mice) were used, imported directly from University of Oslo, Norway. All animal work was performed in accordance with the United Kingdom's Animals (Scientific Procedures) Act of 1986 and was previously approved by UCL's internal Animal Welfare and Ethical Review Body. Mice had unrestricted access to food and water, and were

housed under automatically controlled temperature, humidity, ventilation and 12h light/dark cycle settings.

For pharmacological inhibition of AQP4, TGN-020 (N-1,3,4-Thiadiazol-2-yl-3-pyridinecarboxamide, Tocris Bioscience, Bristol, UK) was used [206]. In order to increase solubility, TGN-020 was dissolved in a cyclodextrin derivative, 20% w/v Captisol (CyDex Pharmaceuticals) in water for injection. For TGN-020 experiments, mice were treated intraperitoneally with either TGN-020 (250mg/kg in 20ml/kg body weight) or vehicle (empty 20% Captisol, 20ml/kg) 15 minutes prior to commencing imaging or injecting tau.

4.3.2 Surgical preparation for contrast enhanced MRI

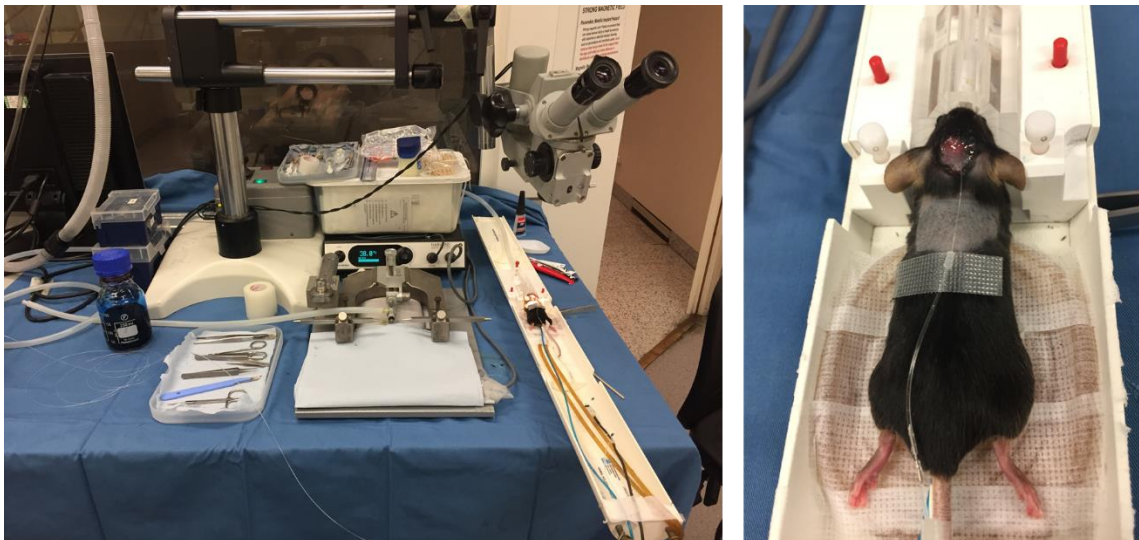


Figure 24. *Surgical setup and MRI bed preparation for intracisternal contrast infusion and DCE-MRI acquisition. Following surgical preparation to place the intrathecal catheter for contrast administration on a stereotaxic setup, the mouse is transferred to the MRI bed equipped with continuous physiological monitoring and maintenance on a feedback system.*

Mice were anaesthetised with 2% isoflurane delivered in O₂ at a delivery rate of 1l/min, and positioned in a stereotaxic frame with the head flexed to 50°. A midline incision was made at a midpoint between the skull base and the occipital margin to the first cervical vertebra. The underlying muscles were parted to expose the atlanto-occipital membrane and dura mater overlaying the cisterna magna, and a durotomy was performed using a 23-gauge needle. An intrathecal catheter (35-40 mm port length, 80-90 mm intravascular tippet length,

Sandown Scientific, Middlesex, UK) extended with polyethylene tubing (0.4 mm x 0.8 mm, Portex) and attached to a 100 μ L glass Hamilton syringe driven by a microinfusion pump (sp210iw syringe pump, World Precision Instruments, Sarasota, Florida, USA) was filled with low molecular weight paramagnetic contrast agent Magnevist® (21mM Gd-DTPA, MW 938 Da; Schering Health Care Ltd., in filtered 0.9% NaCl). The catheter was advanced 1mm into the cisternal space, sealed and anchored in place using superglue and fast setting resin (Araldite). This setup is shown in Figure 24.

4.3.3 Magnetic resonance image acquisition

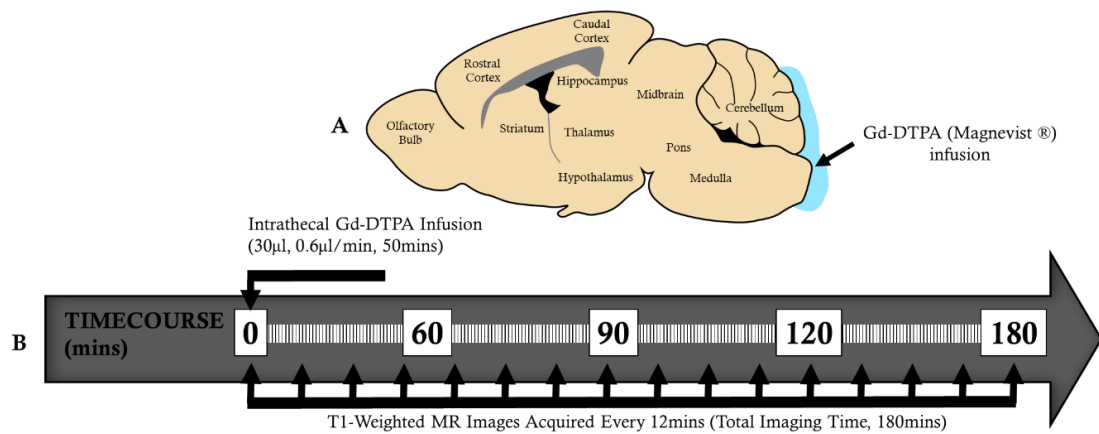


Figure 25. (A) Schematic with brain regions visualised and (B) timeline illustrating experiments used to determine the pattern of glymphatic inflow in the mouse brain. Gd-DTPA was infused into the cisterna magna followed by serial acquisition of T1 weighted MR images.

Following surgery, animals were transferred to an MRI compatible cradle with head held prone and a snout mask positioned to deliver 1.5% isoflurane in O₂ at a delivery rate of 1l/min. Core temperature and respiratory rate were monitored using a rectal probe and pressure pad respectively (SA Instruments). Mice were maintained at 37°C (\pm 2°C) using heated water tubing and a feedback loop controlled warm air blower (SA Instruments). Respiration rate was maintained between 80 and 120 breaths per minute by incrementally adjusting isoflurane dose. All imaging was performed with a 9.4T VNMRS horizontal bore scanner (Agilent Inc., Santa Clara, California, USA). A 72mm inner diameter volume coil (Rapid Biomedical, Rimpar, Germany) was used for RF transmission and signal was

received using a 2 channel array head coil (Rapid Biomedical). A 3D T1-weighted gradient echo sequence was employed to detect the motion of the Gd-DTPA with parameters: TR = 15ms, TE = 3.4ms, flip angle = 15°, NA = 3, FOV = 1.28 × 1.28 × 1.92cm, scanning time = 12 min, acquisition matrix size of 128 × 128 × 128, yielding an image resolution of 0.1 × 0.1 × 0.15mm. Three baseline scans were acquired prior to intracisternal infusion of Gd-DTPA via the indwelling catheter (30µl at 0.6µl/min, total time 50min). Acquisition of each timepoint took 12 minutes per scan. MR images were continually acquired throughout and after intracisternal infusion for a total time of 180min (Figure 25). At the end of the experiment the animal was euthanized by overdose with sodium pentobarbital (10ml/kg, i.p.).

4.3.4 Image processing and analysis

First, the acquired T1-weighted MRI images were converted to the 3D Nifti image format. Second, scan-to-scan misregistration caused by head movement was corrected by rigid-body alignment to the baseline volume. Next, affine registration was performed to correct variability between each mouse brain. Transformed T1-weighted MR images, including the baseline and contrast-enhanced scans, were averaged to create a template image with high-contrast, and this image used to anatomically guide placement of 3D regions-of-interests (ROIs) which encapsulated most of the mouse brain (Figure 26). As the mouse models of AD included in this programme of work were known to present with pathology in the cortical and hippocampal areas, these regions were focussed on in the subsequent studies investigating the effects of pathology. A previous observation made by the histologists processing the rTg4510 brains at Eli Lilly were that the rostral and caudal cortices presented with differential early pathology. Based on this, the cortex was further segmented into these subregions.

A difference image was calculated for each timepoint. Signal intensity measured on the T1 weighted MR images over time in preselected anatomical areas were used to obtain intensity measurements. The intensity signal for each ROI on each timepoint image was extracted and expressed as a % change from the average baseline image. For calculation of kinetic

parameters such as the maximal intensity and the time at which half maximal intensity was achieved in each brain region, signal intensity vs. time data was fitted to a sigmoidal model:

$$y = \frac{Intensity_{Max}}{1 + e^{\left(\frac{Time_{50} - x}{Slope}\right)}}$$

Where $Intensity_{Max}$ is the maximal intensity achieved in the brain region, $Time_{50}$ is the time at which half maximal intensity is achieved, and $Slope$ is the gradient of the linear portion of the fitted sigmoidal curve. Additionally, each ROI's $Intensity_{Max}$ value was divided by its corresponding $Time_{50}$ value to give a measure of 'Penetration Efficiency' for each region.

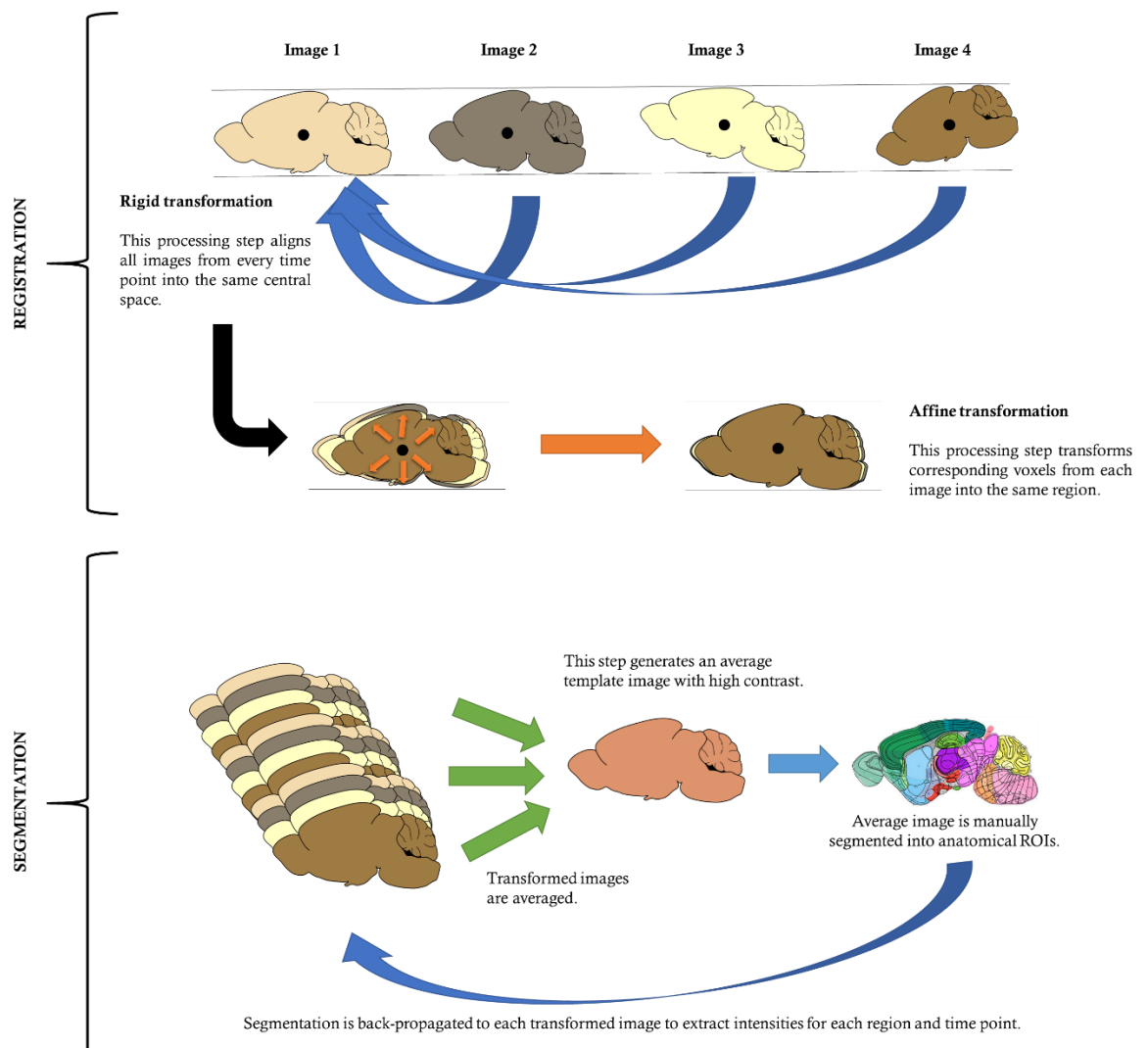


Figure 26. Schematic describing the processing steps following acquisition of T1 weighted MR images. All images are registered to the same space, and then segmented to extract regional intensity measurements as shown here and described above.

4.3.5 Intracerebral infusion of tau homogenate and CSF collection

Tau for intracortical injection was prepared by euthanizing an aged rTg4510 mouse (12 months of age) by overdose with sodium pentobarbital (10ml/kg, i.p.) and dissecting out the cortex and hippocampus. Tissue was quickly frozen in isopentane on dry ice for storage at -80°C. Frozen tissue was weighed, thawed, and gently mixed in a mortar with a few strokes of a pestle in 10% w/v volumes of cold Tris-buffered saline (TBS) containing protease inhibitor cocktail, phosphatase inhibitor cocktails I and II (all Sigma, UK), at a final dilution of 1:100, and 1mM phenylmethylsulfonyl fluoride. To estimate total human tau content, an Enzyme Linked Immunosorbant Assay (ELISA) of brain homogenate was performed (Human Tau (total) ELISA Kit (Invitrogen, UK) as per the manufacturer's instructions, see below) and stock solution tau concentration adjusted to 20µg/ml with homogenisation buffer, and stored at -80°C until intracerebral infusion.

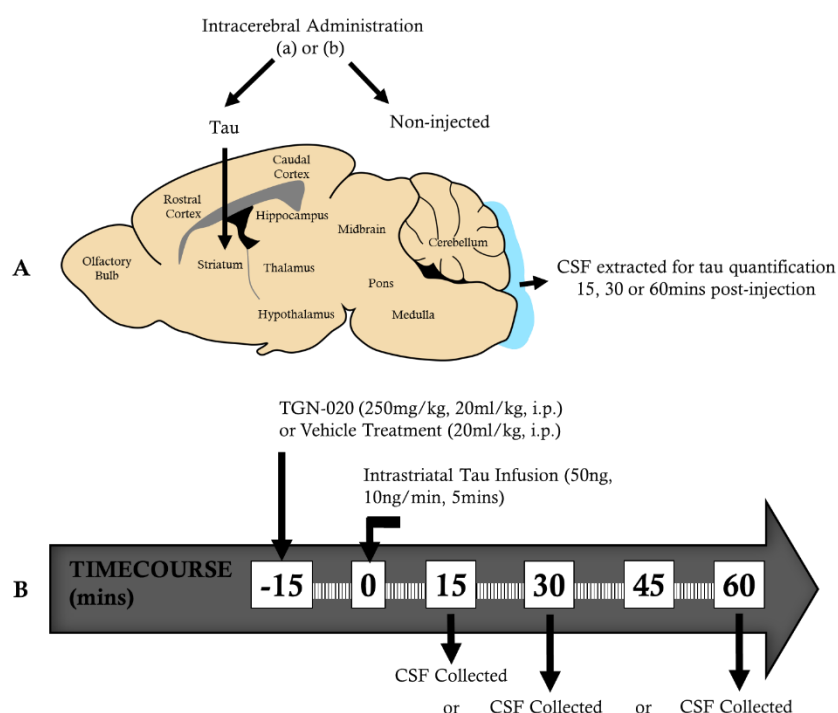


Figure 27. (A) Schematic and (B) timeline illustrating experiments used to determine the effects of pharmacological inhibition of AQP4 on clearance of tau from the mouse brain. TGN-020 or vehicle was administered 15mins prior to injection of tau containing brain homogenate into the striatum, and CSF extracted from the cisterna magna either 15, 30, or 60mins later.

Mice were anaesthetised with 2% isoflurane delivered in O₂ at a delivery rate of 1l/min, and positioned in a stereotaxic frame in the horizontal skull position. A midline incision was made on the top of the head to expose the underlying skull. A small burr hole was made, using a microdrill, above the location of the intracerebral injection. 50ng tau containing brain homogenate was infused into the striatum (anteroposterior, -0.2mm, mediolateral, +2mm and ventral to dura, -1.75mm, relative to bregma) [207] using a 10µl glass Hamilton syringe (2.5µl at 0.25µl/min, total time 10min). Either 15, 30, or 60 minutes after the start of the intracerebral infusion, with the needle left *in situ*, a midline incision was made at a midpoint between the skull base and the occipital margin to the first vertebrae. The underlying muscles were parted to expose the atlanto-occipital membrane and dura mater overlaying the cisterna magna, which was thoroughly cleaned with saline. A durotomy was performed using a 23-gauge needle, allowing CSF to be collected using a narrow bore pipette tip. CSF volume varied between mice: 5-8µl was routinely collected (Figure 27). At the end of the experiment the animal was euthanized by overdose with sodium pentobarbital (10ml/kg, i.p.).

4.3.6 Tau enzyme linked immunosorbant assays

The collected CSF was centrifuged and supernatant was removed and frozen at -20°C until further analysis by ELISA. The remaining pellet was used to assess blood contamination using a NanoDrop ND-1000 spectrophotometer (Thermo Fischer Scientific, Waltham MA). Concentration of human tau in CSF samples was then quantified using ELISAs. CSF total tau was quantified using Human Tau (total) ELISA Kit (#KHB0041, Invitrogen, UK), and CSF phosphorylated tau was quantified using Human Tau (Phospho) [pS199] ELISA Kit (#KHB7041, Invitrogen, UK), as per the manufacturer's instructions. Briefly, CSF samples were diluted in diluent buffer prior to being incubated in capture antibody coated wells for 2hrs at room temperature. Wells were washed several times before being incubated in detection antibody for 1hr at room temperature. Wells were washed again before being incubated with horseradish peroxidase conjugated secondary antibody for 30 minutes at room temperature. Wells were then washed again before being incubated with stabilized chromogen for 30 minutes at room temperature. After this incubation, stop solution was

added to each well and the plate was read at 450nm. A set of standards of known (p)Tau concentration (0, 31.25, 62.5, 125, 250, 500, 1000, 2000pg/ml for total tau, and 0, 15.625, 31.25, 62.5, 125, 250, 500, 1000pg/ml for phospho [pS199] tau), were run in parallel for each experiment for quantification of CSF sample tau content from the standard curve.

4.3.7 Statistical analysis

Statistical comparisons between groups were performed via either a repeated measures two-way analysis of variance (ANOVA) followed by post-hoc Bonferoni post-tests for multiple comparisons (for MRI data), or a regular two-way ANOVA followed by post-hoc Bonferoni post-tests for multiple comparisons (for all other grouped comparisons not containing repeated measures). Unpaired t-tests were used for single comparisons. All statistical testing was performed using GraphPad Prism (v7 for Windows, San Diego, CA, USA). All data is represented as mean \pm SEM for the n number of animals in each group, which are detailed in figure legends.

4.4 Results

4.4.1 Spatial and temporal profile of glymphatic inflow in the mouse brain

This part of the project aimed to carry out an exploratory study to investigate the spatial and temporal patterns of glymphatic inflow in the mouse brain. Glymphatic inflow in healthy wildtype mice was characterised using contrast-enhanced MRI by quantifying the regional pattern of delivery of MR contrast agent Gd-DTPA from the SAS into the brain. Gd-DTPA infused intracisternally with serial T1-weighted images acquired over 3 hours showed a distinct pattern of CSF flow into the mouse brain (Figure 28 A), and mirrored the distribution pattern previously reported in the rat brain [173]. 90 minutes after initiation of the infusion, the MRI signal plateaued in all brain regions (Figure 28 B). T1 contrast was initially observed in the CSF filled aqueduct, progressing to ventral nuclei (the pontine nucleus and pituitary recess) and the caudal cortex. Later timepoints showed advancement of the signal throughout the brain, in the pineal recess and cerebellum, and more rostral regions, such as the rostral cortex and the olfactory bulbs. This distribution pattern is schematised in Figure 29.

Quantification of MR signal in grey matter revealed heterogeneity of glymphatic inflow in the mouse brain. The rostral cortex of wildtype animals exhibited a relatively low level of Gd-DTPA infiltration (IntensityMax (% change from baseline), 7.44%), yet the caudal cortex exhibited a high level of contrast agent infiltration (IntensityMax (% change from baseline), 60.23%, $p < 0.001$ compared to rostral cortex) (Figure 28 C). When 'penetration efficiency' (the metric described in section 4.3.4) of these two regions were calculated, and compared against each other, the caudal cortex was significantly higher than the rostral cortex (Figure 28 D; $p < 0.0001$, difference between means = 1.421 ± 0.1048)

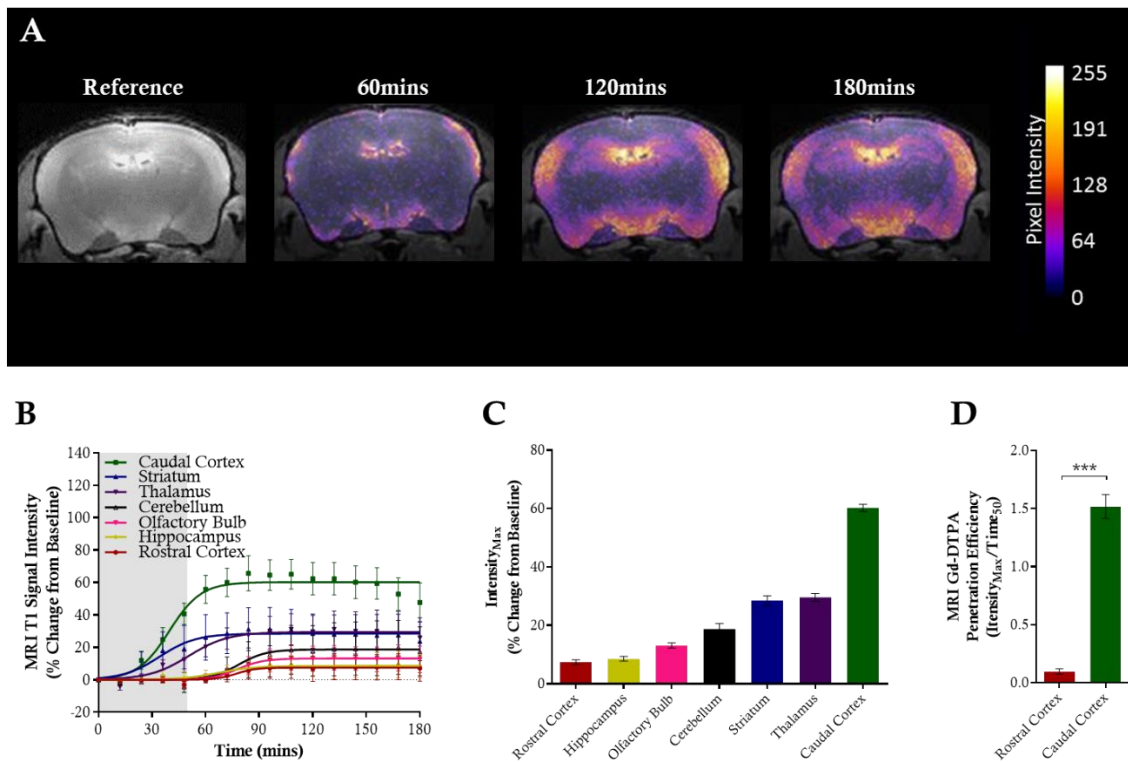


Figure 28. Glymphatic inflow in the mouse brain cortex. (A) Representative T1-weighted structural images of % change from baseline over time showing pseudocoloured entry of Gd-DTPA. (B) MRI T1 signal intensity vs. time data acquired from grey matter regions of the mouse brain showing differences in rates and intensities of glymphatic inflow of Gd-DTPA in anatomically discrete regions over time. (C) $Intensity_{Max}$ values (maximal intensity achieved in region from sigmoidal fitting of data) in each of the brain regions in which raw data and sigmoidal curves are displayed in (A). (D) MRI contrast 'penetration efficiency' for the rostral and caudal cortex, in which raw data and sigmoidal curves are displayed in (B) and (C). $N=5$. Statistical significance denoted by asterisks $***=p<0.001$.

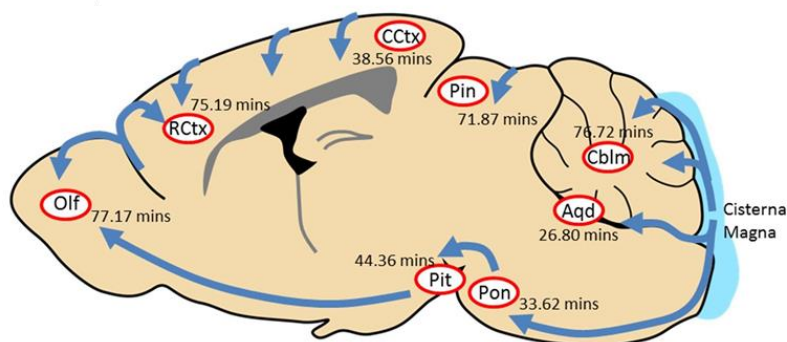


Figure 29. Schematic illustrating direction of contrast agent flow into the brain following cisterna magna infusion, with inclusion of $Time_{50}$ values (the time at which half the maximal intensity is reached), derived from modelling of MRI T1 signal intensity vs. time data (shown in Figure 28 B). Aqd = aqueduct; Cblm = cerebellum; Pon = pontine nucleus; Pit = pituitary recess; Pin = pineal recess; CCtx = caudal cortex; RCtx = rostral cortex; Olf = olfactory bulb. Light blue shaded region denotes the fluid filled cisterna magna. Dark blue arrows denote the proposed direction of CSF inflow based on the $Time_{50}$ values.

4.4.2 Effect of pharmacological inhibition of aquaporin-4 on glymphatic function

The role of AQP4 in glymphatic inflow and clearance was tested by pharmacological blockade, with a specific inhibitor, TGN-020 [185]. To test glymphatic inflow, TGN-020 or vehicle were administered 15 minutes prior to cisternal infusion of Gd-DTPA, followed by serial acquisition of T1-weighted MR images in wildtype mice. Mice treated with TGN-020 exhibited significant reductions in MR signal enhancement in the brain (Figure 30). A hotspot of contrast was visible in the aqueduct, and close to the region near the middle cerebral artery, where the agent appeared to pool in TGN-020 treated animals. This is evident in the cortex, striatum and hippocampus, with significantly reduced MR signal being observed in TGN-020 treated animals from ~80mins after the start of infusion (Figure 31 A - C).

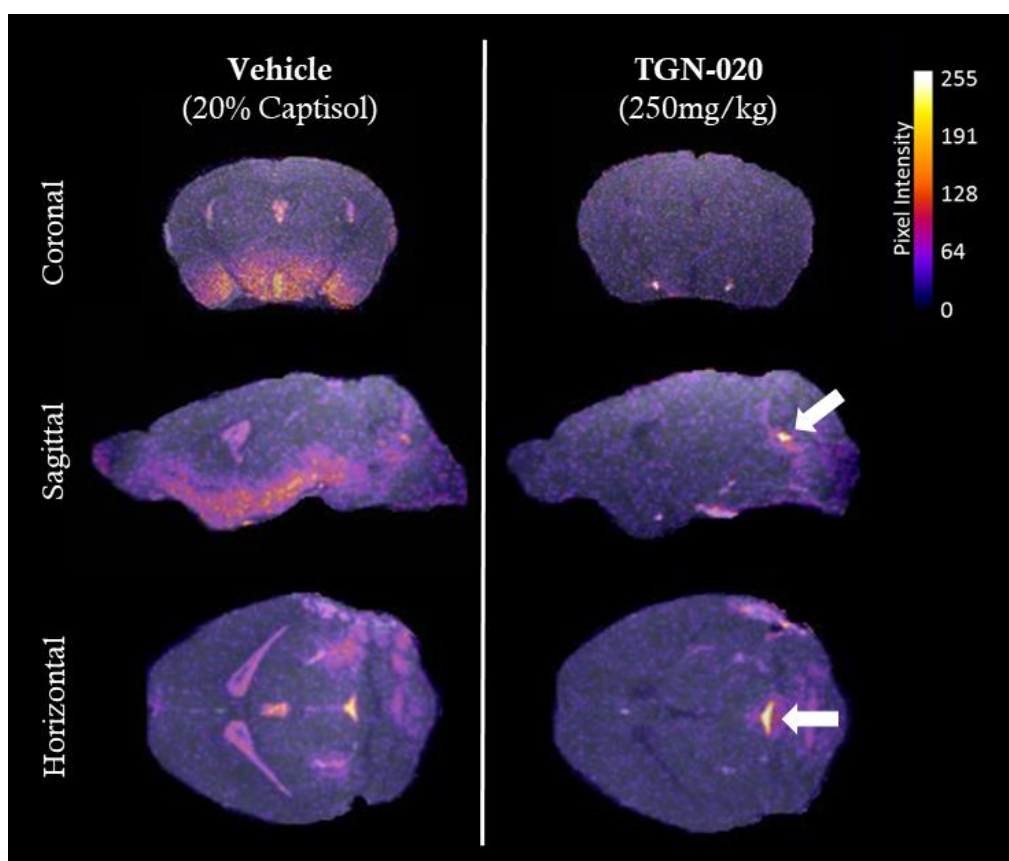


Figure 30. Representative pseudocolored DCE-MRI scans of vehicle (20% Captisol) and TGN-020 treated animals with Gd-DTPA infusion. Image taken at the 60 minute time point, Inflow of contrast into the brain of the TGN-020 treated animal is visibly marred. Contrast agent appears to pool in the fourth ventricle (white arrow), but does not travel beyond this region.

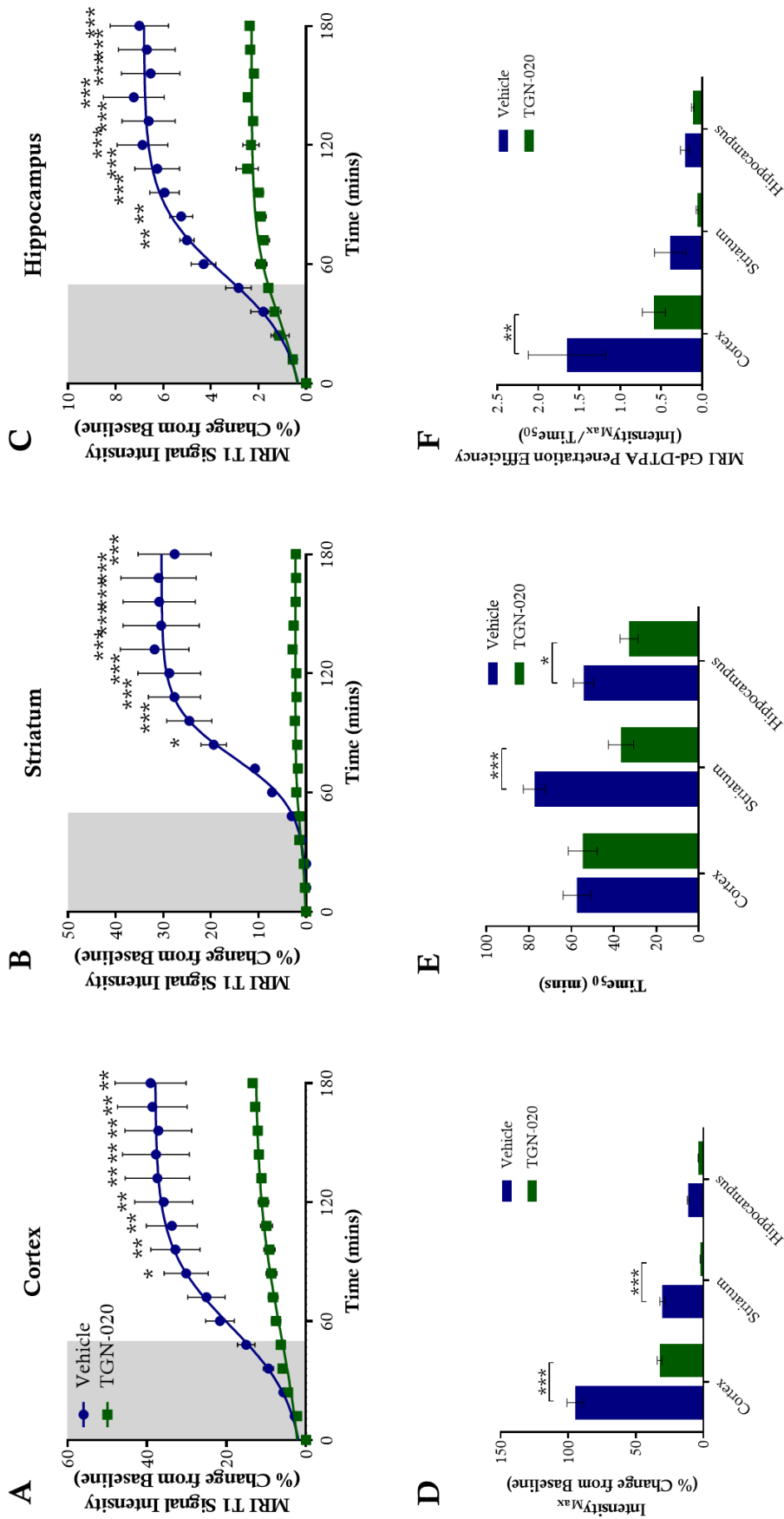


Figure 31. MRI T1 signal intensity vs. time data acquired from the (A) cortex, (B) striatum and (C) hippocampus during these experiments, demonstrating significant inhibition of glymphatic inflow in three aspects of the TGN-020 treated animal brain. Grey area denotes the infusion period. The maximum intensity from the curves in A – C are quantified in (D). (E) shows the time at which half the maximum intensity was reached in the three regions. The inhibition is further exemplified through the calculated Gd-DTPA ‘penetration efficiency’ data shown in (F). N= 4 per group. Statistical significance denoted by asterisks: *= $p < 0.05$, **= $p < 0.01$, ***= $p < 0.001$.

The maximum intensity achieved in the TGN-020 treated cortex and striatum was significantly reduced compared to vehicle treated animals (Figure 31 D; 62.7% less in TGN-020 treated cortex and 28.1% less in TGN-020 treated striatum, $p < 0.001$). The rate of inflow, as calculated by Time_{50} (the time at which half the intensity is achieved) (Figure 31 E) revealed that the rate of inflow was impaired in the hippocampus (21.4 mins less in TGN-020 treated animals, $p < 0.05$) and striatum (40.9 mins less in less in TGN-020 treated animals, $p < 0.001$), with both regions achieving statistical significance. The ‘penetration efficiency’, which factors in both maximal intensity achieved per region and the time required to reach half that intensity, showed that the cortex had the highest contrast between regions compared (Figure 31 F), with this becoming significantly impaired with TGN-020 treatment (1.1 less in TGN-020 treated animals, $p < 0.01$).

To determine if pharmacological blockade of AQP4 exhibited a similar reduction in clearance from the brain, intracerebral injections of tau followed by CSF measurements of tau were performed. Tau was chosen as a substrate to test clearance, given that a central theme of this thesis was to investigate its implication in glymphatic system. Thus, tau extract from the rTg4510 mouse model was used. Wildtype mice were treated with either TGN-020 or vehicle, 15mins prior to intrastriatal infusion of tau containing brain homogenate. CSF was then extracted from the cisterna magna, 15, 30, or 60mins later to determine the extent of clearance into CSF compartments. Reductions in the level of total and phosphorylated (pS199) tau detected in CSF were observed at all timepoints (for example, 15 mins post-striatal infusion, TGN-020 treated animal CSF Tau (pTau) content, 90.1(23.4)ng/ml vs. 953.0(285.0)ng/ml in vehicle treated animals) (Figure 32). Similar experiments were also performed in *Aqp4*^{-/-} mice, where vehicle or TGN-020 was given 15mins prior to intrastriatal infusion of tau containing brain homogenate and CSF extraction 30mins later. Both *Aqp4*^{-/-} vehicle and TGN-020 treated groups showed reductions in CSF tau, similar to TGN-020 treated wildtype animals (vehicle treated *Aqp4*^{-/-} mice CSF total tau, 72.2ng/ml, TGN-020 treated wildtype and *Aqp4*^{-/-} mice CSF total tau, 53.1ng/ml and 99.08ng/ml, respectively, all $p < 0.05$ compared to vehicle treated wildtype mice) (Figure 32 D).

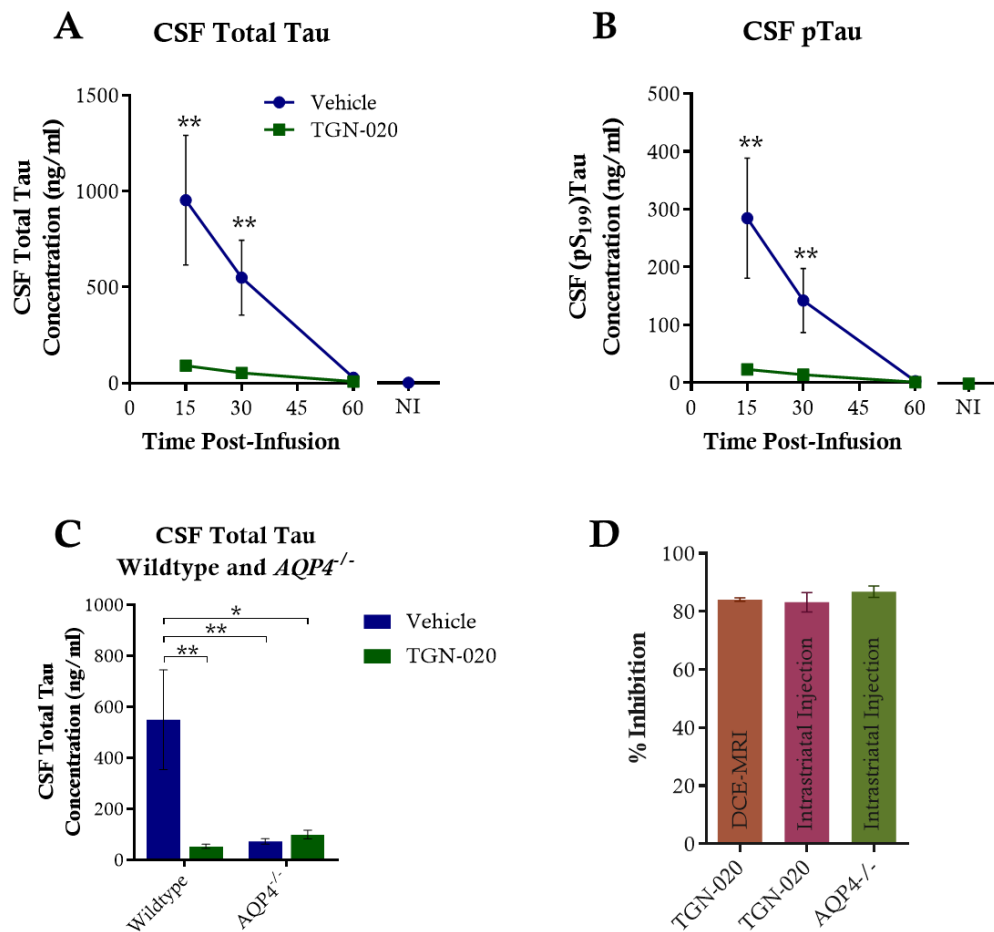


Figure 32. (A) Total tau and (B) pTau concentration of CSF samples extracted from mice injected with tau homogenate demonstrating reduced clearance of tau from the TGN-020 treated animal brain. Intrastriatal injection of tau containing brain homogenate was also performed in a cohort of *Aqp4*^{-/-} animals after TGN-020 or vehicle treatment, and CSF extracted 30mins post-injection for quantification of tau in CSF extracts. (C) CSF tau concentrations demonstrate the specific nature of TGN-020 towards AQP4, given the lack of an effect observed of TGN-020 in *Aqp4*^{-/-} animals. (D) shows the inhibition observed in MRI and injection experiments converted to a percentage from striatal regions. Abbreviations: NI, non-injected. N=5 per group. Statistical significance denoted by asterisks: *= $p < 0.05$, **= $p < 0.01$, ***= $p < 0.001$.

4.5 Discussion

In order to assess glymphatic function in the mouse brain using MRI, a previously published protocol for measurements in the rat brain was adapted [194]. By scaling down both the volume and flow rate at which intracisternal MR contrast agent is administered as established in the previous chapter, glymphatic flow in the mouse brain was characterised. The small size of Gd-DTPA (938 Da) also meant that contrast was expected to travel through the glymphatic route with minimal resistance. This aligns with the observation reported in the previous chapter, where the smallest tracer, Alexa Fluor 594 Hydrazide (760 Da), travelled the furthest into the brain parenchyma (Figure 23).

In these experiments, regional glymphatic inflow was reproducibly imaged and quantified enabling real time visualisation of CSF ingress into the brain. Notably, the regional patterns of contrast ingress all plateaued with time, giving no indication of clearance over the three hours scanned. Nonetheless, this observation and the spatial-temporal dynamics captured here paralleled patterns of glymphatic flow described in the brain using similar contrast infusion techniques in rats [194]. Another study investigating glymphatic flow in a model of stroke has also used a protocol similar to the one I used here. [185]. In that study, the pattern of contrast-enhancement qualitatively described closely followed the regional pattern observed here. However, detailed quantitative assessment was not carried out on discrete brain regions. Interestingly, they identified routes of CSF drainage along sinuses, lymph nodes and cranial nerves – an observation not made here. This may be explained by the higher scan resolution attained in that study enabling more detailed visualisation of contrast enhanced CSF transit. However, characterising the dynamic time course of CSF movement with higher resolution would require a longer scan time. This meant that the adverse implications to the mouse's physiology over longer periods under anaesthesia had to be considered. Thus, a trade-off between resolution and scan time had to be reached. A further disadvantage of this MRI protocol is that the perivascular spaces cannot be resolved, and thus brings into question if the contrast enhancement is truly interstitial. However, based on the small size of the molecule, and the previous experiments using fluorescent dyes that

demonstrated parenchymal ingress, it is probably safe to assume the veracity of the observations made using DCE-MRI. This is further backed by a subsequent study which advanced the aforementioned rat brain glymphatic characterisation upon which this study is modelled, where the authors converted the dynamic T1-weighted MR signal enhancement to concentration maps to quantify parenchymal gadolinium in the rat brain [208].

Next, the role of AQP4 in glymphatic function was probed. The extent to which inflow can be dynamically imaged was tested by pharmacologically blocking AQP4 in wildtype mice. Glymphatic flow of CSF into the brain's interstitium and its clearance out of the parenchyma, is thought to be facilitated by the expression and polarisation of AQP4 to the end feet of astrocytes surrounding blood vessels in the brain [158]. Original data supporting this hypothesis came from the use of AQP4 null mice, in which glymphatic function was impaired by ~70% compared to wildtype animals, resulting in a ~55% reduction in A β clearance from the brain [151]. Subsequently several independent groups have similarly demonstrated that astrocytic AQP4 is essential for fast glymphatic transport, using various approaches of AQP4 gene deletion [188–191]. Here I took an alternative approach, by pharmacologically inhibiting AQP4 function, and in doing so showed that a marked impairment in glymphatic function can be visualised. Pharmacological AQP4 inhibition visibly impairs glymphatic inflow captured by DCE-MRI. Scans of the TGN-020 treated animals did not demonstrate the characteristic pattern of interstitial inflow of Gd-DTPA, and curiously, the contrast agent did not advance beyond the fluid filled aqueduct and fourth ventricle. A pool of contrast was also observed around the region close to the middle cerebral artery. It is possible that the hindrance to AQP4 function caused the infused contrast agent to take the paths of least resistance, the large interconnecting fluid filled spaces and major periarterial spaces, in the absence of glymphatic ingress. The opposing direction of CSF production and flow through the ventricular system may have limited the extent to which the ventricular route could be taken by Gd-DTPA, thus causing it to light up as a bright pool in the third ventricle and aqueduct. Overall, an ~85% reduction in DCE-MRI quantified glymphatic inflow was observed by blocking AQP4.

To further validate these observations, glymphatic outflow was quantified using direct parenchymal injections of tau. These data showed that pathogenic tau is cleared from the wildtype brain and delivered into the CSF. A notable confounder of these experiments was the use of whole brain homogenate from aged rTg4510 brains. Such a crude suspension would include a myriad of non-specific tau conformations, altered neuroinflammatory components that come with the later stages of neurodegeneration [209], glial and neuronal cellular debris. How such a jumble of cellular fragments impacts glymphatic function is unknown, and may thus cloud observations here that are tau-specific. To overcome this, a refined modification of this experiment could be carried out by injecting tau fibrils purified from AD brains, which are known to behave in a more physiologically relevant manner compared to synthetic forms generated *in vitro* [210]. Given the crucial role of astrocytes in glymphatic function [151], possible neuroinflammatory changes resulting from the inoculum of tau homogenate into a healthy wild type brain must also be considered. Nonetheless, given that tau was detected in both the homogenate as well as in the circulating CSF of injected wildtypes, these experiments demonstrated that tau can indeed be cleared into the CSF from the parenchyma. Vivaly, inhibition of AQP4 impaired tau outflow into the CSF to a similar degree to the impairment of tracer inflow observed using DCE-MRI in TGN-020 treated animals. This thus provides requisite evidence that tau is also a participant in glymphatic clearance.

The effect of AQP4 inhibition on glymphatic function may be seen as particularly striking given previous evidence of cerebral blood flow (CBF) elevation (~20%) in the mouse brain upon TGN-020 treatment [211] and thus could be expected to have an opposing effect to what is observed here on glymphatic function. However, increases in CBF can have a reducing effect on pulsatility [212] and given the intrinsic link between arterial pulsatility, and glymphatic function [156,199], a the suppressive effect observed here by the drug may be amplified. Indeed, the implication of AQP4 function is further supported by the observation in *Aqp4*^{-/-} mice which showed that AQP4 ablation via gene deletion has comparable effect in suppressing parenchymal clearance with or without TGN-020 treatment.

Consistent with data from others [184], these data suggested that tau, in the extracellular space, is a substrate for clearance via the glymphatic pathway. These findings demonstrate the importance of AQP4 for appropriate glymphatic clearance from the brain parenchyma, alongside studies using genetic deletion approaches [151,188–191] and suggest a role for AQP4 mediated clearance of tau from the brain, which therefore implies its importance in neurodegenerative tauopathies such as AD [204].

Given the observations reported in AQP4 null mice, this study would have benefited from DCE-MRI of Aqp4^{-/-} animals to assess if the degree of inflow impairment can be visualised in real time. Due to the equipment downtime during the lifespan of these mice at our Centre, these experiments were not carried out. It must be noted however, that Aqp4^{-/-} mice are reported to have reduced ventricular volume and intraventricular pressure, as astroglial and ependymal AQP4 play a role in extra-choroidal CSF production and homeostasis [213]. This indicates that complete and non-specific ablation of AQP4 in the mouse brain, by both genetic and pharmacological approaches, can significantly disrupt CSF dynamics and thus plausibly hinder glymphatic physiology as a consequence. Hence, disentangling the precise role of parenchymal AQP4 in glymphatic function crucially requires the development of a model system in which astroglial AQP4 can be blocked without impeding ependymal AQP4 function. This calls for the generation of an AQP4 mouse model that is inducible, with the ability to silence gene function in a cell-specific manner [214]. Notwithstanding, the work presented here shows that a transient pharmacological blockade of AQP4 can impede both glymphatic inflow and outflow of CSF substrates.

In summary, this work showed that glymphatic inflow can be imaged in the mouse brain. Regional differences in inflow were seen between rostral and caudal cortical regions. Blocking AQP4, a key mediator of glymphatic fluid transit, demonstrably impaired the pattern of inflow observed by imaging, and clearance was also impaired to a similar degree, thus adding confidence to these observations. Tau was also shown to be a substrate for clearance via this AQP4-mediated pathway. In the next chapter, these findings are explored further by assessing glymphatic function in a tauopathy mouse model using MRI.

5. Glymphatic Function in a Tauopathy Model of Alzheimer's Disease

In this chapter, whole brain glymphatic changes are characterised longitudinally in a mouse model of tau pathology, using magnetic resonance imaging, building on the work from the previous chapter.

5.1 Summary

Studying the clearance of pathogenic proteins from the brain such as tau can provide unique insights into the causative mechanisms in elusive diseases such as Alzheimer's disease. The glymphatic system provides a novel approach to understanding the movement and clearance of such proteins from the brain. In this work, glymphatic flow is assessed in the rTg4510 model of tau pathology using magnetic resonance imaging. The early, mid and later stages of pathology are studied in order to understand if early changes on glymphatic function have a relationship to tau accumulation and neurodegeneration. Early changes in glymphatic inflow in the rostral cortex of the brain showed a relationship to tau burden, and late changes in glymphatic flow appeared to be affected by neurodegenerative changes in this model. Aquaporin-4 assessment revealed a loss of polarisation in the rTg4510 brain. This study provides evidence for time-dependant interactions between tau-pathology and measures of glymphatic function, which may be useful to inform future studies that target the role of the glymphatic system in neurodegenerative diseases such as Alzheimer's disease.

The work in this chapter was performed in collaboration with Eli Lilly and Company. I would like to thank Zeshan Ahmed and Alice Fisher for providing the histology included in these data.

5.2 Introduction

Impaired brain clearance mechanisms that result in the accumulation of aberrant proteins that define Alzheimer's disease (AD), provide new diagnostic and therapeutic opportunities to delay or prevent clinical symptoms. One such pathway for parenchymal protein clearance is the glymphatic system [153]. Its involvement in AD, however, is yet to be fully defined. AD is characterised by the extracellular accumulation of amyloid- β ($A\beta$) in the form of plaques, and intracellular accumulation of hyperphosphorylated tau in the form of neurofibrillary tangles (NFTs). Blood brain barrier clearance, intra and extracellular degradation, interstitial fluid (ISF) bulk flow clearance and cerebrospinal fluid (CSF) absorption pathways have all been implicated in removal of parenchymal $A\beta$ [55,151,180,215], while tau is thought to be predominantly cleared by degradation, ISF bulk flow, and CSF absorption clearance mechanisms [184,216]. Recent evidence however has suggested that the glymphatic system may contribute to a larger portion of parenchymal clearance of these protein species than previously thought [151,179,183].

Previous studies of glymphatic function in mouse models of AD have focussed largely on $A\beta$ pathology [217]. In human AD though, it is the tau burden, not $A\beta$ load, that predicts both brain atrophy as well as cognitive status in patients with AD [218]. Furthermore, emerging evidence suggests that the extracellular space, which is cleared by the glymphatic system, acts as a conduit for neuron-to-neuron propagation and regional progression of AD tau pathology [176,219,220]. This raises the intriguing possibility that reduced glymphatic clearance of tau may potentiate disease progression via exacerbated neuron-to-neuron propagation of tangle susceptible tau protein, and as such, would be a powerful target for therapy.

Here I study the glymphatic system using dynamic contrast-enhanced (DCE) magnetic resonance imaging (MRI), in a mouse model which develops tau NFT pathology [95] similar to that seen in neurodegenerative diseases such as AD [16]. By using DCE- MRI, I assess the function of glymphatic clearance in rTg4510 mice across the whole brain using minimally invasive techniques. In addition, I examine the expression pattern of AQP4 in affected

regions. I hypothesised that changes in CSF dynamics may differ with the varying stages of tau pathology and neurodegeneration, and as such, studied three distinct timepoints in this model's pathological timeline. This study provides the first demonstration of impaired glymphatic function in an animal model of tau pathology and implicates the role of AQP4 in the clearance of tau proteins from the brain.

5.3 Methods

5.3.1 Mice

Generation of homozygous rTg4510 transgenic mice has been described previously [221]. The rTg4510 and litter matched wildtype mice were licensed from the Mayo Clinic (Jacksonville, Florida, USA), bred for Eli Lilly by Taconic (Germantown, Maryland, USA), and imported into the United Kingdom for study at University College London's (UCL) Centre for Advanced Biomedical Imaging. Female mice at 2.5 months, 5 months and 7.5 months of age were used. All animal work was performed in accordance with the United Kingdom's Animals (Scientific Procedures) Act of 1986 and was previously approved by UCL's internal Animal Welfare and Ethical Review Body. Mice had unrestricted access to food and water, and were housed under automatically controlled temperature, humidity, ventilation and 12h light/dark cycle settings.

5.3.2 Surgical preparation, magnetic resonance imaging and image analysis

The experimental methods employed in Chapter 4 were replicated for the MRI preparation, imaging and analysis in these experiments, and are detailed in sections 4.3.1 – 4.3.4.

5.3.3 Tau, GFAP and AQP4 Immunohistochemistry

Immunohistochemistry was performed in order to quantify cortical deposition of tau in rTg4510 mice. Mice were perfused with phosphate buffered saline (PBS) followed 10 % buffered formalin (VWR catalogue# 9713.1000) before being processed using the Tissue TEK VIP processor (GMI Inc.) and embedded in paraffin wax. 6µm thick sections of the

brain in the sagittal plane were collected using a rotary microtome and mounted on glass slides. Following de-paraffinisation and rehydration of the tissue sections, antigen retrieval was performed using the Lab Vision PT module system (Thermo Scientific), where sections were heated to 100°C for 20 min in citrate buffer (TA-250-PM1X; Thermo Scientific). Slides were transferred to a Lab Vision Autostainer (Thermo Scientific).

For tau immunohistochemistry, the following incubations were performed: 10 min in H₂O₂ (0.3%); 30 min in normal goat serum (1:20; Vector Laboratories); 60 min in primary antibody for tau phosphorylated at serine 409 (PG-5; 1:8000 from Peter Davies, Albert Einstein College of Medicine, NY, USA); 30 min in biotinylated goat anti-mouse IgG (1:200, BA9200; Vector Laboratories); 30 min avidin-biotin complex solution (PK-7100; Vector Laboratories); 5 min in 3,3'-diaminobenzidine (SK-4105; Vector Laboratories).

The following primary antibodies were used for glial fibrillary acidic protein (GFAP) and AQP4 immunohistochemistry : rabbit monoclonal GFAP (1:3000; PU020-UP, Biogenix) and mouse monoclonal AQP4 (1:200; ab9512, Abcam). Slides were incubated for 60 minutes in primary antibody; 30 minutes in biotinylated goat anti-rabbit (1:200; BA-1000, Vector Labs) or goat anti-mouse (1:200; BA-9200, Vector Labs) secondary antibodies; 30 minutes in avidin-biotin complex solution (PK-7100, Vector Labs); 5 minutes in 3,3'-diaminobenzidine (SK-4105, Vector Labs).

Apart from the last two steps, PBS with 0.05% Tween-20 (PBS-T) was used for diluting reagents and washes between steps. Sections were then counterstained with haematoxylin before dehydration and cover-slipping. Stained sections were digitised using the Scanscope AT slide scanner (Aperio) at 20× magnification.

To quantify PG-5-positive tau pathology, Imagescope software (version 11.1.2.780; Aperio) was used to view the digitised tissue sections and delineate boundaries of the rostral and caudal cortex, and somatomotor and visual cortex areas. PG-5 immunoreactivity was quantified using the positive pixel algorithm (Imagescope, version 11.1.2.780; Aperio), and performed in a blinded fashion.

To quantify GFAP and AQP4 expression, ImageJ software (version 1.44p) was used to view the digitised tissue and uniformly threshold for immunoreactivity. ROIs were drawn on each image for extraction of percentage immunopositive coverage (% immunoreactivity of whole brain region) for each region, in a blinded fashion.

5.3.4 AQP4 Immunofluorescence

Tissue sections for subcellular localisation of AQP4 in relation to cerebral blood vessels were processed as above and immunofluorescently stained for both AQP4 (1:60, ab9512, Abcam) and the blood vessel endothelial cell marker CD31 (1:25, ab28364, Abcam). Following deparaffinisation and antigen retrieval, tissue sections were incubated in a cocktail of primary antibodies overnight at 4°C (CD31, 1:25 (ab28364, Abcam); AQP4, 1:60 (ab9512, Abcam)), washed in PBS-T and then incubated in a cocktail of fluorophore-conjugated goat anti-rabbit (Alexa Fluor 488, 1:500; A11008) and goat anti-mouse (Alexa Fluor 568, 1:500; A11004) secondary antibodies (Invitrogen) for 2hrs at room-temperature. Finally, sections were washed in PSB-T and then dH₂O, before being cover-slipped in VECTASHIELD mounting medium with DAPI (H-1200, Vector Labs). All incubations were performed manually and in a humidity tray, with minimal exposure to light. Immunofluorescence images were taken using a Leica DMLB fluorescent microscope and Q Capture Pro7 software (QImagng). Images were acquired by single excitation of each wavelength (separately) and channels subsequently merged.

5.3.5 Quantification of AQP4 Expression Across Blood Vessel Cross Sections

Evaluation of the localisation of AQP4 to perivascular end feet and glial limitans was performed by measuring the pixel intensities of CD31 and AQP4 immunoreactivity across cross sections of blood vessels in each of the brain regions studied. For this, vessel containing ROIs were identified on DAPI images: identified using flattened nuclei, clusters or lines of nuclei out of focus compared to the surrounding tissue and 'negative' space between nuclei without background fluorescence. Fluorescent intensity for both CD31 and AQP4 markers were measured across a single 4µm axis perpendicular to the vessel orientation, and expressed as intensity, normalised to the intensity of a randomly selected background ROI

in the same image for each antigen, to generate linear plots of fluorescence extending from the brain tissue, into the vessel and again into the surrounding brain tissue.

5.3.6 Quantification of AQP4 Polarisation

Perivascular polarisation of AQP4 was measured as previously described [183]. Briefly, the median immunofluorescence intensity of perivascular regions was measured. A threshold analysis was then used to measure the percentage of the region exhibiting AQP4 immunofluorescence greater than or equal to perivascular AQP4 immunofluorescence (AQP4 % area). Polarisation was expressed as the percentage of the region that exhibited lower AQP4 immunoreactivity than the perivascular end feet. AQP4 vessel coverage was measured by firstly delineating the area of the vessel from the CD31 channel image. This ROI was then placed on the AQP4 channel image thresholded for immunoreactivity for extraction of the percentage vessel coverage (% immunoreactivity of AQP4 of whole delineated vessel).

5.3.7 Statistical analysis

Statistical comparisons between groups were performed via either a repeated measures two-way analysis of variance (ANOVA) followed by post-hoc Bonferoni post-tests for multiple comparisons (for MRI data), or a regular two-way ANOVA followed by post-hoc Bonferoni post-tests for multiple comparisons (for all other grouped comparisons not containing repeated measures). All statistical testing was performed using GraphPad Prism (v7 for Windows, San Diego, CA, USA). All data is represented as mean \pm SEM for the n number of animals in each group, which are detailed in figure legends.

5.4 Results

5.4.1 Glymphatic inflow, tau and AQP4 in rTg4510 transgenic mice with age

The regions most affected by pathology in the rTg4510 model – the cortex and hippocampus, were analysed. Based on the observations in Chapter 4 (section 4.4.1), where a difference in contrast enhancement was seen between the rostral and caudal cortices, the cortex was also further separated into these sub regions. Contrast enhancement to the caudal cortex was elevated in the wild types at all ages compared to the rostral cortex, as previously observed (Figure 33). Compared to the wildtype group, in the transgenic group, glymphatic inflow was reduced in the caudal cortex at 2.5 months (Figure 33 D; $p < 0.05$ from 48 – 60 mins, $p < 0.01$ from 72 – 96 mins, $p < 0.001$ from 108 – 180 mins) and then markedly elevated in the rostral cortex at 7.5 months of age (Figure 33 C; $p < 0.01$ from 108 – 180 mins). This elevation of glymphatic function was also observed in the hippocampus of the transgenic group, but did not attain statistical significance during the time course (Figure 33 I). To then determine if these differences were caused by differences in rates of contrast ingress into these regions, the slopes of the curves were calculated as a surrogate estimate of glymphatic inflow (Figure 34). In these analyses, the hippocampus showed the most marked difference in ingress rate, however, this did not achieve statistical significance.

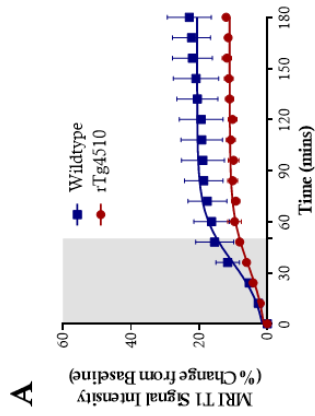
Next, to further probe potential differences in the dynamic MRI timeseries data between the rTg4510 and WT groups, the ‘penetration efficiency’ was calculated as described in Chapter 4, section 4.3.4. This metric revealed an increase in the in the rostral cortex (Figure 35 A; mean difference = 0.51 more in the rTg4510s compared to wildtype, $p = 0.13$) and hippocampus (Figure 35 I; mean difference = 0.18 more in the rTg4510s compared to wildtype, $p = 0.01$) of the rTg4510s in the 7.5 month group when compared to their wildtype counterparts, with the hippocampus (Figure 35 I) achieving statistical significance at this age.

GFAP, a marker of astroglial activation, increased with increasing burden of tau across ages and regions, with the most significance observed in the cortex at 5 months, a stage reflecting mature tangle formation (Figure 35 C, G; rostral cortex mean difference = 5.89% more in

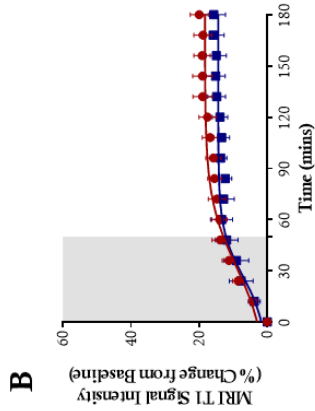
rTg4510s compared to wildtype, $p < 0.0001$; caudal cortex mean difference = 4.54% more in rTg4510s compared to wildtype, $p = 0.0005$), and 7.5 months, during neurodegeneration (Figure 35 C, G; rostral cortex mean difference = 8.19% more in rTg4510s compared to wildtype, $p < 0.0001$; caudal cortex mean difference = 11.22% more in rTg4510s compared to wildtype, $p < 0.0001$). In the hippocampus, the most significant elevation was observed at 7.5 months (Figure 35 K; mean difference = 8.13% more in rTg4510s compared to wildtype, $p = 0.0002$). AQP4 levels mirrored the elevations in GFAP levels, but did not attain significance (Figure 35 D, H, L).

Rostral Cortex

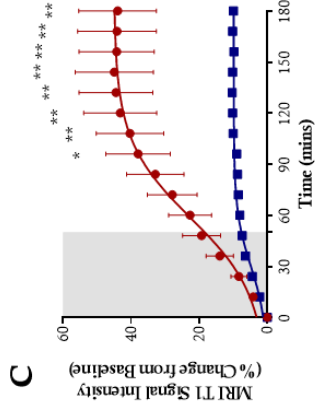
2.5 months



5 months

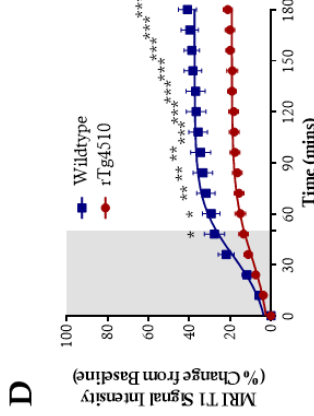


7.5 months

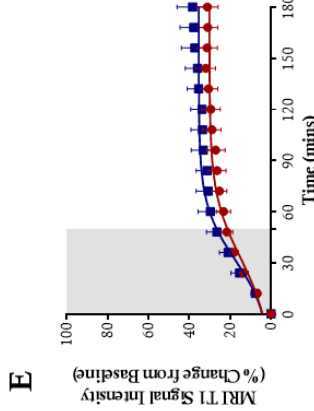


Caudal Cortex

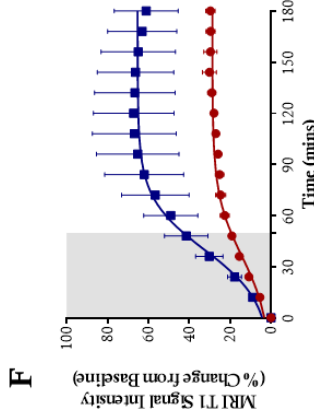
2.5 months



5 months

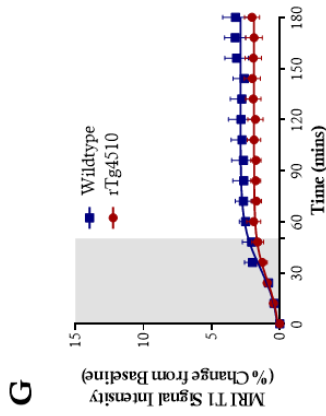


7.5 months

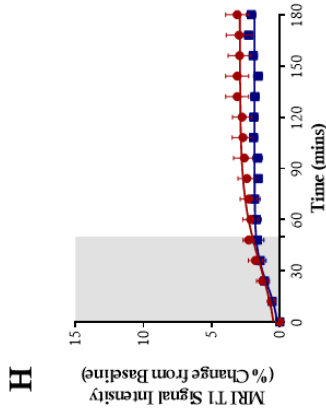


Hippocampus

2.5 months



5 months



7.5 months

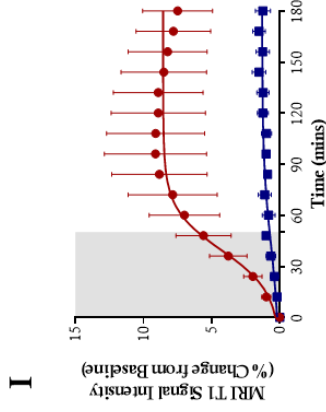


Figure 33. MRI T1 signal intensity (% change from baseline) vs. time data acquired from the 2.5 month ($n = 3$ wildtype and 5 rTg4510), 5 month ($n = 4$ wildtype and 4 rTg4510) and 7.5 month ($n = 4$ wildtype and 4 rTg4510) animals. (A – C) shows time course data from the rostral cortex, (D – F) shows the caudal cortex and (G – I) shows the hippocampal data. Statistical significance denoted by asterisks: *= $p < 0.05$, **= $p < 0.01$, ***= $p < 0.001$.

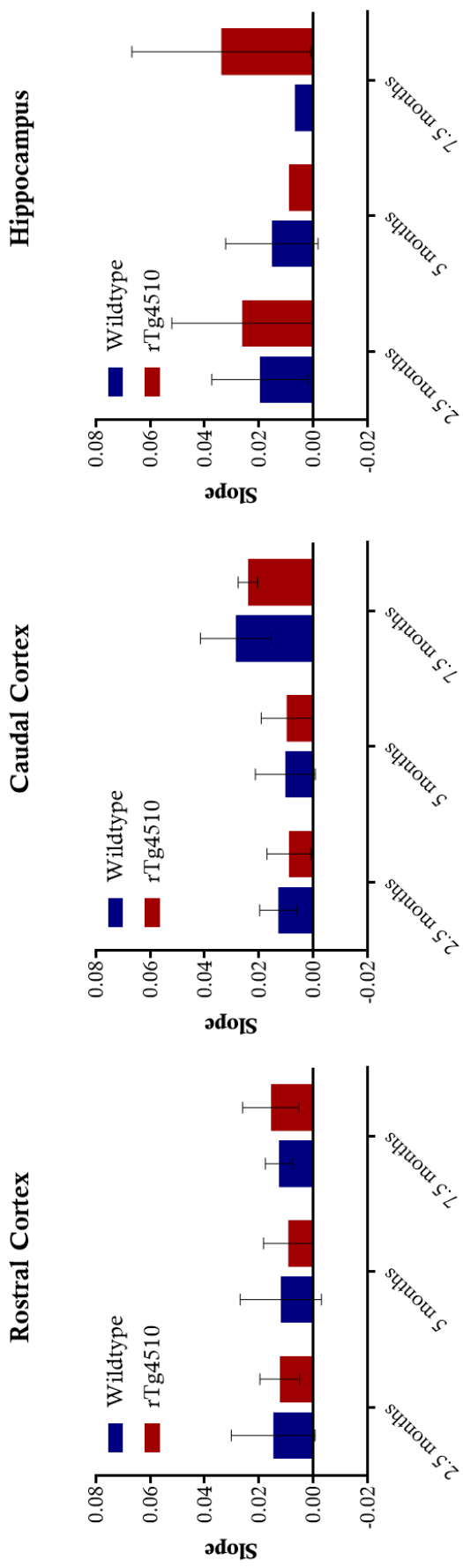


Figure 34. Slopes of the sigmoidal curves of the time course data in each of the brain regions from Figure 32, as a surrogate measure of rates of glymphatic inflow.

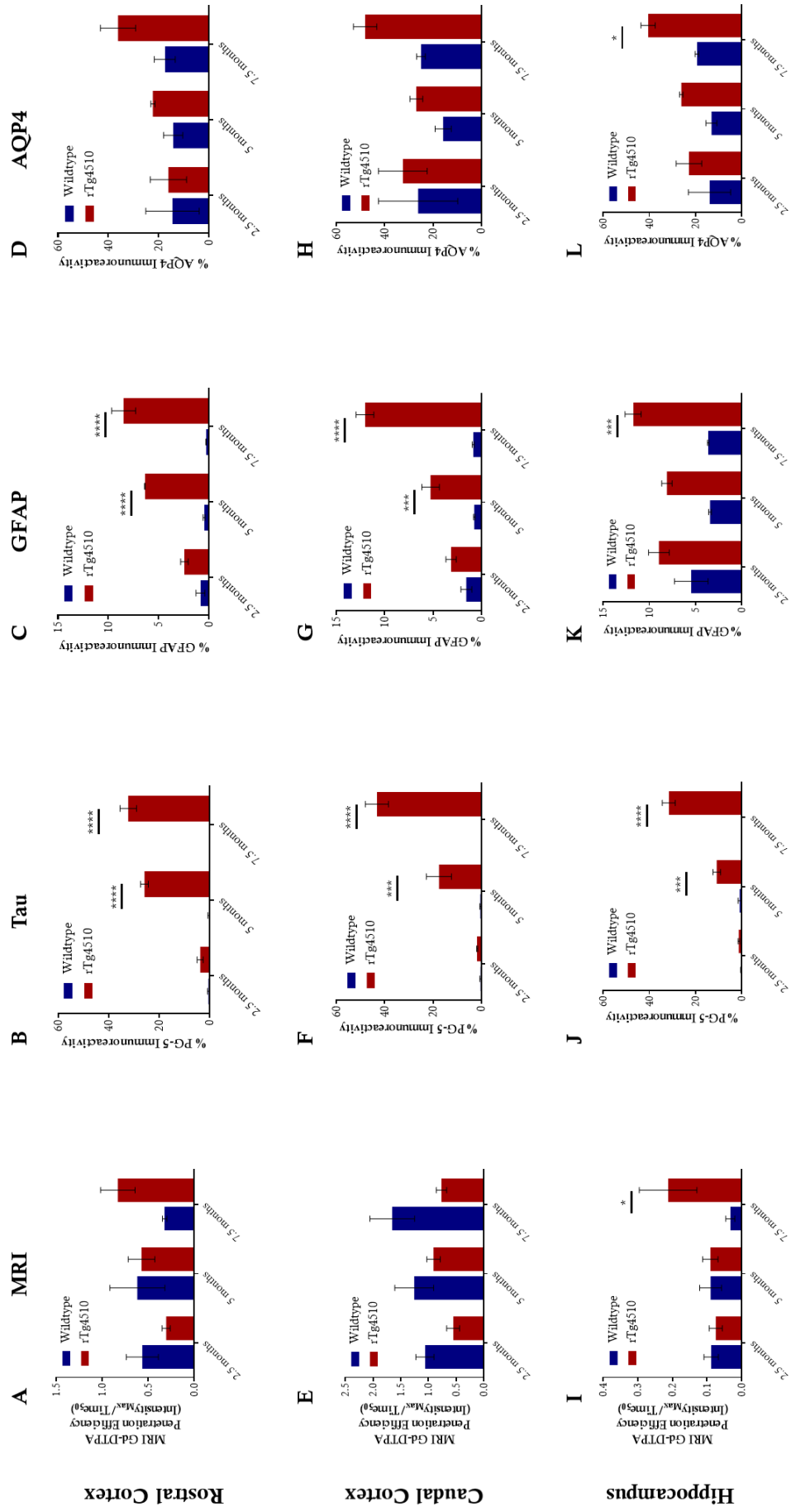


Figure 35. MRI and histological analyses grouped by genotype and age. (A, E, I) MRI contrast penetration efficiency in each of the brain regions in which raw data and sigmoidal curves are displayed in Figure 32. Immunohistochemistry quantification of (B, F, J) tau, (C, G, K) GFAP and (D, H, L) AQP4 for the corresponding regions and groups in A, E, I). Statistical significance denoted by asterisks: * = $p < 0.05$, *** = $p < 0.001$, **** = $p < 0.0001$.

5.4.2 Regional differences between the rostral and caudal cortices of the rTg4510 mouse model

In order to tease out the differences in inflow between the rostral and caudal cortex and study the association to pathological burden, these two cortical regions of the transgenics were next analysed against each other (Figure 36). This was carried out to build on the findings from Chapter 4 (section 4.4.1), where higher contrast enhancement was observed in the caudal cortex compared to the rostral cortex (Figure 28 D).

Here, a significant impairment in contrast enhancement was apparent in the rostral cortex in the 2.5 month group (Figure 36 A; $p \leq 0.05$ from 96 – 168 mins, $p = 0.005$ at 180 mins), a similar trend of which was also seen in the 5 month group (Figure 36 B). In the 7.5 month group however, this trend was reversed, with the caudal cortex showing impairment in contrast enhancement compared to the rostral cortex, but without statistical significance (Figure 36C). Visual assessment of the histological sections (Figure 36 E) revealed a modest increase in tau burden in the rostral cortex at 2.5 months and 5 months, compared to the caudal cortex. PG5 quantification too showed that the tau burden in the rostral cortex was elevated at 5 months compared to the caudal cortex (Figure 36 F; mean difference = 8.25% more in the rostral cortex). The corresponding penetration efficiency from the MRI experiments revealed that this metric was inversely related to tau accumulation at 5 and 7.5 months of age (Figure 36 D; mean difference = 0.33 less at 5 months and 0.6 more at 7.5 months in the rostral cortex).

On studying GFAP (Figure 36 G), this marker increased with age in both rostral and caudal regions, showing increased astroglial activation. A significant increase in GFAP was observed at 7.5 months of age during the most severe stage of pathology, in the caudal cortex compared to the rostral cortex (mean difference = 3.58% more in the caudal cortex compared to the rostral cortex, $p < 0.05$). AQP4 also increased with age in both regions, with the caudal cortex having mildly higher levels at all ages (Figure 36 H).

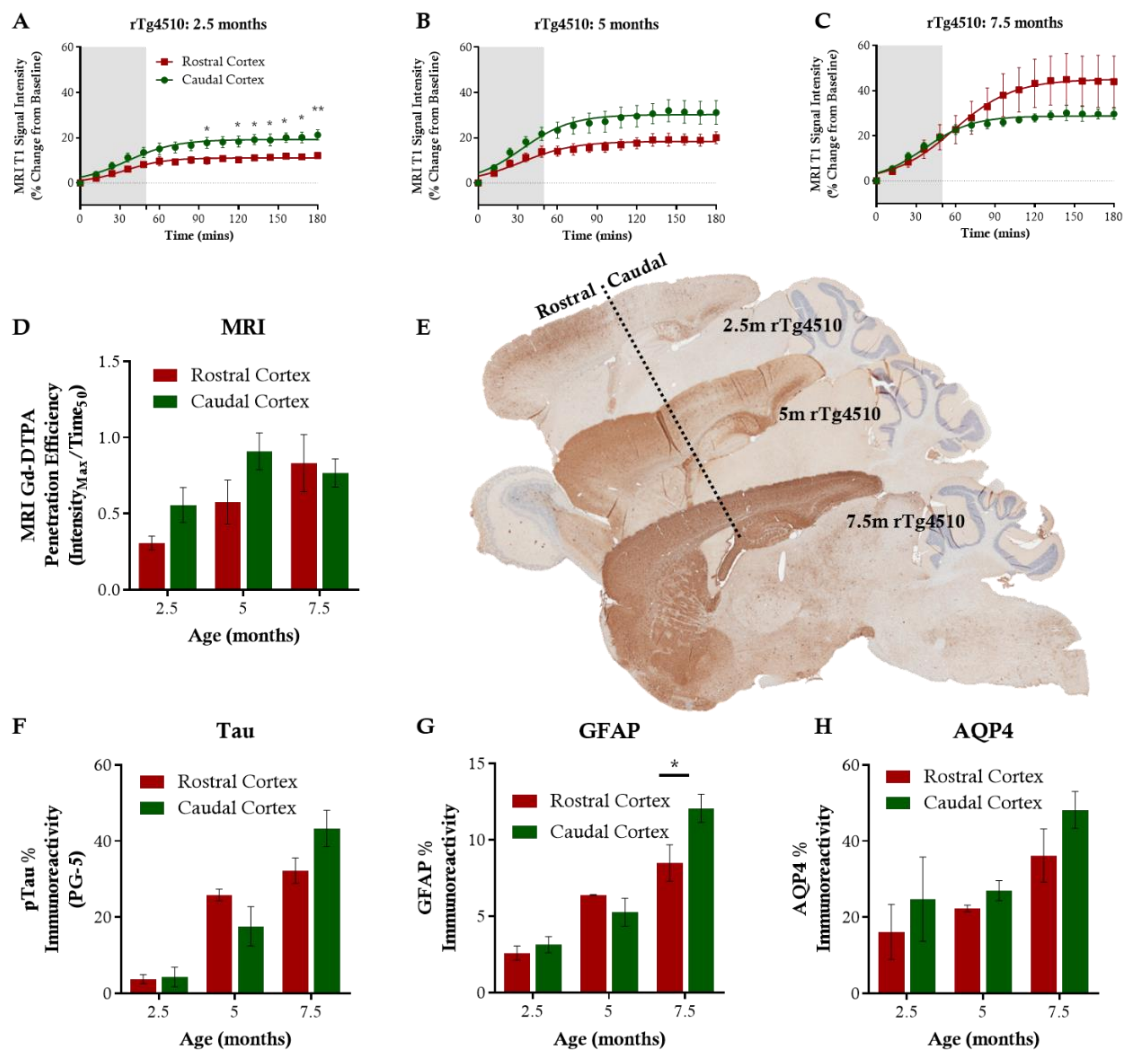


Figure 36. MRI T1 signal intensity (% change from baseline) vs. time data acquired from the rostral and caudal cortices of rTg4510 (A) 2.5 month ($n = 5$), (B) 5 month ($n = 4$) and 7.5 month ($n = 4$) animals. (D) Penetration efficiency in each of the brain regions in which raw data and sigmoidal curves are displayed in A - C. Percentage immunoreactivity of (F) tau, (G) GFAP and (H) AQP4 in the corresponding regions from D. (E) Representative histological images with PG-5 staining demonstrating the gradient of tau accumulation in the rostral cortex from 2.5, 5 and 7.5 months. Statistical significance denoted by asterisks: $*=p<0.05$, $**=p<0.01$.

5.5 Discussion

In this work, whole brain assessment of glymphatic inflow was carried out using the MRI protocol set up in the previous chapter. The rTg4510 model was assessed at 3 stages of pathology – 2.5 months, during the onset of tangle formation; 5 months, where the presence of mature tangles is expected; and 7.5 months, when neurodegeneration commences [94]. This approach attempted to tease out if glymphatic impairment was related to pathological tau burden, and if changes occurred early, prior to the onset of severe pathology. The rTg4510 model expresses pathological mutant tau throughout the cortex and hippocampus given the strong action of the CaMKIIa forebrain promoter [95]. Thus analyses were focused in these regions.

Notably, the overall percentage inflow in the wild type brains was lower compared to the previous C57BL/6J wild type experiments. A reasonable explanation for this variance may be the difference in background genetic strain, as the rTg4510 is on a mixed 129S6xFVB background, and littermates from the transgenic cohort were used here as controls. Strain differences can account for a myriad of brain differences. In one study that compared the 129S6 strain to the C57BL/6, they found the most significant morphological variances in areas corresponding to the motor and the anterior somatosensory cortices [222]. Interestingly, these regions are included in the rostral and caudal cortices analysed in the work presented here, and so regional glymphatic patterns can be expected to vary between morphologically distinct strains. In another study, analyses of vascular branching and cerebral blood flow in C57BL6 and BALB/c strains found morphological differences between arterial branching patterns, which then influenced the values of blood flow between strains [223]. Given the evidence for such inter-strain differences in the brain morphology and perfusion, changes to glymphatic function between strains may be expected. In light of these findings, a future comparison between commonly used inbred strains, which encompasses anatomical differences, blood flow variations and glymphatic changes, is warranted.

Given the difference in contrast intensity observed between the rostral and caudal cortices in the wild type characterisation in Chapter 4 (section 4.4.1), these subregions were segmented separately. This was particularly of interest in this study, given the early histological difference in tau deposition observed between these regions. If the levels of cortical tau in this model solely corresponded to the transgene expression, one would expect homogenous burden throughout the cortex given the strong forebrain CaMKIIa promoter driven pattern of the transgene [95]. The reduction in contrast penetration in the rostral cortex (Figure 35 D), as measured by MRI in the 5 month group, coupled with the increase in tau deposition in this region (Figure 35 F) suggests that the regional differences in glymphatic function may be a contributing factor towards the difference in pathological burden between these regions. Improved glymphatic clearance in the caudal cortex of the mouse brain, prior to neurodegenerative changes, may be reducing the amount of deposited tau in that region. The subsequent loss of this effect by 7.5 months could be attributed to the continued robust expression of the transgene with age. At later stages in the pathological timeline, the severe tau accumulation throughout the forebrain may surpass the benefits of any regional glymphatic clearance efficiencies.

Neurodegenerative changes may also account for the differences observed between transgenics and wild types at 7.5 months. Previous MRI studies of the rTg4510 brain has revealed significant atrophy of the cortex and hippocampus [224] – the regions that suffer the most tau burden, with the progressive nature of this loss markedly detectable by 7.5 months using morphometric analyses [225]. In these data, the earliest tau pathology is apparent in the hippocampus and the rostral cortex (Figure 35E). This places the rostral cortex as the region that closely follows the hippocampus, with the caudal cortex coming in last in the pathological cascade. Taking this view, the elevation in contrast in the hippocampal and rostral cortical regions of the rTg4510s compared to wild types at 7.5 months indicates that the magnitude of inflow is related to the regional degree of tau pathology at this age. This can be explained by the corresponding degree of neurodegeneration within these regions. Extracellular volume [182] and tortuosity [161] are both factors that contribute to glymphatic

efficiency. If the extracellular space increases in volume and becomes less tortuous with increasing cell loss in these regions, the movement of solutes through these regions, including MR contrast agents, may accelerate.

Changes to cytoarchitecture during neurodegeneration may also manifest as glymphatic changes at a cellular scale. GFAP is an astrocytic marker which is known to be upregulated during aging and neurodegeneration [226]. The amount of GFAP in the rostral and caudal cortices closely mirrored the degree of tau pathology within these regions at all time points, demonstrating increasing astrogliosis with progression of pathology. AQP4 also increased with age. In mice, perivascular loss of AQP4 is a feature of the aging brain [183], is associated with glymphatic impairment, and this perivascular loss is accompanied by the redistribution of AQP4 to parenchymal processes of reactive astrocytes [153]. In a study exploring AQP4 in human AD subjects, the loss of perivascular AQP4 was accompanied by an increase in AQP4 expression [205]. It is likely that the regional observations here reflect these discrete cellular changes, brought about by mutant tau overexpression and the subsequent onslaught of the neurodegenerative process. However, it must be noted that experimental factors precluded the broader analysis and interpretation of immunofluorescence data (Section 5.3.6) which was performed to study AQP4 polarisation. Due to limited sample availability, combined with perfusion artefacts giving rise to mouse-on-mouse reactivity, a comprehensive analysis was hindered. This was further mired by the variation in vessel size across collected sections, as well as non-specific fluorescent signals arising from the nuclei and other organelles which pointed to an error in the immunostaining process.

Exploring distinct regional differences in the AD brain is of interest given the staged nature of pathology through the course of the disease. Studies mapping cytoarchitecture indicate that the human homologue of the mouse rostral cortex topographically maps to the human anterior cingulate cortex, whereas the mouse caudal cortex closely resembles the human retrosplenial cortex [227]. Studies segmenting these distinct regions in the brains of familial AD subjects note that volumetric differences exist between these regions despite their close connectivity [228]. As such, it is judicious to study fine and progressive fluctuations in

glymphatic function in the regions most vulnerable to AD pathology, in order to understand how rates of tau clearance may contribute to these detrimental neurodegenerative changes. Furthermore recent observations have suggested that tau, using the extracellular space as a conduit, is able to propagate from neuron-to-neuron via a prion-like mechanism [229]. The functional relevance of appropriate glymphatic clearance of extracellular tau may therefore be of prime importance in neurodegenerative tauopathies, in which propagating pathology is thought to occur.

An additional consideration to take is the recirculating nature of the glymphatic pathway and its contribution to ongoing pathology. CSF tau is highly stable compared to A β (12-14hrs half-life in CSF compared to 2hrs for A β) [230,231]. Once tau is cleared from the parenchyma into the CSF sink, tau-laden CSF may be re-internalised into the parenchyma itself, or at the very least, may enter the periarterial space [157]. Periarterial deposition is known to occur with other parenchymal proteins cleared via this pathway, such as A β , in the form of cerebral amyloid angiopathy (CAA). Interestingly, tau labelling has been shown to colocalise with CAA in AD brains [232]. As such, in understanding the glymphatic contributions towards the mechanisms of AD onset, both tau and A β pathologies must be investigated in tandem to elucidate a clear mechanistic picture. To that end, the study that follows this chapter probes the role of glymphatic function in amyloid pathologies.

6. Glymphatic Function in Amyloidosis Models of Alzheimer's Disease

Following on from the previous chapter, here, whole brain glymphatic changes are investigated in two mouse models of amyloid pathology, using magnetic resonance imaging.

6.1 Summary

Cerebrospinal fluid levels of A β are a vital clinical marker of Alzheimer's disease onset. Thus, understanding the transit of A β species through the fluid compartments of the brain and its causative mechanisms in plaque pathology is beneficial in understanding disease progression. Previous glymphatic studies of Alzheimer's disease and related pathologies have had a particular focus on A β , but have not characterised amyloid-driven glymphatic changes taking a whole brain approach. This study aimed to address that gap and build on the previous work presented, which characterised glymphatic changes in disease models of tauopathy and aquaporin-4 dysfunction. Here, the whole brain magnetic resonance imaging methodology was replicated on two models of amyloid pathology – one which overexpresses mutant human amyloid and a second which expresses mutant amyloid at endogenous levels. This two-tiered approach was designed to elucidate any subtle changes in dynamic fluid exchange in the early stage of amyloidosis.

This work was performed in collaboration with the laboratory of Elizabeth Fisher at the UCL Institute of Neurology and Eli Lilly and Company. I would like to thank Katherine Sung for performing the histology included in these data.

6.2 Introduction

Understanding the various clearance mechanisms of A β and tau from the brain is surely a vital step towards developing new treatment strategies for Alzheimer's disease (AD). Aquaporin-4 mediated glymphatic clearance of amyloid- β (A β) and tau and its role in AD onset is still not fully explored. However, given the presence of both molecules in cerebrospinal fluid (CSF) during AD progression [117], they both present as viable candidates for removal via the glymphatic pathway.

CSF levels of two amyloid species, A β 40 and A β 42, are clinically used biomarkers. Decreases in CSF A β 42 correlates with disease progression and increasing plaque load, and although CSF A β 40 levels are relatively unaffected, a decrease in ratio of CSF A β 42:A β 40 is associated with AD status [118]. If these decreases in CSF levels are caused by A β species being sequestered into plaques, it is important to understand if glymphatics play a part in propagating this pathology – either by recirculating glymphatic delivery of CSF species into the brain encouraging plaque formation, or by a lack of glymphatic removal contributing to an increase of these A β species within the parenchyma.

In the original work that characterised glymphatic function, the movement of A β via this pathway took the spotlight. In that work, Iliff *et al.* showed that clearance of radioactively labelled A β 40 injected into the brain was cleared over time, and fluorescently labelled A β 40 accumulated along large draining veins. Radioactive A β 40 infused intracisternally also entered the brain in a pattern that was characteristic of other glymphatic solutes. Notably, they also showed a reduction in all these measures in AQP4 null mice [151]. Subsequently, using a similar approach, Peng *et al.*, showed glymphatic impairment in the APP/PS1 mouse model of AD. They found that brain uptake and clearance of radioactively labelled A β reduced with advancing age in APP/PS1 mice, with glymphatic impairment being apparent at an age prior to plaque formation. Additionally, by infusing fluorescently labelled A β 40 and A β 42, they showed that these species can enter the brain along penetrating arteries, with the infused A β 40 having an affinity to gather around existing endogenous plaques [217].

Previous studies in this amyloidosis model have also shown that deletion of AQP4 exacerbates memory deficits and A β accumulation in these mice [204].

Taking these findings into account, the next experiments aimed to dynamically image glymphatic flow patterns in amyloidosis models of AD, using dynamic contrast-enhanced (DCE) magnetic resonance imaging (MRI). If perturbances in glymphatic inflow contribute to the aforementioned observations implicating A β as a substrate, I hypothesised that this will be observable by DCE-MRI and provide a wider, more detailed picture of these changes, above and beyond the single snapshot view enabled by florescent and radioactive tracers. Here, I aim to build on the work I presented in Chapter 4, where I showed that glymphatic inflow can be visualised in real time using MRI and this can be visibly altered by pharmacologically blocking AQP4, as well as the work in Chapter 5, where differences in glymphatic function were demonstrated in tauopathy. In this work, to surpass any macroscopic effects due to neurodegeneration and atrophy, the model J20 (PDGF-APP^{Sw,Ind}) was used, as it is one that which accumulates plaque pathology in the brain, but shows minimal neurodegeneration [96]. Given that a significant criticism that mouse models of AD are met with is the artificial exacerbation of phenotypes due to overexpression, a second newer amyloid model, the APP NL-F mouse model, was also included in this study. This mouse model expresses endogenous levels of APP, and develops plaque pathology slower and later in its lifespan [98], thus enabling a more timely study of the preclinical stages of disease.

6.3 Methods

6.3.1 Mice

Generation of homozygous J20 (PDGF-APP^{Sw,Ind}) [96] and APP NL-F [98] transgenic mice have been described previously. The J20 (n = 6) and litter matched wildtype (n = 8) mice were licensed from the J. David Gladstone Institute (San Francisco, California, USA). The NL-F (n = 9) and litter matched wildtype (n = 13) mice were licensed from the Riken

Institute (Tokyo, Japan). Both strains were imported into the United Kingdom, bred at the University College London (UCL) Institute of Neurology, and transferred for study at UCL's Centre for Advanced Biomedical Imaging. For the J20 study, male and female mice at 6 months of age were used. For the NL-F study, male and female mice at 8 months of age were used. All animal work was performed in accordance with the United Kingdom's Animals (Scientific Procedures) Act of 1986 and was previously approved by UCL's internal Animal Welfare and Ethical Review Body. Mice had unrestricted access to food and water, and were housed under automatically controlled temperature, humidity, ventilation and 12h light/dark cycle settings.

6.3.2 Surgical preparation, magnetic resonance imaging and image analysis

The experimental methods employed in Chapter 4 were replicated for the MRI preparation, imaging and analysis in these experiments, and are detailed in sections 4.3.1 – 4.3.4.

6.3.3 Amyloid Immunohistochemistry

Immunohistochemistry was performed in order to quantify cortical deposition of amyloid in J20 and NL-F mice. Mice were perfused with phosphate buffered saline (PBS) followed by 10 % buffered formalin (VWR catalogue# 9713.1000) before being processed using the Tissue TEK VIP processor (GMI Inc.) and embedded in paraffin wax. 6µm thick sections of the brain in the sagittal plane were collected using a rotary microtome and mounted on glass slides. Following de-paraffinisation and rehydration of the tissue sections, antigen retrieval was performed using the Lab Vision PT module system (Thermo Scientific), where sections were heated to 100°C for 20 min in citrate buffer (TA-250-PM1X; Thermo Scientific). Slides were transferred to a Lab Vision Autostainer (Thermo Scientific).

The following incubations were performed: 10 min in H₂O₂ (0.3%); 30 min in normal goat serum (1:20; Vector Laboratories); 60 min in primary antibody for amyloid (b3D6; 1:1000 from Eli Lilly, USA); 30 min in biotinylated goat anti-mouse IgG (1:200, BA9200; Vector Laboratories); 30 min avidin-biotin complex solution (PK-7100; Vector Laboratories); 5 min in 3,3'-diaminobenzidine (SK-4105; Vector Laboratories).

Apart from the last two steps, PBS with 0.05% Tween-20 (PBS-T) was used for diluting reagents and washes between steps. Sections were then counterstained with haematoxylin before dehydration and cover-slipping. Stained sections were digitised using the Scanscope AT slide scanner (Aperio) at 20× magnification.

6.3.4 Statistical Analysis

Statistical comparisons between groups were performed via either a repeated measures two-way analysis of variance (ANOVA) followed by post-hoc Bonferoni post-tests for multiple comparisons (for MRI data), or a regular two-way ANOVA followed by post-hoc Bonferoni post-tests for multiple comparisons (for all other grouped comparisons not containing repeated measures). All statistical testing was performed using GraphPad Prism (v7 for Windows, San Diego, CA, USA). All data is represented as mean \pm SEM for the n number of animals in each group, which are detailed in figure legends.

6.4 Results

6.4.1 Glymphatic inflow in J20 transgenic mice

Glymphatic inflow in the J20 transgenic mice was not altered compared to wildtype littermates at 6 months of age (Figure 37). Inflow in the cortex and hippocampus, areas vulnerable to plaque accumulation in this model, was low, however, this was no different to the wildtypes. Regions closest to the infusion site such as the cerebellum and hindbrain showed the most marked increases in contrast enhancement in all mice.

Histopathological study of the brains revealed few to no visible mature plaques in the cortical and hippocampal regions (Figure 38), confirming that this model did not have profound pathology at the age that was assessed and represents a preclinical phase in its timeline. Quantification of the plaque load confirmed that whilst % burden of pathology was relatively low, the highest amyloid immunoreactivity was seen in the hippocampus (Figure 39).

A notable observation in the J20 cohort was that they were very sensitive to anaesthesia. In order to maintain optimal depth of anaesthesia, the isoflurane levels were continually adjusted throughout the imaging time for some mice. This was particularly apparent in mice that were subsequently revealed to be wildtype (after unblinding, post-analysis), but not restricted to this group. Two mice from this cohort did not complete the MRI protocol due to a leak in the infusion line found after commencement of the experiment. Routine re-genotyping results returned at the end of the project revealed that a further two mice were genotypically ambiguous. These mice were also eliminated from the study, thus resulting in the total loss of four mice in the cohort from the MRI analysis.

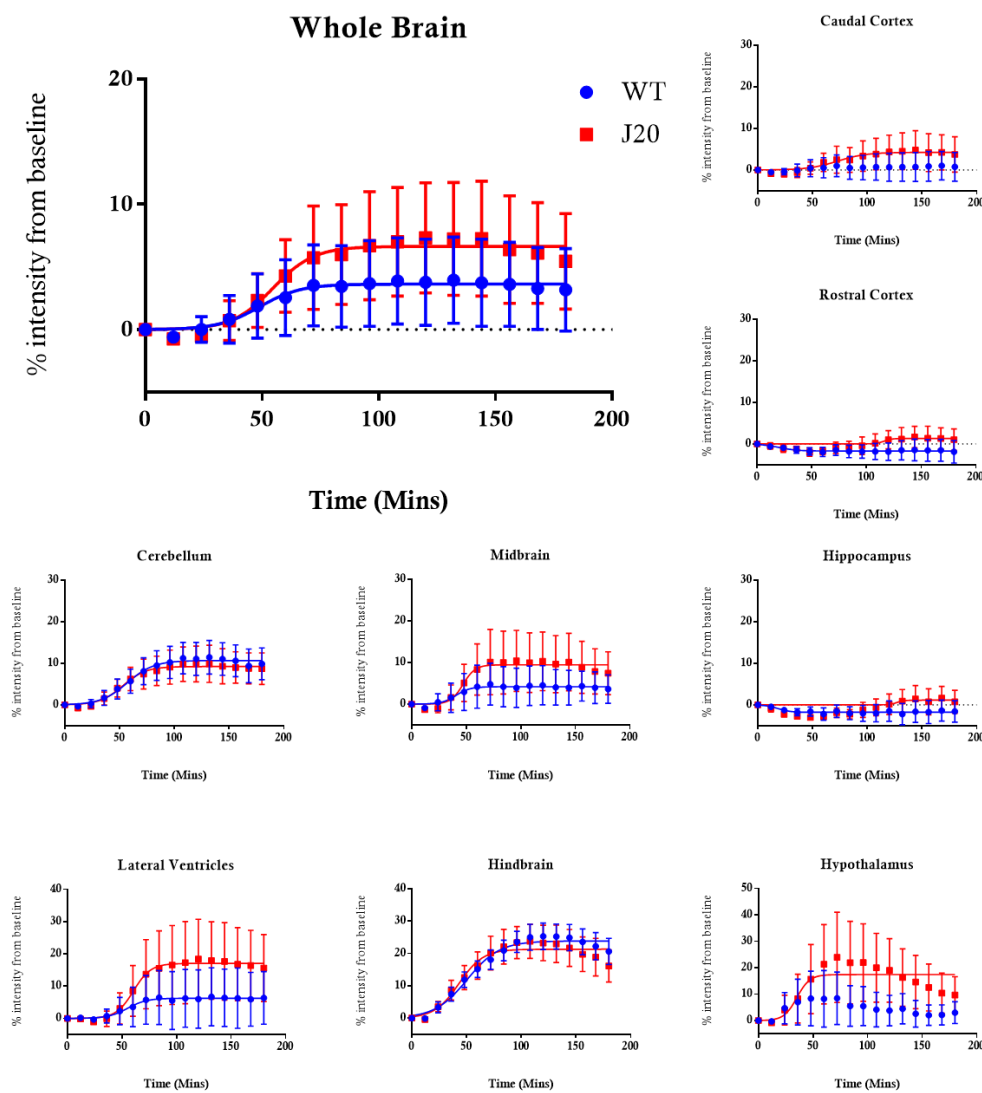


Figure 37. MRI T1 Signal Intensity (% change from baseline) vs. time plots from J20 (PDGF-APP^{Sw,Ind}) ($n = 4$) and wild type (WT) animals ($n = 6$) at 6 months of age, demonstrating penetration of Gd-DTPA tagged CSF over time in whole brain and selected regions.

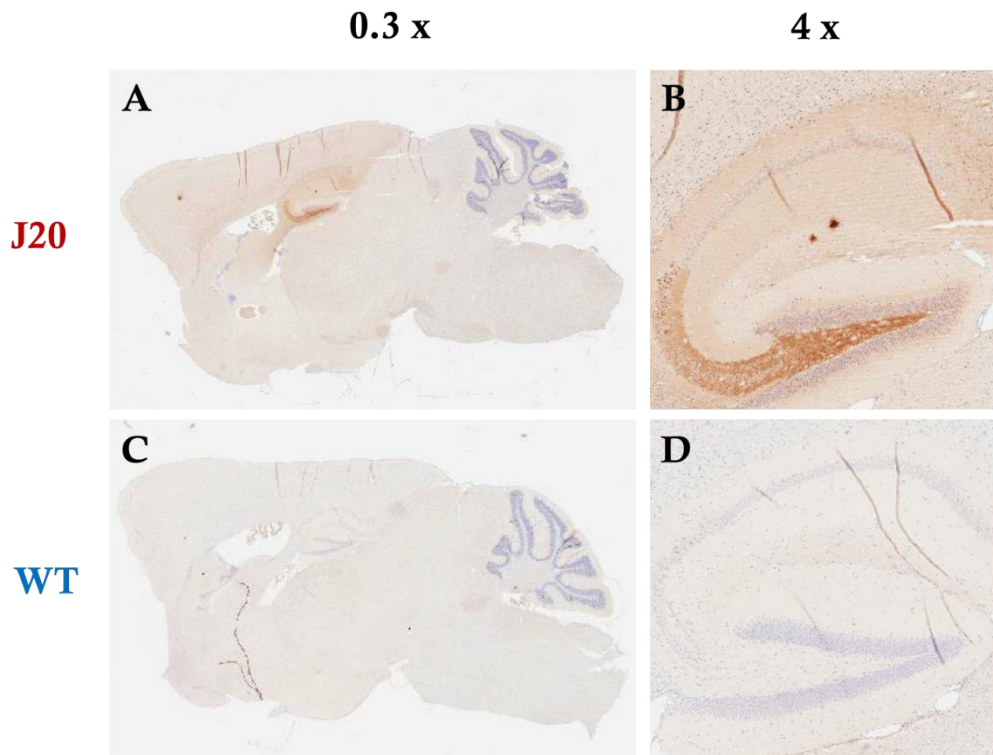


Figure 38. (A - D) Representative immunohistochemistry images of 6 month old J20 (top) and wildtype (WT) (bottom) sections stained with b3D6, taken at 0.3x (left) and 4 (right) magnifications. Limited plaque pathology is seen in J20 mice at this age.

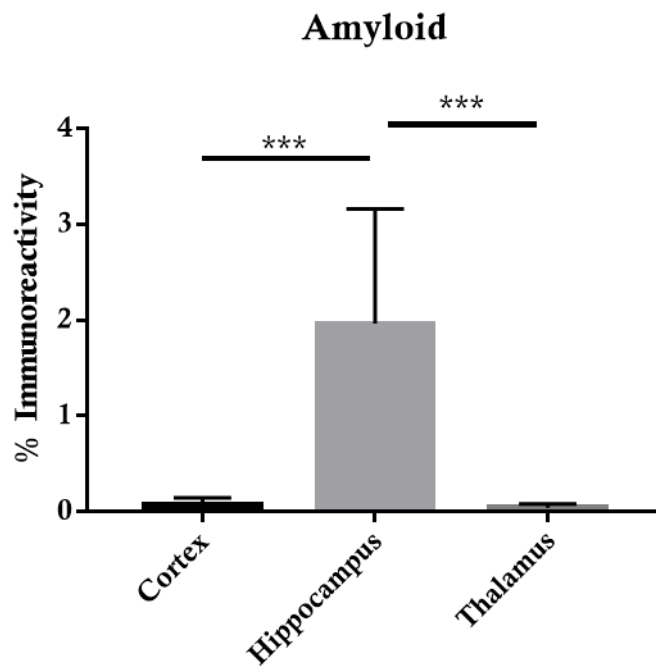


Figure 39. Percentage immunoreactivity of amyloid quantified in a subset ($n = 6$) of brains in the mice from the J20 cohort. The cortex and hippocampal regions are presented as areas of high pathology and the thalamus is presented as a control region. Statistical significance denoted by asterisks: ***= $p < 0.001$.

6.4.2 Glymphatic inflow in NL-F transgenic mice

No changes in glymphatic inflow were observed between NL-F transgenic and wildtype littermates (Figure 40). However, the interpretation of these data were marred by several factors which I believe adversely affected this dataset. Due to delays in shipment, the mice had minimal in-house acclimatisation time. In addition, several mice arrived marked with health concerns, three of which got progressively worse during housing at our Centre, or during experimental set up. These mice were eliminated from the experiments based on advice from the Named Animal Care and Welfare Officer. Routine re-genotyping performed at the end of the project also revealed nine further genotypic changes (with there being ambiguity between mutants and wildtypes), an observation also apparent in the phenotypic characterisation of plaques during histology (Figure 41). Thus, a total of twelve mice from this cohort were eliminated from the MRI analysis.

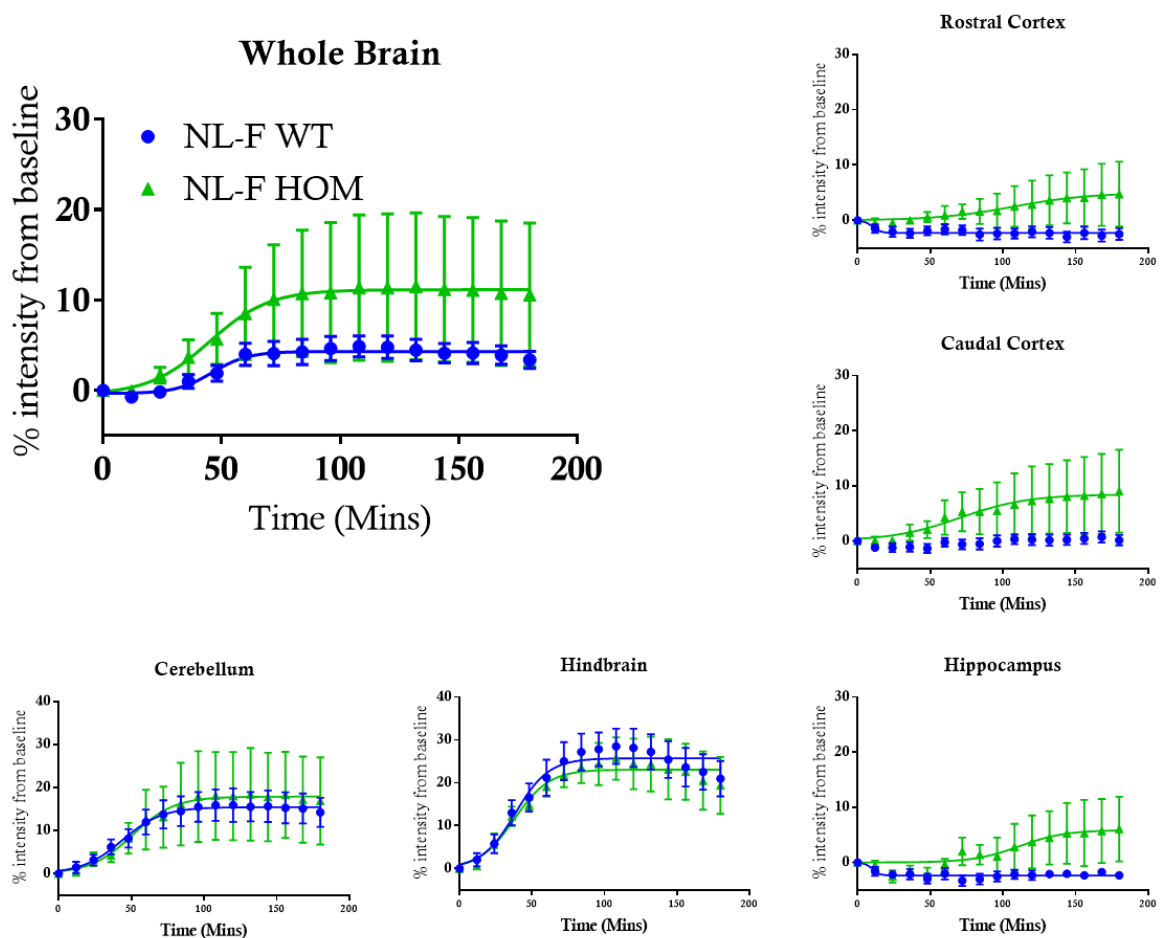


Figure 40. MRI T1 Signal Intensity (% change from baseline) vs. time plots from homozygous transgenic NL-F ($n = 3$) and wildtype (WT) animals ($n = 7$) at 8 months of age, demonstrating penetration of Gd-DTPA tagged CSF over time in selected brain regions.

A subset of histologically confirmed transgenic mice were quantified for amyloid burden in the cortex and hippocampus, regions expected to have high pathology, and thalamus, used as a control region (Figure 42). This analysis confirmed the significant elevation of plaque pathology in phenotypically confirmed NL-F homozygotes, some of which were shipped as wildtypes. Given these discrepancies, no further analysis was carried out on this cohort.

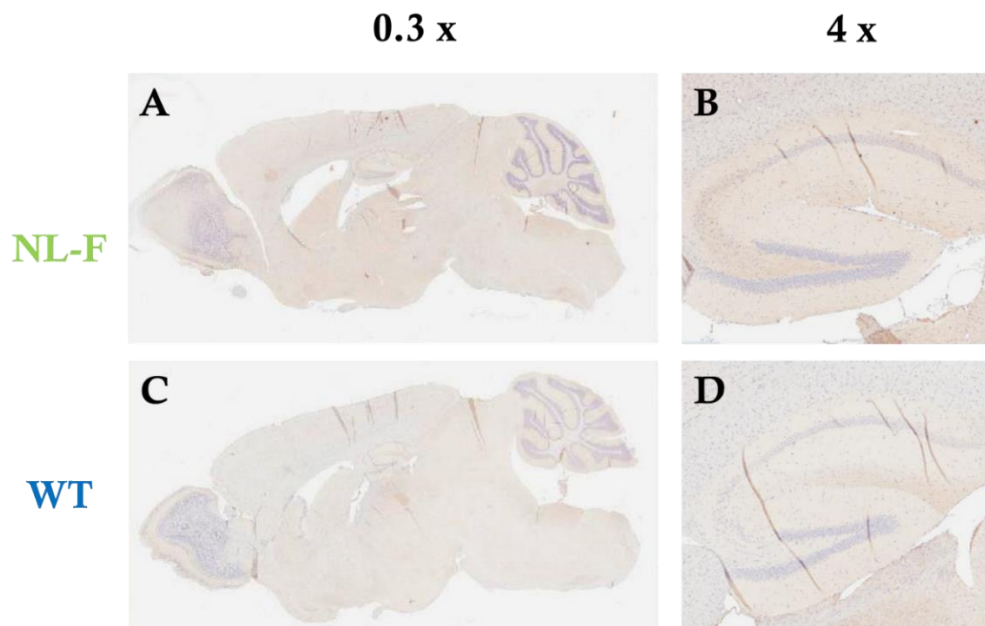


Figure 41. (A - D) Representative immunohistochemistry images of 8 month old NL-F (top) and wildtype (WT) (bottom) sections stained with b3D6, taken at 0.3x (left) and 4 (right) magnifications. Virtually no plaque pathology is seen in NL-F mice at this early age.

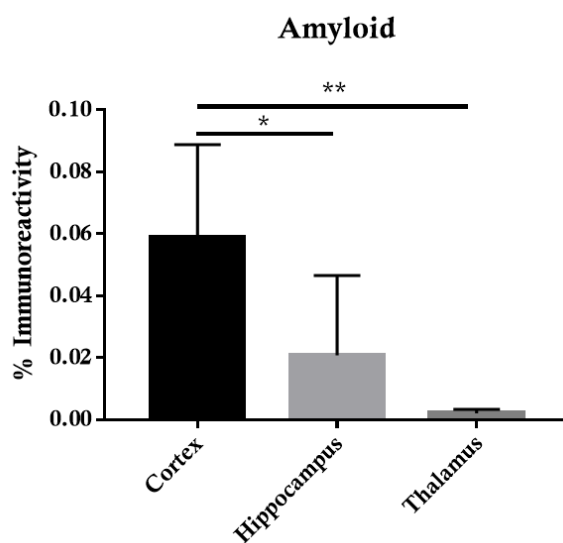


Figure 42. Percentage immunoreactivity of amyloid quantified in a subset ($n = 8$) of brains in the mice from the NL-F cohort. The cortex and hippocampal regions are presented as areas of high pathology and the thalamus is presented as a control region. Statistical significance denoted by asterisks: $*=p<0.05$, $**=p<0.01$.

6.5 Discussion

In this work, glymphatic changes in models of amyloid pathology were probed to advance the observations reported in the two previous chapters. Two different transgenic lines, at the relevant stage in each model's timeline prior to the accumulation of plaques, were used to elucidate if glymphatic changes precede protein accumulation as previously described, and if these changes could be detected regionally and globally across the brain. In both models, no changes in inflow were observed using DCE-MRI, with histology confirming low levels or absence of plaques in the brain. This is at odds with the work published by Peng *et al.* [217], which this work aims to build on, which showed early glymphatic impairment in APP/PS1 mice. However, several procedural and experimental variances may have contributed to these discrepancies.

Looking first to the J20 cohort, at first glance it is tempting to speculate that no changes in glymphatic function are seen prior to plaque formation, and such changes may occur downstream of the neurodegenerative process, particularly taking into account the finding from the rTg4510 study in Chapter 5. But given that APP/PS1 amyloid mice show glymphatic changes even prior to plaque accumulation, which then progresses during pathology [217], it suggests that differences between varying strains of transgenic models may exist.

Previous studies in the J20 mouse have reported a reduction in cerebral perfusion in this model [233]. Changes in perfusion can interplay with a number of physiological parameters including perfusion pressure, vascular radius and changes in blood viscosity [234]. Given that arterial pulsations are thought to be a key driving force in CSF ingress into the brain [156], then it is plausible that changes in cerebral haemodynamics can also affect glymphatic influx by proxy. Additionally, pre-treatment with A β 40 has been shown to reduce glymphatic inflow in the mouse brain [217], and interestingly, this is the species that is more abundant in the interstitial fluid of the J20 brain as early as 3 months [235]. These findings

would collectively imply that J20 mice would be expected to have reduced glymphatic inflow compared to wildtypes.

However, the cohort of J20 mice did not show differences between their wildtype counterparts, with even the wildtypes curiously not fully following the characteristic pattern of inflow previously described. Regions closest to the infusion site such as the cerebellum and hindbrain showed the most contrast enhancement, with deep brain structures such as the hippocampus, and regions furthest away from the route of glymphatic flow, such as the cortex, showing the least contrast. These characteristics point to an experimental shortfall.

A notable observation made during the J20 experiments was the ineptitude of this strain to tolerate isoflurane anaesthesia in the robust way observed in the wildtype C57/BL6J mice used in the TGN-020 experiments, or the rTg4510 transgenic cohort. Several but not all of the mice in the J20 cohort took longer to achieve a depth of anaesthesia required for surgical preparation, and once in the scanner, had to be carefully regulated to maintain an optimal physiological range in parameters that monitor the mouse's welfare, including heart rate and core temperature, during the experiment. In a recent study that investigated glymphatic function under a variety of anaesthetic regimens, choice of anaesthetic was found to be a sensitive factor in determining glymphatic efficiency. Using fluorescent tracer experiments, Hablitz *et al.* showed that ketamine/xylazine anaesthesia enabled the highest tracer influx, and isoflurane had the least, however, influx under isoflurane was markedly increased when supplemented with dexmedetomidine [236]. This observation is in keeping with similar findings from a different study which found that a combination of low dose isoflurane with dexmedetomidine evoked a higher glymphatic response (as measured by DCE-MRI in rats) than a high dose of isoflurane alone. But the authors also noted that the depth of anaesthesia was deeper in the higher dose of isoflurane, as quantified using electroencephalography [237]. This study also noted a 2% increase in the CSF compartment volume in the animals treated with the combination of the two anaesthetics, which contributed to the increased glymphatic efficiency reported.

Isoflurane is also known to have a marked effect on cerebral blood flow and volume [238]. Given the continuous fluctuations in anaesthetic dose that were required to maintain the J20 mice at a physiologically safe and experimentally acceptable depth in this cohort, it is possible that this negatively affected cerebral haemodynamic stability and contributed to data drift, thus marring glymphatic observations during this study. The variable response to isoflurane in the J20 mice was intriguingly more apparent in, but not restricted to the wildtype mice in this study. Since the J20 mice are bred on the C57/BL6J background, a strain which tolerated isoflurane in the previous experiments, this then raises the intriguing possibility that differences in anaesthesia tolerances can differ between lineages of mice bred in different centres or conditions, even on the same genetic background, and thus consequently indirectly contribute to differences in glymphatic and other physiological measures. To rectify this, a repeat study of this nature would ideally benefit from utilising ketamine/xylazine anaesthesia. However, the prolonged dose required for dynamic imaging must be carefully considered, given the deleterious cardiac and respiratory effects brought about by high ketamine/xylazine exposure [239], which may also consequently affect glymphatic measures. This poses a trade-off between experimental design and data integrity when undertaking investigations in whole brain glymphatic function across different strains and lineages.

Surveying the NL-F data, the small number of mice that were retained in the preliminary analysis suggest that no changes in glymphatic inflow are apparent prior to the onset of plaque formation. However, given the unfortunate obstacles faced by the cohort in this study, it is imprudent to make hasty interpretations about this model from this dataset. The NL-F line was included in this experimental plan to study a model with more naturally progressing pathology, as it is not an overexpression model. Although artificial overexpression of amyloid in other models may be perceived as a problem, in practical terms, the extremely slow progression of NL-F mice may also hinder the experimental progress and diminish the high-throughput advantage of using mouse models. Although plaque pathology is expected by 6 months of age, in this study, very few plaques were observed, with very little phenotypic

distinction between transgenics and wild types. An alternative approach to study this model would be the use of the NL-G-F mouse model. Whilst the NL-F mice harbour the Swedish and Iberian familial APP mutations, the NL-G-F mice also carry a third additional mutation from an Arctic kindred, and develops plaque pathology as early as 3 months, but still without overexpression [98]. The use of this transgenic line would seem more practical whilst still presenting a realistic model of disease progression, and may thus be more useful in understanding the glymphatic changes that precede amyloid accumulation. Alternatively, a carefully timed older cohort of NL-F mice with slightly more advanced pathology may be worth studying. This may provide a view of glymphatic changes during the onset of endogenous A β accumulation. Given the logistics required to procure, breed, age and genotype these mice, it was infeasible to schedule these follow up experiments within the duration of this research programme.

With the ups and downs of this study, aquaporin-4 profiles were not characterised in this study. However, given the evidence presented earlier in this thesis and that available in the body of literature, studying the molecular signature of aquaporin-4 in mouse models of AD and in human brains may act as a conduit for glymphatic changes in the brain. In doing so, it may be possible to glean a better understanding of the relationship between altered clearance mechanisms and the onset of AD brought about by the hallmark accumulation of A β and tau lesions.

7. Relationships Between Alzheimer's Disease Pathology and Aquaporin 4 in Humans

This chapter extends the theme of this thesis into human brain, by studying aquaporin-4 profiles in Alzheimer's disease and assessing its relevance to the development of human pathology.

7.1 Summary

There is currently limited evidence that pertains to the function of the glymphatic system in the human brain. Given the invasive nature and challenging experimental set up required for dynamic imaging of the glymphatic system in animal models, quantifying glymphatic changes during Alzheimer's disease progression in human subjects is currently infeasible. With the abundance of evidence showing the role of aquaporin-4 in maintenance of brain homeostasis and glymphatic function, probing this water channel provides a surrogate measure for gauging glymphatic function and possible perturbances to this system in the human brain. Here, by studying aquaporin-4 alongside the gold standard neuropathological confirmatory hallmarks of the disease, amyloid- β and tau, some barriers to studying changes to glymphatic components in humans are partially overcome. Its implication in the human disease is probed by comparing histological measures in Alzheimer's, cognitively impaired and cognitively normal subjects. Additionally, the possible role of polymorphic changes in the aquaporin-4 gene in humans is examined, and changes to dystrobrevin, a protein linked to aquaporin-4, is investigated in mouse models.

The work in this chapter was carried out in the laboratory of Jeffery Iliff during a collaborative research placement at Oregon Health and Science University, USA. I would like to thank Randy Woltjer for preparing the human brain sections and guiding the hippocampal ROI drawings, Natalie Roese for performing the wet laboratory work on these human tissues and Marie Wang for harvesting the mouse tissue used in these experiments prior to the commencement of my placement.

7.2 Introduction

With the desperate lack of disease modifying treatments for Alzheimer's Disease (AD), and no clear indication as to what brings about sporadic AD, much is yet to be resolved on disease onset and modification. The failure of clearance of amyloid beta ($A\beta$) causing build-up, and the prion-like spread of tau and accumulation into neurofibrillary tangles (NFTs), are research themes that provide targets of significant interest. The glymphatic system has been highlighted as a clearance pathway for $A\beta$ [151] and tau [184] via exchange between cerebrospinal fluid (CSF) and interstitial fluid (ISF). Experiments in mouse models have provided evidence that these pathogenic molecules are participants in this clearance pathway, and that aging can deplete the dynamics of this system [183]. This therefore implicates glymphatic clearance as a potential target for the understanding and treatment of AD. Readily visualising this system *in vivo* requires the translation of contrast-dependant imaging techniques which pose several significant hurdles – performing long serial magnetic resonance imaging (MRI) scans in humans is impractical and the administration of contrast has clinical limitations. Furthermore, if arterial pulsations drive inflow [156], then humans would be expected to have slower dynamics than rodents, given the significantly lower heart rate, significantly larger brain volume and differential CSF production rates compared to rodents [240]. Indeed, the precise relationships between these parameters and glymphatic function remain to be seen.

Limited studies exist in demonstrating glymphatics in humans [241–243]. In one study glymphatics were measured in humans with idiopathic normal pressure hydrocephalus, a neurodegenerative disease which relies on CSF diversion as a treatment method. When a bolus of contrast agent gadobutanol was intrathecally administered, they observed the inflow of contrast along leptomeningeal arteries in both patient and healthy control groups, but delayed parenchymal enhancement in the patient cohort [241]. Interestingly, enhancement peaked overnight, which is in line with observations reported in rodents, where sleep was an enhancer of glymphatic function [182]. In another study tracing the draining route of CSF to peripheral lymphatics via glymphatic transit, cervical lymphatic enhancement of

galdobutorol coincided with enhancement in the parenchyma, and not ahead of this time, indicating that CSF was not directly draining into the lymphatic system [242]. These human experiments pave the way for the study of human glymphatic function.

Before these experiments can be extended to the more challenging scenario of AD, it is prudent to study the cellular and molecular components in isolation. Aquaporin-4 (AQP4) is a water channel known to modulate the dynamics of exchange between CSF and ISF. If glymphatics are altered during pathology in the mouse brain, and aquaporin-4 is a key mediator of these alterations [151], then probing AQP4 in human tissue offers a good starting point. Astrocytic AQP4 in rodents is highly polarised to the brain vasculature, but the distribution profile in humans is markedly different. The degree of polarisation to the end foot in humans is 1/3rd of that in mice and parenchymal astrocytic AQP4 expression is higher [244]. It is conceivable that this difference between species would change fluid exchange dynamics.

Loss of perivascular AQP4 associated with plaque formation has been shown in a mouse model of AD [244]. Additionally, recent work in human post mortem brains have shown that AQP4 in the cortex in AD brains is less polarised, and that expression patterns change in the aging human brain [205]. Genetic studies in human subjects with AD have revealed that single nucleotide polymorphisms (SNP) in AQP4 may be predictive of AD status as they show significant associations with AD biomarkers [245]. In particular, one SNP known as rs3763043, is emerging in ongoing studies as a significant candidate for AD prediction (data unpublished, personal communication J. Iliff, 2019). This may allude to a change in the astrocytic end foot profile of AQP4, and as such, associated end foot proteins are also of interest. One such candidate, dystrobrevin (DTNA), part of dystroglycan anchoring complex (DAC) which anchors AQP4 to the membrane (Figure 43), has also emerged as a gene of interest. Recent genetic and expression studies have revealed that DTNA shares a similar developmental expression profile to AQP4 [246], and hippocampal expression of DTNA in AD subjects is elevated, with this elevation being associated with P-tau pathology in the

temporal cortex [247]. Furthermore, SNPs of DTNA are also beginning to show associations with several AD biomarkers (data unpublished, personal communication J. Iliff, 2019).

In this work, these observations are extended upon by novel histological examination of human brain slices. Firstly, A β and tau pathologies are measured using a more comprehensive method than clinicopathological staging, by taking a region-by-region direct quantification approach in areas of interest specific to AD. Next, AQP4 is quantified for expression and polarisation in the same regions and subjects. These measures are then cross examined to establish regional relationships between AQP4 and AD pathology. The data is also interrogated to establish if SNPs in AQP4 can be predictive of AD pathology in the human brain. In addition, changes in DTNA during aging and during AD pathology are examined in mouse models, to build upon my findings from human brain samples.

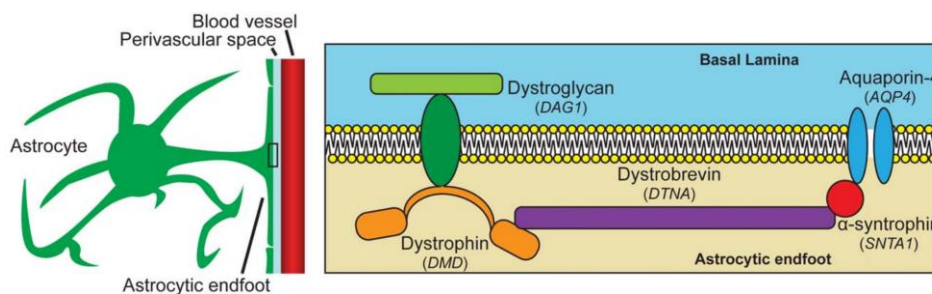


Figure 43. Schematic representation of the dystroglycan anchoring complex and associated end foot elements, including aquaporin-4 and dystrobrevin. Reproduced from Simon et.al, 2018 [246].

7.3 Methods

7.3.1 Human subjects and tissues

Human samples and subject clinical information (which included age, sex, Braak stage, CERAD score, clinical status, clinicopathological status and SNP genotype) were obtained from the Oregon Health and Science University (OHSU) Layton Aging and Alzheimer's Disease Centre and associated post-mortem tissue repository, the Oregon Brain Bank. All tissue came from volunteers that already signed written informed consent. All subjects

underwent brain autopsy after consent was obtained from the next of kin and in accordance with OHSU guidelines. The research protocols for these studies were reviewed and granted ethical approval by the OHSU Institutional Review Board. A total of 76 subjects, both male and female, with an age range of 75 – 105 were included in this study. For the frontal cortex analysis, 54 of the immunostained sections were successfully quality controlled and analysed and 30 underwent Western blotting due to sample availability. For the hippocampal analysis, 36 of the immunostained sections were successfully quality controlled and analysed and 20 underwent Western blotting due to sample availability.

7.3.2 Immunostaining of human brain sections

Following post-mortem processing, brains were fixed for at least 2 weeks in 10% neutral buffered formalin and dissected into regions of interest, and then embedded into paraffin blocks. Sections were sliced on a microtome at 7 μ m thickness. Tissue sections, selected from the hippocampus and the frontal cortex, were deparaffinised and treated with 10% formic acid. Antigen retrieval was performed in sodium citrate buffer (pH 6.0) in a steamer for 20 minutes. Samples were incubated in the primary antibody in 4% normal serum in PBS with 0.3% Triton X overnight at 4°C. Primary antibodies used were as follows: rabbit anti-AQP4 (1:800; Millipore; catalogue #AB3594), mouse anti-human phospho-PHF-Tau monoclonal (AT8; 1:1000; ThermoFisher; catalogue #MN1020), and mouse purified anti- β -Amyloid, 17-24 (1:800; Biolegend; catalogue# 800701). Following overnight primary incubation, sections were incubated with secondary antibody for 1hr at room temperature. Secondary antibodies used were donkey anti-rabbit Alexa Fluor 488 (1:400; Life Technologies, catalogue #A21207) and donkey anti-mouse Alexa Fluor 594 (1:400; Life Technologies; catalogue #A21202). Two batches were stained for each subject and brain region, one batch for tau and AQP4 and a second batch from a consecutive section for A β and AQP4. Slices were mounted using Fluoromount-G mounting medium containing Hoechst 33342 nuclear stain (1:10000; Molecular Probes; catalogue #H3570). Immunofluorescence imaging was performed on the Zeiss Axio Scan.Z1 fluorescent scanner.

7.3.3 Western blotting of human brain sections

Human Western blot data was available for a subset of subjects also selected for this study, and blotting was performed and quantified prior to the commencement of this project as previously described [205,247]. Briefly, frozen frontal and hippocampal sections were homogenised on ice in tissue homogenization buffer (62.5 mM Tris (pH 6.8), 10% glycerol, and 2% SDS) and ultrasonicated. Total protein content in the supernatant was quantified using the Pierce™ BCA protein assay kit (ThermoFisher catalogue #23225). 0.1% bromophenol blue and 50 mM DTT were added to the sample and denatured at 95°C for 5 minutes. 50–100 µg of samples were loaded for electrophoresis. Gels were transferred using a BioRad Trans-Blot® Turbo™ Transfer System. Primary antibody used was rabbit anti-AQP4 (1:500, Millipore catalogue# AB3594) and secondary antibody used was anti-rabbit horseradish peroxidase (1:1000; GE Healthcare catalogue #RPN4301). Transferred blots were imaged on a BioRad ChemiDoc™ Touch Imaging System. Images were background subtracted and band intensities extracted using FIJI ImageJ software (version 1.52i). Bands were normalised to a β -actin loading control (1:1000, Novus Biologicals catalogue # NB600-501) and normalised values for each blot corrected against a nominated running control for each cohort. An average of two replicates for each sample was used. Quantification of the expression of the two isoforms by Western blot has also previously been described by this laboratory. This was performed by taking the dual band near the 35kDa mark, AQP4-M1 was defined as the upper band and AQP4-M23 was defined by the lower band [205].

7.3.4 Manual counting of plaques and tangles

Micrographs were analysed using FIJI ImageJ software (version 1.52i) and the investigator was blinded to subject dementia status. For the cortex, 12 regions of interest (ROI) that were a 1000 x 1000 pixels were placed across the section (Figure 44 A), with 6 spread across the frontal cortex grey (FCG) matter and 6 across the frontal cortex white (FCW) matter. Composite micrographs were then separated into their single channel images for analysis. Each ROI was then extracted and a grid placed across it for ease of counting. For the sections stained for A β , the number of dense core, diffuse and cerebral amyloid angiopathy plaques

were tallied using the manual cell counter function and included as a total count per ROI. The ROI was then converted into mm² area and the total counts were converted to calculate counts per mm². These were averaged across the 6 ROIs to give each subject a single plaque count value. For the hippocampus, ROIs were drawn in the CA1, CA2 and CA3 regions by an experienced pathologist (Figure 44 B). Due to the availability of section, orientation of cutting and section quality, only a subset of hippocampal sections were analysed. Dense core, diffuse and cerebral amyloid angiopathy plaques were tallied using the manual cell counter function and included as a total count per ROI. Each ROI was then converted into mm² area and the plaque counts converted to present them as counts per mm² for CA1, CA2 and CA3 regions separately.

The method was then replicated across the sections stained for tau. ROI placement had to be manually adjusted to account for locational discrepancies between consecutive sections and preparations. FCG and FCW tau counts were presented as counts per mm² across an average of 6 grey matter ROIs and 6 white matter ROIs per subject. Hippocampal CA1, CA2 and CA3 regions were presented as counts per mm² for each region.

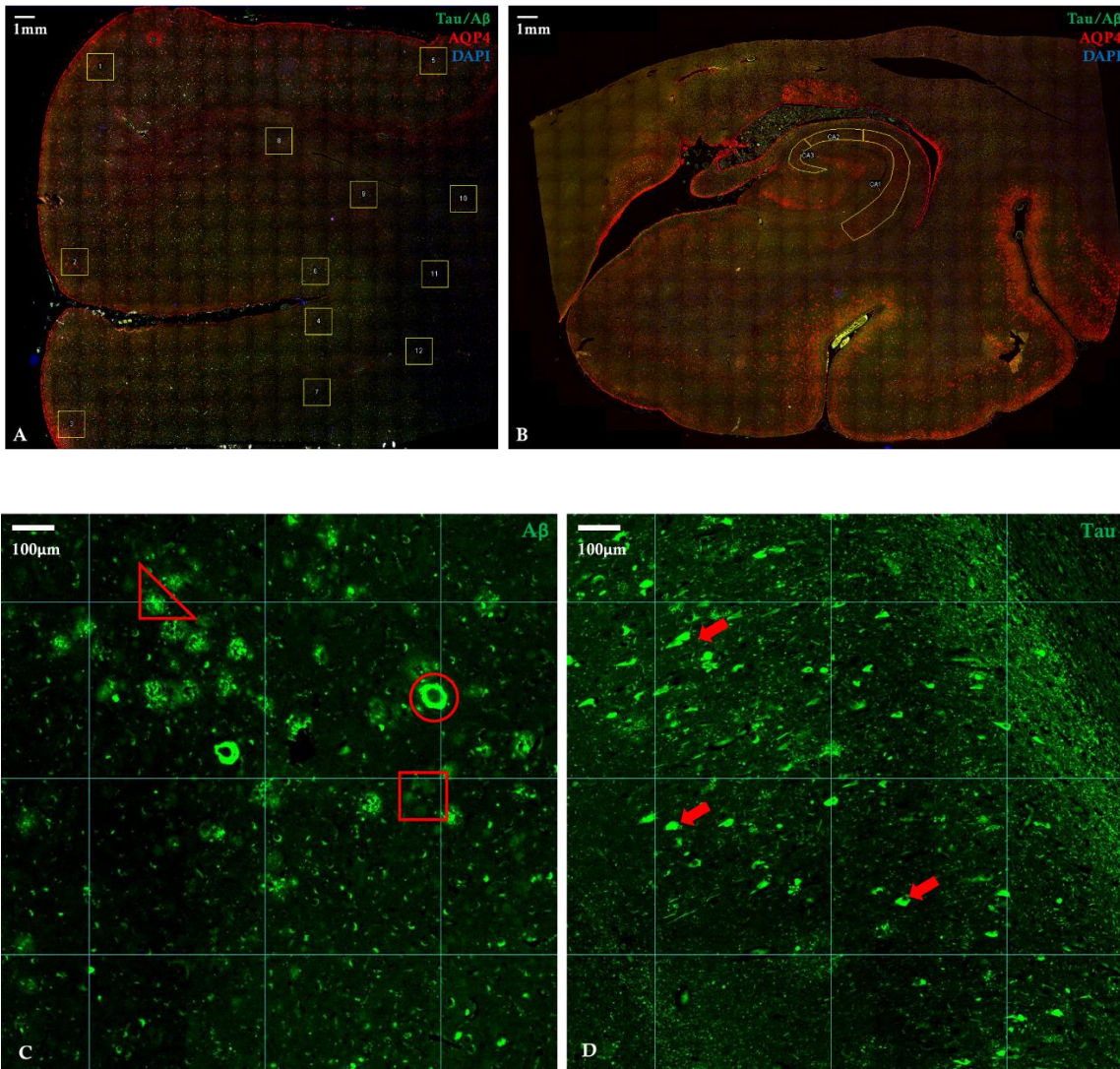


Figure 44. Widefield representative composite (red, green, blue) micrographs of human sections stained for AQP4 (red), nuclear stain DAPI (blue) and tau or A β (green). Consecutive sections were stained for either tau or A β . (A) Frontal cortex. Yellow squares indicate the 1000 x 1000 pixel ROI placements used for analyses: 6 in grey and 6 in white matter). (B) Hippocampus. Yellow ROIs indicate the placement of CA1, CA2 and CA3 regions. (C) Zoomed in view of green channel within one square ROI on A β stained section. Red triangle highlights a dense core plaque, red square highlights a diffuse plaque and red circle indicates CAA. (D) Zoomed in view of green channel within one square ROI on tau stained section. Red arrows indicate NFTs. A blue grid is placed for counting efficiency.

7.3.5 Threshold analysis of aquaporin-4

The tau-stained batch was selected for the AQP4 analysis, except where a micrograph was not of sufficient quality for analysis as determined by the blinded investigator, in which case the A β -stained section was used. Composite micrographs were separated into their respective channels, and ROIs used in the tau and A β analysis opened on the red channel. ROIs were occasionally moved in instances where the red channel section was out of focus. Each ROI

was duplicated and the mean unthresholded intensity and area was measured. A threshold was then applied to highlight the edges of vessels, which was designated as the vessel threshold, and the minimum value at this threshold recorded. A second threshold was then extended to capture the cellular threshold including the intensity at the fine processes of astrocytes where they could be readily identified. This was designated the cellular threshold and the mean value and area of this threshold was recorded. Area coverage and AQP4 polarisation ratio was calculated as described below in Figure 45. The average of 6 ROIs were taken for FCG and FCW per subject. Single values were obtained per subject for the hippocampal CA1, CA2 and CA3 regions.

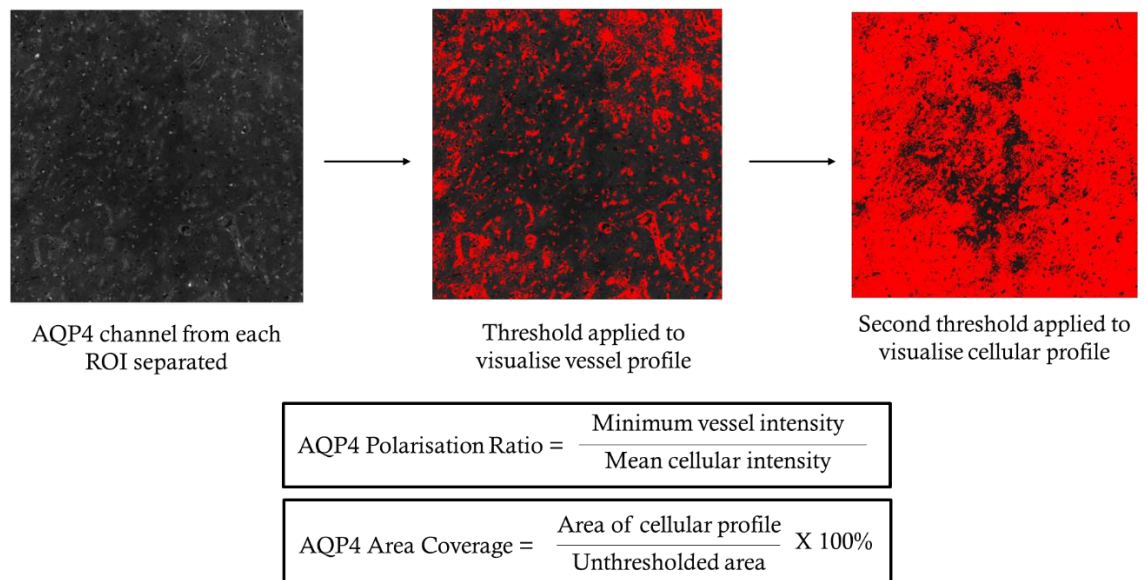


Figure 45. Workflow used for analysing AQP4 stain on micrographs and the formulae used to compute the AQP4 measures investigated in these analyses.

7.3.6 Mice and tissue collection

All animals were treated in accordance with National Institute of Health (NIH) Guidelines for the Care and Use of Animals. All procedures were performed under approved Institutional Animal Care and Use Committee (IACUC) protocols. For the aging study, male and female wildtype (WT) C57BL6 mice that were 3 months (n = 9) and 15 months (n = 7) old were used. For the study of AD pathology, male and female Tg2576 (Tg) mice at

12 months (n = 5) on a C57BL6 background and WT C57BL6 (n = 5) were used. Mice had unrestricted access to food and water, and were housed under automatically controlled temperature, humidity, ventilation and 12h light/dark cycle settings.

Brains were perfused with saline and 1U/ml heparin, and then hemisected. One hemi section was snap frozen by dropping it in isopentane supercooled on dry ice, to maintain fresh tissue for Western blotting. The other hemi section was drop fixed in 4% paraformaldehyde overnight. Following fixation, it was fully sectioned coronally on a cryostat at 50 μ m thickness and cryoprotected in sucrose for long term storage.

7.3.7 Western Blotting of mouse brain samples

For Western blotting, frozen brains were homogenised on ice in Pierce™ RIPA lysis buffer (ThermoFisher catalog #89900) containing proteinase and phosphatase inhibitors and ultrasonicated for 5 minutes. Homogenates were spun at 1800 rpm for 5 minutes to remove cellular debris and the supernatant collected. Total protein content in the supernatant was quantified using the Pierce™ BCA protein assay kit (ThermoFisher catalog #23225). Equivalent volumes for 60 μ g of protein per sample were then prepared for loading in a mix of 5 μ l NuPAGE™ LDS sample buffer (ThermoFisher catalog #NP0007), 2 μ l NuPAGE™ sample reducing agent (ThermoFisher catalog #NP0009) and purified water made up to a total loading volume of 20 μ l. Preparations were denatured at 95°C for 5 minutes, allowed to reach room temp and then loaded on to Bio-Rad Mini-PROTEAN® TGX Stain-Free™ precast gels (Bio-Rad catalog #456-8085) in a Bio-Rad Mini Trans-Blot® Cell tank filled with Tris-glycine SDS buffer, immersed in ice. 5 μ l of 10 to 180 kDa PageRuler™ prestained protein ladder (ThermoFisher catalog #26616) was run alongside the samples on each gel. Gels were run between 90V and 120V for a total time of 1.5 hours. Proteins were then transferred to a mini PDVF membrane using the BioRad Trans-Blot® Turbo™ transfer system at 25V, 1A for 30 minutes. Following transfer, membranes were split between the 85 and 50 kDa mark. The top section was incubated with mouse anti-DTNA (1:500, BD catalogue #BDB610766) and the bottom section was incubated with mouse anti- β -actin (1:1000, Novus Biologicals catalogue # NB600-501) in 3% milk overnight. Primary

antibodies were washed with Tris-buffered saline with 0.1% Tween-20 (TBS-T) and anti-mouse horseradish peroxidase secondary antibody (1:10,000, Jackson ImmunoResearch catalogue #115-035-003) was applied for 2 hours at room temperature. Secondary antibody was washed with TBS-T and the membranes then incubated with chemiluminescent substrates for 5 minutes. For β -actin visualisation, Pierce™ ECL Western blotting substrate (ThermoFisher catalogue #32209) was used and for DTNA, SuperSignal™ West Pico PLUS Chemiluminescent Substrate (ThermoFisher catalogue #34577) was used. Blots were imaged on the BioRad ChemiDoc™ Touch Imaging System. Using FIJI ImageJ software (version 1.52i), images were background subtracted and band intensities extracted. Bands were normalised to the loading control (β -actin) and normalised values for each blot corrected against a nominated running control for each cohort. An average of two replicates for each sample were used.

7.3.8 Immunostaining of mouse brain samples

3 sections were selected per mouse, which included cortical and hippocampal regions. Slices were mounted onto Superfrost slides, and antigen retrieval was performed using sodium citrate buffer (pH 6) with steaming for 30 minutes. Primary antibodies rabbit anti-AQP4 (1:1000; Millipore catalog #AB3594) and mouse anti-DTNA (1:50; BD catalog# BDB610766) were prepared in donkey serum and applied overnight at 4°C. The next day, primary antibodies were thoroughly washed with phosphate buffered saline with 0.1% Triton-X and secondary donkey anti-rabbit Alexa Fluor 488 (1:400; Life Technologies catalog# A21207), donkey anti-mouse Alexa Fluor 594 (1:400; Life Technologies catalog# A21202) and Hoechst 33342 nuclear stain (1:10000; Molecular Probes catalog# H3570) antibodies applied and incubated at room temperature for 5 hours. All incubations were performed manually and in a humidity tray, with minimal exposure to light. Slides were then mounted using Fluoromount medium, dried overnight and then imaged on the Zeiss Laser Scanning Confocal microscope at 20x magnification. Images were acquired by single excitation of each wavelength (separately) and channels subsequently merged. 3 ROIs were imaged per section, per mouse, within the hippocampus and the cortex (Figure 46).

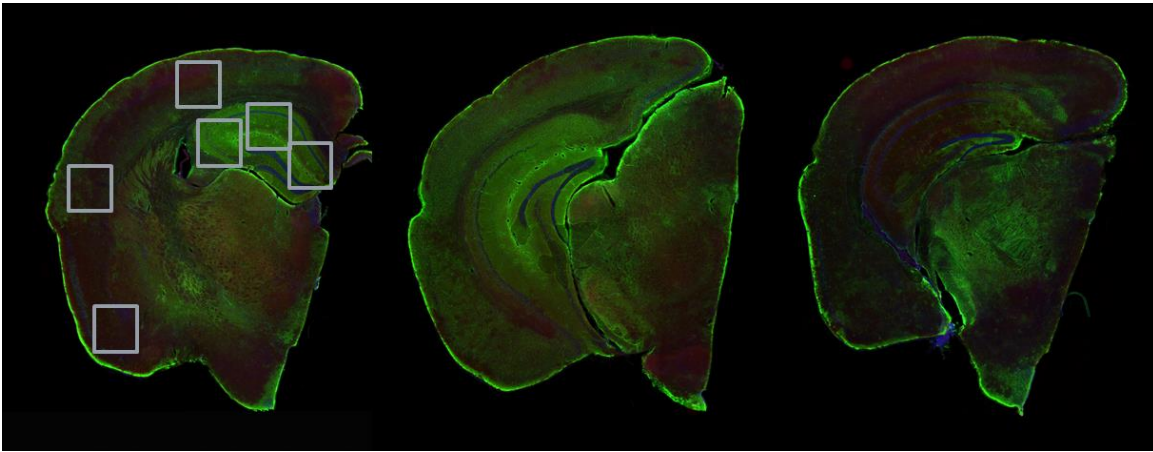


Figure 46. Widefield example micrographs of hemisections of mouse brains used for DTNA analyses. A total of three sections were stained for each mouse. 3 cortical and 3 hippocampal ROIs were placed on each section (shown as grey squares on one section in this example image). Following data extraction, the average of 9 regional ROIs were used per mouse for each measure.

7.3.1 Statistical analyses

Statistical comparisons between groups were performed via either a Mann-Whitney test, a one-way analysis of variance (ANOVA) followed by Dunn's test for multiple comparisons, or a two-way ANOVA followed by Sidak's test for multiple comparisons. A linear regression was performed for correlation analyses. Unpaired t-tests were used for single comparisons. All statistical testing was performed using GraphPad Prism (v7 for Windows, San Diego, CA, USA). All data is represented as mean \pm SEM for the n number in each group, which are detailed in figure legends.

7.4 Results

7.4.1 Measurements of plaque and NFT burden

In order to probe the sensitivity of the manual counting approach to the disease status allocated to each subject, data was assessed categorised by both clinical (in life) diagnosis – classified as “not demented” (ND), “mild cognitive impairment” (MCI) or AD, and clinicopathological (post mortem) diagnoses – classified as “probable AD” (AP) or AD (Figure 47). Using the manual counting approach, when classified by clinicopathological diagnosis, significantly elevated plaque counts were observed in the AD group in the FCG ($p < 0.0001$ AP vs AD), and hippocampal CA1 ($p < 0.0001$ ND vs AD) and CA3 ($p = 0.0014$ AP vs AD) regions. FCW was not different between groups, and hippocampal CA2, though elevated in the AD group, did not achieve statistical significance. When separated by clinical status, significant elevations in plaque counts were seen in FCG in the AD and MCI groups when compared to the ND group ($p = 0.0001$ ND vs AD; $p = 0.0058$ MCI vs AD), as well as in the CA3 ($p = 0.0086$ ND vs AD; $p = 0.0019$ MCI vs AD) region. Plaques in the CA1 region of the AD group was significantly elevated from ND ($p < 0.0001$ ND vs AD), and CA2 though elevated was not significant. FCW was not different between groups (Figure 47).

In the NFT counts, when classified by clinicopathological diagnosis, significantly elevated counts for AD were recorded in FCG ($p = 0.0034$ AP vs AD), CA1 ($p < 0.0001$ AP vs AD), CA2 ($p = 0.0001$ AP vs AD) and CA3 ($p = 0.0025$ AP vs AD) regions. FCW had no difference between groups. When categorised by clinical diagnosis, significantly elevated plaques in the AD group were seen in CA1 ($p = 0.0003$ ND vs AD; $p = 0.019$ MCI vs AD), CA2 ($p = 0.0007$ ND vs AD; $p = 0.0051$ MCI vs AD) and CA3 ($p = 0.0152$ ND vs AD; $p = 0.0122$ MCI vs AD) regions, with the counts being significantly elevated compared to both MCI and ND. By this categorisation, FCG had a trend towards increased NFTs in the MCI group, which increased further in the AD group, however, these differences did not attain statistical significance. FCW showed no significant differences between groups (Figure 47).

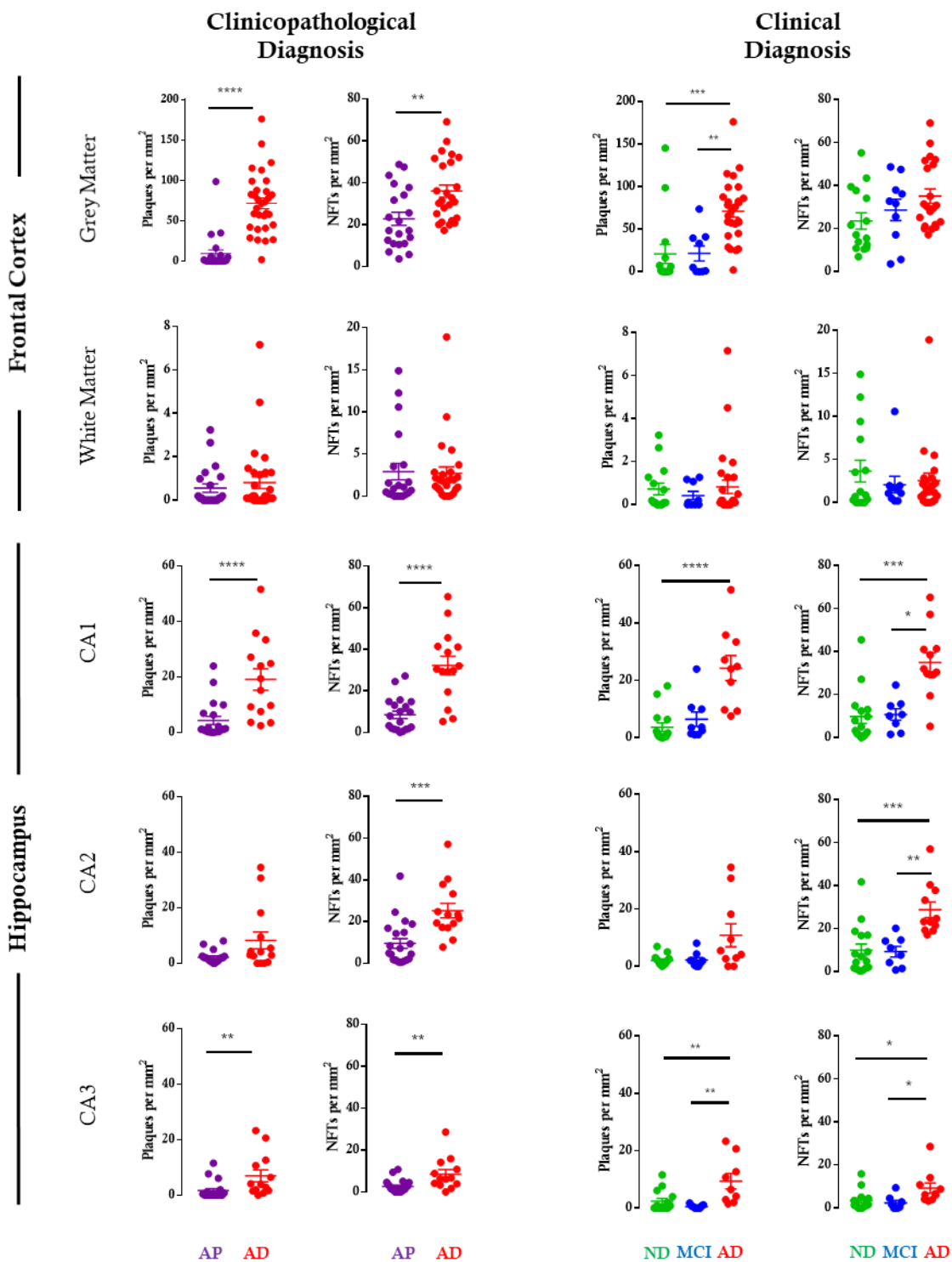


Figure 47. Manually counted plaque and NFT densities in frontal cortex grey matter, white matter and hippocampal CA1, CA2 and CA3 regions. The left panel shows data categorised by clinicopathological diagnosis: AP = Probable Alzheimer's (n = 21 frontal cortex and 20 hippocampus); AD = Alzheimer's Disease (n = 26 frontal cortex and 13 hippocampus). The right panel shows data categorised by clinical diagnosis: ND = Not Demented (n = 15 frontal cortex and 14 hippocampus); MCI = Mild Cognitive Impairment (n = 9 frontal cortex and 9 hippocampus); AD = Alzheimer's Disease (n = 27 frontal cortex and 9 hippocampus). Statistical significance denoted by asterisks: * = $p < 0.05$, ** = $p < 0.01$, *** = $p < 0.001$, **** = $p < 0.0001$.

To assess the robustness of these measures, manual counts were correlated against the clinically relevant CERAD and Braak scores. Positive correlations were observed for plaque counts in FCG ($r^2=0.4447$, $p<0.0001$), CA1 ($r^2=0.5729$, $p<0.0001$), CA2 ($r^2=0.1737$, $p=0.0142$) and CA3 ($r^2=0.2627$, $p=0.0027$) and for NFT counts in FCG ($r^2=0.1389$, $p=0.0108$), CA1 ($r^2=0.4294$, $p<0.0001$), CA2 ($r^2=0.4026$, $p<0.0001$) and CA3 ($r^2=0.2193$, $p=0.006$), thus validating these counts (Figure 48).

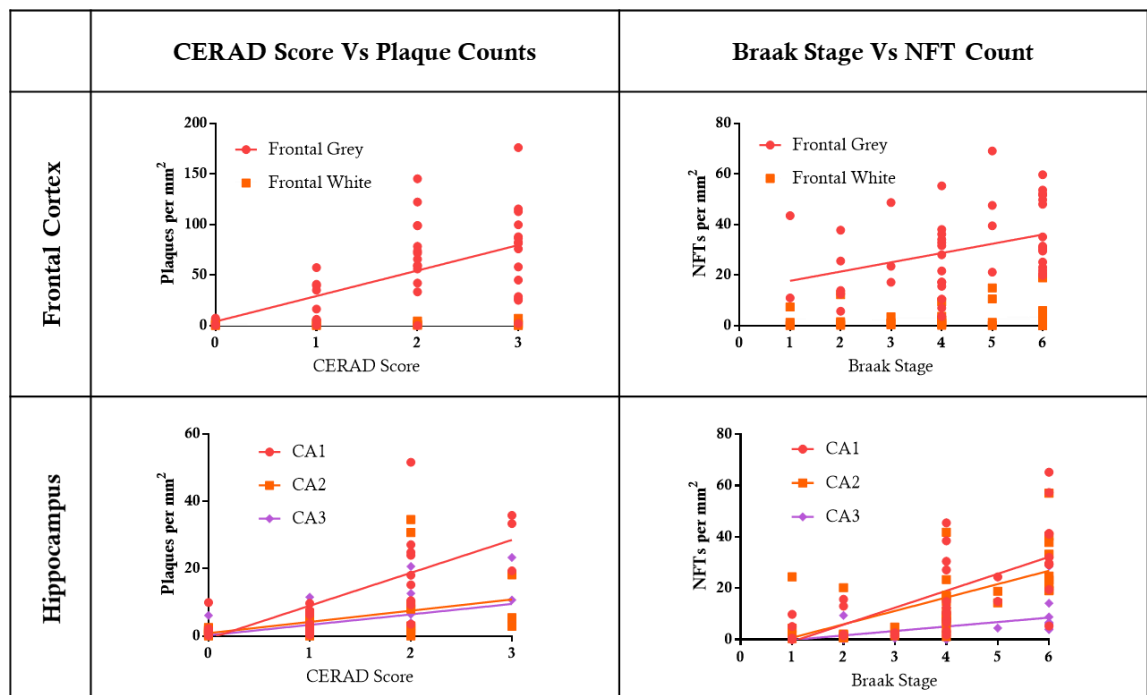


Figure 48. Manually counted pathology correlated to clinical scores. Solid line through data points indicates a significant correlation. Upper left: frontal cortex ($n = 76$) plaques vs CERAD score (frontal grey $r^2 = 0.44$, $p<0.0001$) ; upper right: frontal cortex ($n = 76$) NFTs vs Braak stage (frontal grey $r^2 = 0.13$, $p=0.01$). Lower left: hippocampal ($n = 75$) plaques vs CERAD score (CA1 $r^2 = 0.57$, $p<0.0001$; CA2 $r^2 = 0.17$, $p=0.01$; CA3 $r^2 = 0.26$, $p=0.003$) lower right: hippocampal ($n = 75$) NFTs vs Braak stage score (CA1 $r^2 = 0.43$, $p<0.0001$; CA2 $r^2 = 0.40$, $p<0.0001$; CA3 $r^2 = 0.22$, $p=0.006$).

7.4.2 Quantification of aquaporin-4

To test the AQP4 polarisation measure, a subset of ROIs were first manually scored as “polarised” or “not polarised” under a blinded analysis alongside the threshold approach (Figure 49). Following completion and unblinding, the metric (minimum vessel intensity to mean cellular intensity ratio) proved sensitive to detecting polarisation. Having verified this, all cases were subjected to the threshold analysis described above.

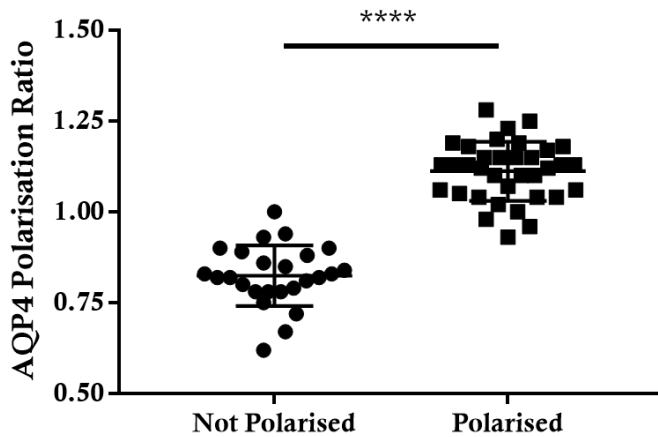


Figure 49. Test analyses of AQP4 polarisation ratio on a subset of ROIs, carried out on a mixed range of subjects with the user blinded to subject information. Based on visual intensity of the AQP4 stain at the vessels using the threshold analysis (Section 6.3.5), ROIs were classified as “polarised” or “not polarised” and ratios calculated using this threshold analysis. Of $n = 60$ square ROIs from frontal cortex grey sections analysed here, 25 were not polarised and 35 were polarised. Statistical significance denoted by asterisks: **** = $p < 0.0001$

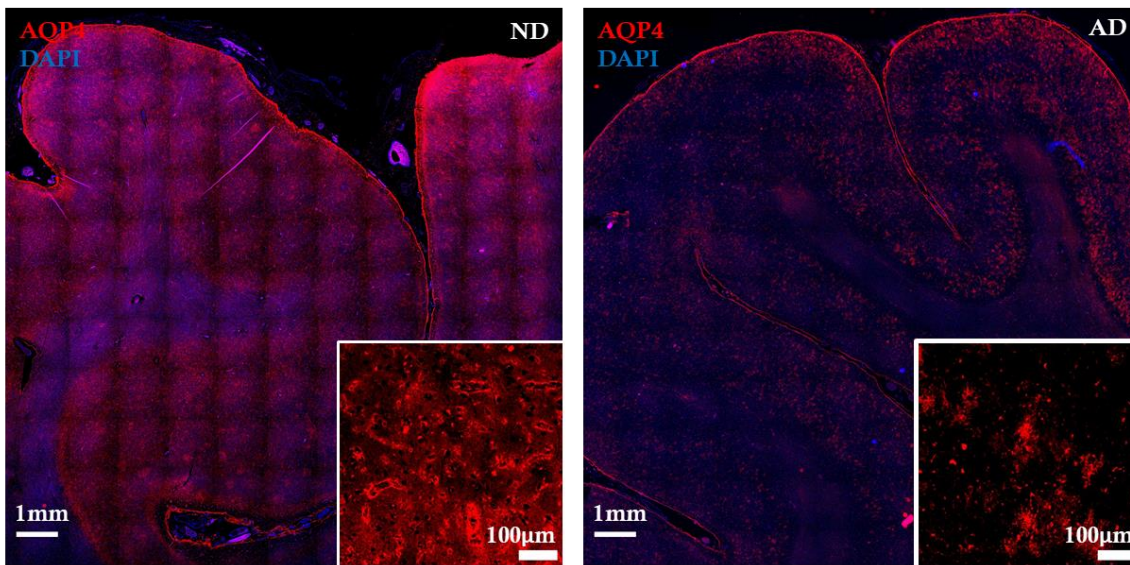


Figure 50. Composite micrographs of frontal cortex sections showing AQP4 (red) and DAPI nuclear (blue) stains. The left micrograph was taken from a representative non-demented (ND) subject and the right from an Alzheimer’s disease (AD) subject. Insets: zoomed in ROIs showing a high degree of AQP4 polarisation around vessels on the non-demented subject and depleted polarisation with patchy AQP4 staining with uniform astrocytic profiles on the Alzheimer’s disease subject.

FCG polarisation in the AD group was significantly reduced compared to ND when categorised by clinical diagnosis ($p=0.0301$) and the same was observed in the clinicopathological categorisation ($p=0.0209$), where AD polarisation was reduced compared to AP (Figure 52). Figure 50 shows an example the appearance of a very polarised

cortical section in an ND, with homogenous AQP4 expression also apparent through the cortical layers, compared to an AD individual with reduced polarisation, where a depletion of cortical AQP4 signal was also noted. Western blot data for a subset of subjects in this cohort has previously revealed no differences between AD and non-AD subjects [247]. Here, when reclassified by clinical status no differences are seen between groups (Figure 51).

No changes were observed in FCW in both categorisations. No differences in area coverage were seen between groups categorised by clinicopathological diagnosis. When classified by clinical diagnosis, in the hippocampus CA1, the MCI group had significantly reduced polarisation compared to AD ($p=0.0467$) but not ND. No other changes were observed in any other hippocampal regions in this analysis. When area coverage was measured, CA1 in the MCI group was significantly lower compared to ND ($p=0.0196$) but not AD (Figure 52).

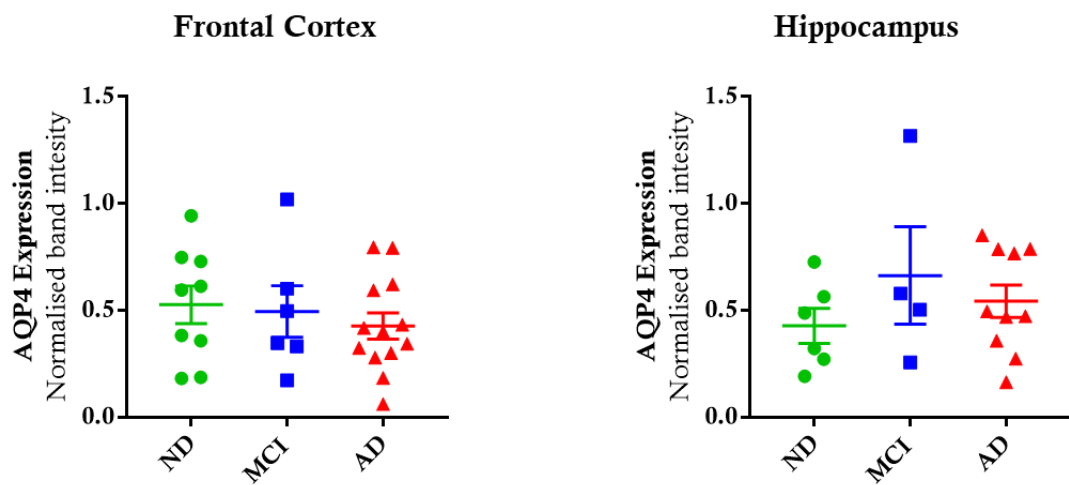


Figure 51. AQP4 expression by Western blot. Data is categorised by clinical diagnosis: ND = Not Demented ($n = 9$ frontal cortex and 6 hippocampus); MCI = Mild Cognitive Impairment ($n = 6$ frontal cortex and 4 hippocampus); AD = Alzheimer's Disease ($n = 13$ frontal cortex and 10 hippocampus).

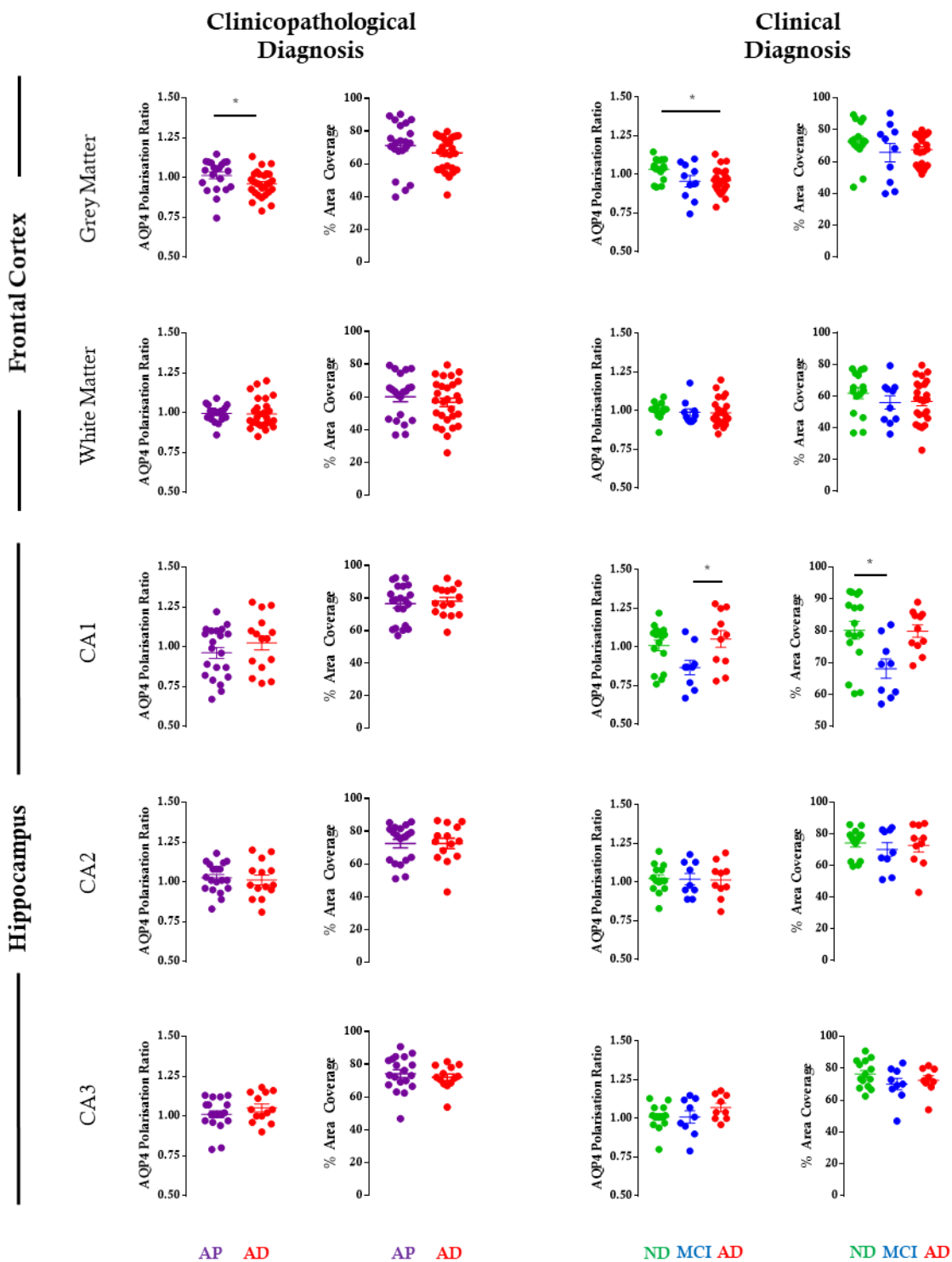


Figure 52. AQP4 polarisation and area coverage measures calculated using threshold analyses in frontal cortex grey matter, white matter and hippocampal CA1, CA2 and CA3 regions. The left panel shows data categorised by clinicopathological diagnosis: AP = Probable Alzheimer's ($n = 21$ frontal cortex and 20 hippocampus); AD = Alzheimer's Disease ($n = 26$ frontal cortex and 13 hippocampus). The right panel shows data categorised by clinical diagnosis: ND = Not Demented ($n = 15$ frontal cortex and 14 hippocampus); MCI = Mild Cognitive Impairment ($n = 9$ frontal cortex and 9 hippocampus); AD = Alzheimer's Disease ($n = 27$ frontal cortex and 9 hippocampus). Statistical significance denoted by asterisks: $*=p<0.05$.

Correlating AQP4 measures against measures of plaque and NFT counts revealed that there was a negative correlation between NFTs and area coverage in the FCG (Figure 53; $r^2=0.14$, $p=0.0113$). Next, these data were also correlated to the different isoforms of AQP4 quantified by Western blot in a previous study. The purpose of this exploratory analysis was to determine if protein expression levels had relationships to the novel measures of AQP4 polarisation and coverage developed here in this study. When AQP4 measures were correlated to Western blot expression of the different isoforms, a positive correlation was seen between polarisation ratio and total AQP4 ($r^2=0.3123$, $p=0.0037$), M1 ($r^2=0.3999$, $p=0.00007$) and M23 ($r^2=0.2307$, $p=0.0151$) isoforms. Area coverage positively correlated with the M1 isoform ($r^2=0.1674$, $p=0.0423$) but not with M23 or total AQP4 (Figure 53).

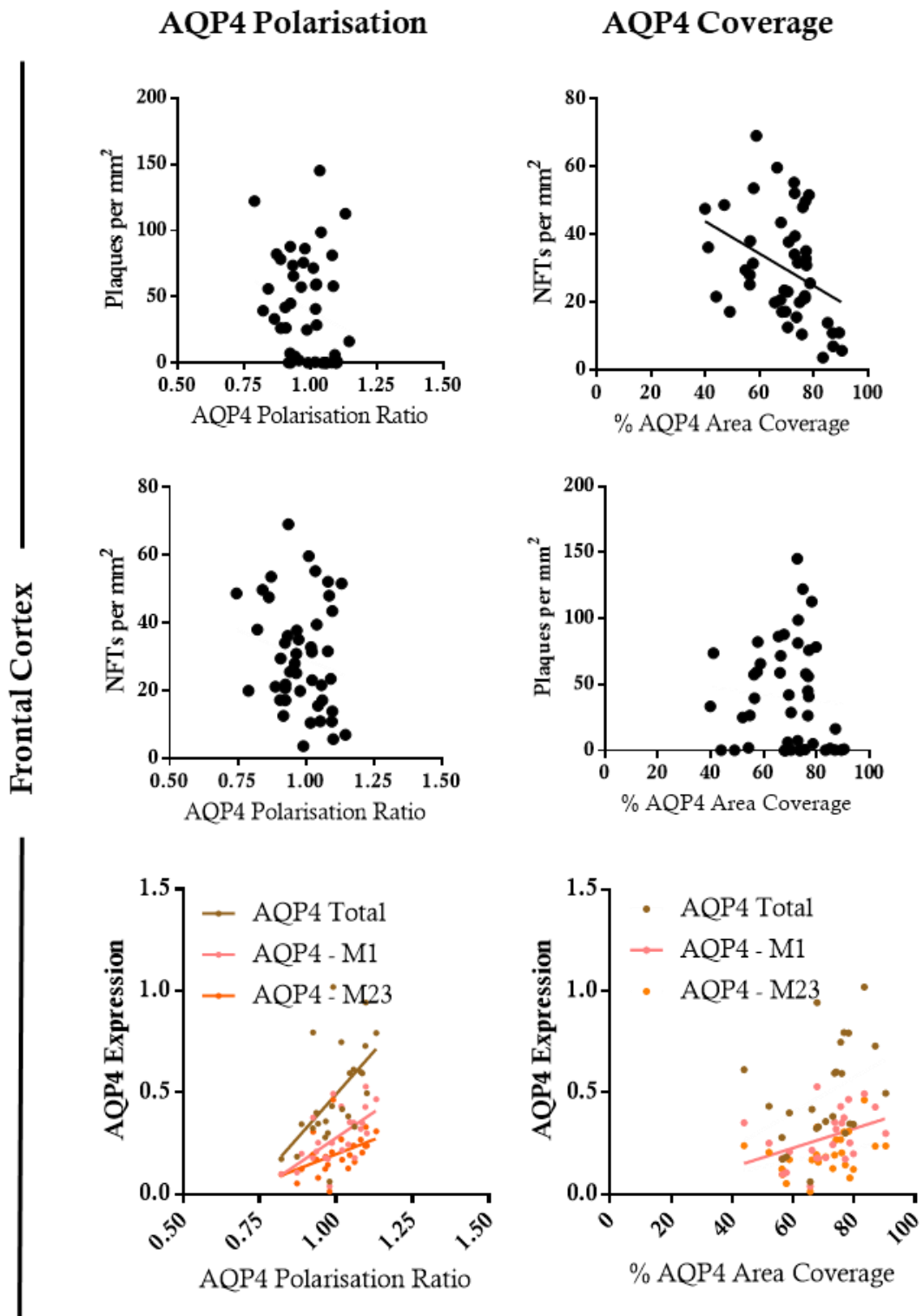


Figure 53. AQP4 polarisation and area coverage measures in the frontal cortex grey matter correlated to manual plaque counts ($n = 53$), manual NFT counts ($n = 46$) and AQP4 expression by Western blot ($n = 30$). Solid line through data points indicates a significant correlation. Upper right: NFT counts vs AQP4 coverage ($r^2 = 0.14$, $p = 0.01$). Lower left: AQP4 expression vs AQP4 polarisation (AQP4 total $r^2 = 0.31$, $p = 0.004$; AQP4-M1 $r^2 = 0.40$, $p = 0.0007$; AQP4-M23 $r^2 = 0.23$, $p = 0.02$). Lower right: AQP4 expression vs AQP4 coverage (AQP4-M1 $r^2 = 0.17$, $p = 0.04$).

7.4.3 Testing relationship to the rs3763043 SNP

To test if the rs3763043 SNP was influential on AQP4 and dementia status, subjects were assessed by SNP status and by dementia status (ND vs MCI & AD). rs3763043 SNP carriers had an increase in AQP4 polarisation which was not significant (Figure 54 A). When subjects were split by dementia status, MCI & AD subjects collectively categorised as the demented group (“cognitively impaired” - CI) had significantly increased polarisation in the FCG compared to undemented (“not demented” - ND) subjects used as controls (Figure 54 B; $p=0.0114$). AQP4 coverage showed no differences here (Figure 54 C). When burden of pathology was assessed by this categorisation, plaque load and NFT burden was lower in the rs3763043 SNP group within the demented cohort, but this did not achieve statistical significance (Figure 54 D & E).

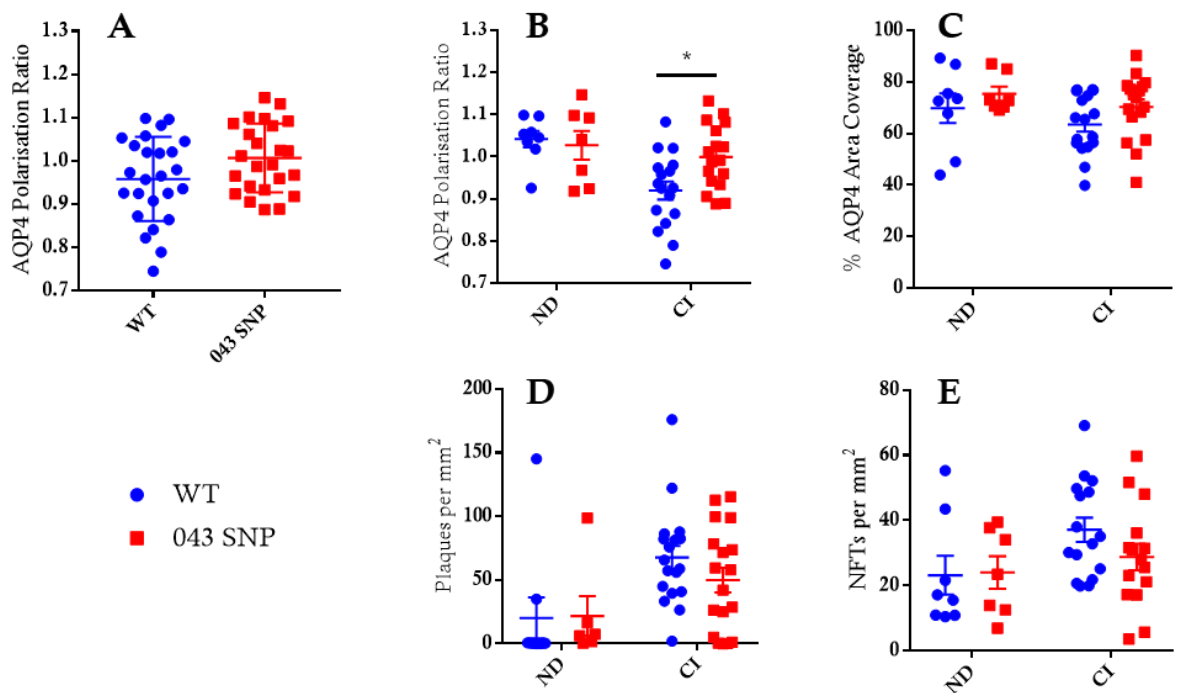


Figure 54. AQP4 measures and pathology by SNP status. (ND = not demented; CI = cognitively impaired which includes Mild Cognitive Impairment and Alzheimer's Disease subjects. 043 = rs3763043 SNP carriers; WT = wild type for rs3763043). (A) AQP4 polarisation by SNP status. (B – C) AQP4 measures by SNP and dementia status. (D – E) Plaque and tangle pathology by SNP and dementia status. Statistical significance denoted by asterisks: $*=p<0.05$.

7.4.4 Probing DTNA changes during aging and A β pathology in the mouse brain

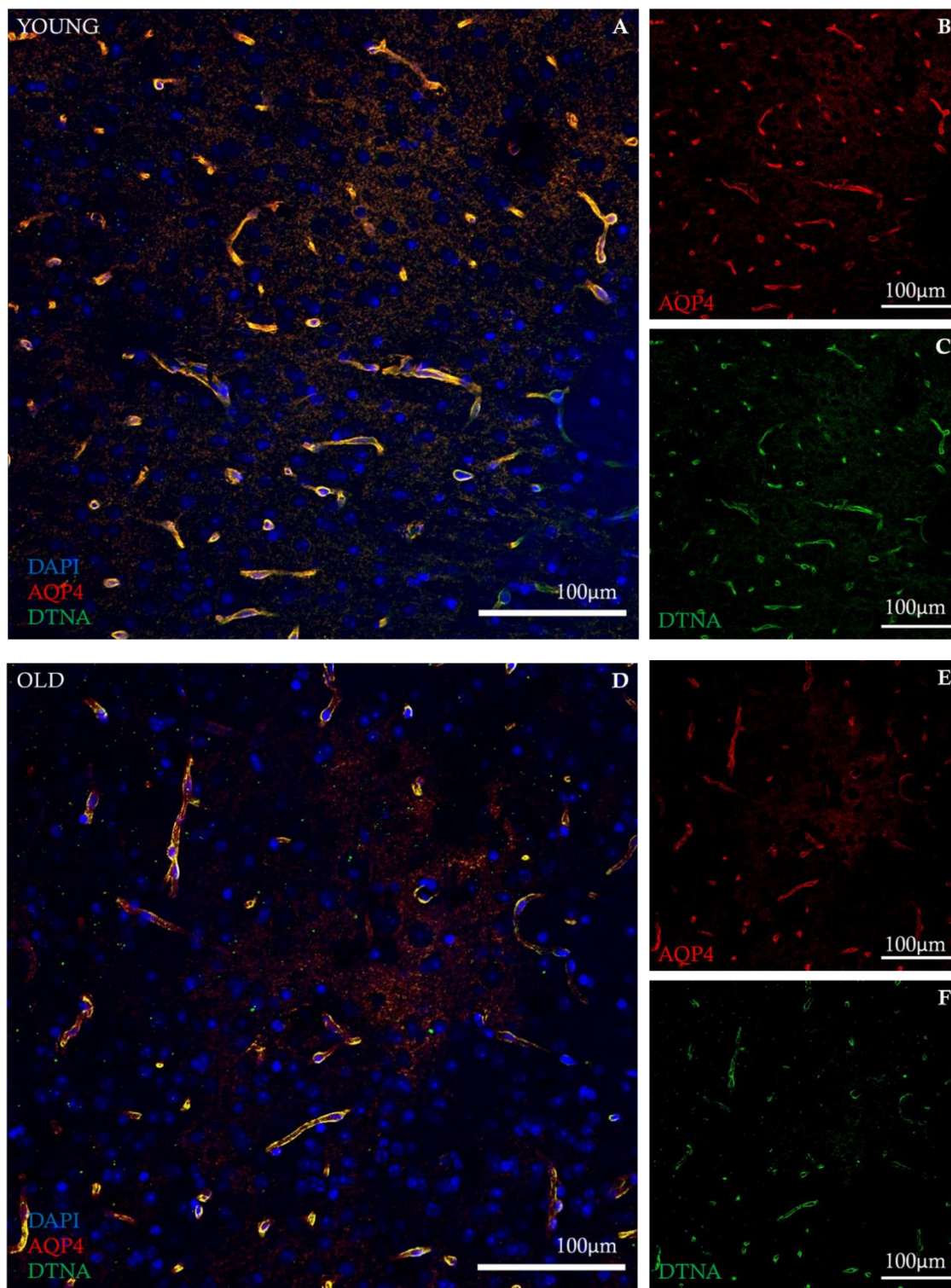


Figure 55. Representative micrographs of young (A-C) and aged (D-F) mouse brain sections stained for AQP4 (red), nuclear stain DAPI (blue) and DTNA (green). Composite (red, green, blue) images (A, D) show merged channels and single channel images (B, C, E, F) show the same view of the individual stains.

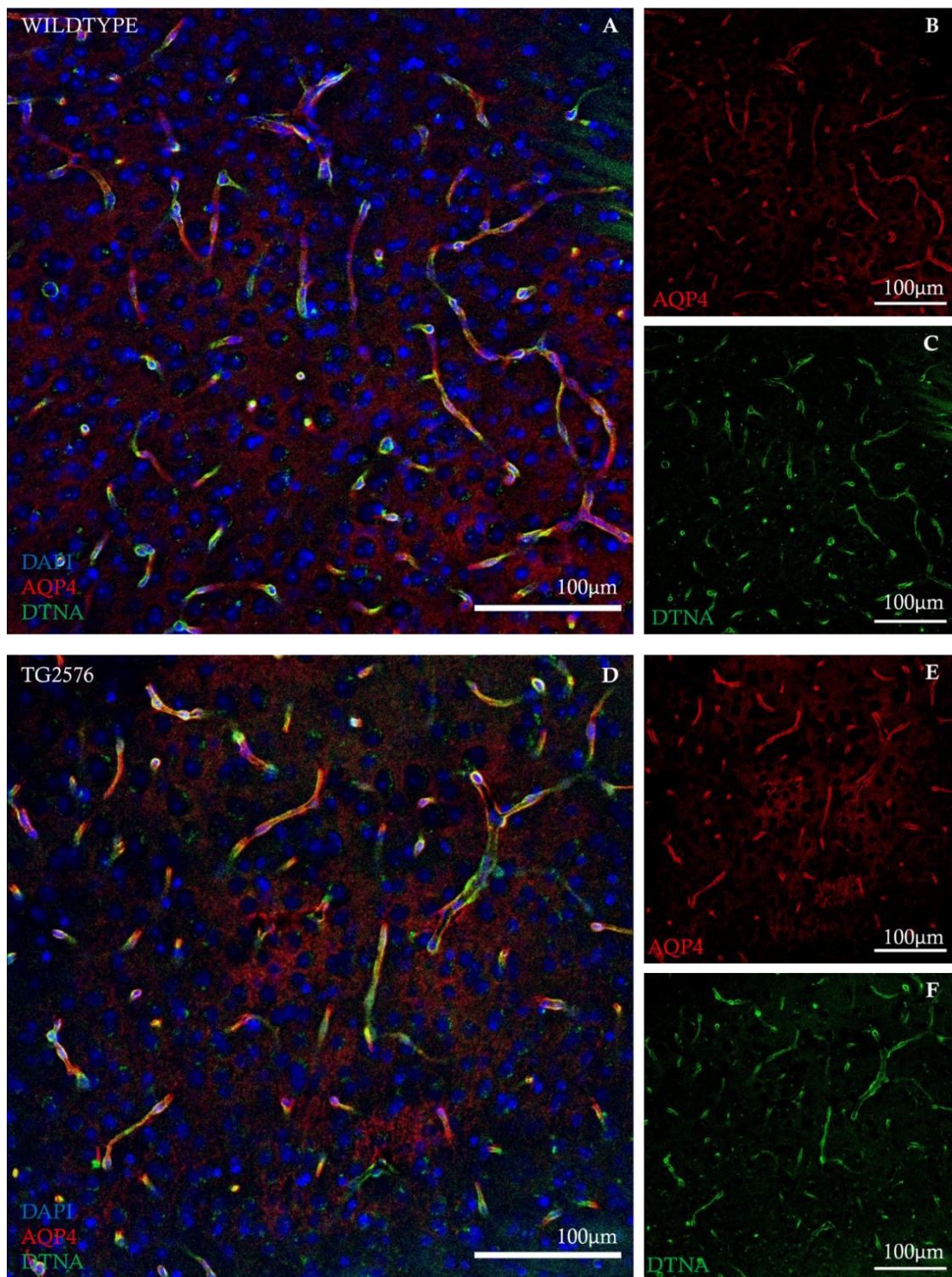


Figure 56. Representative micrographs of wildtype (A-C) and Tg2576 (D-F) mouse brain sections stained for AQP4 (red), nuclear stain DAPI (blue) and DTNA (green). Composite (red, green, blue) images (A, D) show merged channels and single channel images (B, C, E, F) show the same view of the individual stains.

DTNA expression and polarisation was assessed in a cohort of Tg2576 APP mice. Figures 55 to 56 show representative immunofluorescence images for each cohort. No differences in

polarisation were observed between young and old mice (Figure 57 D, F). However, a reduction in overall whole brain expression was seen in the aged mice in the Western Blot analyses (Figure 57 B; $p=0.0079$). A reduction in polarisation of DTNA was observed in the cortex of Tg2576 mice (Figure 57 E; $p=0.0465$), but not in the hippocampus (Figure 57 G). Overall expression of DTNA was not different between the WT and Tg2576 groups (Figure 57 C).

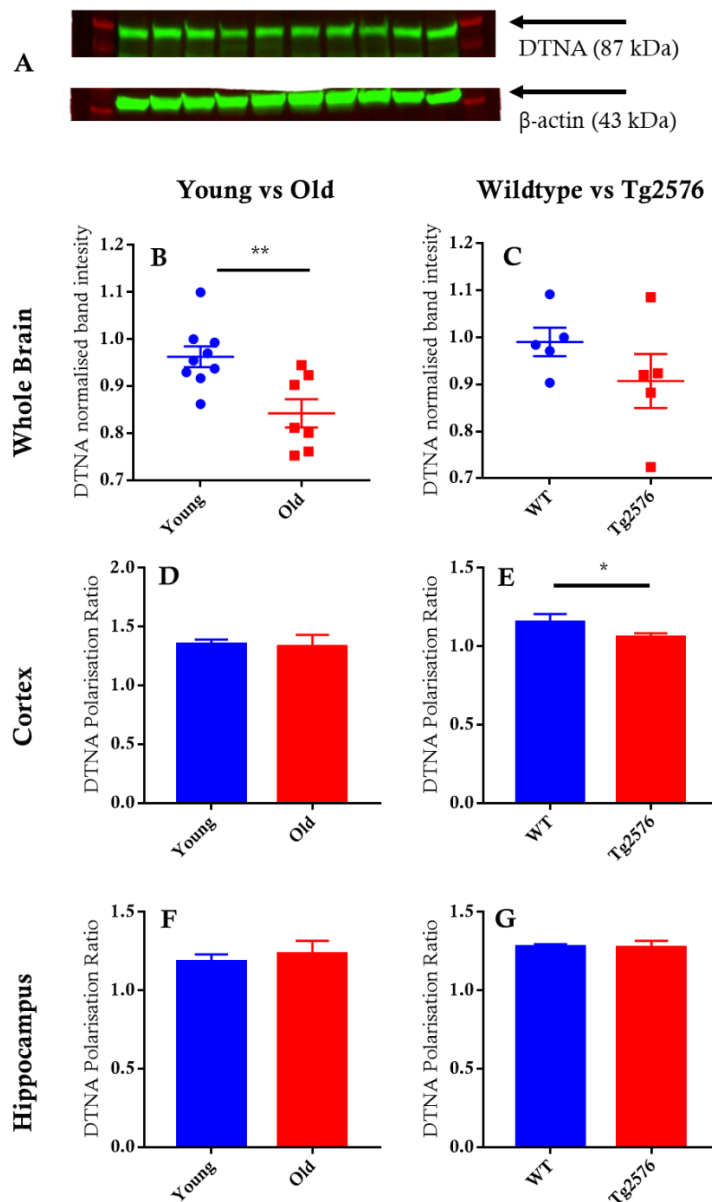


Figure 57. (A) A single representative image of a Western blot indicating bands for DTNA and β -actin loading control, presented as an example blot and taken from the wildtype vs Tg2576 analysis batch. (B) Whole brain DTNA expression by Western blot quantified in young vs aged mice and (C) wildtype vs Tg2576 mice. (D) DTNA polarisation in the cortex and (F) hippocampus of young and aged mice. (E) DTNA polarisation in the cortex and (G) hippocampus of wildtype and Tg2576 mice. Statistical significance denoted by asterisks: $*=p<0.05$, $**=p<0.01$.

7.5 Discussion

In this section of my thesis, the work attempted to undertake a paradigm shift in the methodological approach to the study of glymphatic clearance in AD. By moving from preclinical mouse work to the clinical human condition I attempted to begin to bridge the gap between mouse and human studies of the glymphatic system. Possible changes to glymphatic function in human AD was probed by examining AQP4 profiles in human subjects diagnosed with AD, MCI and undemented individuals, and correlating these measures to A β and tau burden with precision. AQP4 polarisation was found to be reduced in the frontal cortex of AD subjects, and NFT burden inversely correlated with AQP4 coverage. Carriers of the rs3763043 SNP who had been diagnosed with MCI or AD had increased AQP4 polarisation in the frontal cortex.

The detailed histological characterisation of A β and tau employed here enabled a thorough evaluation of the relationship between these recognised correlates of AD and molecular features that are mechanistically important to glymphatic function. This approach also aimed to get a more refined value of pathology than the gold-standard of Braak and CERAD scoring, which takes a more global qualitative approach based on select brain regions [15,16]. In doing this, a more direct correlation to AQP4 was enabled, as the same smaller regions could be interrogated for AQP4 measures against A β and tau burden. Manual counting of a range of smaller ROIs has notable benefits. First, it does not assume uniform pathology across the whole anatomical region in question. By taking a more direct region by region count and averaging across multiple regions, it provides each subject with a value of A β and tau burden that is more representative as to the discreet, regional nature of the pathology across the brain. When these measures were categorised by clinicopathological status, it reliably separated confirmed AD subjects from probable AD on several measures, including FCG, CA1 and CA3 for plaque burden and FCG, and all CA regions for NFT burden. These counts were appraised by their positive correlation to CERAD and Braak scores. Of interest were the clinically diagnosed MCI and ND subjects who showed a high level of pathology that was histopathologically comparable to AD subjects. It is plausible that these subjects

represent the range of the AD pathological continuum, and this supports the notion that some individuals are protected from the neurotoxic effects of AD pathology. Previous studies have reported that high-pathology nondemented individuals do not suffer synaptic loss to the degree that symptomatic AD sufferers do [248], preserve brain morphology in the hippocampal regions usually vulnerable to neuronal loss [249], and have larger brains with higher volumes even in the face of pathology [250]. It is therefore conceivable that these individuals benefited from having a higher brain reserve, that is, they possessed greater brain volume or larger numbers of neurons that made them less likely to present with clinical outcomes. Or perhaps, they had a higher cognitive reserve, where their neural networks were more capable of coping with or compensating for the pathological changes that were occurring and prevented them from manifesting as clinical AD [39]. This could be further investigated by correlating pathological burden against measures of CNS volume, hippocampal volume or cognitive scores. However, in the prior data acquisition phase of this study, brain volume data were not collected for MCI subjects within this cohort and insufficient data on cognition was available for the already small number of MCI subjects, and thus could not be corroborated.

AQP4 expression was assessed in a subset of subjects and showed no differences in expression by Western blot, but a reduction in perivascular polarisation was observed in the frontal cortex of AD subjects. This is in keeping with previous findings. In mice, glymphatic impairment has been reported in the presence of A β pathology [217]. Loss of end foot processes along with reduced AQP4 polarisation has also been observed in the presence of CAA in both mice and humans [251]. Zeppenfeld *et al.* showed that loss of cortical perivascular AQP4 was associated with AD status and they suggested that this loss may contribute to impairments in glymphatic clearance, thus bringing about signature AD pathology [205]. In this study, the findings of Zeppenfeld *et al.* are extended upon, by quantifying regional A β and tau levels and correlating these to measures of AQP4 in the corresponding regions. Although an AD-related reduction in polarisation is reported, no correlations were observed between polarisation and A β and tau burden. However, a

negative correlation was observed between NFT burden and AQP4 area coverage across all subjects. Thus, this may suggest that a reduction in NFT burden may be brought about by a high amount of aquaporin-4 coverage across the brain. Studies in mice have shown that the loss of perivascular polarisation is accompanied by a redistribution of AQP4 to non-end foot domains [252]. Perhaps then, a greater distribution of AQP4 is more beneficial over greater polarisation in reducing tau pathology. Interestingly here, a positive correlation between AQP4 area coverage and the AQP4 M1 isoform is also observed. AQP4 M1 is known for its propensity to move freely across the plasma membrane and towards extending processes, thus facilitating cellular migration, over the M23 isoform which is responsible for the formation of rigid orthogonal arrays at the end foot [166]. This indicates that the M1 isoform is more beneficial in facilitating expansive coverage of AQP4 whereas the M23 isoform is more important in maintenance of polarisation integrity. Thus, the positive correlation between AQP4 M1 and AQP4 coverage here is appropriate.

In a study that mathematically modelled AQP4 mediated water movement, a reported observation was that the removal of non-perivascular connecting astrocytic units resulted in a reduction in fluid flow between periarterial and perivenous compartments [162]. This indicates that the formation of a network of an AQP4 via a continuous astrocytic syncytium is crucial for fluid movement, above and beyond the perivascular presence of AQP4, to maintain solute movement through the brain parenchyma. It has been reported that perivascular astrocytic AQP4 is a third less in human astrocytes compared to mice, due to a higher degree of AQP4 expression in parenchymal astrocytes [244]. Continuous parenchymal expression may be more beneficial in glymphatic movement of solutes such as tau from the parenchyma and may explain the negative correlation observed here between NFT burden and AQP4 coverage.

Curiously, in the hippocampal CA1 region, a reduction in polarisation and area coverage of AQP4 was observed in the MCI group. However, no associations were observed between AD pathology and AQP4 measures. The CA1 region is known to suffer both tau and A β pathology from the mid to late stages of the disease [14], and in the subjects tested here,

significant pathology was observed in this region. In the mouse brain, hippocampal astrocytes express higher AQP4 in the CA1 region in particular [253]. Reactive astrogliosis is a feature of the AD brain, and studies using transgenic mice have also shown that astroglial atrophy with diminished processes and decreased numbers are associated with increasing AD pathology [254]. Taken together, it is plausible that AQP4 changes are no longer detectable in the hippocampal regions given the significant pathological changes. Nonetheless, this study for the first time reports an association between cortical tau pathology and AQP4 in the human brain.

Looking to the AQP4 rs3763043 SNP associations, while I report that AD subjects have reduced polarisation, I found that the demented carriers of this SNP had increased polarisation, with a trend towards reduced plaque and tangle pathology in these subjects. In the study that originally identified this as one of several SNPs associated with AD outcomes, the rs3763043 SNP was associated with faster cognitive decline [245]. Interestingly, this SNP has been investigated in the context of other brain anomalies including sudden infant death syndrome [255], traumatic brain injury (TBI) [256], neuromyelitis optica [257,258], oedema [259], migraine [260] and intracerebral haemorrhage [261]. In these studies, the rs3763043 SNP was associated with poorer outcomes in TBI [256] and higher incidence of neuromyelitis optica [257], both neurodegenerative conditions. Given these findings and the growing body of experimental evidence implicating AQP4 changes in glymphatic clearance of A β and tau pathology, further pursual of this SNP in the AD setting is warranted.

In this study, I find that in the dementia setting in the presence of this SNP, AQP4 is more polarised than usual. Thus this may suggest that this SNP offers a protective effect towards maintaining AQP4 end foot integrity. An ongoing larger cohort study indicates that the rs3763043 SNP is associated with reduced tau, P-tau and rate of change of cortical thickness (data unpublished, personal communication J. Iliff, 2019). If these isolated findings are taken in concert, it then drives new mechanistic hypotheses: it is conceivable that this SNP improves AQP4 profile, and therefore may help clear more tau, thus reducing CSF tau levels and slowing atrophy to a certain degree. Perhaps this helps these individuals maintain a

higher brain and cognitive reserve even in the face of AD. Given that individuals who have a high cognitive reserve suffer a faster cognitive decline once diagnosed with AD [39], the previous observation of faster cognitive decline with this SNP may allude to this phenomenon. The data here do not enable such conclusive connections to be made, but helps drive future experimental design around these hypotheses. In order to test this, an ideal cohort requires a large group of AD and healthy age matched subjects, containing both carriers of the SNP and wild type alleles, studied longitudinally, with cognitive measures and brain volume measures longitudinally collected from the point of diagnosis, and followed up post-mortem with detailed histological study for AQP4 measures and pathology. Collecting these detailed in-life and post-mortem measures in the same subjects will tease out if the rs3763043 SNP of AQP4 modulates brain changes in the mechanistic way hypothesised here.

The precise molecular pathways through which this SNP acts to change pathology by changing AQP4 profile also needs to be verified. rs3763043 is a noncoding SNP found in the 3' untranslated region (3' UTR) of the *AQP4* gene [245]. The 3' UTR can post-translationally influence the expression a gene via a myriad of regulatory mechanisms: from altered translation which can change overall protein expression levels, to variants via alternative splicing [262]. Biological aspects of this noncoding region could be explored to understand how these SNPs change AQP4 structure, function or location. The previous study that found reduced polarisation of AQP4 in AD subjects reported that the ratio of AQP4-M1 to AQP4-M23 was decreased, and was thought to contribute to this altered polarisation [205]. It is plausible that SNPs may contribute to such a mechanistic change, however, this was not probed in that study. The Western blot data in this study was unable to probe isoform expression levels by SNP status due to a lack of sample numbers on this assay, but probing this in a future comprehensive study is of benefit given the previous findings. In order to overcome the limitations of studying the human brain *in vivo*, these mechanisms could be modelled and studied *in vitro*. Generation of human induced pluripotent stem cells (iPSC) from SNP carriers enables a feasible *in vitro* laboratory approach to study the influence of SNPs on protein behaviour, as well as their response to experimentally controlled modifiable

factors [263]. This may provide a novel window into the study of the components of human glymphatics in AD.

In trying to understand how glymphatic changes play out in human AD, exploring other astrocytic end foot elements, particularly those associated with AQP4, may offer additional pieces in the puzzle. AQP4 is anchored to the astrocytic end foot by the DAC [264], of which DTNA is also member [265]. In addition to DTNA expression being predictive of AD status [247], a large ongoing cohort study is revealing several DTNA SNPs to be associated with AD markers (data unpublished, personal communication, J. Iliff 2019).

Here, I observed a decrease in age related expression of DTNA but not polarisation and a decrease in DTNA polarisation in the presence of A β pathology in mice. Previous studies have shown that AQP4 polarisation is reduced in the aging brain [183,205]. These data suggest that DTNA does not undergo the same polarisation change despite having a reduction in overall expression with age. However, AQP4 polarisation has been reported to be reduced with the presence of A β pathology [252]. Given that DTNA and AQP4 share expression profiles [246], it is conceivable that this decrease is also expected with A β pathology. Yet in humans, an increase in DTNA is associated with cortical tau pathology [247]. Thus, alterations in DTNA profiles may be distinct between the two pathologies or even species. Nonetheless, this is the first time DTNA has been probed directly in models of aging and amyloid pathology, and these findings warrant further investigation. Verifying these changes in expression and polarisation against other models that demonstrate AQP4 mislocalisation would be beneficial – one such example would be knockout mice of alpha1-syntrophin (SNTA), another DAC candidate. SNTA has been shown to colocalise with AQP4 at the astrocytic end feet in mice, and mice lacking SNTA show an absence of polarised AQP4 [266].

The pursuit of gene variants that are associated with AD has the potential to uncover as yet undiscovered mechanisms in the AD continuum. If glymphatic failure in clearance of pathogenic proteins is one pathway towards disease onset, studying gene variants of the molecular components of the glymphatic system is prudent. In understanding the

relationships between the molecular components of the glymphatic system and the proteinaceous aggregates implicated in AD, we may be able to modulate this mechanism via AQP4 and related proteins, thus exposing a unique therapeutic target. As such, understanding these mechanisms in the laboratory setting of mouse models as well as in the clinical context of the human disease will help paint a clearer mechanistic picture. The data presented here provide a step in this direction.

8. Concluding Remarks

Despite significant research advances in various avenues of Alzheimer's disease (AD) research, finding a disease modifying cure has been challenging. The precise mechanisms that bring about the pathogenic accumulation of amyloid- β ($A\beta$) plaques and tau neurofibrillary tangles (NFTs) are still a conundrum. These however have been major focal points in the AD research sphere and studying these proteins have given rise to several strands of new and interesting research areas.

Clearance of proteins from the brain via the glymphatic system is one such novel research avenue. Both $A\beta$ and tau have been implicated as candidates for clearance via this system, demonstrated via a myriad of experiments including two photon imaging, fluorescence microscopy, radioactive counting and histological analyses [151,179,183,217]. However, these studies only provided a snapshot view of isolated components of the glymphatic pathway, and thus gave room for whole brain characterisation and real-time observation of glymphatic flow. In the work presented in this thesis, I attempted to address this gap by using magnetic resonance imaging (MRI) on mouse models of AD.

By first reproducing parts of the experimental work in Iliff *et al.*'s seminal publication [151], I demonstrated the size based dependence of the spatial pattern and ingress of solutes from the cerebrospinal fluid (CSF) into the brain tissue. These experiments provided the foundations for the large part of the subsequent methods used in this thesis, and revealed the intricacies of working with a surgically manipulated mouse model system of CSF-ISF exchange measurement. The work enabled me to attain a suitable flowrate to use in long MRI experiments which aimed to use dynamic contrast enhancement (DCE) to track and quantify solute ingress in real time. However, a key learning point that was highlighted through these and the succeeding MRI experiments in the tau and amyloid mouse models was that when undertaking experiments of this nature, several other factors need to be considered. Burdens to physiology as a result of surgery and anaesthesia, genetic background strain, origin of mouse cohort and health status all contributed to variability in quantifying glymphatic ingress by DCE-MRI.

Despite these challenges, I show here that glymphatic inflow can be characterised in the mouse brain, with temporal and spatial clarity, and this pattern was diminished with pharmacological blockade of the water channel aquaporin-4 (AQP4). The demonstration of AQP4 blockade was crucial in this characterisation given the imperative role of this protein previously demonstrated in glymphatic study and its association with neurodegeneration. Whilst the MRI protocol does not resolve the perivascular space, the question of whether it was indeed glymphatic ingress that was observed in the DCE-MRI experiments was supported here with these observations.

The regional pattern in the cortex of wild type C57BL/6J mice combined with the early observation of a corresponding regional variance in tau deposition in the rTg450 mice provides evidence that clearance rates can potentiate levels of pathology at an early stage. This was buoyed by the observations in the experiments that injected tau into the brain and observed a reduction in clearance when AQP4 was blocked. Further indications towards the role of glymphatic function in tau burden was also alluded to in the human post mortem investigations, with an increase in AQP4 coverage showing decrease in tau burden.

The data investigating human brains also paved way for several novel hypotheses to be investigated. In particular, understanding the role of single nucleotide polymorphisms (SNPs) in AQP4 function, as well as the link to dementia status could provide novel, as yet undiscovered genetic markers for AD. Furthermore, exploring other cellular components related to AQP4, such as dystrobrevin (DTNA) or associated dystroglycan anchoring complex proteins may also provide new markers and biological insights into the relationship between fluid exchange, clearance and disease onset.

Several challenges currently exist with this field. First, the precise driving mechanisms underlying glymphatic function need to be fully resolved and reproducibly quantified. Additionally, the body of evidence towards perivascular fluid movement and clearance in the direction opposing blood flow [267] as well as the recently discovered meningeal lymphatics in the mouse brain [152] must also be considered. A key question that remains to be answered in the body of neuroscience research being undertaken in clearance

mechanisms, is the precise contributions and coexistence of these various pathways. It remains to be seen if one specific pathway failure contributes to the specific cascade of events that bring about AD. Quantifying these in tandem presents a major challenge for this field given the scarcity of combined data in these emerging strands of research, but also presents as a necessity. More broadly, the existence of glymphatic clearance in the human brain needs to be confirmed. While some imaging studies have functionally alluded to this [241–243], emerging studies that are attempting to characterise perivascular spaces may provide the requisite physiological evidence of the physical features that form this clearance network in the human brain [268].

A key advantage of working within the glymphatic component of the various fluid networks of the brain is that, first, it provides an alternative route to the blood brain barrier (BBB). Second, if AQP4 can be pharmacologically manipulated to stop CSF ingress, it may also theoretically present a therapeutic target. Drugs to help speed up the clearance of toxic proteinaceous molecules via AQP4 mediation may provide a promising approach; one such agent, TGN-073 [269] is currently being investigated for its neuroprotective potential in a murine model of tauopathy, within our laboratory.

A significant limitation in the work presented in this thesis, is the inability of the techniques used here to resolve the perivascular space in the rodent brain. But new work emerging from our laboratory, that stemmed from the work I presented here, is showing promise towards this goal [270]. Given the invasive nature and technical setup required to quantify glymphatic function, the next major challenge this body of work presents is the ability to quantify glymphatic changes non-invasively and without the use of contrast. The development of a non-invasive imaging method is particularly crucial if we are to develop a protocol that can be clinically translated to clearly quantify glymphatic changes during the onset of neurodegenerative pathologies. The work I presented here provides significant insights into the relationship between AQP4 and AD pathology in the context of glymphatic clearance, and as such, paves the way for the development of non-invasive characterisation of glymphatic function.

References

- [1] Strassnig M, Ganguli M (2005) About a peculiar disease of the cerebral cortex: Alzheimer's original case revisited. *Psychiatry (Edgmont)*.
- [2] Pantel J (2017) Alzheimer-Demenz von Auguste Deter bis heute. *Z. Gerontol. Geriatr.*
- [3] Engelhardt E, Gomes M da M (2015) Alzheimer's 100th anniversary of death and his contribution to a better understanding of Senile dementia. *Arq. Neuropsiquiatr.*
- [4] Goedert M (2009) Oskar Fischer and the study of dementia. *Brain.*
- [5] Jellinger KA (2003) Alzheimer Disease: The Changing View. Robert Katzman and Katherine Bick. Academic Press, San Diego, San Francisco, New York, Boston, London, Sydney, Tokyo 2000. 387 pp., ISBN 0-12-401955-2. *Eur. J. Neurol.*
- [6] Hippus H, Neundörfer G (2003) The discovery of Alzheimer's disease. *Dialogues Clin. Neurosci.*
- [7] Hardy J (2006) A Hundred Years of Alzheimer's Disease Research. *Neuron.*
- [8] Katzman R (2008) The Prevalence and Malignancy of Alzheimer Disease. A Major Killer. *Alzheimer's Dement.*
- [9] Graeber MB, Kösel S, Grasbon-Frodol E, Möller HJ, Mehraein P (1998) Histopathology and APOE genotype of the first Alzheimer disease patient, Auguste D. *Neurogenetics.*
- [10] Dening T, Sandilyan MB (2015) Dementia: definitions and types. *Nurs. Stand.*
- [11] Evidence and Research, Global Health Estimates 2015: Deaths by Cause, Age, Sex, by Country and by Region, 2000-2015., Last updated 2016, Accessed on 2016.
- [12] Alzheimer's Disease International (2015) World Alzheimer report 2015: The global impact of dementia. *Alzheimer's Dis. Int.*

- [13] Sperling RA, Aisen PS, Beckett LA, Bennett DA, Craft S, Fagan AM, Iwatsubo T, Jack CR, Kaye J, Montine TJ, Park DC, Reiman EM, Rowe CC, Siemers E, Stern Y, Yaffe K, Carrillo MC, Thies B, Morrison-Bogorad M, Wagster M V., Phelps CH (2011) Toward defining the preclinical stages of Alzheimer's disease: Recommendations from the National Institute on Aging-Alzheimer's Association workgroups on diagnostic guidelines for Alzheimer's disease. *Alzheimer's Dement.* **7**, 280–292.
- [14] Braak H, Braak E (1991) Neuropathological staging of Alzheimer-related changes. *Acta Neuropathol.*
- [15] Mirra SS, Heyman A, McKeel D, Sumi SM, Crain BJ, Brownlee LM, Vogel FS, Hughes JP, van Belle G, Berg L (1991) The Consortium to Establish a Registry for Alzheimer's Disease (CERAD). Part II. Standardization of the neuropathologic assessment of Alzheimer's disease. *Neurology.*
- [16] Braak H, Alafuzoff I, Arzberger T, Kretschmar H, Tredici K (2006) Staging of Alzheimer disease-associated neurofibrillary pathology using paraffin sections and immunocytochemistry. *Acta Neuropathol.*
- [17] McKhann GM, Knopman DS, Chertkow H, Hyman BT, Jack CR, Kawas CH, Klunk WE, Koroshetz WJ, Manly JJ, Mayeux R, Mohs RC, Morris JC, Rossor MN, Scheltens P, Carrillo MC, Thies B, Weintraub S, Phelps CH (2011) The diagnosis of dementia due to Alzheimer's disease: Recommendations from the National Institute on Aging-Alzheimer's Association workgroups on diagnostic guidelines for Alzheimer's disease. *Alzheimer's Dement.*
- [18] Glenner GG, Wong CW (1984) Alzheimer's disease: Initial report of the purification and characterization of a novel cerebrovascular amyloid protein. *Biochem. Biophys. Res. Commun.*
- [19] Hardy J, Allsop D (1991) Amyloid deposition as the central event in the aetiology of

Alzheimer's disease. *Trends Pharmacol. Sci.*

- [20] Hardy J, Selkoe DJ (2002) The amyloid hypothesis of Alzheimer's disease: Progress and problems on the road to therapeutics. *Science* (80-).
- [21] Selkoe D (2002) Cell Biology of the Amyloid beta-Protein Precursor and the Mechanism of Alzheimer's Disease. *Annu. Rev. Cell Dev. Biol.*
- [22] Yamada M, Itoh Y, Suematsu N, Otomo E, Matsushita M (1997) Vascular Variant of Alzheimer's Disease Characterized by Severe Plaque-Like β Protein Angiopathy. *Dement. Geriatr. Cogn. Disord.* **8**, 163–168.
- [23] Priller C, Bauer T, Mitteregger G, Krebs B, Kretzschmar HA, Herms J (2006) Synapse Formation and Function Is Modulated by the Amyloid Precursor Protein. *J. Neurosci.* **26**, 7212–7221.
- [24] Gunawardena S, Goldstein LSB (2001) Disruption of Axonal Transport and Neuronal Viability by Amyloid Precursor Protein Mutations in *Drosophila*. *Neuron* **32**, 389–401.
- [25] Chen GF, Xu TH, Yan Y, Zhou YR, Jiang Y, Melcher K, Xu HE (2017) Amyloid beta: Structure, biology and structure-based therapeutic development. *Acta Pharmacol. Sin.*
- [26] Kaether C, Haass C, Steiner H (2006) Assembly, trafficking and function of γ -secretase. In *Neurodegenerative Diseases*.
- [27] Kaye R, Head E, Thompson JL, McIntire TM, Milton SC, Cotman CW, Glabe CG (2003) Common structure of soluble amyloid oligomers implies common mechanism of pathogenesis. *Science* (80-).
- [28] Jarrett JT, Berger EP, Lansbury PT (1993) The Carboxy Terminus of the β Amyloid Protein Is Critical for the Seeding of Amyloid Formation: Implications for the

- [29] MANN DMA, BROWN A, PRINJA D, DAVIES CA, LANDON M, MASTERS CL, BEYREUTHER K (1989) AN ANALYSIS OF THE MORPHOLOGY OF SENILE PLAQUES IN DOWN'S SYNDROME PATIENTS OF DIFFERENT AGES USING IMMUNOCYTOCHEMICAL AND LECTIN HISTOCHEMICAL TECHNIQUES. *Neuropathol. Appl. Neurobiol.*
- [30] Iwatsubo T, Mann DMA, Odaka A, Suzuki N, Ihara Y (1995) Amyloid beta protein (ABeta) deposition: Abeta42(43) precedes Abeta40 in down Syndrome. *Ann. Neurol.*
- [31] Van Broeckhoven C, Haan J, Bakker E, Hardy JA, Van Hul W, Wehnert A, Vegter-Van Der Vlis M, Roos RAC (1990) Amyloid β protein precursor gene and hereditary cerebral hemorrhage with amyloidosis (Dutch). *Science (80- .)*
- [32] Goate A, Chartier-Harlin MC, Mullan M, Brown J, Crawford F, Fidani L, Giuffra L, Haynes A, Irving N, James L, Mant R, Newton P, Rooke K, Roques P, Talbot C, Pericak-Vance M, Roses A, Williamson R, Rossor M, Owen M, Hardy J (1991) Segregation of a missense mutation in the amyloid precursor protein gene with familial Alzheimer's disease. *Nature*.
- [33] Mullan M, Crawford F, Axelman K, Houlden H, Lilius L, Winblad B, Lannfelt L (1992) A pathogenic mutation for probable Alzheimer's disease in the APP gene at the N-terminus of β -amyloid. *Nat. Genet.*
- [34] Scheuner D, Eckman C, Jensen M, Song X, Citron M, Suzuki N, Bird TD, Hardy J, Hutton M, Kukull W, Larson E, Levy-Lahad E, Viitanen M, Peskind E, Poorkaj P, Schellenberg G, Tanzi R, Wasco W, Lannfelt L, Selkoe D, Younkin S (1996) Secreted amyloid β -protein similar to that in the senile plaques of Alzheimer's disease is increased in vivo by the presenilin 1 and 2 and APP mutations linked to familial Alzheimer's disease. *Nat. Med.*

- [35] Bentahir M, Nyabi O, Verhamme J, Tolia A, Horré K, Wiltfang J, Esselmann H, De Strooper B (2006) Presenilin clinical mutations can affect γ -secretase activity by different mechanisms. *J. Neurochem.*
- [36] Cai XD, Golde TE, Younkin SG (1993) Release of excess amyloid β protein from a mutant amyloid β protein precursor. *Science (80-)*.
- [37] Tamaoka A, Odaka A, Ishibashi Y, Usami M, Sahara N, Suzuki N, Nukina N, Mizusawa H, Shoji S, Kanazawa I, Mori H (1994) APP717 missense mutation affects the ratio of amyloid β protein species (A β 1-42/43 and A β 1-40) in familial Alzheimer's disease brain. *J. Biol. Chem.*
- [38] Brier MR, Gordon B, Friedrichsen K, McCarthy J, Stern A, Christensen J, Owen C, Aldea P, Su Y, Hassenstab J, Cairns NJ, Holtzman DM, Fagan AM, Morris JC, Benzinger TLS, Ances BM (2016) Tau and A β imaging, CSF measures, and cognition in Alzheimer's disease. *Sci. Transl. Med.* **8**, 338ra66.
- [39] Stern Y (2012) Cognitive reserve in ageing and Alzheimer's disease. *Lancet Neurol.*
- [40] Grundke-Iqbal I, Wang GP, Iqbal K, Tung YC, Wisniewski HM (1985) Alzheimer paired helical filaments: Identification of polypeptides with monoclonal antibodies. *Acta Neuropathol.*
- [41] Grundke-Iqbal I, Iqbal K, Tung YC, Quinlan M, Wisniewski HM, Binder LI (1986) Abnormal phosphorylation of the microtubule-associated protein tau (tau) in Alzheimer cytoskeletal pathology. *Proc. Natl. Acad. Sci. U. S. A.*
- [42] Mandelkow EM, Mandelkow E (1998) Tau in Alzheimer's disease. *Trends Cell Biol.*
- [43] Spillantini MG, Crowther RA, Kamphorst W, Heutink P, Van Swieten JC (1998) Tau pathology in two Dutch families with mutations in the microtubule-binding region of tau. *Am. J. Pathol.*

- [44] Lee VM-Y, Goedert M, Trojanowski JQ (2002) Neurodegenerative Tauopathies. *Annu. Rev. Neurosci.*
- [45] Cleveland DW, Hwo SY, Kirschner MW (1977) Purification of tau, a microtubule-associated protein that induces assembly of microtubules from purified tubulin. *J. Mol. Biol.*
- [46] Drewes G, Ebner A, Mandelkow EM (1998) MAPs, MARKs and microtubule dynamics. *Trends Biochem. Sci.*
- [47] Noble W, Hanger DP, Miller CCJ, Lovestone S (2013) The importance of tau phosphorylation for neurodegenerative diseases. *Front. Neurol.*
- [48] Buée L, Bussière T, Buée-Scherrer V, Delacourte A, Hof PR (2000) Tau protein isoforms, phosphorylation and role in neurodegenerative disorders. *Brain Res. Rev.*
- [49] Takashima A (2013) Tauopathies and tau oligomers. *J. Alzheimer's Dis.*
- [50] Shafiei SS, Guerrero-Muñoz MJ, Castillo-Carranza DL (2017) Tau oligomers: Cytotoxicity, propagation, and mitochondrial damage. *Front. Aging Neurosci.*
- [51] Kimura T, Yamashita S, Fukuda T, Park JM, Murayama M, Mizoroki T, Yoshiike Y, Sahara N, Takashima A (2007) Hyperphosphorylated tau in parahippocampal cortex impairs place learning in aged mice expressing wild-type human tau. *EMBO J.*
- [52] Lewis J, McGowan E, Rockwood J, Melrose H, Nacharaju P, Van Slegtenhorst M, Gwinn-Hardy K, Murphy MP, Baker M, Yu X, Duff K, Hardy J, Corral A, Lin WL, Yen SH, Dickson DW, Davies P, Hutton M (2000) Neurofibrillary tangles, amyotrophy and progressive motor disturbance in mice expressing mutant (P301L)tau protein. *Nat. Genet.*
- [53] Götz J, Chen F, Van Dorpe J, Nitsch RM (2001) Formation of neurofibrillary tangles in P301L tau transgenic mice induced by A β 42 fibrils. *Science (80-).*

- [54] Haneka M et. al. (2015) Neuroinflammation in Alzheimer's disease. *Dementia, Fifth Ed.*
- [55] Lee CYD, Landreth GE (2010) The role of microglia in amyloid clearance from the AD brain. *J. Neural Transm.*
- [56] Mrak RE, Sheng JG, Griffin WST (1995) Glial cytokines in Alzheimer's disease: Review and pathogenic implications. *Hum. Pathol.*
- [57] Verkhratsky A, Olabarria M, Noristani HN, Yeh C-Y, Rodriguez JJ (2010) Astrocytes in Alzheimer's Disease. *Neurotherapeutics* **7**, 399–412.
- [58] Apelt J, Ach K, Schliebs R (2003) Aging-related down-regulation of neprilysin, a putative β -amyloid-degrading enzyme, in transgenic Tg2576 Alzheimer-like mouse brain is accompanied by an astroglial upregulation in the vicinity of β -amyloid plaques. *Neurosci. Lett.* **339**, 183–186.
- [59] Wyss-Coray T, Loike JD, Brionne TC, Lu E, Anankov R, Yan F, Silverstein SC, Husemann J (2003) Adult mouse astrocytes degrade amyloid- β in vitro and in situ. *Nat. Med.* **9**, 453–457.
- [60] Ahmad MH, Fatima M, Mondal AC (2019) Influence of microglia and astrocyte activation in the neuroinflammatory pathogenesis of Alzheimer's disease: Rational insights for the therapeutic approaches. *J. Clin. Neurosci.* **59**, 6–11.
- [61] Bartus RT, 3rd DR, B B, AS. L (1982) The cholinergic hypothesis of geriatric memory dysfunction. *Science (80-.).*
- [62] H. Ferreira-Vieira T, M. Guimaraes I, R. Silva F, M. Ribeiro F (2016) Alzheimer's disease: Targeting the Cholinergic System. *Curr. Neuropharmacol.*
- [63] Hampel H, Mesulam MM, Cuello AC, Farlow MR, Giacobini E, Grossberg GT, Khachaturian AS, Vergallo A, Cavado E, Snyder PJ, Khachaturian ZS (2018) The

cholinergic system in the pathophysiology and treatment of Alzheimer's disease. *Brain*.

- [64] Ramos-Rodriguez JJ, Pacheco-Herrero M, Thyssen D, Murillo-Carretero MI, Berrocoso E, Spires-Jones TL, Bacskai BJ, Garcia-Alloza M (2013) Rapid β -amyloid deposition and cognitive impairment after cholinergic denervation in APP/PS1 mice. *J. Neuropathol. Exp. Neurol.*
- [65] Wong TP, Debeir T, Duff K, Cuello AC (2018) Reorganization of Cholinergic Terminals in the Cerebral Cortex and Hippocampus in Transgenic Mice Carrying Mutated Presenilin-1 and Amyloid Precursor Protein Transgenes. *J. Neurosci.*
- [66] Alzheimer's Association (2018) *2018 Alzheimer's Disease Facts and Figures. Alzheimers Dement* 2018;14(3):367-429.
- [67] Loy CT, Schofield PR, Turner AM, Kwok JBJ (2014) Genetics of dementia. *Lancet*.
- [68] Bateman RJ, Aisen PS, De Strooper B, Fox NC, Lemere CA, Ringman JM, Salloway S, Sperling RA, Windisch M, Xiong C (2011) Autosomal-dominant Alzheimer's disease: A review and proposal for the prevention of Alzheimer's disease. *Alzheimer's Res. Ther.*
- [69] Kim J, Basak JM, Holtzman DM (2009) The Role of Apolipoprotein E in Alzheimer's Disease. *Neuron*.
- [70] Yu J-T, Tan L, Hardy J (2014) Apolipoprotein E in Alzheimer's Disease: An Update. *Annu. Rev. Neurosci.*
- [71] Liao F, Yoon H, Kim J (2017) Apolipoprotein e metabolism and functions in brain and its role in Alzheimer's disease. *Curr. Opin. Lipidol.*
- [72] Guerreiro R, Wojtas A, Bras J, Carrasquillo M, Rogaeva E, Majounie E, Cruchaga C, Sassi C, Kauwe JSK, Younkin S, Hazrati L, Collinge J, Pocock J, Lashley T,

- Williams J, Lambert J-C, Amouyel P, Goate A, Rademakers R, Morgan K, Powell J, St George-Hyslop P, Singleton A, Hardy J, Alzheimer Genetic Analysis Group TAGA (2013) TREM2 variants in Alzheimer's disease. *N. Engl. J. Med.* **368**, 117–27.
- [73] Jay TR, von Saucken VE, Landreth GE (2017) TREM2 in Neurodegenerative Diseases. *Mol. Neurodegener.* **12**, 56.
- [74] Ulrich JD, Holtzman DM (2016) TREM2 Function in Alzheimer's Disease and Neurodegeneration. *ACS Chem. Neurosci.*
- [75] Mutations Search | ALZFORUM.
- [76] Piaceri I, Nacmias B, Sorbi S (2013) Genetics of familial and sporadic Alzheimer's disease. *Front. Biosci. (Elite Ed).*
- [77] "Physical activity." The AlzRisk Database. Alzheimer Research Forum.
- [78] "Dietary pattern." The AlzRisk Database. Alzheimer Research Forum.
- [79] "Alcohol Intake." The AlzRisk Database. Alzheimer Research Forum.
- [80] Sando SB, Melquist S, Cannon A, Hutton M, Sletvold O, Saltvedt I, White LR, Lydersen S, Aasly J (2008) Risk-reducing effect of education in Alzheimer's disease. *Int. J. Geriatr. Psychiatry.*
- [81] "Cognitive activity." The AlzRisk Database. Alzheimer Research Forum.
- [82] Shankar A, Hamer M, McMunn A, Steptoe A (2013) Social isolation and loneliness: relationships with cognitive function during 4 years of follow-up in the English Longitudinal Study of Ageing. *Psychosom. Med.* **75**, 161–70.
- [83] Wilson RS, Krueger KR, Arnold SE, Schneider JA, Kelly JF, Barnes LL, Tang Y, Bennett DA (2007) Loneliness and Risk of Alzheimer Disease. *Arch. Gen. Psychiatry* **64**, 234.

- [84] Donovan NJ, Okereke OI, Vannini P, Amariglio RE, Rentz DM, Marshall GA, Johnson KA, Sperling RA (2016) Association of Higher Cortical Amyloid Burden With Loneliness in Cognitively Normal Older Adults. *JAMA Psychiatry* **73**, 1230.
- [85] Lin FR, Yaffe K, Xia J, Xue Q-L, Harris TB, Purchase-Helzner E, Satterfield S, Ayonayon HN, Ferrucci L, Simonsick EM, Health ABC Study Group for the (2013) Hearing Loss and Cognitive Decline in Older Adults. *JAMA Intern. Med.* **173**, 293.
- [86] Castellani RJ, Perry G (2019) Tau Biology, Tauopathy, Traumatic Brain Injury, and Diagnostic Challenges. *J. Alzheimer's Dis.* **67**, 447–467.
- [87] Rubenstein R (2012) Traumatic Brain Injury: Risk Factors and Biomarkers of Alzheimer's Disease and Chronic Traumatic Encephalopathy. *Curr. Transl. Geriatr. Exp. Gerontol. Rep.* **1**, 143–148.
- [88] Macedo AC, Balouch S, Tabet N (2017) Is Sleep Disruption a Risk Factor for Alzheimer's Disease? *J. Alzheimer's Dis.* **58**, 993–1002.
- [89] Lim ASP, Kowgier M, Yu L, Buchman AS, Bennett DA (2013) Sleep Fragmentation and the Risk of Incident Alzheimer's Disease and Cognitive Decline in Older Persons. *Sleep* **36**, 1027–1032.
- [90] Alzforum: AlzRisk AD Epidemiology Database.
- [91] Austin CP, Battey JF, Bradley A, Bucan M, Capecchi M, Collins FS, Dove WF, Duyk G, Dymecki S, Eppig JT, Grieder FB, Heintz N, Hicks G, Insel TR, Joyner A, Koller BH, Lloyd KCK, Magnuson T, Moore MW, Nagy A, Pollock JD, Roses AD, Sands AT, Seed B, Skarnes WC, Snoddy J, Soriano P, Stewart DJ, Stewart F, Stillman B, Varmus H, Varticovski L, Verma IM, Vogt TF, von Melchner H, Witkowski J, Woychik RP, Wurst W, Yancopoulos GD, Young SG, Zambrowicz B (2004) The knockout mouse project. *Nat. Genet.* **36**, 921–4.
- [92] Research Models Search | ALZFORUM.

- [93] Elder GA, Gama Sosa MA, De Gasperi R (2010) Transgenic mouse models of Alzheimer's disease. *Mt. Sinai J. Med.* **77**, 69–81.
- [94] SantaCruz K, Lewis J, Spires T, Paulson J, Kotilinek L, Ingelsson M, Guimaraes A, DeTure M, Ramsden M, McGowan E, Forster C, Yue M, Orne J, Janus C, Mariash A, Kuskowski M, Hyman B, Hutton M, Ashe KH (2005) Tau suppression in a neurodegenerative mouse model improves memory function . *Sci.* **309**, 476–481.
- [95] Ramsden M, Kotilinek L, Forster C, Paulson J, McGowan E, SantaCruz K, Guimaraes A, Yue M, Lewis J, Carlson G, Hutton M, Ashe KH (2005) Age-dependent neurofibrillary tangle formation, neuron loss, and memory impairment in a mouse model of human tauopathy (P301L). *J. Neurosci.* **25**, 10637–47.
- [96] Mucke L, Masliah E, Yu G-Q, Mallory M, Rockenstein EM, Tatsuno G, Hu K, Kholodenko D, Johnson-Wood K, McConlogue L (2000) High-Level Neuronal Expression of Abeta 1-42 in Wild-Type Human Amyloid Protein Precursor Transgenic Mice: Synaptotoxicity without Plaque Formation. *J. Neurosci.* **20**, 4050–4058.
- [97] Wright AL, Zinn R, Hohensinn B, Konen LM, Beynon SB, Tan RP, Clark IA, Abdipranoto A, Vissel B (2013) Neuroinflammation and Neuronal Loss Precede A β Plaque Deposition in the hAPP-J20 Mouse Model of Alzheimer's Disease. *PLoS One* **8**,.
- [98] Saito T, Matsuba Y, Mihira N, Takano J, Nilsson P, Itohara S, Iwata N, Saido TC (2014) Single App knock-in mouse models of Alzheimer's disease. *Nat. Neurosci.* **17**, 661–663.
- [99] Hsiao K, Chapman P, Nilsen S, Eckman C, Harigaya Y, Younkin S, Yang F, Cole G (1996) Correlative memory deficits, Abeta elevation, and amyloid plaques in transgenic mice. *Science* **274**, 99–102.

- [100] ALZFORUM - Research Models.
- [101] Therapeutics Search | ALZFORUM.
- [102] Singh M, Kaur M, Kukreja H, Chugh R, Silakari O, Singh D (2013) Acetylcholinesterase inhibitors as Alzheimer therapy: From nerve toxins to neuroprotection. *Eur. J. Med. Chem.* **70**, 165–188.
- [103] Lipton SA (2006) Paradigm shift in neuroprotection by NMDA receptor blockade: Memantine and beyond. *Nat. Rev. Drug Discov.* **5**, 160–170.
- [104] Li F, Tsien JZ (2009) Memory and the NMDA receptors. *N. Engl. J. Med.* **361**, 302–3.
- [105] Cummings J, Lee G, Ritter A, Zhong K (2018) Alzheimer's disease drug development pipeline: 2018. *Alzheimer's Dement. (New York, N. Y.)* **4**, 195–214.
- [106] Klafki H-W, Staufenbiel M, Kornhuber J, Wiltfang J (2006) Therapeutic approaches to Alzheimer's disease. *Brain* **129**, 2840–2855.
- [107] Citron M (2004) Strategies for disease modification in Alzheimer's disease. *Nat. Rev. Neurosci.* **5**, 677–685.
- [108] Panza F, Lozupone M, Solfrizzi V, Sardone R, Piccininni C, Dibello V, Stallone R, Giannelli G, Bellomo A, Greco A, Daniele A, Seripa D, Logroscino G, Imbimbo BP (2018) BACE inhibitors in clinical development for the treatment of Alzheimer's disease. *Expert Rev. Neurother.* **18**, 847–857.
- [109] Barrera-Ocampo A, Lopera F (2016) Amyloid-beta immunotherapy: the hope for Alzheimer disease? *Colomb. medica (Cali, Colomb.* **47**, 203–212.
- [110] Congdon EE, Sigurdsson EM (2018) Tau-targeting therapies for Alzheimer disease. *Nat. Rev. Neurol.* **14**, 399–415.

- [111] McKhann G, Drachman D, Folstein M, Katzman R, Price D, Stadlan EM (1984) Clinical diagnosis of Alzheimer's disease: report of the NINCDS-ADRDA Work Group under the auspices of Department of Health and Human Services Task Force on Alzheimer's Disease. *Neurology* **34**, 939–44.
- [112] Petersen RC, Doody R, Kurz A, Mohs RC, Morris JC, Rabins P V., Ritchie K, Rossor M, Thal L, Winblad B (2001) Current Concepts in Mild Cognitive Impairment. *Arch. Neurol.* **58**, 1985.
- [113] Jack CR, Knopman DS, Jagust WJ, Shaw LM, Aisen PS, Weiner MW, Petersen RC, Trojanowski JQ (2010) Hypothetical model of dynamic biomarkers of the Alzheimer's pathological cascade. *Lancet Neurol.* **9**, 119–28.
- [114] Jack CR, Knopman DS, Jagust WJ, Petersen RC, Weiner MW, Aisen PS, Shaw LM, Vemuri P, Wiste HJ, Weigand SD, Lesnick TG, Pankratz VS, Donohue MC, Trojanowski JQ, Trojanowski JQ (2013) Tracking pathophysiological processes in Alzheimer's disease: an updated hypothetical model of dynamic biomarkers. *Lancet Neurol.* **12**, 207–16.
- [115] Iturria-Medina Y, Sotero RC, Toussaint PJ, Mateos-Pérez JM, Evans AC (2016) Early role of vascular dysregulation on late-onset Alzheimer's disease based on multifactorial data-driven analysis. *Nat. Commun.* **7**, 11934.
- [116] Blennow K, Hampel H, Weiner M, Zetterberg H (2010) Cerebrospinal fluid and plasma biomarkers in Alzheimer disease. *Nat. Rev. Neurol.* **6**, 131–144.
- [117] Olsson B, Lautner R, Andreasson U, Öhrfelt A, Portelius E, Bjerke M, Hölttä M, Rosén C, Olsson C, Strobel G, Wu E, Dakin K, Petzold M, Blennow K, Zetterberg H (2016) CSF and blood biomarkers for the diagnosis of Alzheimer's disease: a systematic review and meta-analysis. *Lancet Neurol.* **15**, 673–684.
- [118] Blennow K, Zetterberg H (2018) Biomarkers for Alzheimer's disease: current status

and prospects for the future. *J. Intern. Med.* **284**, 643–663.

- [119] Klunk WE, Engler H, Nordberg A, Wang Y, Blomqvist G, Holt DP, Bergström M, Savitcheva I, Huang G-F, Estrada S, Ausén B, Debnath ML, Barletta J, Price JC, Sandell J, Lopresti BJ, Wall A, Koivisto P, Antoni G, Mathis CA, Långström B (2004) Imaging brain amyloid in Alzheimer's disease with Pittsburgh Compound-B. *Ann. Neurol.* **55**, 306–319.
- [120] Valotassiou V, Malamitsi J, Papatriantafyllou J, Dardiotis E, Tsougos I, Psimadas D, Alexiou S, Hadjigeorgiou G, Georgoulas P (2018) SPECT and PET imaging in Alzheimer's disease. *Ann. Nucl. Med.* **32**, 583–593.
- [121] Klunk WE, Mathis CA (2008) The future of amyloid-beta imaging: a tale of radionuclides and tracer proliferation. *Curr. Opin. Neurol.* **21**, 683–7.
- [122] Landau SM, Breault C, Joshi AD, Pontecorvo M, Mathis CA, Jagust WJ, Mintun MA, Alzheimer's Disease Neuroimaging Initiative (2013) Amyloid- β imaging with Pittsburgh compound B and florbetapir: comparing radiotracers and quantification methods. *J. Nucl. Med.* **54**, 70–7.
- [123] Wolk DA, Zhang Z, Boudhar S, Clark CM, Pontecorvo MJ, Arnold SE (2012) Amyloid imaging in Alzheimer's disease: comparison of florbetapir and Pittsburgh compound-B positron emission tomography. *J. Neurol. Neurosurg. Psychiatry* **83**, 923–6.
- [124] Villemagne VL, Furumoto S, Fodero-Tavoletti M, Harada R, Mulligan RS, Kudo Y, Masters CL, Yanai K, Rowe CC, Okamura N (2012) The challenges of tau imaging. *Future Neurol.* **7**, 409–421.
- [125] Okamura N, Harada R, Ishiki A, Kikuchi A, Nakamura T, Kudo Y (2018) The development and validation of tau PET tracers: current status and future directions. *Clin. Transl. imaging* **6**, 305–316.

- [126] Maruyama M, Shimada H, Suhara T, Shinotoh H, Ji B, Maeda J, Zhang M-R, Trojanowski JQ, Lee VM-Y, Ono M, Masamoto K, Takano H, Sahara N, Iwata N, Okamura N, Furumoto S, Kudo Y, Chang Q, Saido TC, Takashima A, Lewis J, Jang M-K, Aoki I, Ito H, Higuchi M (2013) Imaging of tau pathology in a tauopathy mouse model and in Alzheimer patients compared to normal controls. *Neuron* **79**, 1094–108.
- [127] Sander K, Lashley T, Gami P, Gendron T, Lythgoe MF, Rohrer JD, Schott JM, Revesz T, Fox NC, Årstad E (2016) Characterization of tau positron emission tomography tracer [18F]AV-1451 binding to postmortem tissue in Alzheimer's disease, primary tauopathies, and other dementias. *Alzheimers. Dement.* **12**, 1116–1124.
- [128] Leuzy A, Chiotis K, Lemoine L, Gillberg P-G, Almkvist O, Rodriguez-Vieitez E, Nordberg A (2019) Tau PET imaging in neurodegenerative tauopathies—still a challenge. *Mol. Psychiatry* 1.
- [129] Fox NC, Scahill RI, Crum WR, Rossor MN (1999) Correlation between rates of brain atrophy and cognitive decline in AD. *Neurology* **52**, 1687–9.
- [130] Scahill RI, Schott JM, Stevens JM, Rossor MN, Fox NC (2002) Mapping the evolution of regional atrophy in Alzheimer's disease: unbiased analysis of fluid-registered serial MRI. *Proc. Natl. Acad. Sci. U. S. A.* **99**, 4703–7.
- [131] Frisoni GB, Fox NC, Jack CR, Scheltens P, Thompson PM (2010) The clinical use of structural MRI in Alzheimer disease. *Nat. Rev. Neurol.* **6**, 67–77.
- [132] Kehoe EG, McNulty JP, Mullins PG, Bokde ALW (2014) Advances in MRI biomarkers for the diagnosis of Alzheimer's disease. *Biomark. Med.* **8**, 1151–1169.
- [133] McAleese KE, Walker L, Graham S, Moya ELJ, Johnson M, Erskine D, Colloby SJ, Dey M, Martin-Ruiz C, Taylor J-P, Thomas AJ, McKeith IG, De Carli C, Attems J (2017) Parietal white matter lesions in Alzheimer's disease are associated with cortical

neurodegenerative pathology, but not with small vessel disease. *Acta Neuropathol.* **134**, 459–473.

- [134] Fellgiebel A, Wille P, Müller MJ, Winterer G, Scheurich A, Vucurevic G, Schmidt LG, Stoeter P (2004) Ultrastructural Hippocampal and White Matter Alterations in Mild Cognitive Impairment: A Diffusion Tensor Imaging Study. *Dement. Geriatr. Cogn. Disord.* **18**, 101–108.
- [135] Gyebnár G, Szabó Á, Sirály E, Fodor Z, Sákovics A, Salacz P, Hidasi Z, Csibri É, Rudas G, Kozák LR, Csukly G (2018) What can DTI tell about early cognitive impairment? – Differentiation between MCI subtypes and healthy controls by diffusion tensor imaging. *Psychiatry Res. Neuroimaging* **272**, 46–57.
- [136] Austin BP, Nair VA, Meier TB, Xu G, Rowley HA, Carlsson CM, Johnson SC, Prabhakaran V (2011) Effects of Hypoperfusion in Alzheimer’s Disease. *J. Alzheimer’s Dis.* **26**, 123–133.
- [137] Wierenga CE, Hays CC, Zlatar ZZ (2014) Cerebral blood flow measured by arterial spin labeling MRI as a preclinical marker of Alzheimer’s disease. *J. Alzheimers. Dis.* **42 Suppl 4**, S411-9.
- [138] Buckner RL, Andrews-Hanna JR, Schacter DL (2008) *The Brain’s Default Network.* *Ann. N. Y. Acad. Sci.* **1124**, 1–38.
- [139] Wermke M, Sorg C, Wohlschläger AM, Drzezga A (2008) A new integrative model of cerebral activation, deactivation and default mode function in Alzheimer’s disease. *Eur. J. Nucl. Med. Mol. Imaging* **35**, 12–24.
- [140] Hampel H, O’Bryant SE, Molinuevo JL, Zetterberg H, Masters CL, Lista S, Kiddle SJ, Batrla R, Blennow K (2018) Blood-based biomarkers for Alzheimer disease: mapping the road to the clinic. *Nat. Rev. Neurol.* **14**, 639–652.
- [141] Wildsmith KR, Holley M, Savage JC, Skerrett R, Landreth GE (2013) Evidence for

- impaired amyloid β clearance in Alzheimer's disease. *Alzheimers. Res. Ther.* **5**, 33.
- [142] Enzmann DR, Pelc NJ (1992) Brain motion: measurement with phase-contrast MR imaging. *Radiology* **185**, 653–60.
- [143] Yamada S, Miyazaki M, Yamashita Y, Ouyang C, Yui M, Nakahashi M, Shimizu S, Aoki I, Morohoshi Y, McComb J (2013) Influence of respiration on cerebrospinal fluid movement using magnetic resonance spin labeling. *Fluids Barriers CNS* **10**, 36.
- [144] Ghersi-Egea J-F, Finnegan W, Chen J-L, Fenstermacher J. (1996) Rapid distribution of intraventricularly administered sucrose into cerebrospinal fluid cisterns via subarachnoid velae in rat. *Neuroscience* **75**, 1271–1288.
- [145] Linninger AA, Tangen K, Hsu C-Y, Frim D (2016) Cerebrospinal Fluid Mechanics and Its Coupling to Cerebrovascular Dynamics. *Annu. Rev. Fluid Mech.* **48**, 219–257.
- [146] Cipolla M (2010) Chapter 2 Anatomy and Ultrastructure. In *The Cerebral Circulation*.
- [147] Zlokovic B V. (2011) Neurovascular pathways to neurodegeneration in Alzheimer's disease and other disorders. *Nat. Rev. Neurosci.* **12**, 723–738.
- [148] Abbott NJ, Patabendige AAK, Dolman DEM, Yusof SR, Begley DJ (2010) Structure and function of the blood–brain barrier. *Neurobiol. Dis.* **37**, 13–25.
- [149] Mathiisen TM, Lehre KP, Danbolt NC, Ottersen OP (2010) The perivascular astroglial sheath provides a complete covering of the brain microvessels: An electron microscopic 3D reconstruction. *Glia* **58**, 1094–1103.
- [150] Scemes E, Spray DC (2003) The astrocytic syncytium. *Adv. Mol. Cell Biol.*
- [151] Iliff JJ, Wang M, Liao Y, Plogg BA, Peng W, Gundersen GA, Benveniste H, Vates GE, Deane R, Goldman SA, Nagelhus EA, Nedergaard M (2012) A Paravascular Pathway Facilitates CSF Flow Through the Brain Parenchyma and the Clearance of Interstitial Solutes, Including Amyloid β . *Sci. Transl. Med.* **4**, 147ra111-147ra111.

- [152] Louveau A, Smirnov I, Keyes TJ, Eccles JD, Rouhani SJ, Peske JD, Derecki NC, Castle D, Mandell JW, Lee KS, Harris TH, Kipnis J (2015) Structural and functional features of central nervous system lymphatic vessels. *Nature*.
- [153] Jessen NA, Munk ASF, Lundgaard I, Nedergaard M (2015) The Glymphatic System: A Beginner's Guide. *Neurochem. Res.* **40**, 2583–99.
- [154] Cserr HF, Cooper DN, Suri PK, Patlak CS (1981) Efflux of radiolabeled polyethylene glycols and albumin from rat brain. *Am. J. Physiol.* **240**, F319-28.
- [155] Rennels ML, Gregory TF, Blaumanis OR, Fujimoto K, Grady PA (1985) Evidence for a 'Paravascular' fluid circulation in the mammalian central nervous system, provided by the rapid distribution of tracer protein throughout the brain from the subarachnoid space. *Brain Res.* **326**, 47–63.
- [156] Iliff JJ, Wang M, Zeppenfeld DM, Venkataraman A, Plog BA, Liao Y, Deane R, Nedergaard M (2013) Cerebral arterial pulsation drives paravascular CSF-interstitial fluid exchange in the murine brain. *J. Neurosci.* **33**, 18190–9.
- [157] Nedergaard M (2013) Garbage truck of the brain. *Science (80-.)*.
- [158] Mestre H, Hablitz LM, Xavier AL, Feng W, Zou W, Pu T, Monai H, Murlidharan G, Castellanos Rivera RM, Simon MJ, Pike MM, Plá V, Du T, Kress BT, Wang X, Plog BA, Thrane AS, Lundgaard I, Abe Y, Yasui M, Thomas JH, Xiao M, Hirase H, Asokan A, Iliff JJ, Nedergaard M (2018) Aquaporin-4-dependent glymphatic solute transport in the rodent brain. *Elife* **7**,.
- [159] Abbott NJ (2004) Evidence for bulk flow of brain interstitial fluid: significance for physiology and pathology. *Neurochem. Int.* **45**, 545–552.
- [160] Asgari M, de Zélicourt D, Kurtcuoglu V (2016) Glymphatic solute transport does not require bulk flow. *Sci. Rep.* **6**, 38635.

- [161] Ray L, Iliff JJ, Heys JJ (2019) Analysis of convective and diffusive transport in the brain interstitium. *Fluids Barriers CNS* **16**, 6.
- [162] Asgari M, de Zélicourt D, Kurtcuoglu V (2015) How astrocyte networks may contribute to cerebral metabolite clearance. *Sci. Rep.* **5**, 15024.
- [163] Nielsen S, Smith BL, Christensen EI, Knepper MA, Agre P (1993) CHIP28 water channels are localized in constitutively water-permeable segments of the nephron. *J. Cell Biol.* **120**, 371–83.
- [164] Nielsen S, Nagelhus EA, Amiry-Moghaddam M, Bourque C, Agre P, Ottersen OP (1997) Specialized membrane domains for water transport in glial cells: high-resolution immunogold cytochemistry of aquaporin-4 in rat brain. *J. Neurosci.* **17**, 171–80.
- [165] Badaut J, Lasbennes F, Magistretti PJ, Regli L (2002) Aquaporins in Brain: Distribution, Physiology, and Pathophysiology. *J. Cereb. Blood Flow Metab.* **22**, 367–378.
- [166] Smith AJ, Jin B-J, Ratelade J, Verkman AS (2014) Aggregation state determines the localization and function of M1- and M23-aquaporin-4 in astrocytes. *J. Cell Biol.* **204**, 559–73.
- [167] Manley GT, Fujimura M, Ma T, Noshita N, Filiz F, Bollen AW, Chan P, Verkman AS (2000) Aquaporin-4 deletion in mice reduces brain edema after acute water intoxication and ischemic stroke. *Nat. Med.* **6**, 159–163.
- [168] Lu DC, Zador Z, Yao J, Fazlollahi F, Manley GT (2011) Aquaporin-4 Reduces Post-Traumatic Seizure Susceptibility by Promoting Astrocytic Glial Scar Formation in Mice. *J. Neurotrauma* neu.2011.2114.
- [169] Ren Z, Iliff JJ, Yang L, Yang J, Chen X, Chen MJ, Giese RN, Wang B, Shi X, Nedergaard M (2013) ‘Hit & Run’ Model of Closed-Skull Traumatic Brain

Injury (TBI) Reveals Complex Patterns of Post-Traumatic AQP4 Dysregulation. *J. Cereb. Blood Flow Metab.* **33**, 834–845.

- [170] Lim J, Yue Z (2015) Neuronal aggregates: formation, clearance, and spreading. *Dev. Cell* **32**, 491–501.
- [171] Song H-L, Shim S, Kim D-H, Won S-H, Joo S, Kim S, Jeon NL, Yoon S-Y (2014) β -Amyloid is transmitted via neuronal connections along axonal membranes. *Ann. Neurol.* **75**, 88–97.
- [172] Kane MD, Lipinski WJ, Callahan MJ, Bian F, Durham RA, Schwarz RD, Roher AE, Walker LC (2000) Evidence for seeding of beta -amyloid by intracerebral infusion of Alzheimer brain extracts in beta -amyloid precursor protein-transgenic mice. *J. Neurosci.* **20**, 3606–11.
- [173] LaFerla FM, Green KN, Oddo S (2007) Intracellular amyloid- β in Alzheimer's disease. *Nat. Rev. Neurosci.* **8**, 499–509.
- [174] Gaspar RC, Villarreal SA, Bowles N, Hepler RW, Joyce JG, Shughrue PJ (2010) Oligomers of β -amyloid are sequestered into and seed new plaques in the brains of an AD mouse model. *Exp. Neurol.* **223**, 394–400.
- [175] Medina M, Avila J (2014) The role of extracellular Tau in the spreading of neurofibrillary pathology. *Front. Cell. Neurosci.* **8**, 113.
- [176] Ahmed Z, Cooper J, Murray TK, Garn K, McNaughton E, Clarke H, Parhizkar S, Ward MA, Cavallini A, Jackson S, Bose S, Clavaguera F, Tolnay M, Lavenir I, Goedert M, Hutton ML, O'Neill MJ (2014) A novel in vivo model of tau propagation with rapid and progressive neurofibrillary tangle pathology: the pattern of spread is determined by connectivity, not proximity. *Acta Neuropathol.* **127**, 667–683.
- [177] Clavaguera F, Bolmont T, Crowther RA, Abramowski D, Frank S, Probst A, Fraser G, Stalder AK, Beibel M, Staufenbiel M, Jucker M, Goedert M, Tolnay M (2009)

- Transmission and spreading of tauopathy in transgenic mouse brain. *Nat. Cell Biol.* **11**, 909–913.
- [178] Jackson SJ, Kerridge C, Cooper J, Cavallini A, Falcon B, Cella C V, Landi A, Szekeres PG, Murray TK, Ahmed Z, Goedert M, Hutton M, O’Neill MJ, Bose S (2016) Short Fibrils Constitute the Major Species of Seed-Competent Tau in the Brains of Mice Transgenic for Human P301S Tau. *J. Neurosci.* **36**, 762–72.
- [179] Tarasoff-Conway JM, Carare RO, Osorio RS, Glodzik L, Butler T, Fieremans E, Axel L, Rusinek H, Nicholson C, Zlokovic B V, Frangione B, Blennow K, Ménard J, Zetterberg H, Wisniewski T, De Leon MJ (2015) Clearance systems in the brain—implications for Alzheimer disease HHS Public Access. *Nat Rev Neurol* **11**, 457–470.
- [180] Weller RO, Subash M, Preston SD, Mazanti I, Carare RO (2007) SYMPOSIUM: Clearance of A β from the Brain in Alzheimer’s Disease: Perivascular Drainage of Amyloid- β Peptides from the Brain and Its Failure in Cerebral Amyloid Angiopathy and Alzheimer’s Disease. *Brain Pathol.* **18**, 253–266.
- [181] Kang J-E, Lim MM, Bateman RJ, Lee JJ, Smyth LP, Cirrito JR, Fujiki N, Nishino S, Holtzman DM (2009) Amyloid-beta dynamics are regulated by orexin and the sleep-wake cycle. *Science* **326**, 1005–7.
- [182] Xie L, Kang H, Xu Q, Chen MJ, Liao Y, Thiyagarajan M, O’Donnell J, Christensen DJ, Nicholson C, Iliff JJ, Takano T, Deane R, Nedergaard M (2013) Sleep drives metabolite clearance from the adult brain. *Science* **342**, 373–7.
- [183] Kress BT, Iliff JJ, Xia M, Wang M, Wei H, Zeppenfeld D, Xie L, Kang H, Xu Q, Liew J, Plog BA, Ding F, Deane R, Nedergaard M (2014) Impairment of paravascular clearance pathways in the aging brain. *Ann Neurol* **76**, 845–861.
- [184] Iliff JJ, Chen MJ, Plog BA, Zeppenfeld DM, Soltero M, Yang L, Singh I, Deane R, Nedergaard M (2014) Impairment of glymphatic pathway function promotes tau

pathology after traumatic brain injury. *J. Neurosci.* **34**, 16180–93.

- [185] Gaberel T, Gakuba C, Goulay R, De Lizarrondo SM, Hanouz J-L, Emery E, Touze E, Vivien D, Gauberti M (2014) Impaired Glymphatic Perfusion After Strokes Revealed by Contrast-Enhanced MRI. *Stroke* **45**, 3092–3096.
- [186] Lundgaard I, Wang W, Eberhardt A, Vinitzky HS, Reeves BC, Peng S, Lou N, Hussain R, Nedergaard M (2018) Beneficial effects of low alcohol exposure, but adverse effects of high alcohol intake on glymphatic function. *Sci. Rep.* **8**, 2246.
- [187] von Holstein-Rathlou S, Petersen NC, Nedergaard M (2018) Voluntary running enhances glymphatic influx in awake behaving, young mice. *Neurosci. Lett.* **662**, 253–258.
- [188] Lundgaard I, Lu ML, Yang E, Peng W, Mestre H, Hitomi E, Deane R, Nedergaard M (2017) Glymphatic clearance controls state-dependent changes in brain lactate concentration. *J. Cereb. Blood Flow Metab.* **37**, 2112–2124.
- [189] Achariyar TM, Li B, Peng W, Verghese PB, Shi Y, McConnell E, Benraiss A, Kasper T, Song W, Takano T, Holtzman DM, Nedergaard M, Deane R (2016) Glymphatic distribution of CSF-derived apoE into brain is isoform specific and suppressed during sleep deprivation. *Mol. Neurodegener.* **11**, 74.
- [190] Murlidharan G, Crowther A, Reardon RA, Song J, Asokan A (2016) Glymphatic fluid transport controls paravascular clearance of AAV vectors from the brain. *JCI Insight* **1**,.
- [191] Plog BA, Dashnaw ML, Hitomi E, Peng W, Liao Y, Lou N, Deane R, Nedergaard M (2015) Biomarkers of traumatic injury are transported from brain to blood via the glymphatic system. *J. Neurosci.* **35**, 518–26.
- [192] Thrane VR, Thrane AS, Plog BA, Thiyagarajan M, Iliff JJ, Deane R, Nagelhus EA, Nedergaard M (2013) Paravascular microcirculation facilitates rapid lipid transport

and astrocyte signaling in the brain. *Sci. Rep.* **3**, 2582.

- [193] Oshio K, Watanabe H, Song Y, Verkman AS, Manley GT (2005) Reduced cerebrospinal fluid production and intracranial pressure in mice lacking choroid plexus water channel Aquaporin-1. *FASEB J.* **19**, 76–78.
- [194] Iliff JJ, Lee H, Yu M, Feng T, Logan J, Nedergaard M, Benveniste H (2013) Brain-wide pathway for waste clearance captured by contrast-enhanced MRI. *J. Clin. Invest.* **123**, 1299–1309.
- [195] Xavier ALR, Hauglund NL, Holstein-Rathlou S von, Li Q, Sanggaard S, Lou N, Lundgaard I, Nedergaard M (2018) Cannula Implantation into the Cisterna Magna of Rodents. *J. Vis. Exp.*
- [196] Mathieu E, Gupta N, Macdonald R, Ai J, Yücel YH (2013) In Vivo Imaging of Lymphatic Drainage of Cerebrospinal Fluid in Mouse. *Fluids Barriers CNS* **10**, 35.
- [197] Bedussi B, Almasian M, de Vos J, VanBavel E, Bakker EN (2018) Paravascular spaces at the brain surface: Low resistance pathways for cerebrospinal fluid flow. *J. Cereb. Blood Flow Metab.* **38**, 719–726.
- [198] Yang L, Kress BT, Weber HJ, Thiyagarajan M, Wang B, Deane R, Benveniste H, Iliff JJ, Nedergaard M (2013) Evaluating glymphatic pathway function utilizing clinically relevant intrathecal infusion of CSF tracer. *J. Transl. Med.* **11**, 107.
- [199] Bedussi B, van der Wel NN, de Vos J, van Veen H, Siebes M, VanBavel E, Bakker EN (2017) Paravascular channels, cisterns, and the subarachnoid space in the rat brain: A single compartment with preferential pathways. *J. Cereb. Blood Flow Metab.* **37**, 1374–1385.
- [200] Bolon B, Butt MT (2011) *Fundamental neuropathology for pathologists and toxicologists : principles and techniques*, John Wiley & Sons.

- [201] Pardridge W. (1991) Transnasal and intraventricular delivery of drugs. In *Peptide Drug Delivery to the Brain* Raven Press, p. 112.
- [202] Thorne RG, Nicholson C (2006) In vivo diffusion analysis with quantum dots and dextrans predicts the width of brain extracellular space. *Proc. Natl. Acad. Sci.* **103**, 5567–5572.
- [203] Syková E, Nicholson C (2008) Diffusion in Brain Extracellular Space. *Physiol. Rev.* **88**, 1277–1340.
- [204] Xu Z, Xiao N, Chen Y, Huang H, Marshall C, Gao J, Cai Z, Wu T, Hu G, Xiao M Deletion of aquaporin-4 in APP/PS1 mice exacerbates brain A β accumulation and memory deficits.
- [205] Zeppenfeld DM, Simon M, Haswell JD, D'Abreo D, Murchison C, Quinn JF, Grafe MR, Woltjer RL, Kaye J, Iliff JJ (2017) Association of Perivascular Localization of Aquaporin-4 With Cognition and Alzheimer Disease in Aging Brains. *JAMA Neurol.* **74**, 91.
- [206] Huber VJ, Tsujita M, Nakada T (2009) Identification of Aquaporin 4 inhibitors using in vitro and in silico methods. *Bioorganic Med. Chem.*
- [207] Paxinos G, Franklin KBJ (2012) *Paxinos and Franklin's the Mouse Brain in Stereotaxic Coordinates.*
- [208] Lee H, Mortensen K, Sanggaard S, Koch P, Brunner H, Quistorff B, Nedergaard M, Benveniste H (2018) Quantitative Gd-DOTA uptake from cerebrospinal fluid into rat brain using 3D VFA-SPGR at 9.4T. *Magn. Reson. Med.* **79**, 1568–1578.
- [209] Robshaw AE, Kawabe TT, Caouette D, Brown TM, Soares HD, Hicks CD, Milici AJ, JoAnn Dumin (2010) Characterization of rTg4510 mice yields evidence of significant neuroinflammation. *Alzheimer's Dement.*

- [210] Guo JL, Narasimhan S, Changolkar L, He Z, Stieber A, Zhang B, Gathagan RJ, Iba M, McBride JD, Trojanowski JQ, Lee VMY (2016) Unique pathological tau conformers from Alzheimer's brains transmit tau pathology in nontransgenic mice. *J. Exp. Med.* **213**, 2635–2654.
- [211] Igarashi H, Tsujita M, Suzuki Y, Kwee IL, Nakada T (2013) Inhibition of aquaporin-4 significantly increases regional cerebral blood flow. *Neuroreport* **24**, 324–8.
- [212] Nagai H, Moritake K, Takaya M (1997) Correlation Between Transcranial Doppler Ultrasonography and Regional Cerebral Blood Flow in Experimental Intracranial Hypertension. *Stroke* **28**, 603–608.
- [213] Trillo-Contreras JL, Toledo-Aral JJ, Echevarría M, Villadiego J (2019) AQP1 and AQP4 Contribution to Cerebrospinal Fluid Homeostasis. *Cells* **8**,.
- [214] Saunders TL (2011) Inducible Transgenic Mouse Models. In Humana Press, pp. 103–115.
- [215] Zlokovic B V., Yamada S, Holtzman D, Ghiso J, Frangione B (2000) Clearance of amyloid β -peptide from brain: transport or metabolism? *Nat. Med.* **6**, 718–718.
- [216] Chesser AS, Pritchard SM, Johnson GW (2013) Tau Clearance Mechanisms and Their Possible Role in the Pathogenesis of Alzheimer Disease. *Front. Neurol.* **4**, 122.
- [217] Peng W, Achariyar TM, Li B, Liao Y, Mestre H, Hitomi E, Regan S, Kasper T, Peng S, Ding F, Benveniste H, Nedergaard M, Deane R (2016) Suppression of glymphatic fluid transport in a mouse model of Alzheimer's disease. *Neurobiol. Dis.* **93**, 215–25.
- [218] Giannakopoulos P, Herrmann FR, Bussi re T, Bouras C, Kovari E, Perl DP, Morrison JH, Gold G, Hof PR (2003) Tangle and neuron numbers, but not amyloid load, predict cognitive status in Alzheimer's disease. *Neurology* **60**, 1495–500.
- [219] Santacruz K, Lewis J, Spires T, Paulson J, Kotilinek L, Ingelsson M, Guimaraes A,

- DeTure M, Ramsden M, McGowan E, Forster C, Yue M, Orne J, Janus C, Mariash A, Kuskowski M, Hyman B, Hutton M, Ashe KH (2005) Tau suppression in a neurodegenerative mouse model improves memory function. *Science* **309**, 476–81.
- [220] Wu JW, Hussaini SA, Bastille IM, Rodriguez GA, Mrejeru A, Rilett K, Sanders DW, Cook C, Fu H, Boonen RACM, Herman M, Nahmani E, Emrani S, Figueroa YH, Diamond MI, Clelland CL, Wray S, Duff KE (2016) Neuronal activity enhances tau propagation and tau pathology in vivo. *Nat. Neurosci.* **19**, 1085–1092.
- [221] Ramsden M, Kotilinek L, Forster C, Paulson J, McGowan E, SantaCruz K, Guimaraes A, Yue M, Lewis J, Carlson G, Hutton M, Ashe KH (2005) Age-Dependent Neurofibrillary Tangle Formation, Neuron Loss, and Memory Impairment in a Mouse Model of Human Tauopathy (P301L). *J. Neurosci.* **25**, 10637–10647.
- [222] Scholz J, LaLiberté C, van Eede M, Lerch JP, Henkelman M (2016) Variability of brain anatomy for three common mouse strains. *Neuroimage* **142**, 656–662.
- [223] Kang H-M, Sohn I, Kim S, Kim D, Jung J, Jeong J-W, Park C (2015) Optical measurement of mouse strain differences in cerebral blood flow using indocyanine green. *J. Cereb. Blood Flow Metab.* **35**, 912–6.
- [224] Wells JA, O’Callaghan JM, Holmes HE, Powell NM, Johnson RA, Siow B, Torrealdea F, Ismail O, Walker-Samuel S, Golay X, Rega M, Richardson S, Modat M, Cardoso MJ, Ourselin S, Schwarz AJ, Ahmed Z, Murray TK, O’Neill MJ, Collins EC, Colgan N, Lythgoe MF (2015) In vivo imaging of tau pathology using multi-parametric quantitative MRI. *Neuroimage* **111**, 369–378.
- [225] Holmes HE, Colgan N, Ismail O, Ma D, Powell NM, O’Callaghan JM, Harrison IF, Johnson RA, Murray TK, Ahmed Z, Heggenes M, Fisher A, Cardoso MJ, Modat M, Walker-Samuel S, Fisher EMC, Ourselin S, O’Neill MJ, Wells JA, Collins EC, Lythgoe MF (2016) Imaging the accumulation and suppression of tau pathology using

multiparametric MRI. *Neurobiol. Aging* **39**,.

- [226] Middeldorp J, Hol EM (2011) GFAP in health and disease. *Prog. Neurobiol.* **93**, 421–443.
- [227] Vogt BA, Paxinos G (2014) Cytoarchitecture of mouse and rat cingulate cortex with human homologies. *Brain Struct. Funct.* **219**, 185–192.
- [228] Jones BF, Barnes J, Uylings HBM, Fox NC, Frost C, Witter MP, Scheltens P (2005) Differential Regional Atrophy of the Cingulate Gyrus in Alzheimer Disease: A Volumetric MRI Study. *Cereb. Cortex* **16**, 1701–1708.
- [229] Goedert M, Eisenberg DS, Crowther RA (2017) Propagation of Tau Aggregates and Neurodegeneration. *Annu. Rev. Neurosci.* **40**, 189–210.
- [230] David DC, Layfield R, Serpell L, Narain Y, Goedert M, Spillantini MG (2002) Proteasomal degradation of tau protein. *J. Neurochem.* **83**, 176–185.
- [231] Cirrito JR, May PC, O'Dell MA, Taylor JW, Parsadanian M, Cramer JW, Audia JE, Nissen JS, Bales KR, Paul SM, DeMattos RB, Holtzman DM (2003) In vivo assessment of brain interstitial fluid with microdialysis reveals plaque-associated changes in amyloid-beta metabolism and half-life. *J. Neurosci.* **23**, 8844–53.
- [232] Merlini M, Wanner D, Nitsch RM (2016) Tau pathology-dependent remodelling of cerebral arteries precedes Alzheimer's disease-related microvascular cerebral amyloid angiopathy. *Acta Neuropathol.* **131**, 737–752.
- [233] Hébert F, Grand'Maison M, Ho M-K, Lerch JP, Hamel E, Bedell BJ (2013) Cortical atrophy and hypoperfusion in a transgenic mouse model of Alzheimer's disease. *Neurobiol. Aging* **34**, 1644–1652.
- [234] Fantini S, Sassaroli A, Tgavalekos KT, Kornbluth J (2016) Cerebral blood flow and autoregulation: current measurement techniques and prospects for noninvasive

optical methods. *Neurophotonics* **3**, 031411.

- [235] Hong S, Quintero-Monzon O, Ostaszewski BL, Podlisny DR, Cavanaugh WT, Yang T, Holtzman DM, Cirrito JR, Selkoe DJ (2011) Dynamic Analysis of Amyloid - Protein in Behaving Mice Reveals Opposing Changes in ISF versus Parenchymal A during Age-Related Plaque Formation. *J. Neurosci.*
- [236] Hablitz LM, Vinitzky HS, Sun Q, Stæger FF, Sigurdsson B, Mortensen KN, Lilius TO, Nedergaard M (2019) Increased glymphatic influx is correlated with high EEG delta power and low heart rate in mice under anesthesia. *Sci. Adv.* **5**, eaav5447.
- [237] Benveniste H, Lee H, Ding F, Sun Q, Al-Bizri E, Makaryus R, Probst S, Nedergaard M, Stein EA, Lu H (2017) Anesthesia with Dexmedetomidine and Low-dose Isoflurane Increases Solute Transport via the Glymphatic Pathway in Rat Brain When Compared with High-dose Isoflurane. *Anesthesiology* **127**, 976–988.
- [238] Todd MM, Weeks J (1996) Comparative effects of propofol, pentobarbital, and isoflurane on cerebral blood flow and blood volume. *J. Neurosurg. Anesthesiol.* **8**, 296–303.
- [239] Giroux M-C, Hélie P, Burns P, Vachon P (2015) Anesthetic and pathological changes following high doses of ketamine and xylazine in Sprague Dawley rats. *Exp. Anim.* **64**, 253–60.
- [240] Pardridge WM (2016) CSF, blood-brain barrier, and brain drug delivery. *Expert Opin. Drug Deliv.* **13**, 963–975.
- [241] Ringstad G, Vatnehol SAS, Eide PK (2017) Glymphatic MRI in idiopathic normal pressure hydrocephalus. *Brain* **140**, 2691–2705.
- [242] Eide PK, Vatnehol SAS, Emblem KE, Ringstad G (2018) Magnetic resonance imaging provides evidence of glymphatic drainage from human brain to cervical lymph nodes. *Sci. Rep.* **8**, 7194.

- [243] Ringstad G, Valnes LM, Dale AM, Pripp AH, Vatnehol S-AS, Emblem KE, Mardal K-A, Eide PK (2018) Brain-wide glymphatic enhancement and clearance in humans assessed with MRI. *JCI insight* **3**,.
- [244] Eidsvaag VA, Enger R, Hansson H-A, Eide PK, Nagelhus EA (2017) Human and mouse cortical astrocytes differ in aquaporin-4 polarization toward microvessels. *Glia* **65**, 964–973.
- [245] Burfeind KG, Murchison CF, Westaway SK, Simon MJ, Erten-Lyons D, Kaye JA, Quinn JF, Iliff JJ (2017) The effects of noncoding aquaporin-4 single-nucleotide polymorphisms on cognition and functional progression of Alzheimer’s disease. *Alzheimer’s Dement. Transl. Res. Clin. Interv.* **3**, 348–359.
- [246] Simon MJ, Murchison C, Iliff JJ (2018) A transcriptome-based assessment of the astrocytic dystrophin associated complex in the developing human brain. *J. Neurosci. Res.* **96**, 180.
- [247] Simon MJ, Wang MX, Murchison CF, Roese NE, Boespflug EL, Woltjer RL, Iliff JJ (2018) Transcriptional network analysis of human astrocytic endfoot genes reveals region-specific associations with dementia status and tau pathology. *Sci. Rep.* **8**, 12389.
- [248] Lue LF, Brachova L, Civin WH, Rogers J (1996) Inflammation, A beta deposition, and neurofibrillary tangle formation as correlates of Alzheimer’s disease neurodegeneration. *J. Neuropathol. Exp. Neurol.* **55**, 1083–8.
- [249] West MJ, Kawas CH, Stewart WF, Rudow GL, Troncoso JC (2004) Hippocampal neurons in pre-clinical Alzheimer’s disease. *Neurobiol. Aging* **25**, 1205–1212.
- [250] Erten-Lyons D, Woltjer RL, Dodge H, Nixon R, Vorobik R, Calvert JF, Leahy M, Montine T, Kaye J (2009) Factors associated with resistance to dementia despite high Alzheimer disease pathology. *Neurology* **72**, 354–360.

- [251] Wilcock DM, Vitek MP, Colton CA (2009) Vascular amyloid alters astrocytic water and potassium channels in mouse models and humans with Alzheimer's disease. *Neuroscience* **159**, 1055–1069.
- [252] Yang J, Lunde LK, Nuntagij P, Oguchi T, Camassa LMA, Nilsson LNG, Lannfelt L, Xu Y, Amiry-Moghaddam M, Ottersen OP, Torp R (2011) Loss of Astrocyte Polarization in the Tg-ArcSwe Mouse Model of Alzheimer's Disease. *J. Alzheimer's Dis.* **27**, 711–722.
- [253] Hsu MS, Seldin M, Lee DJ, Seifert G, Steinhäuser C, Binder DK (2011) Laminar-specific and developmental expression of aquaporin-4 in the mouse hippocampus. *Neuroscience* **178**, 21–32.
- [254] Olabarria M, Noristani HN, Verkhratsky A, Rodríguez JJ (2010) Concomitant astroglial atrophy and astrogliosis in a triple transgenic animal model of Alzheimer's disease. *Glia* **58**, NA-NA.
- [255] Opdal SH, Vege Å, Stray-Pedersen A, Rognum TO (2010) Aquaporin-4 Gene Variation and Sudden Infant Death Syndrome. *Pediatr. Res.* **68**, 48–51.
- [256] Dardiotis E, Paterakis K, Tsivgoulis G, Tsintou M, Hadjigeorgiou GF, Dardioti M, Grigoriadis S, Simeonidou C, Komnos A, Kapsalaki E, Fountas K, Hadjigeorgiou GM (2014) AQP4 Tag Single Nucleotide Polymorphisms in Patients with Traumatic Brain Injury. *J. Neurotrauma* **31**, 1920–1926.
- [257] Wei Q, Yanyu C, Rui L, Caixia L, Youming L, Jianhua H, Weihua M, Xiaobo S, Wen X, Ying C, Zhengqi L, Xueqiang H (2014) Human aquaporin 4 gene polymorphisms in Chinese patients with neuromyelitis optica. *J. Neuroimmunol.* **274**, 192–196.
- [258] Qiu W, Chang Y, Li R, Long Y, Huang J, Mai W, Sun X, Lu Z, Hu X (2015) [Correlation of AQP4 gene polymorphism with NMO clinical phenotypes and its

- underlying mechanism]. *Zhonghua Yi Xue Za Zhi* **95**, 501–6.
- [259] Sorani MD, Zador Z, Hurowitz E, Yan D, Giacomini KM, Manley GT (2008) Novel variants in human Aquaporin-4 reduce cellular water permeability. *Hum. Mol. Genet.* **17**, 2379–2389.
- [260] Rubino E, Rainero I, Vaula G, Crasto F, Gravante E, Negro E, Brega F, Gallone S, Pinessi L (2009) Investigating the genetic role of aquaporin4 gene in migraine. *J. Headache Pain* **10**, 111–114.
- [261] Dardiotis E, Siokas V, Marogianni C, Aloizou A-M, Sokratous M, Paterakis K, Dardioti M, Grigoriadis S, Brotis A, Kapsalaki E, Fountas K, Jagiella J, Hadjigeorgiou GM (2019) AQP4 tag SNPs in patients with intracerebral hemorrhage in Greek and Polish population. *Neurosci. Lett.* **696**, 156–161.
- [262] Matoulkova E, Michalova E, Vojtesek B, Hrstka R (2012) The role of the 3' untranslated region in post-transcriptional regulation of protein expression in mammalian cells. *RNA Biol.* **9**, 563–576.
- [263] Hamazaki T, El Roubi N, Fredette NC, Santostefano KE, Terada N (2017) Concise Review: Induced Pluripotent Stem Cell Research in the Era of Precision Medicine. *Stem Cells* **35**, 545–550.
- [264] Lunde LK, Camassa LMA, Hoddevik EH, Khan FH, Ottersen OP, Boldt HB, Amiry-Moghaddam M (2015) Postnatal development of the molecular complex underlying astrocyte polarization. *Brain Struct. Funct.* **220**, 2087–2101.
- [265] Bragg AD, Das SS, Froehner SC (2010) Dystrophin-associated protein scaffolding in brain requires alpha-dystrobrevin. *Neuroreport* **21**, 695–9.
- [266] Inoue M, Wakayama Y, Liu JW, Murahashi M, Shibuya S, Oniki H (2002) Ultrastructural localization of aquaporin 4 and alpha1-syntrophin in the vascular feet of brain astrocytes. *Tohoku J. Exp. Med.* **197**, 87–93.

- [267] Carare RO, Bernardes-Silva M, Newman TA, Page AM, Nicoll JAR, Perry VH, Weller RO (2008) Solutes, but not cells, drain from the brain parenchyma along basement membranes of capillaries and arteries: significance for cerebral amyloid angiopathy and neuroimmunology. *Neuropathol. Appl. Neurobiol.* **34**, 131–144.
- [268] Boespflug EL, Schwartz DL, Lahna D, Pollock J, Iliff JJ, Kaye JA, Rooney W, Silbert LC (2018) MR Imaging–based Multimodal Autoidentification of Perivascular Spaces (mMAPS): Automated Morphologic Segmentation of Enlarged Perivascular Spaces at Clinical Field Strength. *Radiology* **286**, 632–642.
- [269] Huber VJ, Igarashi H, Ueki S, Kwee IL, Nakada T (2018) Aquaporin-4 facilitator TGN-073 promotes interstitial fluid circulation within the blood–brain barrier. *Neuroreport* **29**, 697–703.
- [270] Harrison IF, Siow B, Akilo AB, Evans PG, Ismail O, Ohene Y, Nahavandi P, Thomas DL, Lythgoe MF, Wells JA (2018) Non-invasive imaging of CSF-mediated brain clearance pathways via assessment of perivascular fluid movement with diffusion tensor MRI. *Elife* **7**,.